# Stony Brook University

# Investigations of Silver Vanadium Oxide and Silver Vanadium Phosphorous Oxide Solubility: Impact on Battery Performance

A Dissertation Presented

by

**David Charles Bock**

to

The Graduate School

in Partial Fulfillment of the

Requirements

for the Degree of

**Doctor of Philosophy**

in

**Chemistry**

Stony Brook University

**May 2015**

**Stony Brook University**

The Graduate School

**David Charles Bock**

We, the dissertation committee for the above candidate for the

Doctor of Philosophy degree, hereby recommend

acceptance of this dissertation.

**Dr. Esther S. Takeuchi – Dissertation Advisor**
**Distinguished Professor, Chemistry**

**Dr. Kenneth J. Takeuchi – co-Advisor**
**Distinguished Teaching Professor, Chemistry**

**Dr. Amy Marschilok – co-Advisor**
**Research Associate Professor, Chemistry**

**Dr. Stanislaus S. Wong - Chairperson of Defense**
**Professor, Chemistry**

**Dr. Andreas Mayr – Committee Member**
**Professor, Chemistry**

**Dr. Hong Gan – Outside Committee Member**
**Energy Storage Group Leader, Sustainable Technologies Dept., Brookhaven National Laboratory**

This dissertation is accepted by the Graduate School

Charles Taber
Dean of the Graduate School

Abstract of the Dissertation

**Investigations of Silver Vanadium Oxide and Silver Vanadium Phosphorous Oxide Solubility: Impact on Battery Performance**

by

**David Charles Bock**

**Doctor of Philosophy**

in

**Chemistry**

Stony Brook University

**2015**

Extended battery lifetime has increased significance with the prospect of long life applications such as electric vehicles and the integration of energy storage with the electric grid. Thus, consideration of parasitic reactions that occur over long periods of time has elevated significance. A life limiting mechanism for several battery systems is cathode solubility, which results in the formation of deposits on the anode surface. These deposits can increase the cell impedance, resulting in loss of delivered capacity and capacity fade. The research herein investigates cathode solubility in the battery system used to power internal cardioverter defibrillators (ICD's), which are implantable medical devices designed to apply a high energy shock to a patient's heart in the event of ventricular fibrillation. A metal oxide based battery system, lithium/silver vanadium oxide ($Ag_2V_4O_{11}$, SVO), is used to power these devices. However, the battery has an unpredictable long term stability limitation attributed to cathode material solubility. Soluble species in the electrolyte form deposits on the anode, which

increase the resistance of the electrochemical cell. This is a crucial issue in the ICD application where the battery must supply high power for consistent pulse performance.

In order to understand and mitigate the problem of $Ag_2V_4O_{11}$ cathode dissolution in non-aqueous solvents, the research herein investigates the silver vanadium phosphorous oxide ($Ag_wV_xP_yO_z$, SVPO) family of cathode materials, which exhibit electrochemical performance characteristics which are suitable for ICDs and other high rate applications, yet are structurally reminiscent of $Ag_2V_4O_{11}$. The $Ag_wV_xP_yO_z$ materials were anticipated to reduce cathode component concentrations in the electrolyte based on the demonstrated thermal and chemical stability of phosphate based materials, where strong covalent P-O bonds stabilize the molecular framework. The collected results have supported the initial hypothesis, with $Ag_wV_xP_yO_z$ compounds exhibiting reduced solubility relative to $Ag_2V_4O_{11}$.

Relatively few reports exist on cathode solubility pertaining to non-aqueous battery systems, and this research represents the first example of a systematic investigation of cathode dissolution using multiple classes of materials. Experimental methods were developed to accurately quantify the low levels of solubility (concentration levels in the parts per million and parts per billion ranges in organic solvent) for the various target materials. Concentration vs. time data was interpreted from a kinetic perspective to gain insight into the mechanisms by which the dissolution process took place. The impact of material structure, stoichiometry, and physical properties were investigated in consideration of the solubility measurements.

Further experiments were performed to understand the relationships between cathode solubility and electrochemical performance. Lithium/silver vanadium oxide and lithium/silver vanadium phosphorous oxide electrochemical cells were subjected to long term constant current discharge, and subsequent pulse testing indicated differences in the cell resistances. The negative

electrodes were recovered and investigated by several techniques including mapping by synchrotron based x-ray microfluorescence (XRμF) and oxidation state determination by microbeam x-ray absorption spectroscopy (μXAS). Quantitative analysis of digested samples was done using inductively coupled plasma-optical emission spectroscopy (ICP-OES). These methods enabled visualization of the anode surface and solid electrolyte interphase (SEI) through mapping, determination of the vanadium oxidation state, and quantification of the silver and vanadium content of the recovered anodes. The results suggest that SVPO materials can reduce cathode solubility and anode passivation compared to SVO, making them promising alternative cathode materials for the ICD application.

## Table of Contents

## List of Figures

Chapter 1



Chapter 2

## List of Tables

## Acknowledgments

I would like to express my sincere gratitude to my advisors, Dr. Esther Takeuchi, Dr. Kenneth Takeuchi, and Dr. Amy Marschilok for their guidance and continuous support throughout my Ph.D. candidature. They have encouraged me to grow not only as an experimentalist and chemist, but also as an independent thinker. At the same time, their knowledge and creative vision have provided me with tremendous research opportunities. Their tireless work ethic and numerous achievements are constant source of inspiration for me. I am truly fortunate to have had the privilege of working in their research group.

I would also like to thank my doctoral committee members, Dr. Stanislaus Wong, Dr. Andreas Mayr, and Dr. Hong Gan for the guidance and thought-provoking suggestions that each of them have offered to me.

I would like to recognize past and present members of the Takeuchi research group for the support they have given me over the years. In particular, I would like to thank Dr. Chai-Ying Lee, Dr. Roberta DiLeo, and Dr. Kevin Kirshenbaum, who have provided me with valuable insight into my research projects.

I could not have done this without my family. My parents, David and Leslie, have always given me their unconditional love. They taught me the value of an education and have given me the support I needed to accomplish my goals. I also thank my brother Chris for his encouragement when I needed it most. Finally, I would like to thank my fiancé Megan. We first met when I started graduate school, and the sacrifice and patience she has shown is a testament to her love for me. It has been an amazing five years and I am excited to move on to the next chapter of our lives together.

# Chapter 1

## General Background and Introduction

Reproduced in part from [Bock, D. C.; Marschilok, A. C.; Takeuchi, K. J.; Takeuchi, E. S., Batteries used to power implantable biomedical devices. *Electrochim. Acta* **2012,** 84, 155-164] with permission from Elsevier (Copyright 2012).

### 1.1. Introduction

Advancement of energy storage systems including batteries with high energy and power densities remains critical for the next era of energy generation. One issue which must be considered when designing these future batteries is cathode solubility. Cathode solubility is the loss of electroactive material from the solid cathode into the electrolyte. It can be a significant life limiting mechanism in electrochemical cells for two primary reasons: (1) the loss of electrode material decreases the capacity of the battery, and (2) dissolved species in the electrolyte can form a passivation layer on the anode surface, increasing the cell resistance.[1-3] The increased resistance limits the amount of current which may be drawn from the cell, a significant problem in batteries used for high rate applications.

The purpose of this study is to gain understanding of the mechanisms of cathode solubility in non-aqueous media with a focus on electrode materials having application in batteries for implantable biomedical devices. More specifically, the silver vanadium phosphorous oxide family of cathode materials, with chemical formula $Ag_wV_xP_yO_z$, are targeted as alternative cathode materials for reducing solubility relative to silver vanadium oxide, the primary battery powering implantable cardioverter defibrillators and for which cathode solubility is particularly problematic. This is accomplished through kinetic analysis of dissolution data and

systematic investigation of the impact of the structure and physical properties of the target materials. The impact of cathode solubility on electrochemical performance is explored in battery systems by analyzing lithium electrodes from cells containing silver vanadium oxide or silver vanadium oxide based cathode systems retrieved after long term testing was conducted.

This chapter includes a detailed discussion of the requirements and types of batteries used in implantable biomedical devices. Details of the Li/SVO battery system used in implantable cardioverter defibrillators, for which cathode dissolution is a significant life-limiting mechanism, are reported. Other battery systems where cathode solubility is an issue are discussed, illustrating that the dissolution of cathode materials into non-aqueous electrolyte is a widespread issue for many battery systems in addition to Li/SVO system. Finally, literature regarding the kinetics of dissolution and ion exchange are reviewed herein.

### 1.2 Batteries Used to Power Implantable Biomedical Devices

Batteries developed for implantable biomedical devices have helped enable the successful deployment of the devices and their treatment of human disease. The medical devices are permanently implanted to continually monitor a patient and provide therapy on a predetermined schedule or as needed. Numerous devices have been developed to address diverse human health issues. While functional requirements for the batteries used to power these devices vary with the type of device and therapy, there are some characteristics that are demanded by all applications. The batteries must provide service over many years to minimize surgical frequency, be safe during installation and use, have predictable performance that can be interrogated to provide state of discharge information and be highly reliable. Additionally, the batteries must have high volumetric energy density to enable the design of small devices that minimize discomfort for the

patient. Thus, long term stability during use, predictable performance, high volumetric energy density and outstanding reliability are key characteristics that define successful systems for biomedical implants.

This section focuses on battery systems that are used to power medical implants. The cell potential, capacity and energy density characteristics of relevant battery systems are summarized in Table 1. The battery systems are described beginning with primary batteries arranged in order of increasing current and power capability. The lithium/iodine system that functions in the microampere current range is described first, followed by batteries that function in the milliampere range including lithium/manganese oxide, lithium/carbon monofluoride, and hybrid cathode systems based on silver vanadium oxide in conjunction with carbon monofluoride. Battery systems that function under ampere level currents are then discussed, including cathodes based on silver vanadium oxide in conjunction with carbon monofluoride. Finally secondary batteries that are used for implantable devices are described. In each section, the chemistry of the system is described along with the battery requirements of the device.

| Battery system | Open Circuit potential | Nominal Potential | Theoretical gravimetric capacity cathode material (mAh/g) | Theoretical volumetric capacity of cathode material ($mAh/cm^3$) | Theoretical energy density of cathode Material (mWh/g) | Energy Density of Battery (mWh/g) |
|---|---|---|---|---|---|---|
| $Li/I_2$ | 2.8[4] | 2.8[5] | 211 | 1041 | 591 | 210-270[4] |
| $Li/MnO_2$ | 3.3[5] | 3.0[5] | 308 | 1540 | 924 | 270 (low rate)<br>230 (high rate[5] |
| Li/CFx | 3.1[5] | 3.0[5] | 865 | 2335 | 2595 | 440[5] |
| Li/SVO | 3.24[5] | 3.2[5] | 315 | 1510 | 1008 | 270[5] |
| $C/LiCoO_2$ | 4.2[6] | 3.88[6] | 155[6] | 783 | 601 | 155[6] |

**Table 1.** Voltage and energy density of cathode materials used for implantable medical batteries.

### 1.2.1 Lithium/iodine batteries

Implantable cardiac pacemakers require a reliable power source capable of providing currents in the microampere range. The lithium/iodine-polyvinylpyridine (PVP) system, first patented by Scheider and Moser[7,8], has been used to power these devices since the 1970's.[9] $Li/I_2$-PVP cells are the principal option for this application because of their high energy density, safety, and reliability.[10]

The basic cell reaction in a lithium iodine battery is[11]

$$Li + 1/2I_2 \rightarrow LiI \qquad [1]$$

This reaction results in a cell open circuit voltage of 2.8V.[4] The cathode material is a mixture of iodine and poly-2-vinylpyridine (PVP) in a ratio of 30/1 to 50/1, contingent upon the manufacturer's specifications.[12] When heated to a high temperature, the materials react to produce a conductive charge transfer complex.[13] Cell construction involves adding the molten cathode material to the cell, forming a LiI layer at the anode. The LiI layer formed *in situ* acts as both a separator and solid electrolyte.[10] An alternative construction method of lithium/iodine cell cathodes that has also been commercially used entails pelletizing a mixture of iodine, polyvinylpyridine, and a charge transfer complex of the two materials.[14] One of the notable characteristics of the lithium/iodine cell system is that as the cell is discharged, the LiI layer continues to increase in thickness, in effect raising the impedance.[11] The impedance of the cell can be reduced by coating the lithium anode with a layer of poly-2vinylpyridine (P2VP).[15] The anode coating results in formation of an electrolyte liquid phase through chemical reaction of the LiI, $I_2$ and P2VP components.[16] This liquid phase has the ability to transport Li ions and results in an improvement in lithium iodide ionic conductivity of between one and two orders of magnitude versus lithium iodide formed in cells with uncoated anodes.[17] The discharge process

in lithium iodine cells has been characterized by impedance spectroscopy as a means of assessing the performance of new battery designs.[18]

Several characteristics of the $Li/I_2$-PVP cell make the technology suitable for cardiac pacemakers. As the cell is discharged, because of the increasing level of impedance, the loaded cell potential decreases such that the cell potential can be used to indicate when the battery requires replacement.[12] The microampere current levels supplied by the system are adequate for the pacemaker application.[11] The volumetric energy density of the cell is near 1.0 $Wh/cm^{-3}$, allowing for small battery size.[9] Furthermore, the Li/I layer formed through the cell reaction affords the system with a reliable electrolyte/separator.[10] Lithium/iodine-polyvinylpyridine batteries have proven to be safe over several decades in clinical use as a power source for implantable pacemakers.[12]

Recent investigations of lithium/iodine batteries include examination of using the system as a secondary battery. A solid state, rechargeable thin film $Li/I_2$ battery has been constructed by coating a thin LiI(3-hydroxypropionitrile)$_2$ (LiI$(HPN)_2$) electrolyte film onto a Li anode plate, which is then reacted with $I_2$ vapor.[19] In this system, $I^-$ anions are the principal source of ionic conductivity in the electrolyte. The system utilizes LiI$(HPN)_2$-$I_2$ as the cathode material and unreacted LiI$(HPN)_2$ as a solid electrolyte. The cells display reversibility as well as improved rate performance versus $Li/I_2$ batteries[19] made by previously reported methods. Other work has investigated electrochemically self-assembled lithium-iodine batteries where the cells consist of a polyiodide cathode, lithium anode, and LiI electrolyte.[20]

### 1.2.2 Lithium/manganese dioxide batteries

Biomedical devices such as neurostimulators, drug delivery systems, and pacemakers

with additional functionality require batteries capable of delivering power in the milliwatt range. The lithium/manganese dioxide primary battery, first commercialized by Ikeda et al. [21,] in the 1970's, is one option for these medium-rate applications. Manganese dioxide had previously seen use in zinc carbon dry cells and alkaline $MnO_2$ cells, but the development of heat treatment allowed for the material to be used in a lithium nonaqueous system.[21,,22] The lithium/manganese dioxide system has been widely used as a power source because of its high operating voltage, high specific energy density, and excellent storage and discharge characteristics.[22]

The cell reaction in a lithium/manganese dioxide battery is: [22]

$$MnO_2 + Li \rightarrow LiMnO_2 \qquad [2]$$

Synthetic manganese dioxides can be prepared chemically (chemically prepared $MnO_2$, CMD) or electrochemically (electrolytic $MnO_2$, EMD).[23] The material must be anhydrous and have the ability to intercalate lithium.[22] Heat treated EMD is used in commercialized lithium/manganese dioxide batteries.[22] Prior to heating, EMD has a mainly $\gamma$-$MnO_2$ type crystal structure with intergrowths of a major $\gamma$-$MnO_2$ ramsdellite phase and a $\beta$-$MnO_2$ pyrolusite impurity.[22] The ramsdellite is characterized by 1x2 tunnels formed by $MnO_6$ edge sharing polyhedra.[22] Heat treatment increases the concentration of pyrolusite, which has a crystal structure made up of both 1 x1 and 1 x 2 tunnels.[22, 24,25] There is general agreement that EMD contains both 1 x 1 and 2 x 2 tunnels in a hexagonally close-packed oxygen matrix..

The discharge characteristics of the Li/$MnO_2$ system are dependent on the choice of electrolyte solution as a result of differences in electrolyte conductivity and resistance at the electrolyte-lithium electrode interface.[23] The high rate discharge behavior of cells having a 1 M $LiClO_4$ salt concentration in various solvents containing propylene carbonate and a non-cylic di-ether was investigated.[26] The electrolyte solution comprised of a 1:1 mixture of propylene

carbonate and 1,2-dimethyoxyethane had the highest discharge capacity, and the discharge capacity increased with increasing conductivity of the electrolyte solution.[26] Other work has explored the impact of various lithium salts on the discharge capacity of $MnO_2$.[23]

Various studies have investigated the mechanism of the discharge reaction in the $Li/MnO_2$ system, which involves three distinct regions corresponding to three stages of lithium insertion into the $MnO_2$ lattice.[27,28, 29] The initial stage is a homogeneous insertion reaction characterized by a sloping discharge voltage curve.[29] The second stage is a two-phase reaction indicated by a long flat region of the discharge voltage, followed by a sloping region signifying the final homogenous lithium insertion.[10,29]

An impedance model of a $Li/MnO_2$ cell specifically designed for use in implantable cardiac pacemakers was developed in order to predict the battery longevity.[30,31] The model allows for the voltage drop to be calculated for a given current pulse .[30] Further work updated the model to include the impedance contribution of the interface between the cathode and current collector.[31]

The lithium manganese dioxide cell has various properties which are advantageous for its utilization as a power source for implantable applications. The relatively flat discharge profile of the system results in a stable nominal voltage of 3.0V.[22,29,5] The theoretical specific energy of the cell is high at 924 mWh $g^{-1}$. As previously stated, the medium rate currents supplied by $Li/MnO_2$ batteries widen the application range for this power source. Moreover, these cells have a low self-discharge rate and a high level of stability.[22]

Recent work involving the lithium-manganese dioxide system centers on using it as a secondary battery.[32,25, 33, 34] The interest in $MnO_2$ based cathode materials for rechargeable Li-ion batteries derives from its low cost compared to $LiCoO_2$, the current preferred cathode

material in secondary cells.[33] An EMD/C composite material which is prepared by mechanical milling followed by heat treatment at 400 C has been described.[34] Other work by Bowden et al. involves ion exchange of structural protons in EMD with lithium prior to heat treatment, and results in lithium substituted, ordered $MnO_2$ materials. [25] Of these, the most crystalline form exhibits good reversibility after multiple cycles and a discharge capacity of 210 mAh/g.[25]

### 1.2.3 Lithium/carbon monofluoride batteries

An alternative option for implantable biomedical devices requiring current outputs in the milliampere range is the lithium/ polycarbon monofluoride ($Li/CF_x$) system. Polycarbon monofluoride was first developed as a cathode material for lithium primary batteries in the early 1970's.[35-36] The low self-discharge, high working voltage and high energy density of the $Li\text{-}CF_x$ system have made it useful as a medium rate power source.[37]

Polycarbon monofluoride ($CF_x$) is a solid state cathode material prepared by direct fluorination of carbon with $F_2$ at temperatures ranging from 400 to 600 C.[38] The highly stable structure consists of sp3 hybridized carbon layers, with fluorine covalently bonded to carbon.[38] The carbon/fluorine ratio of the material can be varied. While higher fluorine content increases the theoretical capacity of the material, it decreases its electrical conductivity.[39-40] Because the material is an insulator, $CF_x$ is mixed with a conductive additive during cathode preparation, along with a binder so that a cathode pellet may be pressed.[10] Cell construction includes the solid cathode, a lithium anode, and a separator between the two electrodes. The electrolyte used is usually lithium tetrafluorborate ($LiBF_4$) dissolved in γ-butyrolactone.[37]

The cell overall reaction in Li/CFx cells is [37]

$$Li + CF_x \rightarrow LiF + C \qquad [3]$$

The discharge reaction has been described as proceeding by initial insertion of solvated lithium ions into the graphite fluoride layer, forming an intermediate phase consisting of carbon, fluoride, and lithium ions. [41,42] The intermediate phase, considered to be a diffusion layer, gradually decomposes into lithium fluoride, carbon, and solvent molecules as the cell is discharged. [41,42] The open circuit potential of Li-$CF_x$ cells is typically around 3.1 V, which is significantly lower than the calculated electromotive force of 4.57V for the overall reaction.[5,43] The observed OCV differs from the calculated thermodynamic value because the electron transfer reaction in the intermediate phase determines the equilibrium voltage.[42] Thus, the magnitude of the overpotential has been explained by solvated lithium ion transfer in the intermediate phase, and is therefore dependent on the solvent molecule size, solvation number, and interlayer spacing of the graphite fluoride cathode material.[42, 43] The thickness of the intermediate phase is maintained through discharge, keeping the overpotential constant and providing a relatively flat discharge potential.[42]

Researchers have proposed methods to simulate the Li-$CF_x$ system under conditions of both constant low rate discharge and periodic pulse discharge.[44,45] Li-$CF_x$ cells were constructed and discharged over a period of 0.27 to 7.19 years. A dual intercalation model was formulated to simulate the constant discharge condition. Compiled cell data was in agreement with the behavior predicted by the model, and the system was determined to follow Tafel kinetics. For the pulse discharge condition, a zero dimensional model was used to successfully predict the experimental results.[45]

The lithium/carbon monofluoride system is attractive as a power source for implantable medical devices for a number of reasons. The discharge profile is predictable over time, allowing the battery's end of service point to be determined electronically. The low internal

impedance allows the battery to be used in medium rate applications requiring milliampere level currents. The theoretical volumetric capacity of the cathode material is high at 2335 mAh/$cm^3$. Furthermore, the self-discharge of the system is low and the cell chemistry has a history of stability and safety.[37] Batteries using Li/$CF_x$ specifically for medical devices have been described in the literature. Miniature pin-type cells using a spiral wound battery design have been developed that can produce pulse currents of up to 10 mA and have a volume of only 0.155 $cm^3$.[46] These cells are hermetically sealed and are appropriate for implantable applications. The discharge characteristics of Li/$CF_x$ batteries designed for low rate devices have also been reported. [44-45, 47]

Recent investigations of the lithium/ carbon monofluoride system involve optimization of cathode materials. Thermal treatment of $CF_x$ just below the decomposition temperature has been reported to increase discharge cell potential.[48] Carbothermal treatment with carbon black has also shown to increase discharge performance by increasing the reaction kinetics of the cathode.[49] Other research has investigated the use of multi-walled carbon nanotubes (MWCNT's) as an alternative conductive additive.[50]

Additional studies have focused on improving the understanding of the Li/$CF_x$ discharge mechanism and electrochemistry. Cathode swelling in discharged Li/$CF_x$ cells has been proposed to be due to deposition of LiF in the internal carbon surfaces of the cathode.[51] Other work has utilized dc-polarization and ac-impedance techniques to show that overall cell impedance is dominated by resistance of the cathode.[52]

### 1.2.4 Li/CFx - SVO hybrid batteries

The high energy density of lithium/ carbon monofluoride system allow batteries of this type to provide the longevity needed for implantable biomedical devices requiring medium rate currents. In order to provide even higher pulse current capability than $CF_x$ alone, lithium batteries with hybrid cathodes combining $CF_x$ and silver vanadium oxide, $Ag_2V_4O_{11}$, have been developed.[53, 54] A more detailed discussion of the lithium/silver vanadium oxide system is located in the section on high rate batteries. In addition improving the power density compared cells using only the Li/$CF_x$ system, these hybrid batteries offer enhanced end of service detection due to the appearance of a lower voltage plateau at the end of discharge.

There are two basic designs of hybrid Li/CFx - SVO hybrid batteries described in the literature. The first utilizes a cathode consisting of physically mixed silver vanadium oxide and carbon monofluoride materials.[54] An alternative cell design utilizing a laminated cathode[53] is able to deliver high current pulses and is included in the high rate battery section.

The discharge behavior of Li/CFx – SVO hybrid cells using the physically mixed cathode model has been described.[54] At low current rates, the SVO material is partially reduced first, followed by complete discharge of $CF_x$ , followed by reduction of the remaining SVO.[54] At higher rates, SVO is expected to provide most of the energy due to its higher current carrying capability, lowering its potential relative to $CF_x$. The $CF_x$ then recharges the SVO so that the potential of the two materials is at equilibrium.[54] Hybrid cells of this type have a detectable end of service point in the voltage profile, and those optimized to deliver medium rate currents have an energy density of approximately 1 Wh $cm^{-3}$.[54] Furthermore, composition of the mixture can be adjusted to suit the application, depending on whether additional capacity or power density is required.[54]

Physically based mathematical models of Li/$CF_x$-SVO hybrid cathode batteries using the mixed cathode design have been described.[55,56,57] These models were developed using the assumptions that the cathode determines battery capacity, is kinetically limited and contributes most of the resistance. The models do not take heat generation or parasitic reactions into account, and make assumptions regarding the morphology and size of the particles. [55,56,57] The models estimate kinetic and thermodynamic parameters from experimental data and are able to predict the discharge behavior of the hybrid batteries over a range of conditions. [55,56,57]

### 1.2.5 High Rate Batteries – Silver Vanadium Oxide

Implantable cardioverter defibrillators (ICDs) are medical devices designed to continuously monitor a patient's heart and sense tachycardia (rapid heartbeat).[11] If ventricular fibrillation is detected which cannot be addressed by pacing, a high energy shock is applied so that heartbeat is restored to a normal rate. The high power demands of ICD's necessitate a battery which is capable of delivering high current pulses of 2-3 A in order to charge the capacitors of the device.[11] Furthermore, the battery must supply a constant low current to power the heart monitoring functions of the ICD.[11] The battery should also be of a suitable size and remain highly stable throughout its lifetime implanted in the patient.[11] The lithium/silver vanadium oxide (Li/SVO) system meets all of the above requirements and is the most commonly used battery in ICDs today.

While the Li/SVO system was initially intended for non-medical use,[58] it was the implementation of the system for implantable medical applications that fully realized its benefits and capabilities.[59] Since its initial implementation in the 1980s, numerous improvements have optimized the Li/SVO system as a high rate ICD battery.[60, 61, 62, 63, 64]

The SVO cathode material, $Ag_2V_4O_{11}$, is conventionally prepared using a solid state synthesis method.[65] SVO has a layered structure comprised of edge and corner sharing distorted $VO_6$ octahedra, as shown in Figure 1. The overall discharge reaction is [11]

$$7Li + Ag_2V_4O_{11} \rightarrow Li_7Ag_2V_4O_{11} \quad [4]$$

Seven moles of lithium can be incorporated into the structure, corresponding to a theoretical specific capacity of 315 mAh/g. The volumetric capacity of cathode material is high at 1510 $mAh/cm^3$ and the open circuit voltage of Li/SVO cells is approximately 3.2 V.[5] The system is able to deliver high current therapy pulses for the implantable ICD application.

The discharge process in the Li/SVO system has been extensively studied through characterization of the cathode material at various stages reduction.[66, 67] XRD analysis of $Li_xAg_2V_4O_{11}$ discharge products, where x is the moles of $Li^+$ intercalated into the material, indicate that the reduction of $Ag^+$ to $Ag^0$ occurs from $0 < x < 2.4$ and is accompanied by a loss of crystallinity.[66] The reduction of silver comprises 30% of the cathode's capacity and significantly improves the conductivity, permitting the Li/SVO system to be used in high rate applications.[66] While some vanadium reduction occurs earlier in the discharge process, from $2.4 < x > 3.8$ the discharge process is dominated by reduction of $V^{5+}$ to $V^{4+}$. Upon further reduction at $x > 3.8$, $V^{4+}$ to $V^{3+}$ reduction results in mixed valence materials containing vanadium at (III), (IV), and (V) oxidation states.[66] The multi-stage reduction reaction results in a stepped voltage profile, which allows physicians to determine when battery replacement is needed.[11] Recent studies of the discharge process using nuclear magnetic resonance and x-ray absorption spectroscopy indicate that reduction of vanadium (V) initiates simultaneous to silver reduction in the initial discharge step.[68] Other work has indicated that the rate capability of the system is limited by diffusion transport during lithium intercalation.[69]

Li/SVO cells employ an electrolyte consisting of propylene carbonate and dimethoxyethane with a dissolved lithium salt.[11] A polypropylene or polyethylene separator is used to prevent the battery from shorting.[11] Batteries may be constructed using multi-plate cathode design, which connects numerous cathodes in parallel to raise the current output of the cell.[60] A second design features of strips of anode and cathode wound together in a flattened coil as a means of improving efficiency.[70] Mathematical models of these cells have been developed to account for changes in cell resistance during discharge.[71] Experimental data indicates that resistance increases due to concentration polarization and is dependent on discharge rate.

Recent investigations involving the Li/SVO system have focused on the optimization of the active cathode material. A recently reviewed approach to enhancing performance is the development of SVO nanomaterials.[72] It is reasoned that decreasing particle size will result in higher diffusion rates of lithium during the intercalation process.[72] Furthermore, the unique electronic properties of nano-sized materials may lead to increased capacities and higher cell potentials.[72] A molten salt synthesis method has been developed to prepare nanocrystalline $Ag_2V_4O_{11}$ .[73] Materials synthesized through this process at 300C are capable of delivering a discharge capacity of 269 mA h/g to a cutoff voltage of 2 V, notably higher than the 210 mAh/g delivered by bulk SVO material.[73] The behavior of nanocrystalline SVO particles as also been described in comparison to SVO synthesized by the conventional solid state synthesis.[74,75] Electrochemical testing indicates that the particles are able to deliver a gravimetric capacity of 320 mAh/g at C and 250 mAh/g at 5C to a 1.5 V cutoff.

The electrochemical performance of $Ag_2V_4O_{11}$ nanowires synthesizing using a low temperature hydrothermal method has been reported.[76] When these nanowires were used as the cathode material in two electrode cells, the initial open circuit voltage was 3.52 V, and the

discharge capacity was 366 mAh $g^{-1}$ to a 1.5V cutoff. By comparison, $Ag_2V_4O_{11}$ bulk material prepared using the conventional solid state synthesis method had an open circuit voltage which was 200 mV lower, and was only able to deliver a discharge capacity of 319 mAh/g.[76]

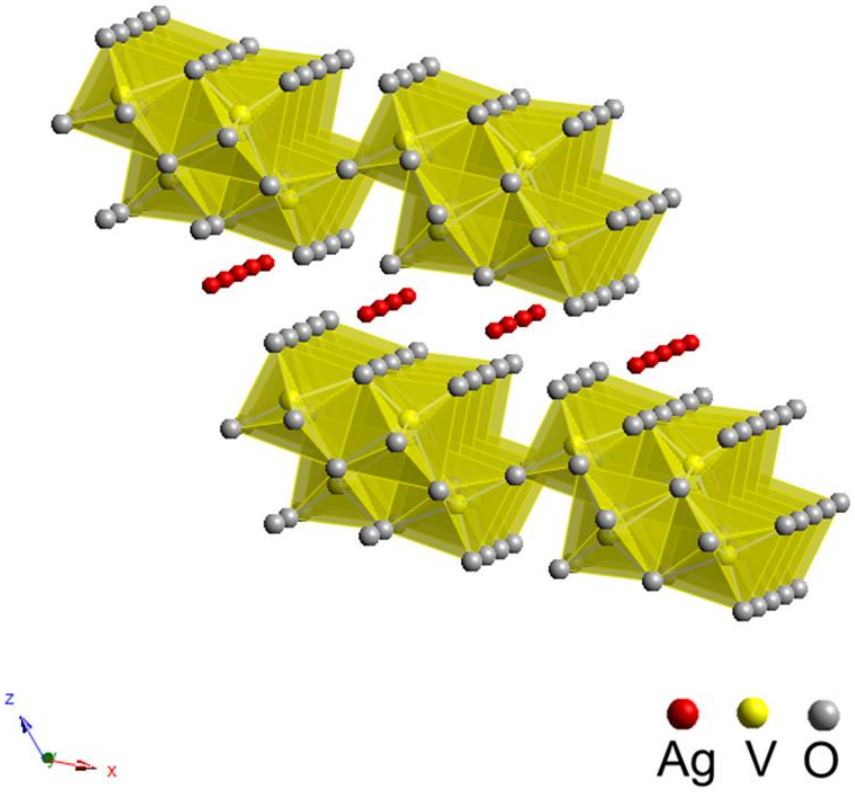


**Figure 1.** $Ag_2V_4O_{11}$ is a layered structure consisting of edge and corner sharing distorted $VO_6$ octahedra.[77]

### 1.2.6 High Rate Batteries – Lithium/Manganese Dioxide

The $Li/MnO_2$ system is an alternative to Li/SVO for powering implantable defibrillators. Cells have been developed which are able to meet the power source requirements for ICD's described in the previous section. Manganese dioxide has an acceptable energy density and the system is capable of delivering high current pulses.[78] Furthermore, the resistance of $Li/MnO_2$ cells does not increase until the end of discharge, so performance at high rates does not diminish with time.[78]

$Li/MnO_2$ batteries suitable for the ICD application have been developed where the cathode consists of manganese dioxide mixed with chromium oxide and lead oxides.[79] The addition of these compounds results in a discharge profile which indicates when capacity is low and the battery needs to be replaced.[79]

A high rate $Li/MnO_2$ battery based on a double cell concept has also been produced.[80] The design incorporates two cathode-limited cells, connected in series by the battery casing in order to reduce volume. The nominal voltage of the battery is 6V. The use of two cells connected in series lowers the current density on the electrodes, improving the high rate performance relative to the single cell design.[80] The battery has a pulse power density of 540 W $L^{-1}$, compared to 420 W $l^{-1}$ for the cell single version from which the double cell was adapted.[80]

High rate $Li/MnO_2$ double cell batteries have been improved by integrating them into a hybrid system.[81] This configuration consists of a lithium manganese dioxide 6 V double cell in addition to a lithium iodine cell. The lithium iodine cell provides capacity for the low rate discharge functions of the defibrillator, and its high energy density increases the lifetime of the battery. Compared to the double cell only battery, the hybrid system has a larger low rate capacity at a smaller volume, with only a minor loss of pulse-power capability.[81] The discharge

behavior of Li/$MnO_2$ cells designed for ICD devices has been predicted through the use of mathematical models.[78] The experimental discharge curves were modeled using a function which accounts for excess free energy arising from lithium ion – cathode interactions.[78]

### 1.2.7 High Rate Batteries - Li/CFx - SVO hybrid

Li/CFx –SVO hybrid cells using a novel electrode design are reported which are able to deliver high current pulses, also enabling their use in ICD's.[53] The cathode consists of $CF_x$ sandwiched between two layers of SVO material. Both $CF_x$ and SVO are mixed with binder and a conductive additive, and the two materials are separated by titanium screens.[53] Each cathode assembly is heat sealed in polypropylene separator and placed between lithium anodes, also sealed in polypropylene (Figure 14.) The cells described in the literature were configured with six cathode assemblies in stainless steel can filled with 1 M $LiAsF_6$ in 1:1 PC:DME electrolyte.[53]

The discharge profile of the hybrid cells exhibits plateaus at 3.2V, 2.8V, and 2.6V, which correspond to the respective discharge of SVO, $CF_x$, and SVO.[53] After initial reduction of SVO, most of the energy for low rate currents is provided by $CF_x$. However, if the cell is pulsed under heavy loads, SVO is preferentially discharged, and the resulting potential of SVO is then less than that of $CF_x$.[53] The stepped voltage profile of these dual cathode cells indicates when the battery needs to be replaced.[53] The hybrid cells have higher capacity than SVO cells and analogous rate capability, making them useful in medium and high-current applications.[53]

### 1.2.8 Li-ion batteries – milliwatt power levels

Some applications having high power usage rates can benefit from the use of rechargeable batteries in order to improve implant lifetime and reduce size. Secondary power

sources for implantable medical devices must satisfy the same general requirements as primary batteries, including safety, reliability, high energy density, and low self-discharge. Neurostimulators, which operate in the milliwatt power range, are one type of device for which secondary batteries have been developed. These cells operate using lithium-ion technology.

Li-ion cells typically consist of a carbonaceous anode and a metal oxide cathode, with both electrode materials having the ability to intercalate lithium ions reversibly.[10] Cells are constructed using a discharged cathode material containing the source of lithium ions for the cell. During initial charge, the lithium from the cathode is extracted and inserted into the anode.[10] The reverse process occurs during discharge. Common cathode materials include nickel, manganese, and cobalt based oxides.[10] Lithium cobalt oxide ($LiCoO_2$) is most often used and has a gravimetric capacity of 155 mAh/g.[6]

Safety considerations are especially significant in implantable medical applications Overcharging and short circuit conditions present the possibility of excess heating and cell rupture.[82, 83] Prismatic Li-ion cells utilizing $LiCoO_2$ cathodes and graphite anodes were tested to determine the effects of overcharge rate on internal cell temperature and hermeticity. Short circuit testing increased the temperature of the cells, which remained sealed.[82] However, the study determined that at charging currents greater than C/5, the cells may rupture.[82]

The performance of Li-ion cells developed specifically for biomedical applications has been described in the literature and studies of their performance have been conducted.[84, 85] Cells with capacities of 200 mAh were cycled at 37°C to various depths of discharge. Results indicated that after 1000 cycles, the capacity retention using the 80% DOD condition was 98%.[84] A study of the solvent disproportion mechanism in lithium ion cells was also reported, providing an opportunity to develop a more stable electrolyte.[86] Spirally wound miniature pin-type batteries

utilizing a $LiNiCoAlO_2$ cathode have been developed. Cycle life testing indicates that the capacity retention is over 80% after 500 cycles.[46] These batteries exemplify the opportunity presented by Li-ion technology to engineer extremely small volume medical batteries with a rechargeable capacity.

### 1.2.9 Cathode Solubility in Batteries for Implantable Biomedical Devices

Cathode solubility is an important consideration when choosing battery systems for use in implantable biomedical devices. Solubility results in the loss of electrode material, which reduces capacity as well as the implantable lifetime of the battery. Of even greater significance is that dissolved species containing transition metal ions passivate the anode surface. This increases resistance and limits the current which may be drawn from the cell. This phenomenon is particularly problematic in the lithium/silver vanadium oxide system (Li/SVO) used for the implantable cardioverter defibrillator, detailed in section 1.2.5.

It is reported that vanadium species from the SVO cathode material dissolve into the electrolyte solution and are subsequently deposited on the lithium anode, increasing the cell resistance.[3, 87] (**Figure 2**) Consequently, more time is needed to charge the ICD's capacitors, reducing its effectiveness and depending on the severity of the resistance layer, necessitating battery replacement. Much of the motivation for this research is to study new cathode materials which meet the power and safety requirements of the ICD application while minimizing solubility and the resulting increase in impedance.

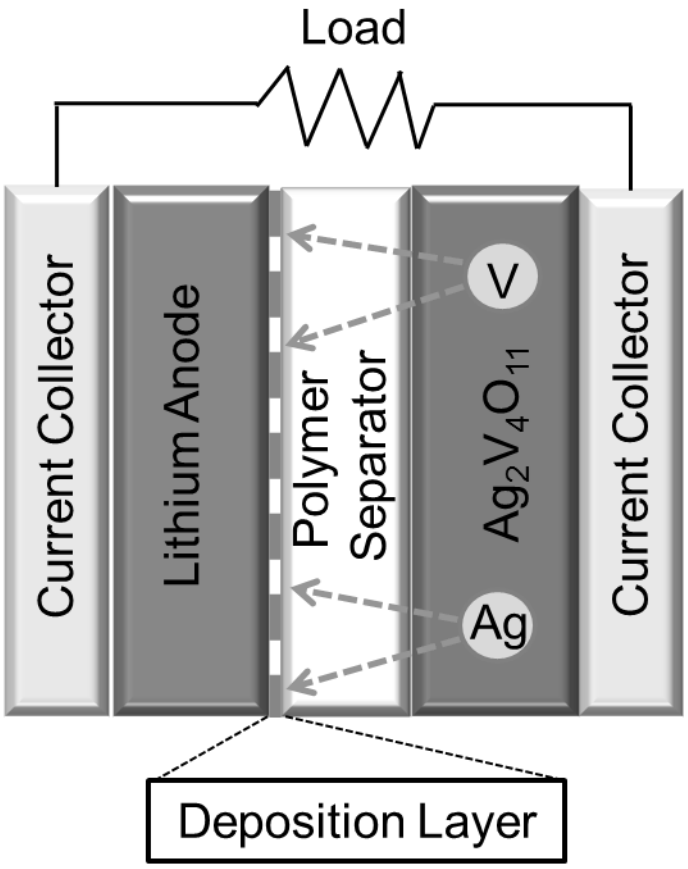


**Figure 2.** Model of cathode solubility and subsequent deposition on the anode in the $Li/Ag_2V_4O_{11}$ system.

### 1.3 Cathode dissolution in Li-based battery systems

Notably, in addition to Li/SVO batteries, there are several other systems which show solubility as a function of state of discharge, indicating that the dissolution of cathode materials into non-aqueous electrolyte is a widespread problem. These systems include rechargeable lithium ion batteries based on the cathode materials $LiCoO_2$, $LiMn_2O_4$, and $LiV_3O_8$. Based on these reports, the development of quantitative analysis techniques for determining the kinetics of dissolution will benefit a wide array of battery systems.

#### 1.3.1 Cathode dissolution in Li-based battery systems – $LiCoO_2$

One battery material for which several studies relating to dissolution have been completed is the secondary battery material $LiCoO_2$.[2, 88-92] In this system, Co ions dissolve from the cathode and are reduced at the anode as metallic cobalt and cobalt compounds.[91] Amatucci et al. investigated cobalt dissolution in $LiCoO_2$ secondary batteries to understand its impact on capacity loss.[88] The $LiCoO_2$ was assembled into coin cells with lithium metal anodes, and after cycling the cells with various discharge/charge conditions, the Li anodes were analyzed by energy dispersive spectroscopy (EDS) for cobalt content. The electrolyte used was 1M $LiPF_6$ in 2EC:DMC. It was found that capacity fade increased for cells cycled above 4.2V and directly correlated with the level of cobalt deposited measured on the anode. Cobalt dissolution was also found to correspond with structural changes as determined by in-situ X-ray diffraction.

Further investigation of dissolution in $LiCoO_2$ based systems was completed by analyzing electrolyte by ICP-AES after storage and cycling experiments at 25, 45 and 60 °C.[92] All of the electrolyte solutions measured contained cobalt concentrations equivalent to approximately 0.1-0.3% of the cobalt content in the $LiCoO_2$ used to make the electrochemical

cells. The Li anodes used in the cells were also analyzed by X-ray photoelectron spectroscopy (XPS). The XPS results indicated that surface films only contain deposited Co at higher temperatures, and that an organo-borate complex based film-forming additive suppresses Co deposition. XRD analysis showed that Co dissolution had an insignificant effect on the structure of the bulk material. The authors interpreted this finding as proof that capacity fading in $LiCoO_2$ cells is due to surface changes on the cathode rather than bulk structural alterations from Co dissolution.[89, 92]

The impact of adding PVDF binder to $LiCoO_2$ electrodes on the stability of the material has also been explored through storage of binder free or composite electrodes at elevated temperature in various $LiPF_6$ electrolyte solutions.[91] Analysis of the solutions by ICP indicated that Co dissolution does not occur without a salt present, and is accelerated in the presence of water. Further analysis by Raman spectroscopy showed that $LiCoO_2$ decomposes to form $Co_3O_4$, from which $Co^{2+}$ ions can dissolve. The decomposition is complemented by oxidation of alkyl carbonates in the electrolyte. The authors propose the decomposition reaction as$3LiCoO_2 + Li^+ + e^+ \rightarrow Co_3O_4 + 4Li_2O$, and theorize that HF in solution is the probable driving force for the reaction through its reaction with $Li_2O$.

### 1.3.2 Cathode dissolution in Li-based battery systems – $LiMn_2O_4$

Another secondary battery material for which transition metal ion dissolution has been studied is the spinel $LiMn_2O_4$.[93-100] Jang et. al investigated capacity losses in 4V $Li/Li_xMn_2O_4$ cells with composite cathodes. Based upon dissolved Mn concentration in the electrolyte of three electrode cells analyzed by differential pulse polarography, it was determined that cathode material loss was the cause of approximately 1/5 to 1/3 of the overall capacity loss. Mn

dissolution was found to increase in the charged state at voltages above 4.1V vs. $Li/Li^+$. It was theorized that at these voltages the electrolyte is oxidized on carbon surfaces of composite cathodes, forming intermediates which accelerate Mn dissolution. The remaining portion of capacity loss was attributed to an increase in cathode resistance as Mn dissolution progressed. Further study of $LiMnO_4$ cathodes sought to increase understanding of the dissolution process with respect to the electrolyte.[96] It was found that acids were generated by oxidation of electrolyte solvents when the cathodes were cycled in the potential range of 3.6 to 4.3V vs. $Li/Li^+$, with ether based solvents being more likely to be oxidized. The presence of acid in the electrolyte results in the loss of Li and Mn ions from the structure. Furthermore, the authors noted that fluorinated salts are less likely to be oxidized, but have the disadvantage of producing acid through HF formation if trace water is present in the electrolyte solution.

Other work on spinel lithium manganate investigated the kinetics of Mn dissolution at elevated temperatures.[98] $LiMn_2O_4$ powder was soaked in electrolyte and the Mn concentration was quantified as a function of time by AAS. Kinetic analysis of the data was performed using the shrinking core model for fluid-particle reactions. Results indicated that the rate of Mn dissolution is controlled by the dissolution reaction occurring at the surface of the unreacted core of the particles, as opposed to the process being diffusion dependent. Later analysis of the dissolution behavior of spinel lithium manganate doped with chromium revealed that the doping suppresses Mn dissolution at elevated temperatures.[99] However, Cr-doped samples displayed Cr dissolution, which will affect the stability of the spinel structure.

Several studies have been performed to investigate the nature of Mn deposition in $LiMn_2O_4$ based cells through the use of XAS as well as other techniques. Yang et al. studied the electrodes from disassembled cycled Carbon/$LiMn_2O_4$ cells with Cu anode current collectors

using XPS and SEM.[101] EDS of the anodes indicated that Cu dissolved from the current collector and Mn dissolved from the cathode were both present in the SEI layer on the carbon anode. The majority of these deposits were detected on the separator side of the anode. XPS results indicated that Cu and Mn ions were deposited in the SEI as $Cu_2O$ and MnO or $MnO_2$, respectively. Metal ions in the electrolyte were analyzed by ICP-OES and were found to be less than 1 ppm. This was attributed to most of the metal ions in solution having been reduced onto the anode surface due to the negative potential. The deposits of Cu oxide and Mn oxide in the SEI layer block intercalation of lithium ions and cause capacity fade in these batteries.

Recent work which further investigated the influence of Mn dissolution and anode deposition was performed by analysis of highly oriented pyrolytic graphite (HOPG)/ $LiMnO_2$ cells.[102] The performance of the cells was studied with a standard 1M $LiClO_4$/ EC+DEC electrolyte and with an electrolyte contaminated with Mn ion at a concentration of 90 ppm. AC impedance measurements showed that the impedance corresponding to surface film and Li-ion transfer resistance was on the order of ~15 times greater when the Mn containing electrolyte was used. Subsequent XPS analysis of the anodes indicated that Mn metal was initially reduced onto the HOPG during cycling, then oxidized at open circuit conditions.

The effect of manganese contamination on the solid electrolyte interphase in lithium ion batteries was studied using a model system with an inert Cu electrode.[103] $Mn(ClO_4)_2$ was used to contaminate the electrode surface. X-ray absorption spectroscopy indicated that Mn in the electrode film was present in the $2^+$ oxidation state. The authors hypothesize that Mn ions in the electrolyte are initially reduced to $Mn^0$ on the anode surface, and that reactions with the solvent oxidize Mn back to the 2+ oxidation state. The detection of Mn in the 2+ oxidation state agrees with work done by Zhan et al. which analyzed the surface of Li, lithium titanate, and graphite

anodes from cycled cells with $LiMn_2O_4$ cathodes.[104] In this case, the oxidation state was determined using the fluorescence intensity of X-ray absorption near edge spectra (XANES). A correlation between manganese anode deposition with increased impedance was confirmed by comparing results of cells with and without Mn contaminated electrolyte.

In addition to deposition as $Mn^{2+}$, presence of $Mn^0$ on graphite anodes from $LiMn_2O_4$ based cells has also been detected using XANES.[105] For this study, the battery electrolyte was contaminated with $Mn(ClO_4)$ at a concentration of 200 ppm. XANES features indicate that both the 0 and 2+ oxidation states are present on the electrode. Similar results were found when $Mn^{2+}$ ions were generated in-situ by dissolution from the cathode material. The authors theorize that $Mn^{2+}$ reduction may occur via defect sites or via electronic transport through a preformed SEI.

### 1.3.3 Cathode dissolution in Li-based battery systems – $LiFePO_4$ and $LiV_3O_8$

Studies relating to dissolution of transition metal ions have also been published for cathode materials including lithium iron phosphate[1, 106-107] and lithium vanadates[108]. The methodology of these works involves storage of the cathode materials at elevated temperatures and analysis of the dissolution species by ICP. The stability of $LiFePO_4$ in solution was found to be several times greater than $LiMn_2O_4$.[106] $LiFePO_4$ was determined to be highly stable in electrolytes without acidic or protic contaminants, even at elevated temperatures.[1] The impedance of $LiFePO_4$ electrodes remained stable with prolonged storage in solution, indicating that the phosphate based material is less prone to dissolution than other oxide based materials, including $LiCoO_2$, $LiNiO_2$, and $LiMn_2O_4$.[1]

$LiV_3O_8$ is another cathode material which has been reported to dissolve in non-aqueous electrolytes.[108-111] The dissolution is observed as the material is discharged, and is thought to

contribute to capacity fade upon cycling. A dissolution mechanism based on V ion exchange with Li was proposed for $Li_{4+y}V_3O_8$.[108] Similar to $LiMn_2O_4$, deposition of the dissolved species on the anode has been reported.[109] A polyaniline conductive binder was found to buffer the dissolution of $LiV_3O_8$, improving the cycling performance of the material.[109]

### 1.3.4 Cathode dissolution in Li-based battery systems – $LiNi_{1/3}Co_{1/3}Mn_{1/3}O_2$

A significant cause of capacity fade and poor long term cycling behavior in $LiNi_{1/3}Co_{1/3}Mn_{1/3}O_2$ (NCM) cathodes is the dissolution of the electrode material into the electrolyte.[112-116] NCM cathodes may be charged using voltage limits from 4.2 to 4.7 V vs. $Li/Li^+$, with higher limits resulting in increased specific capacity and energy density.[112, 116] However, at higher voltages, dissolution of Ni, Co, and Mn species into the electrolyte is observed. The dissolution is problematic for two reasons: (1) the loss of electrode material decreases the capacity, and (2) transition metal ions in the electrolyte deposit onto the anode, increasing the cell impedance.[89] Zheng et al. first performed experiments to determine dissolution behavior of NCM cathode at different states of charge and its influence on capacity fade.[116] Coulombic efficiencity was observed to decrease with increasing charge voltage. Post cycling $LiNi_{1/3}Co_{1/3}Mn_{1/3}O_2$ electrodes were stored in electrolyte for one month and concentration of dissolved Mn, Co, and Ni in the electrolyte was quantified. Dissolution of metal ions increased at charging potentials higher than 4.6V vs. $Li/Li^+$ ,which was in agreement with high capacity fade observed at that charging voltage. In the cycled cells, dissolved metals had deposited on the graphite negative electrode, causing a large rise in impedance which was attributed to be the main factor responsible for capacity fade.

Further work to characterize NCM cathode dissolution focused on the influence of different electrolyte salts.[112] $LiNi_{1/3}Co_{1/3}Mn_{1/3}O_2$ (NCM) electrodes were stored in 1M EC/DMC electrolytes containing $LiPF_6$, $LiBF_4$, $LiClO_4$ salts, and metal ion concentrations were determined by ICP-OES. It was determined that metal dissolution could be reduced by using $LiBF_4$ and $LiClO_4$ instead of the $LiPF_6$, due to minimization of HF formation in the electrolyte which degrades the electrode.[112] Additional studies have also observed a correlation between capacity fade and dissolution in NCM cathodes. $LiNi_{0.6}Co_{0.2}Mn_{0.2}O_2$ cathode materials which were surface modified with a dual conductive polymer coating exhibited reduced transition metal dissolution and more stable cycling performance.[113] Similarly, tris(trimethylsilyl) phosphate electrolyte additives[114] and LiF surface modification of NCM cathodes[115] both result in enhanced cycling stability, believed to be due to suppression of electrode dissolution.

### 1.4. Dissolution Kinetics

Cathode solubility can occur through the dissolution process, during which the crystal lattice of the cathode material is broken down into individual ions and atoms. The dissolution of solid particles in solution is a complex topic for which several models have been developed. The solubility, crystallinity, and particle size of a material may all play a role in influencing the kinetics of dissolution.[117] The first experiments concerning dissolution of solids in solution were performed by Arthur A. Noyes and Willis R. Whitney in 1897, and many subsequent models of dissolution kinetics have a basis in their work.[118] The experiments investigated the dissolution of two compounds of different physical and chemical properties, benzoic acid and lead chloride, in aqueous solution. The following relation was developed between rate of dissolution and the

difference between the bulk concentration, C, at time t and the saturation solubility of the compound, $C_s$:

$$dC/dt = K(C_s-C) \quad [5]$$

where dC/dt is the change in solute concentration in time t, and k is a first order constant. [117] Integration of this equation yields[119] [6], which is corresponds to the integrated rate equation for first order kinetics.[120]

$$C=C_s[1-\exp(-kt)] \quad [6]$$

As reviewed by Dokoumetzidis,[121] Brunner et. al. later determined that the area of exposed surface is proportional to dissolution rate and thus modified the Noyes-Whitney equation to include the surface area of the dissolving solid[122]:

$$dC/dt = K_1S(C_s-C) \quad [7]$$

where $K_1$ is the corresponding rate constant and S is the surface area. Through further investigation, in 1904 Nernst and Brunner found that $K_1$ is proportional to the diffusion coefficient or diffusivity D by Fick's law[123]:

$$k_1=D/Vh \quad [8]$$

where V is volume of solution and h is diffusion layer width. Substitution back into equation [7] yields:

$$dC/dt = (DS/Vh)(C_s - C) \quad [9]$$

This equation for dissolution represents a physical mechanism which involves molecules from the solid diffusing through a thin diffusion layer to the bulk solution (Figure 3).[121] It is assumed that the transport process is rate limiting as opposed to solvation of the solid by the liquid phase at the material surface.[124] The driving force for the process is the concentration gradient between the surface of the solid and the bulk solution. In the diffusion controlled

model, any factor which impacts diffusional transport will affect the dissolution rate, including agitation speed, viscosity of the liquid, temperature, and particle size.[125-126] Although it is evident from [7] and [9] that surface area is directly related to dissolution rate, according to van de Waterbeemd[126] it is difficult to correctly determine the surface area of suspended particles, particularly if the particles tend to agglomerate. This often leads to an overestimation of the surface area of a material in solution.[126]

Further major work regarding dissolution is attributed to Hixson and Crowell in 1931 through their investigation of the relationship between reaction rate and agitation speed.[127] Their work was also based on the diffusion layer model first developed by Noyes and Whitney.

Hixon and Crowell derived a cube root law by first expressing equation [7] in terms of weight of the solid:

$$dW/dt = KS(C_s-C) \qquad [10]$$

where dw/dt is the instantaneous weight change and the surface area S changes as the solid dissolves into solution. This is accomplished by multiplying both sides of the Noyes-Whitney equation by V and setting $K=k_1V$. If the crystal shape does not change during dissolution, because S is proportional to $V^{2/3}$, and W/D = V, then S is also proportional to $W^{2/3}$. Substitution of S into equation [9] and subsequent integration results in an expression relating the instantaneous weight change to the cubic root of the weight. In the special case of sparingly soluble compounds, for which concentration change is negligible, $(C_s-C)$ is constant and the rate is proportional to weight only. The integrated equation becomes:

$$k_2t = W_o^{1/3} - W^{1/3} \qquad [11]$$

where $W_o$ is the initial weight of the solid and $k_2$ is a constant which depends on the density and shape of the solid particle.[127] Equation 10 may be rewritten as

$$W_o^{1/3} - W^{1/3} = (K'N^{1/3}DC_st)/\delta \quad [12]$$

where N is the number of particles, D is the diffusion layer and δ is the diffusion layer thickness.[117] An important consideration for the Hixson-Crowell model is that the geometrical shape of the particles dissolving over time must remain constant for the model to be accurate.[117] Dokoumetzidis[121] writes that explanations of dissolution have been developed which have a different physical basis from the diffusion layer model. As reviewed by Dokoumetzidis and Macheras,[121] the interfacial barrier model was theorized by Zdanovski in 1946, and assumes that interfacial transport is the limiting phenomena in dissolution.[128] Another alternative model was developed by Danckwerts in 1951.[129] It is based on a "surface renewal mechanism" - the idea that a particle in solution is continually exposed to fresh solvent which absorbs the solid.[129] The diffusion layer concept, however, is still the dominant model used to describe dissolution profiles.[119]

Another important method of interpreting dissolution data found in the literature is based upon an empirical distribution function described by Weibull in 1951.[130] The Weibull function was first used to describe dissolution in 1972 by Langenbucher.[131]

$$m = 1\text{-}\exp\left[-(t-T_i)^b/a\right] \quad [13]$$

where m is the accumulated fraction of dissolved material at time t, and $T_i$ is the time difference between the initial system state and the onset of dissolution. In most instances, the onset of dissolution is instantaneous and $T_i = 0$. The parameter a is a time scaling constant, and b is a constant which defines the shape of the curve. In cases where the dissolution curve has an exponential shape, b=1. If the curve is S-shaped, b>1, and if the curve has a higher initial slope followed by consistency with the exponential, $b < 1$.[117] Equation [13] may be rearranged to estimate the parameters a and b:

$$\log [-\ln(1-m)] = b*\log(t-T_i) - \log a \quad [14]$$

If log[-ln(1-m)] is plotted vs. log(t), b may be obtained from the slope of the line, while a is estimated from the intercept. Because $T_i$ is generally zero, a common way of expressing the Weibull equation is:

$$m = 1-\exp(-\alpha t^b) \quad [15]$$

where $\alpha=1/a$.[132] The Weibull model has been successfully used to fit numerous dissolution profiles, including those with a steep initial slope for which diffusion based models may not provide an adequate fit.[126, 132]

The Weibull model has been criticized because it is empirical function lacking parameters which characterize the kinetics of the dissolution process.[117] However, work has been done to validate its use.[132] Macheras and Dokoumetzidis approach the problem by arguing that a time-dependent rate coefficient is needed to account for nonhomogeneous conditions such as changes in surface area, diffusion layer thickness, and diffusivity D as the dissolution process proceeds.[132] In particular, the diffusion layer thickness and diffusivity are not constant when particles are polydisperse or if there is an initial de-aggregation of particles.[132] By expressing the Noyes Whitney equation [5] in terms of the amount of dissolved material instead of concentration, replacing the classical rate constant with a time-dependent rate coefficient, and integrating the resulting equation, they obtain: [132]

$$m=1-\exp[(-k_1/(1-h)) *t^{1-h}] \quad [16]$$

where m is the fraction of material in solution, and $k_1$ and h describe the time-dependent rate coefficient k, which is equal to:

$$k=k_1t^{-h} \quad [17]$$

Equation 15 is identical to the Weibull equation [14] if $\alpha=k_1/(1-h)$ and $b=1-h$. Furthermore, equation 15 is equivalent to the Noyes Whitney equation (expressed in terms of dissolution fraction) when h=0 and the rate constant is not time dependent (homogenous).[132] This work is significant because it provides an indirect, physical basis to the Weibull model when analyzing dissolution data.

The process of dissolution of solid particles in liquids may also be described using reaction models for fluid-particle reactions. The general reaction in [18] is used in the derivation of these models:

$$aA(\text{fluid}) + bB(\text{solid}) \rightarrow \text{fluid and solid products} \qquad [18]$$

Two idealized simulations exist for non-catalytic particle-fluid reactions: the progressive core model and the shrinking unreacted core model.[133] The progressive conversion model assumes that the fluid continuously reacts throughout the entire volume of the particle at the same time. In contrast, according to the shrinking core model, reaction occurs first at the outside interface of a non-porous particle.[133] As time progresses the reaction moves inwards, leaving behind converted material referred to as "ash." A core of unreacted solid exists inside the reacted ash. Observation of cross sections of partially reacted solid particles provides evidence that the shrinking core model is a more realistic representation than the progressive conversion model.[133]

The shrinking core model was first developed by Yagi and Kunni in 1955.[134] It has been used to analyze dissolution data in several studies.[98, 135-140] The shrinking core model assumes that the solid particle reacts with the surrounding fluid at constant temperature, and that the fluid concentration is constant or in excess.[141] The rate controlling expressions for the model are determined by the rate determining step in the reaction, which may be one of three successive processes: (1) diffusion through the fluid film surrounding the particle, (2) penetration and

diffusion through the ash layer, and (3) reaction of the fluid with the solid at the surface of the unreacted core.[133] Using equation 15, for a process in which film diffusion is the rate limiting step and the particles are spherical,

$$X_B = k_m t \quad [19]$$

where $k_m = 3bk_gC_A/\rho_B R$.[133] $X_B$ is the fractional conversion of solid reactant B, $k_m$ is the film diffusion rate constant, t is reaction time, $k_g$ is the mass transfer coefficient between fluid and particle, $C_A$ is the constant concentration of fluid A, $\rho_B$ is the density of B, and R is the particle diameter.

When the reaction is controlled by ash diffusion,

$$1-3(1-X_B)^{2/3} + 2(1-X_B) = k_d t \quad [20]$$

where $k_d = 6bD_eC_A/\rho_B R^2$. $K_d$ is the ash diffusion rate constant and $D_e$ is the effective diffusion coefficient.

When the rate limiting step is reaction controlled,

$$1-(1-X_B)^{1/3} = k_r t \quad [21]$$

where $k_r = bk''C_A/\rho_B R$. $k_r$ is the reaction controlled rate constant and k" is the first order rate constant for the surface reaction.

The preceding equations may be used to elucidate the rate determining step in a dissolution experiment by graphically determining which model best fits experimental $X_B$ vs. t data.[98, 135, 137, 139-140] Other data may be collected which also reveal information about the rate determining step. Performing the dissolution experiment at a range of temperatures can help discriminate between diffusion controls or chemical reaction controls, as the chemical reaction step is much more temperature sensitive than the dissolution steps.[133] Furthermore, if reaction rate is dependent upon agitation speed, this suggests that the process is dissolution controlled.[139]

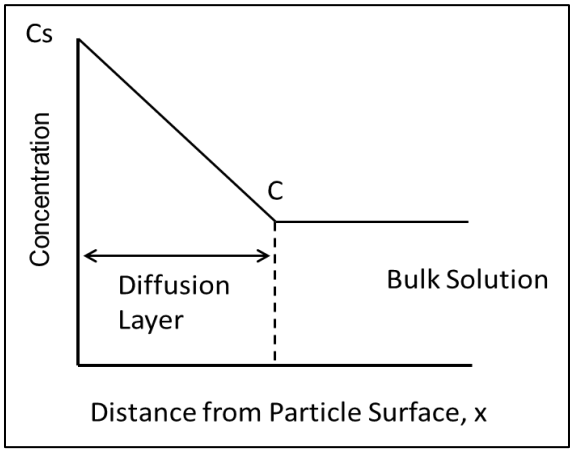


**Figure 3.** A schematic representation of the diffusion-controlled dissolution model first proposed by Noyes and Whitney.[125]

## 1.5. Ion Exchange Kinetics

In addition to cathode solubility proceeding through dissolution, ion exchange of transition metal ions from the cathode material with ions in the electrolyte may also occur. An ion exchange material is defined as a being an insoluble solid having cations or anions which may be exchanged with other ions of the same charge.[142] The structure of an ion exchange material consists of a lattice of atoms held together through chemical bonds or lattice energy. This lattice has an excess of charge which is balanced by counter ions that can move in and out of the matrix.[142] Ion exchange is a stoichiometric process so that the electroneutrality of the material is maintained. Furthermore, the process is reversible, with counter ions being exchanged until equilibrium is reached.[142]

The kinetics of the ion exchange process are complex, depending upon multiple factors including concentration and electrical charge gradients, ionic interactions, structure of the exchanger, and chemical reactions occurring in the exchanger or the electrolyte.[143] In the model system where a spherical ion-exchange particles containing counter ion $A^+$ are stirring in electrolyte with the salt $B^+Y^-$, three rate controlling steps must be considered when determining the kinetics of the ion exchange process: film diffusion, particle diffusion, and chemical exchange reaction.[144]

The first step, film diffusion, involves diffusion of $B^+$ through the film surrounding the ion exchange particles.[143] A thin stagnant film of solution will exist around a particle immersed in solution, even if that solution is well stirred. Mass transfer by diffusion is the lone process by which an ion can reach the exchanger surface through the film. This type of mass transfer may be described as *coupled* because it requires flux of equal amounts of $B^+$ and $A^+$ ions to maintain

electroneutrality.[143] The driving force for film diffusion is the concentration gradient across the film and is described by Fick's first law of diffusion:

$$J = -D^* (dC/dx) \qquad [22]$$

where J is flux of the ion, D is the diffusion coefficient, and dC/dx is the concentration gradient across the film.

The second possible rate determining step, particle diffusion, is physically described as the ions diffusing through the pores within the ion exchanger to reach potential exchange sites.[143] Again, the mass transfer of ions may be referred to as coupled because both B and A must diffuse to maintain electroneutrality. If particle diffusion is the rate determining step, the exchange rate will initially be fast and get progressively slower. This is because exchange occurs quickly at sites on the surface of the particle, and slows down as ions must diffuse further into the particle to reach additional exchange sites.

The third possible rate controlling step is the chemical reaction at the exchange site, where $B^+$ is exchanged with $A^+$. In practice, evidence for the chemical exchange process as the rate limiting kinetic step is only observed for ion exchange involving chelate type formation occurring with iminodiacetate or phosphonate functional groups.[143] Reactions between free ions are typically much faster than diffusion and therefore cannot be rate controlling.[143]

The nature of the rate determining step in ion exchange, whether controlled by film diffusion or particle diffusion, is dependent on several factors of the individual system under investigation.[142] Helfferich writes that the rate determining step can be predicted by the following:

$(XD'\delta/CDr_o) * (5 + 2\alpha) \ll 1$ particle diffusion control

$(XD'\delta/CDr_o) * (5 + 2\alpha) \gg 1$ film diffusion control

where X is the concentration of fixed charges on the particle, C is the concentration of ions in solution, D' is the interdiffusion coefficient in the exchanger particle, D is the interdiffusion coefficient in the film, and α is the separation factor- the preference of the ion exchanger particle for one of the concentration units.[142]

Although it is known that the rates of ion exchange processes are diffusion controlled, limited progress has been made in deriving rate laws for ion exchange systems using diffusion equations.[142-143] This is because of additional complexities in the ion exchange process, including: the distinct selectivities of specific ions for exchange, electric forces arising from ion diffusion, and the swelling of ion exchanger particles due to uptake of solution.

**1.6 Summary**

Batteries for biomedical implants must have characteristics which include high volumetric energy density, predictable performance, and long term stability during use. While several battery systems meet these qualifications, selecting which one to use is dependent on the power requirements of the application. For batteries used in implantable cardioverter defibrillators, where high power is needed, the $Li/Ag_2V_4O_{11}$ system is primarily used. While this system is the benchmark ICD battery technology, solubility of the $Ag_2V_4O_{11}$ cathode material and subsequent deposition of dissolved species on the lithium anode results in increased cell resistance and reduced lifetime. Further chapters will explore the solubility of this system and investigate the silver vanadium phosphorous oxide family of cathode materials as candidates for reducing solubility in the ICD application.

Few reports discuss cathode solubility in non-aqueous systems, particularly with regards to the kinetics of the dissolution process and the impact of material structure on solubility. However, the kinetics of dissolution and ion exchange, primarily developed in aqueous media, can be applied to dissolution battery systems to gain more insight into the mechanisms by which dissolution processes occur.

Several notable lithium-ion cathode materials are reported to dissolve into electrolyte, including $LiCoO_2$, $LiMn_2O_4$, and $LiV_3O_8$, and $LiNi_{1/3}Co_{1/3}Mn_{1/3}O_2$. As such, cathode solubility is a widespread problem, and the development of quantitative and kinetic analysis techniques to characterize the dissolution process will aid the broader community in more fully understanding this battery failure mechanism.

## 1.7 References


(1) Koltypin, M.; Aurbach, D.; Nazar, L.; Ellis, B., On the Stability of LiFePO4 Olivine Cathodes under Various Conditions (Electrolyte Solutions, Temperatures). *Electrochem. Solid-State Lett.* **2007,** 10, A40-A44.

(2) Aurbach, D.; Markovsky, B.; Salitra, G.; Markevich, E.; Talyossef, Y.; Koltypin, M.; Nazar, L.; Ellis, B.; Kovacheva, D., Review on electrode-electrolyte solution interactions, related to cathode materials for Li-ion batteries. *J. Power Sources* **2007,** 165, 491-499.

(3) Root, M. J., Resistance Model for Lithium-Silver Vanadium Oxide Cells. *J. Electrochem. Soc.* **2011,** 158, A1347-A1353.

(4) Owens, B. B.; Skarstad, P. M.; Untereker, D. F.; Passerini, S., Solid-electrolyte Batteries. In *Handbook of Batteries*, 3rd ed.; Linden, D.; Reddy, T. B., Eds. McGraw-Hill: **2002**.

(5) Linden, D.; Reddy, T. B., Lithium batteries. In *Handbook of Batteries*, Linden, D.; Reddy, T. B., Eds. McGraw-Hill: **2002**; Vol. 3rd.

(6) Ehrlich, G. M., Lithium-ion batteries. In *Handbook of Batteries*, 3rd ed.; Linden, D.; Reddy, T. B., Eds. McGraw-Hill: **2002**.

(7) Schneider, A. A.; Moser, J. R. Primary Cells and iodine-containing cathodes therefor. US Patent 3674562, **1972**.

(8) Moser, J. R. Solid State lithium iodine primary battery. US Patent 36660163, **1972**.

(9) Holmes, C. F., The Bourner Lecture: Electrochemical power sources - an important contributor to modern health care. *J. Power Sources* **1997,** 65, xv,xvi,xvii,xviii,xix,xx.

(10) Brodd, R. J.; Bullock, K. R.; Leising, R. A.; Middaugh, R. L.; Miller, J. R.; Takeuchi, E., Batteries, 1977 to 2002. *J. Electrochem. Soc.* **2004,** 151, K1-K11.

(11) Takeuchi, E. S.; Leising, R. A., Lithium batteries for biomedical applications. *MRS Bull.* **2002,** 27, 624-627.

(12) Holmes, C. F., The lithium/iodine-polyvinylpyridine battery - 35 years of successful clinical use. *ECS Trans.* **2007,** 6, 1-7.

(13) Gutmann, F.; Hermann, A. M.; Rembaum, A., Solid-state electrochemical cells based on charge transfer complexes. *J. Electrochem. Soc.* **1967,** 114, 323-9.

(14) Schneider, A. A.; Bowser, G. C.; Foxwell, L. H. Lithium Iodine Primary Cells Having Novel Pelletized Depolarizer. Patent 4148975, **1979**.

(15) Greatbatch, W.; Mead, R. T.; Rudolph, F. Lithium-Iodine Battery having Coated Anode U.S. Patent 3957533, **1976**.

(16) Phipps, J. B.; Hayes, T. G.; Skarstad, P. M.; Untereker, D. F., In-situ formation of a solid/liquid composite electrolyte in lithium-iodine batteries. *Solid State Ionics* **1986,** 18-19, 1073-7.

(17) Holmes, C. F., Lithium/Halogen Batteries. In *Batteries for Implantable Biomedical Devices*, Owens, B. B., Ed. Plenum Press: New York, **1986**, pp 133-180.

(18) Schmidt, C. L.; Skarstad, P. M., Development of an equivalent-circuit model for the lithium/iodine battery. *J. Power Sources* **1997,** 65, 121-128.

(19) Liu, F.-C.; Liu, W.-M.; Zhan, M.-H.; Fu, Z.-W.; Li, H., An all solid-state rechargeable lithium-iodine thin film battery using LiI(3-hydroxypropionitrile)2 as an I- ion electrolyte. *Energy Environ. Sci.* **2011,** 4, 1261-1264.

(20) Weinstein, L.; Yourey, W.; Gural, J.; Amatucci, G. G., Electrochemical Impedance Spectroscopy of Electrochemically Self-Assembled Lithium-Iodine Batteries. *J. Electrochem. Soc.* **2008,** 155, A590-A598.

(21) Ikeda, H.; Saito, T.; Tamura, H., Lithium-manganese dioxide cell. (1). *Denki Kagaku oyobi Kogyo Butsuri Kagaku* **1977,** 45, 314-18.

(22) Nishio, K., PRIMARY BATTERIES - NONAQUEOUS SYSTEMS | Lithium-Manganese Dioxide. In *Encyclopedia of Electrochemical Power Sources*, x00Fc; rgen, G., Eds. Elsevier: Amsterdam, **2009**, pp 83-92.

(23) Kim, H.-S.; Kim, H.-J.; Cho, W.-I.; Cho, B.-W.; Ju, J.-B., Discharge characteristics of chemically prepared MnO2 and electrolytic MnO2 in non-aqueous electrolytes. *J. Power Sources* **2002,** 112, 660-664.

(24) Shao-Horn, Y.; Hackney, S. A.; Cornilsen, B. C., Structural characterization of heat-treated electrolytic manganese dioxide and topotactic transformation of discharge products in the Li-MnO2 cells. *J. Electrochem. Soc.* **1997,** 144, 3147-3153.

(25) Bowden, W.; Bofinger, T.; Zhang, F.; Iltchev, N.; Sirotina, R.; Paik, Y.; Chen, H.; Grey, C.; Hackney, S., New manganese dioxides for lithium batteries. *J. Power Sources* **2007,** 165, 609-615.

(26) Nishio, K.; Yoshimura, S.; Saito, T., Discharge characteristics of manganese dioxide/lithium cells in various electrolyte solutions. *J. Power Sources* **1995,** 55, 115-17.

(27) Pistoia, G., Some restatements on the nature and behavior of manganese(IV) oxide for lithium batteries. *J. Electrochem. Soc.* **1982,** 129, 1861-5.

(28) Ohzuku, T.; Kitagawa, M.; Hirai, T., Electrochemistry of manganese dioxide in lithium nonaqueous cell. I. X-ray diffractional study on the reduction of electrolytic manganese dioxide. *J. Electrochem. Soc.* **1989,** 136, 3169-74.

(29) Nardi, J. C., Characterization of the lithium/manganese dioxide multistep discharge. *J. Electrochem. Soc.* **1985,** 132, 1787-91.

(30) Merritt, D. R.; Schmidt, C. L., Impedance modeling of the lithium/manganese dioxide battery. *Proc. - Electrochem. Soc.* **1993**, 138-45.

(31) Merritt, D. R.; Schmidt, C. L., Investigation of cathodic current collection in lithium/manganese dioxide cells by electrochemical impedance spectroscopy. *Proc. - Electrochem. Soc.* **1994,** 94-4, 169-76.

(32) Nagao, M.; Pitteloud, C.; Kamiyama, T.; Otomo, T.; Itoh, K.; Fukunaga, T.; Kanno, R., Further Understanding of Reaction Processes in Electrolytic Manganese Dioxide Electrodes for Lithium Cells. *J. Electrochem. Soc.* **2005,** 152, E230-E237.

(33) Johnson, C. S., Development and utility of manganese oxides as cathodes in lithium batteries. *J. Power Sources* **2007,** 165, 559-565.

(34) Lee, J.; Lee, J.-M.; Yoon, S.; Kim, S.-O.; Sohn, J.-S.; Rhee, K.-I.; Sohn, H.-J., Electrochemical characteristics of manganese oxide/carbon composite as a cathode material for Li/MnO2 secondary batteries. *J. Power Sources* **2008,** 183, 325-329.

(35) Watanabe, K.; Fukuda, M. Primary cell for electric batteries. U.S. Patent No. 3536532, **1970**.

(36) Watanabe, K.; Fukuda, M. High energy density battery. U.S. Patent Number 3700502, **1972**.

(37) Greatbatch, W.; Holmes, C. F.; Takeuchi, E. S.; Ebel, S. J., Lithium/carbon monofluoride (Li/CFx): a new pacemaker battery. *Pacing Clin Electrophysiol* **1996,** 19, 1836-40.

(38) Amatucci, G. G.; Pereira, N., Fluoride based electrode materials for advanced energy storage devices. *J. Fluorine Chem.* **2007,** 128, 243-262.

(39) Nakajima, T.; Hagiwara, R.; Moriya, K.; Watanabe, N., Discharge characteristics of poly(carbon monofluoride) prepared from the residual carbon obtained by thermal decomposition of poly(dicarbon monofluoride) and graphite oxide. *J. Electrochem. Soc.* **1986,** 133, 1761-6.

(40) Nakajima, T.; Mabuchi, A.; Hagiwara, R.; Watanabe, N.; Nakamura, F., Discharge characteristics of graphite fluoride prepared via graphite oxide. *J. Electrochem. Soc.* **1988,** 135, 273-7.

(41) Touhara, H.; Fujimoto, H.; Watanabe, N.; Tressaud, A., Discharge reaction mechanism in graphite fluoride-lithium batteries. *Solid State Ionics* **1984,** 14, 163-70.

(42) Watanabe, N.; Nakajima, T.; Hagiwara, R., Discharge reaction and overpotential of the graphite fluoride cathode in a nonaqueous lithium cell. *J. Power Sources* **1987,** 20, 87-92.

(43) Hagiwara, R.; Nakajima, T.; Watanabe, N., Kinetic study of discharge reaction of lithium-graphite fluoride cell. *J. Electrochem. Soc.* **1988,** 135, 2128-33.

(44) Davis, S.; Takeuchi, E. S.; Tiedemann, W.; Newman, J., Simulation of the Li-CFx system. *J. Electrochem. Soc.* **2007,** 154, A477-A480.

(45) Davis, S.; Takeuchi, E. S.; Tiedemann, W.; Newman, J., Simulation of pulse discharge of the Li-CFx system. *J. Electrochem. Soc.* **2007,** 155, A24-A28.

(46) Nagata, M.; Saraswat, A.; Nakahara, H.; Yumoto, H.; Skinlo, D. M.; Takeya, K.; Tsukamoto, H., Miniature pin-type lithium batteries for medical applications. *J. Power Sources* **2005,** 146, 762-765.

(47) Zhu, H. J.; Gavril, M.; Feng, L.; Karpinet, D., Li/CFx medical battery development. *ECS Trans.* **2008,** 11, 11-17.

(48) Zhang, S. S.; Foster, D.; Read, J., Enhancement of discharge performance of Li/CFx cell by thermal treatment of CFx cathode material. *J. Power Sources* **2009,** 188, 601-605.

(49) Zhang, S. S.; Foster, D.; Read, J., Carbothermal treatment for the improved discharge performance of primary Li/CFx battery. *J. Power Sources* **2009,** 191, 648-652.

(50) Li, Y.; Chen, Y.; Feng, W.; Ding, F.; Liu, X., The improved discharge performance of Li/CFx batteries by using multi-walled carbon nanotubes as conductive additive. *J. Power Sources* **2011,** 196, 2246-2250.

(51) Read, J.; Collins, E.; Piekarski, B.; Zhang, S., LiF Formation and Cathode Swelling in the Li/CFx Battery. *J. Electrochem. Soc.* **2011,** 158, A504-A510.

(52) Zhang, S. S.; Foster, D.; Wolfenstine, J.; Read, J., Electrochemical characteristic and discharge mechanism of a primary Li/CFx cell. *J. Power Sources* **2009,** 187, 233-237.

(53) Gan, H.; Rubino, R. S.; Takeuchi, E. S., Dual-chemistry cathode system for high-rate pulse applications. *J. Power Sources* **2005,** 146, 101-106.

(54) Chen, K.; Merritt, D. R.; Howard, W. G.; Schmidt, C. L.; Skarstad, P. M., Hybrid cathode lithium batteries for implantable medical applications. *J. Power Sources* **2006,** 162, 837-840.

(55) Gomadam, P. M.; Merritt, D. R.; Scott, E. R.; Schmidt, C. L.; Skarstad, P. M.; Weidner, J. W., Mathematical modeling of Li/CFx-SVO batteries. *ECS Trans.* **2007,** 3, 45-54.

(56) Gomadam, P. M.; Merritt, D. R.; Scott, E. R.; Schmidt, C. L.; Skarstad, P. M.; Weidner, J. W., Modeling Li/CFx-SVO hybrid-cathode batteries. *J. Electrochem. Soc.* **2007,** 154, A1058-A1064.

(57) Gomadam, P. M.; Merritt, D. R.; Scott, E. R.; Schmidt, C. L.; Weidner, J. W., Modeling transients in Li/CFx-SVO hybrid-cathode batteries. *ECS Trans.* **2008,** 11, 1-6.

(58) Liang, C. C.; Bolster, M. E.; Murphy, R. M. Metal oxide composite cathode material for high energy density batteries. US patent 4310609 **1982**.

(59) Takeuchi, E. S.; Piliero, P., Lithium/silver vanadium oxide batteries with various silver to vanadium ratios. *J. Power Sources* **1987,** 21, 133-41.

(60) Takeuchi, K. J.; Marschilok, A. C.; Davis, S. M.; Leising, R. A.; Takeuchi, E. S., Silver vanadium oxides and related battery applications. *Coord. Chem. Rev.* **2001,** 219-221, 283-310.

(61) Leising, R. A.; Takeuchi, E. S., Solid-State Synthesis and Characterization of Silver Vanadium Oxide for Use as a Cathode Material for Lithium Batteries. *Chem. Mater.* **1994,** 6, 489-95.

(62) Takeuchi, E. S., Reliability systems for implantable cardiac defibrillator batteries. *J. Power Sources* **1995,** 54, 115-19.

(63) Takeuchi, K. J.; Leising, R. A.; Palazzo, M. J.; Marschilok, A. C.; Takeuchi, E. S., Advanced lithium batteries for implantable medical devices: mechanistic study of SVO cathode synthesis. *J. Power Sources* **2003,** 119-121, 973-978.

(64) Takeuchi, E. S.; Marschilok, A. C.; Leising, R. A.; Takeuchi, K. J., Sol-gel synthesis and controlled sintering of silver vanadium oxide. *J. Power Sources* **2007,** 174, 552-553.

(65) Leising, R. A.; Takeuchi, E. S., Solid-state cathode materials for lithium batteries: effect of synthesis temperature on the physical and electrochemical properties of silver vanadium oxide. *Chem. Mater.* **1993,** 5, 738-42.

(66) Leising, R. A.; Thiebolt, W. C., III; Takeuchi, E. S., Solid-State Characterization of Reduced Silver Vanadium Oxide from the Li/SVO Discharge Reaction. *Inorg. Chem.* **1994,** 33, 5733-40.

(67) Takeuchi, E. S.; Thiebolt, W. C., III, The reduction of silver vanadium oxide in lithium/silver vanadium oxide cells. *J. Electrochem. Soc.* **1988,** 135, 2691-4.

(68) Leifer, N. D.; Colon, A.; Martocci, K.; Greenbaum, S. G.; Alamgir, F. M.; Reddy, T. B.; Gleason, N. R.; Leising, R. A.; Takeuchi, E. S., Nuclear Magnetic Resonance and X-Ray Absorption Spectroscopic Studies of Lithium Insertion in Silver Vanadium Oxide Cathodes. *J. Electrochem. Soc.* **2007,** 154, A500-A506.

(69) Ramasamy, R. P.; Feger, C.; Strange, T.; Popov, B. N., Discharge characteristics of silver vanadium oxide cathodes. *J. Appl. Electrochem.* **2006,** 36, 487-497.

(70) Crespi, A. M.; Somdahl, S. K.; Schmidt, C. L.; Skarstad, P. M., Evolution of power sources for implantable cardioverter defibrillators. *J. Power Sources* **2001,** 96, 33-38.

(71) Crespi, A.; Schmidt, C.; Norton, J.; Chen, K.; Skarstad, P., Modeling and characterization of the resistance of lithium/SVO batteries for implantable cardioverter defibrillators. *J. Electrochem. Soc.* **2001,** 148, A30-A37.

(72) Cheng, F.; Chen, J., Transition metal vanadium oxides and vanadate materials for lithium batteries. *J. Mater. Chem.* **2011,** 21, 9841-9848.

(73) Cao, X.; Xie, L.; Zhan, H.; Zhou, Y., Facile preparation of Ag2V4O11 nanoparticles via low-temperature molten salt synthesis method. *Inorg. Mater.* **2008,** 44, 886-889.

(74) Sauvage, F.; Bodenez, V.; Vezin, H.; Morcrette, M.; Tarascon, J. M.; Poeppelmeier, K. R., Structural and transport evolution in the LixAg2V4O11 system. *J. Power Sources* **2010,** 195, 1195-1201.

(75) Sauvage, F.; Bodenez, V.; Tarascon, J.-M.; Poeppelmeier, K. R., Room-Temperature Synthesis Leading to Nanocrystalline Ag2V4O11. *J. Am. Chem. Soc.* **2010,** 132, 6778-6782.

(76) Zhang, S.; Li, W.; Li, C.; Chen, J., Synthesis, Characterization, and Electrochemical Properties of Ag2V4O11 and AgVO3 1-D Nano/Microstructures. *J. Phys. Chem. B* **2006,** 110, 24855-24863.

(77) Onoda, M.; Kanbe, K., Crystal structure and electronic properties of the Ag2V4O11 insertion electrode. *J. Phys. Condens. Matter* **2001,** 13, 6675-6685.

(78) Root, M. J., Lithium-manganese dioxide cells for implantable defibrillator devices-Discharge voltage models. *J. Power Sources* **2010,** 195, 5089-5093.

(79) Fehrmann, G.; Frommel, R.; Wolf, R. Galvanic Cell having improved cathode. US Patent 5587258, 19960105., **1996**.

(80) Drews, J.; Wolf, R.; Fehrmann, G.; Staub, R., High-rate lithium/manganese dioxide batteries; the double cell concept. *J. Power Sources* **1997,** 65, 129-132.

(81) Drews, J.; Wolf, R.; Fehrmann, G.; Staub, R., Development of a hybrid battery system for an implantable biomedical device, especially a defibrillator/cardioverter (ICD). *J. Power Sources* **1999,** 80, 107-111.

(82) Leising, R. A.; Palazzo, M. J.; Takeuchi, E. S.; Takeuchi, K. J., Abuse testing of lithium-ion batteries characterization of the overcharge reaction of LiCoO2/graphite cells. *J. Electrochem. Soc.* **2001,** 148, A838-A844.

(83) Leising, R. A.; Palazzo, M. J.; Takeuchi, E. S.; Takeuchi, K. J., A study of the overcharge reaction of lithium-ion batteries. *J. Power Sources* **2001,** 97-98, 681-683.

(84) Dodd, J.; Kishiyama, C.; Nagata, M.; Nakahara, H.; Yumoto, H.; Tsukamoto, H., Implantable rechargeable lithium ion batteries for medical applications: neurostimulation and cardiovascular devices. *Proc. - Electrochem. Soc.* **2004,** 2003-28, 360-367.

(85) Rubino, R. S.; Gan, H.; Takeuchi, E. S., A study of capacity fade in cylindrical and prismatic lithium-ion batteries. *J. Electrochem. Soc.* **2001,** 148, A1029-A1033.

(86) Takeuchi, E. S.; Gan, H.; Palazzo, M.; Leising, R. A.; Davis, S. M., Anode passivation and electrolyte solvent disproportionation: Mechanism of ester exchange reaction in lithium-ion batteries. *J. Electrochem. Soc.* **1997,** 144, 1944-1948.

(87) Gan, H.; Takeuchi, E. In *Correlation of anode surface film composition and voltage delay*, 198th Electrochemical Society Meeting, **2000**.

(88) Amatucci, G. G.; Tarascon, J. M.; Klein, L. C., Cobalt dissolution in LiCoO2-based non-aqueous rechargeable batteries. *Solid State Ionics* **1996,** 83, 167-73.

(89) Markovsky, B.; Rodkin, A.; Cohen, Y. S.; Palchik, O.; Levi, E.; Aurbach, D.; Kim, H. J.; Schmidt, M., The study of capacity fading processes of Li-ion batteries: major factors that play a role. *J. Power Sources* **2003,** 119-121, 504-510.

(90) Wang, Z.; Huang, X.; Chen, L., Characterization of Spontaneous Reactions of LiCoO2 with Electrolyte Solvent for Lithium-Ion Batteries. *J. Electrochem. Soc.* **2004,** 151, A1641-A1652.

(91) Markevich, E.; Salitra, G.; Aurbach, D., Influence of the PVdF binder on the stability of LiCoO2 electrodes. *Electrochem. Commun.* **2005,** 7, 1298-1304.

(92) Aurbach, D.; Markovsky, B.; Rodkin, A.; Levi, E.; Cohen, Y. S.; Kim, H. J.; Schmidt, M., On the capacity fading of LiCoO2 intercalation electrodes: the effect of cycling, storage, temperature, and surface film forming additives. *Electrochim. Acta* **2002,** 47, 4291-4306.

(93) Blyr, A.; Sigala, C.; Amatucci, G.; Guyomard, D.; Chabre, G. Y.; Tarascon, J. M., Self-discharge of LiMn2O4/C Li-ion cells in their discharged state. Understanding by means of three-electrode measurements. *J. Electrochem. Soc.* **1998,** 145, 194-209.

(94) du Pasquier, A.; Blyr, A.; Courjal, P.; Larcher, D.; Amatucci, G.; Gerand, B.; Tarascon, J. M., Mechanism for limited 55°C storage performance of Li1.05Mn1.95O4 electrodes. *J. Electrochem. Soc.* **1999,** 146, 428-436.

(95) Jang, D. H.; Shin, Y. J.; Oh, S. M., Dissolution of spinel oxides and capacity losses in 4 V Li/LixMn2O4 cells. *J. Electrochem. Soc.* **1996,** 143, 2204-2211.

(96) Jang, D. H.; Oh, S. M., Electrolyte effects on spinel dissolution and cathodic capacity losses in 4 V Li/LixMn2O4 rechargeable cells. *J. Electrochem. Soc.* **1997,** 144, 3342-3348.

(97) Aoshima, T.; Okahara, K.; Kiyohara, C.; Shizuka, K., Mechanisms of manganese spinels dissolution and capacity fade at high temperature. *J. Power Sources* **2001,** 97-98, 377-380.

(98) Lu, C.-H.; Lin, S.-W., Dissolution kinetics of spinel lithium manganate and its relation to capacity fading in lithium ion batteries. *J. Mater. Res.* **2002,** 17, 1476-1481.

(99) Wang, H.-C.; Lu, C.-H., Dissolution behavior of chromium-ion doped spinel lithium manganate at elevated temperatures. *J. Power Sources* **2003,** 119-121, 738-742.

(100) Amine, K.; Liu, J.; Kang, S.; Belharouak, I.; Hyung, Y.; Vissers, D.; Henriksen, G., Improved lithium manganese oxide spinel/graphite Li-ion cells for high-power applications. *J. Power Sources* **2004,** 129, 14-19.

(101) Yang, L.; Takahashi, M.; Wang, B., A study on capacity fading of lithium-ion battery with manganese spinel positive electrode during cycling. *Electrochim. Acta* **2006,** 51, 3228-3234.

(102) Ochida, M.; Domi, Y.; Doi, T.; Tsubouchi, S.; Nakagawa, H.; Yamanaka, T.; Abe, T.; Ogumi, Z., Influence of manganese dissolution on the degradation of surface films on edge plane graphite negative-electrodes in lithium-ion batteries. *J. Electrochem. Soc.* **2012,** 159, A961-A966.

(103) Delacourt, C.; Kwong, A.; Liu, X.; Qiao, R.; Yang, W. L.; Lu, P.; Harris, S. J.; Srinivasan, V., Effect of manganese contamination on the solid-electrolyte-interphase properties in Li-ion batteries. *J. Electrochem. Soc.* **2013,** 160, A1099-A1107.

(104) Zhan, C.; Lu, J.; Kropf, A. J.; Wu, T.; Jansen, A. N.; Sun, Y.-K.; Qiu, X.; Amine, K., Mn(II) deposition on anodes and its effects on capacity fade in spinel lithium manganate-carbon systems. *Nat. Commun.* **2013,** 4, 3437, 8 pp.

(105) Gowda, S. R.; Gallagher, K. G.; Croy, J. R.; Bettge, M.; Thackeray, M. M.; Balasubramanian, M., Oxidation state of cross-over manganese species on the graphite electrode of lithium-ion cells. *Phys. Chem. Chem. Phys.* **2014,** 16, 6898-6902.

(106) Iltchev, N.; Chen, Y.; Okada, S.; Yamaki, J.-i., LiFePO4 storage at room and elevated temperatures. *J. Power Sources* **2003,** 119-121, 749-754.

(107) Amine, K.; Liu, J.; Belharouak, I., High-temperature storage and cycling of C-LiFePO4/graphite Li-ion cells. *Electrochem. Commun.* **2005,** 7, 669-673.

(108) Jouanneau, S.; Le, G. L. S. A.; Verbaere, A.; Guyomard, D., The Origin of Capacity Fading upon Lithium Cycling in Li1.1V3O8. *J. Electrochem. Soc.* **2005,** 152, A1660-A1667.

(109) Gao, X.-W.; Wang, J.-Z.; Chou, S.-L.; Liu, H.-K., Synthesis and electrochemical performance of LiV3O8/polyaniline as cathode material for the lithium battery. *J. Power Sources* **2012,** 220, 47-53.

(110) Jouanneau, S.; Verbaere, A.; Lascaud, S.; Guyomard, D., Improvement of the lithium insertion properties of Li1.1V3O8. *Solid State Ionics* **2006,** 177, 311-315.

(111) Shi, Q.; Hu, R.; Zeng, M.; Dai, M.; Zhu, M., The cycle performance and capacity fading mechanism of a LiV3O8 thin-film electrode with a mixed amorphous-nanocrystalline microstructure. *Electrochim. Acta* **2011,** 56, 9329-9336.

(112) Gallus, D. R.; Schmitz, R.; Wagner, R.; Hoffmann, B.; Nowak, S.; Cekic-Laskovic, I.; Schmitz, R. W.; Winter, M., The influence of different conducting salts on the metal dissolution and capacity fading of NCM cathode material. *Electrochim. Acta* **2014,** 134, 393-398.

(113) Ju, S. H.; Kang, I.-S.; Lee, Y.-S.; Shin, W.-K.; Kim, S.; Shin, K.; Kim, D.-W., Improvement of the Cycling Performance of LiNi0.6Co0.2Mn0.2O2 Cathode Active Materials by a Dual-Conductive Polymer Coating. *ACS App Mater Inter* **2014,** 6, 2546-2552.

(114) Mai, S.; Xu, M.; Liao, X.; Hu, J.; Lin, H.; Xing, L.; Liao, Y.; Li, X.; Li, W., Tris(trimethylsilyl) phosphite as electrolyte additive for high voltage layered lithium nickel cobalt manganese oxide cathode of lithium ion battery. *Electrochim. Acta* **2014,** 147, 565-571.

(115) Shi, S. J.; Tu, J. P.; Tang, Y. Y.; Zhang, Y. Q.; Liu, X. Y.; Wang, X. L.; Gu, C. D., Enhanced electrochemical performance of LiF-modified LiNi1/3Co1/3Mn1/3O2 cathode materials for Li-ion batteries. *J. Power Sources* **2013,** 225, 338-346.

(116) Zheng, H.; Sun, Q.; Liu, G.; Song, X.; Battaglia, V. S., Correlation between dissolution behavior and electrochemical cycling performance for LiNi1/3Co1/3Mn1/3O2-based cells. *J. Power Sources* **2012,** 207, 134-140.

(117) Costa, P.; Sousa Lobo, J. M., Modeling and comparison of dissolution profiles. *Eur. J. Pharm. Sci.* **2001,** 13, 123-133.

(118) Noyes, A. A.; Whitney, W. R., The rate of solution of solid substances in their own solutions. *J. Am. Chem. Soc.* **1897,** 19, 930-4.

(119) Dokoumetzidis, A.; Papadopoulou, V.; Macheras, P., Analysis of Dissolution Data Using Modified Versions of Noyes-Whitney Equation and the Weibull Function. *Pharm. Res.* **2006,** 23, 256-261.

(120) Moore, J. W.; Pearson, R. G., *Kinetics and Mechanism. 3rd Ed*. **1981**; p 455 pp.

(121) Dokoumetzidis, A.; Macheras, P., A century of dissolution research: From Noyes and Whitney to the Biopharmaceutics Classification System. *Int. J. Pharm.* **2006,** 321, 1-11.

(122) Bruner, L.; Tolloczko, S., On the dissolution speed of firm bodies. [machine translation]. *Z. physik. Ch.* **1900,** 35, 283-90.

(123) Nernst, W., Theory of the Reaction Rate in Heterogeneous Systems. [machine translation]. *Z. f. physik. Ch.* **1904,** 47, 52-55.

(124) Dash, S.; Murthy Padala, N.; Nath, L.; Chowdhury, P., Kinetic modeling on drug release from controlled drug delivery systems. *Acta Pol Pharm* **2010,** 67, 217-23.

(125) Gerbino, P. P., *Remington: The Science and Practice of Pharmacy*. 21st Edition ed.; Lippincott Williams and Wilkins: **2005**; p 2393.

(126) van de Waterbeemd, H.; Testa, B.; Editors, *Drug Bioavailability; Estimation of Solubility, Permeability, Absorption and Bioavailability; Second, Completely Revised Edition. [In: Methods Princ. Med. Chem., 2009; 40]*. **2009**; p 623 pp.

(127) Hixson, A. W.; Crowell, J. H., Dependence of reaction velocity upon surface and agitation. I. Theoretical considerations. *J. Ind. Eng. Chem. (Washington, D. C.)* **1931,** 23, 923-31.

(128) Zdanovskii, A. B., The role of the interphase solution in the kinetics of the solution of salts. *Zh. Fiz. Khim.* **1946,** 20, 869-80.

(129) Danckwerts, P. V., Significance of liquid-film coefficients in gas absorption. *J. Ind. Eng. Chem. (Washington, D. C.)* **1951,** 43, 1460-7.

(130) Weibull, W., A statistical distribution of wide applicability. *Journal of Applied Mechanics* **1951,** 18, 293-297.

(131) Langenbucher, F., Linearization of dissolution rate curves by the Weibull distribution. *J. Pharm. Pharmacol.* **1972,** 24, 979-81.

(132) Macheras, P.; Dokoumetzidis, A., On the heterogeneity of drug dissolution and release. *Pharm. Res.* **2000,** 17, 108-112.

(133) Levenspiel, O., *Chemical Reaction Engineering, 3rd Edition*. **1998**; p 656 pp.

(134) Yagi, S.; Kunii, D., Combustion of carbon particles in flames and fluidized beds. *5th Symposium on Combustion, Pittsburgh* **1955**, 231-44.

(135) Antonijevic, M. M.; Jankovic, Z. D.; Dimitrijevic, M. D., Kinetics of chalcopyrite dissolution by hydrogen peroxide in sulphuric acid. *Hydrometallurgy* **2004,** 71, 329-334.

(136) Dicinoski, G. W.; Gahan, L. R.; Lawson, P. J.; Rideout, J. A., Application of the shrinking core model to the kinetics of extraction of gold(I), silver(I) and nickel(II) cyanide complexes by novel anion exchange resins. *Hydrometallurgy* **2000,** 56, 323-336.

(137) Gulfen, M.; Aydin, A. O., Dissolution kinetics of calcined chalcopyrite ore in sulphuric acid solution. *Indian J. Chem. Technol.* **2008,** 15, 180-185.

(138) Hsu, W.-L.; Lin, M.-J.; Hsu, J.-P., Dissolution of solid particles in liquids: a shrinking core model. *Int. J. Chem. Biomol. Eng.* **2009,** 2, 205-210.

(139) Kuecuek, O.; Kocakerim, M. M.; Yartasi, A.; Copur, M., Dissolution of Kestelek's Colemanite Containing Clay Minerals in Water Saturated with Sulfur Dioxide. *Ind. Eng. Chem. Res.* **2002,** 41, 2853-2857.

(140) Laçin, O.; Dönmez, B.; Demir, F., Dissolution kinetics of natural magnesite in acetic acid solutions. *Int. J. Miner. Process.* **2005,** 75, 91-99.

(141) Gbor, P. K.; Jia, C. Q., Critical evaluation of coupling particle size distribution with the shrinking core model. *Chem. Eng. Sci.* **2004,** 59, 1979-1987.

(142) Helfferich, F., *Ion Exchange*. **1962**.

(143) Harland, C. E., *Ion Exchange: Theory and Practice*. 2 ed.; **1994**.

(144) Paterson, R., *An Introduction to Ion Exchange*. **1970**.

# Chapter 2

## A kinetics and equilibrium study of vanadium dissolution from silver vanadium phosphorous oxide and silver vanadium oxide in battery electrolyte: Impact on future ICD battery lifetimes

Reproduced in part from [Bock, D. C.; Marschilok, A. C.; Takeuchi, K. J.; Takeuchi, E. S., A kinetics and equilibrium study of vanadium dissolution from vanadium oxides and phosphates in battery electrolytes: Possible impacts on ICD battery performance. *J. Power Sources* **2013,** 231, 219-235] with permission from Elsevier (Copyright 2013).

### 2.1. Introduction

In seeking to minimize cathode solubility in batteries for the ICD application, this study compares the solubility behavior of silver vanadium oxide with the phosphate-based cathode silver vanadium phosphorous oxide ($Ag_2VO_2PO_4$, SVPO). As it has been reported that the Li/SVO system is negatively affected by vanadium ion dissolution into the electrolyte solution and subsequent deposition onto the lithium anode,[1-2] this study characterizes vanadium dissolution from silver vanadium phosphorous oxide and compares it to the benchmark material. Although the solubility of cathode materials is influenced by physical properties such as surface area, the nature of the crystal structure also plays a large role in the determination of solution properties. The solvation process is less likely to be thermodynamically favorable for materials with stable crystal lattices. Thus, a potential strategy for minimizing cathode solubility is to use cathodes with high chemical stability. Phosphate-based cathode materials are suitable candidates for reducing solubility due to their demonstrated structural and chemical stability.[3-4] The stability of phosphate structures vs. oxides is owed to the strength of the P-O bonds that stabilize the molecular framework. When $PO_4^{3-}$ polyanions are introduced into the lattice, electronegative

phosphorous atoms polarize electrons in the P-O bond, thus reducing the covalency of the M-O bond.[3, 5-6] This inductive effect raises the voltage of the redox couple[5] and stabilizes the structure by making oxygen atoms more difficult to extract.[7]

The silver vanadium phosphorous oxides, $Ag_wV_xP_yO_z$, have been identified as a material family of interest, with the goal of achieving the in-situ formation of conductive silver nanoparticles and multiple electron transfers per formula unit exhibited by SVO, coupled with the high material stability of phosphate based material. Previous physical and electrochemical characterization has shown SVPO to be a promising cathode material for high rate applications such as ICD's.[8-13] The lack of change in interlayer spacing upon discharge of the material supports the idea that phosphorous oxide moieties in the molecular framework impart stability and rigidity,[11] while also suggesting that the material will exhibit relatively low levels of cathode solubility. Based on this data, our hypothesis is that SVPO cathode materials will minimize cathode solubility and anode passivation compared to SVO, resulting in more stable charge times when employed in the ICD application. Thus, for this study, the solubility behavior was investigated and compared for the oxide based cathode material and its phosphate analog. Kinetic analysis of vanadium solubility data was performed to gain understanding of the mechanism of dissolution, and AC impedance measurements as well as pulse tests of cells containing vanadium-treated lithium surfaces were used to demonstrate the effects of solubility on cell resistance. The data demonstrate the improved stability and reduced solubility of SVPO relative to SVO, showing SVPO to be a worthy material for additional investigations relevant to its use in ICD batteries.

## 2.2. Target Materials for Study

### 2.2.1. Silver vanadium oxide, $Ag_2V_4O_{11}$

The structure and electrochemical properties of $Ag_2V_4O_{11}$ are detailed in section 1.2.5.

### 2.2.2. Silver vanadium phosphorous oxide, $Ag_2VO_2PO_4$

Silver vanadium phosphorous oxide, $Ag_2VO_2PO_4$, has been identified as an alternative cathode material for high rate applications.[8-14] SVPO crystallizes in the monoclinic c2/*m* space group. As shown in Figure 1, the structure is characterized by layers of edge sharing $VO_6$ octahedra and $PO_4$ tetrahedra which are parallel to the (001) crystallographic plane.[15] The $Ag^+$ ions located between the layers are in a distorted octahedral coordination with oxygen.

SVPO may be prepared through hydrothermal[15] or reflux-based[13] synthesis techniques. When the material is used as a cathode in lithium batteries, the discharge reaction may be expressed as:[10]

$$Ag_2VO_2PO_4 + 4Li \rightarrow Li_4VO_2PO_4 + 2Ag^0 \qquad [1]$$

The theoretical specific capacity of $Ag_2VO_2PO_4$ is 272 mAh/g, corresponding to the transfer of four electrons and the reduction of $Ag^+$ to $Ag^0$ and $V^{5+}$ to $V^{3+}$. With a measured true density of 5.32 g/cm$^3$, the corresponding volumetric energy density is 1440 mAh/cm$^3$.[9] The open circuit voltage of Li/SVPO cells is approximately 3.4 V.

The lithiation of SVPO has been investigated by characterizing cathodes isolated at various steps of discharge.[10] Scanning electron microscopy indicated that silver nanoparticles form upon reduction of the material. Further analysis of $Li_xAg_{2-x}VO_2PO_4$ discharge products by XRD revealed that Ag metal forms from x=0 to x=2.4. This data suggests that initially the discharge is dominated by Ag reduction, but that some V reduction occurs simultaneously. Ex-

situ magnetic susceptibility measurements and AC impedance values were consistent with the XRD data and indicate that from 0-50% DOD the discharge process is dominated by reduction of $Ag^{+}$ to $Ag^{0}$.[11] At greater DOD's, $V^{5+}$ to $V^{4+}$ and $V^{4+}$ to $V^{3+}$ are the dominant reduction mechanisms. A more recent investigation of the SVPO employed X-ray absorption spectroscopy to obtain a detailed understanding of the geometric and electronic changes in the material upon discharge.[14]

One of the largest obstacles for using phosphate-based materials as cathodes is their inherent low electrical conductivity.[16-17] In SVPO, the formation of silver metal upon discharge imparts conductivity to the material. AC impedance measurements of $Li/Ag_2VO_2PO_4$ cells after discharging only 2% of theoretical capacity exhibited a 15000 fold increase in conductivity.[10] This finding is highly significant because it allows the material to be discharged at high rates without the use of conductive additives, which decrease volumetric capacity.

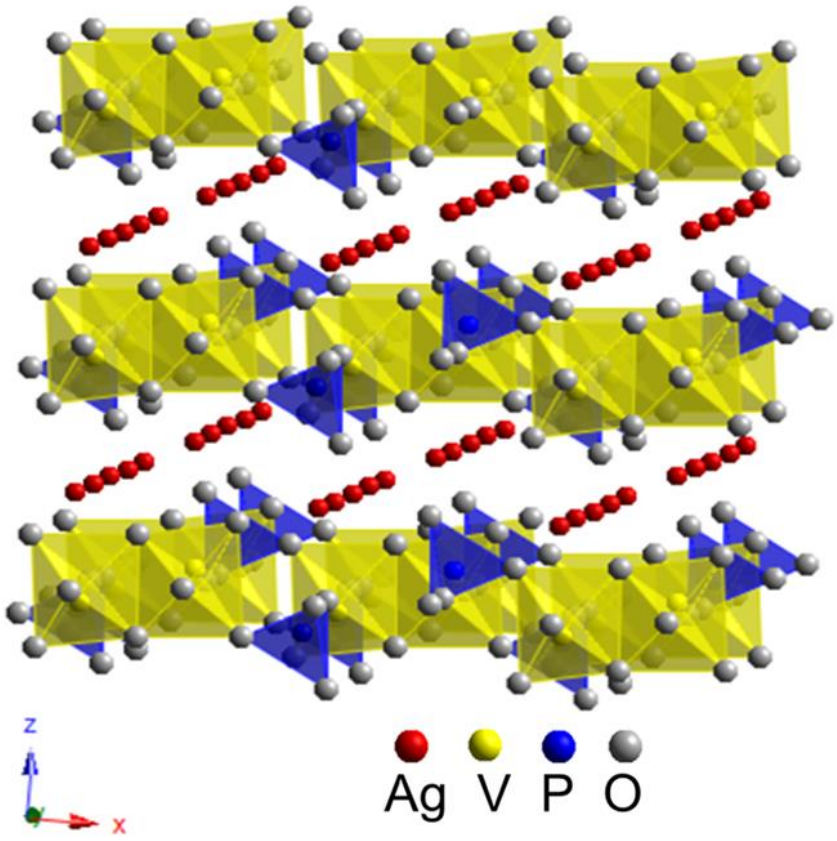


**Figure 1.** Silver vanadium phosphorous oxide is a layered structure consisting of edge sharing $VO_6$ octahedra and $PO_4$ tetrahedra.[15]

## 2.3. Experimental

### 2.3.1. Material Synthesis and Characterization

Silver vanadium phosphorous oxide ($Ag_2VO_2PO_4$) was synthesized by a previously reported hydrothermal method.[15] The material was prepared by heating silver (I) oxide ($Ag_2O$), vanadium (V) oxide ($V_2O_5$) and phosphoric acid ($H_3PO_4$, 85%) for 96 h at 230 C. Silver vanadium oxide ($Ag_2V_4O_{11}$) was prepared through the literature method.[18]

Various characterization techniques were utilized to interrogate the target materials. Differential scanning calorimetry (DSC) analysis was performed using a TA instruments Q20 with a temperature range of 40-580C. Powder X-ray diffraction (XRD) measurements were recorded with a Rigaku Ultima IV X-ray diffractometer. Cu Kα radiation was used with Bragg-Brentano focusing geometry for the XRD measurements, and the collected data was analyzed using MDI Jade 8 software. Particle size of the materials was measured using a Horiba LA-950V2 laser scattering particle size analyzer. Surface area was determined with a Micromeritics Tristar II 3020 through multipoint BET (Brunauer, Emmett, and Teller) method. Scanning electron microscope (SEM) images were collected on a Hitachi SU-70 field emitting scanning electron microscope.

### 2.3.2. Dissolution analysis

To investigate the solubility of the cathode materials, each compound was immersed in under inert Ar atmosphere conditions and ambient temperature. The electrolyte consisted of 1 M $LiBF_4$ dissolved in PC-DME (1:1 by volume) and was analyzed for water content using the Karl Fisher titration method to ensure that the water content by Karl Fischer titration was less than 40 ppm. The conductivity of the prepared electrolyte solution was recorded with a YSI 3100

conductivity instrument. The prepared samples were stored in capped amber vials at ambient temperature and stirred at 1200 rpm. At specified time intervals a low volume of electrolyte was removed from each sample and analyzed via inductively coupled plasma – optical emission spectroscopy (ICP-OES) to determine the dissolved concentration of silver and vanadium ions. A Thermofisher iCAP 6300 series ICP-OES was utilized to collect the concentration measurements.

All of the solubility experiments were continued over an approximate 3 week period in order to adequately monitor the relatively slow kinetics of the dissolution process. This technique required multiple samples to be removed from the same vial. In order to account for the small volumes of electrolyte removed from the parent samples at each measurement point, a correction calculation was applied to the data. This volume correction technique has been used previously to determine the mole ratio of nickel and cobalt dissolved from limonitic laterite,[19] and vanadium from black shale.[20] The equation describing the calculation for each data point is:

$$C_{corr.} = \frac{[(V - \sum_{i=1}^{i-1} v_i)C_i + \sum_{i=1}^{i-1} v_i C_i]}{V} \quad [2]$$

where $C_{corr.}$ is the corrected concentration mg/L, V is the initial volume (L) of solution, $C_{i.}$ is the uncorrected concentration (mg/L) of each sample *i* , and $v_i$ is the volume (L) of each sample *i* removed from the parent sample at each measurement.

2.3.3. AC Impedance Spectroscopy of Doped Li-Li cells

Lithium metal foil anodes were exposed to a vanadium containing solution in PC-DME (1:1 by volume) solvent for a fixed time in order to control the concentration of ions deposited

onto the anode surface. Two electrode, coin-type electrochemical cells were constructed using the doped Li and fresh cut Li foil as electrodes. Control cells using two fresh Li anodes were also constructed. The electrolyte utilized was 1 M $LiBF_4$ dissolved in PC-DME (1:1 by volume). AC impedance measurements were collected using a BioLogic VSP multichannel potentiostat using a 5 mV sinus amplitude and a frequency range of 10 mHz to 100 kHz. Analysis of AC impedance data was performed using ZView software, Version 3.3b. The data was fit to an equivalent circuit model to quantify the cell resistance.

2.3.4. Pulse test of Control and V-treated Li-SVPO cells

Coin cell type experimental cells were assembled using SVPO cathodes and lithium metal anodes. Two sets of cells were prepared where the first group of cells used fresh lithium metal anodes to serve as control cells and the second group used V-treated lithium metal anodes. The cells were tested by application of a pulse train of three 10 s pulses in a row where each pulse at a current density of 20 mA $cm^{-2}$ was followed by 10 s of open circuit voltage.

## 2.4. Results and Discussion

2.4.1 Materials Synthesis and Characterization

X-ray diffraction characterization of the target materials was performed, and the experimentally recorded patterns were matched to those reported in the literature to confirm the crystal structures presented in the target materials section (Figures 2 and 3).

Thermal analysis using differential scanning calorimetry verified single endothermic transitions for the two materials. The absence of additional endotherms suggests that the synthesized materials were comprised of single phases (Figure 4 and 5).[9, 13]

SEM images revealed some differences in morphology and particle size among the target materials of interest. The SVPO sample was comprised of both larger rod shaped structures and smaller granular particles (Figure 6). The rods typically ranged from 15-35 µm in length with a width of 3-4 µm, whereas the smaller particles had typical dimensions of 0.5-3µm. In contrast, SVO also exhibited a distinct morphology consisting of needle shaped particles with an average length of 4 µm and width of approximately 0.5 µm, mixed with larger, irregular masses with a diameter of 5 to 50 µm (Figure 7).

Laser scattering particle size measurements were performed to further quantify the dimensions of the particles. Table 1 lists typical D10, D50 and D90 values for the target materials. A typical particle size distribution for SVPO-H displayed maxima at 0.6, 4 and 25 µm. (Figure 8) The wide distribution of particle sizes for this material is typical of rod shaped particles and corresponds to the SEM images. The particle size data for SVO was also consistent with the SEM analysis. The material exhibited at narrow distribution at approximately 0.6 µm and a broader distribution at 25 µm, which corresponds to the needles and larger masses observed via SEM .

The measured BET surface area of the samples associated closely with the particle size distributions. Average surface area values are listed in Table 1. The surface area of the relatively large SVPO-H particles was approximately $0.7 \pm 0.1$ $m^2g^{-1}$, while the $0.8 \pm 0.2$ $m^2g^{-1}$ average surface area of SVO particles was similar to that of SVOP-H.

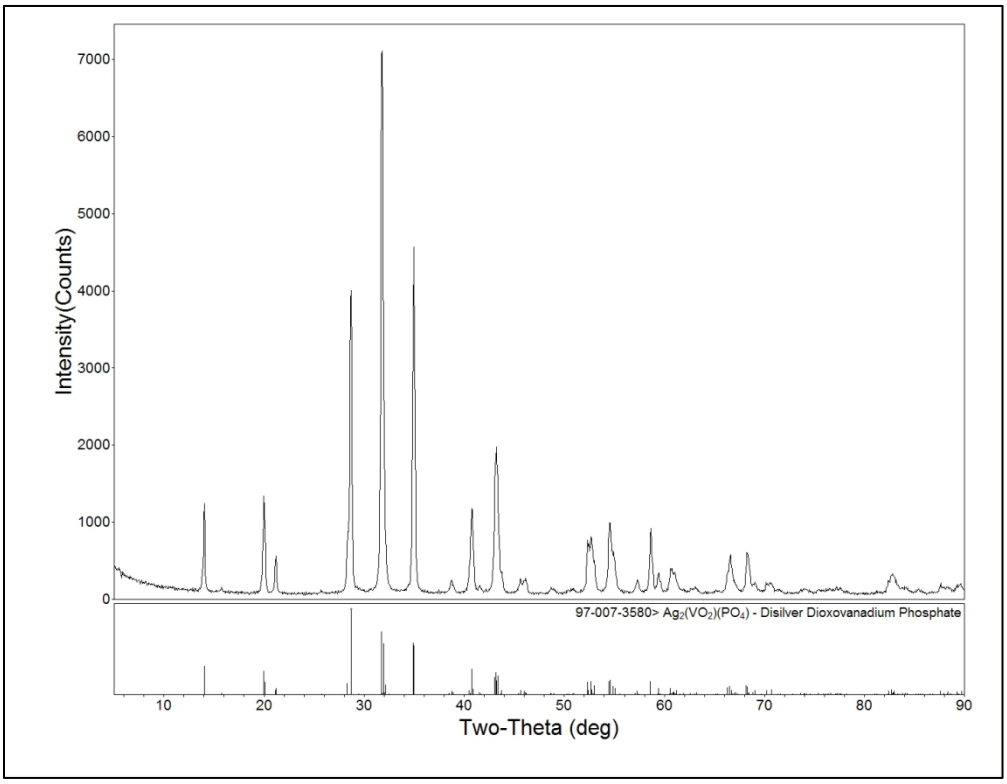


**Figure 2**. Experimentally recorded XRD pattern of $Ag_2VO_2PO_4$ and the literature pattern.[15]

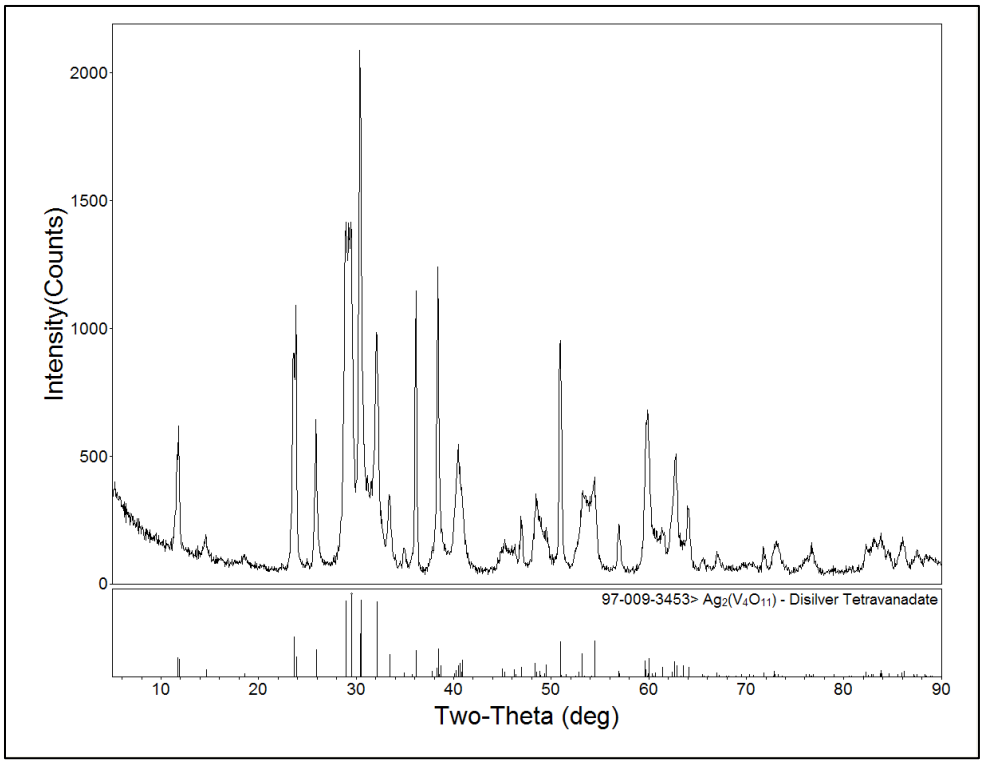


**Figure 3.** Experimentally recorded XRD pattern of $Ag_2V_4O_{11}$ and the literature pattern.[21]

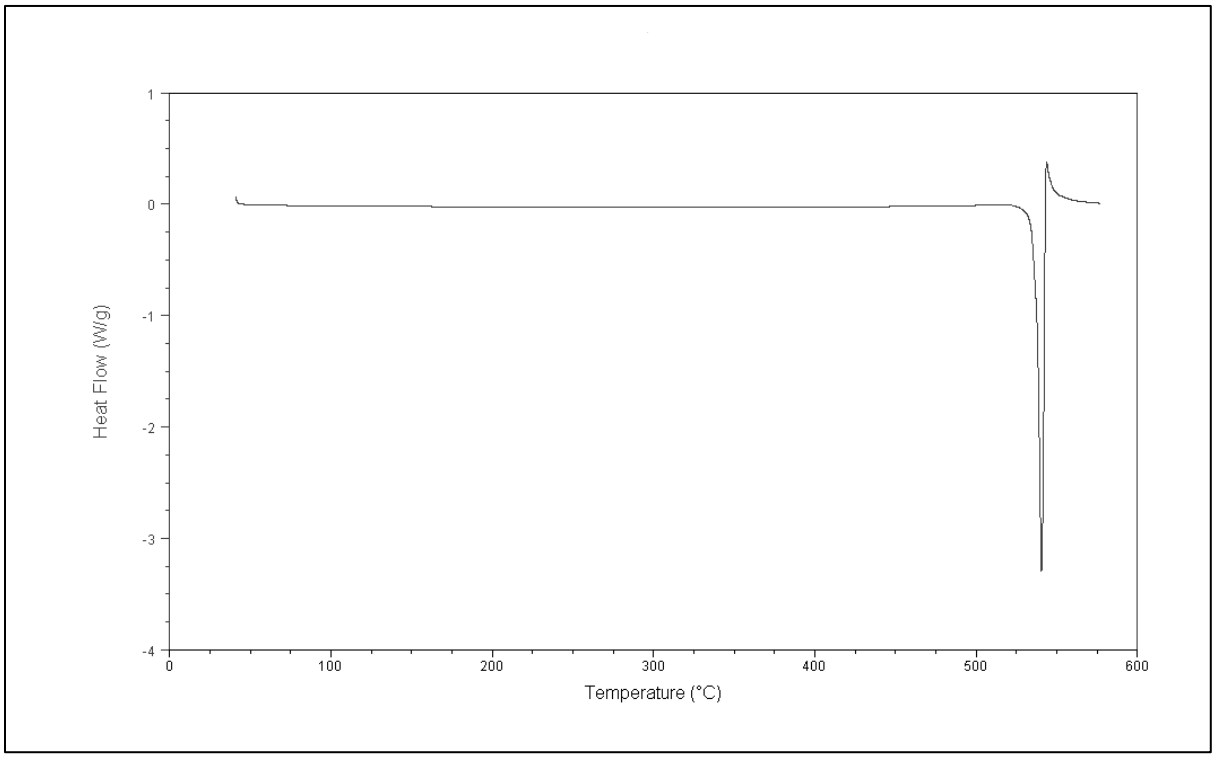


**Figure 4**. DSC spectrum of $Ag_2VO_2PO_4$.

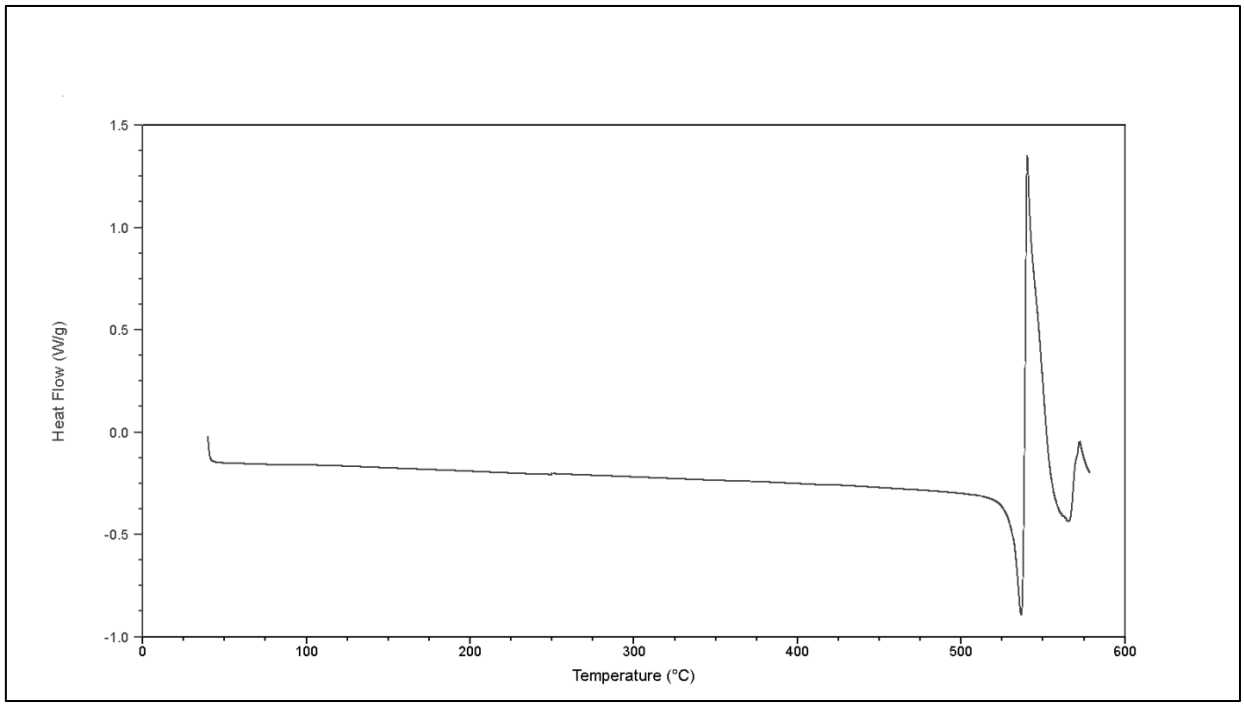


**Figure 5.** DSC spectrum of $Ag_2V_4O_{11}$.

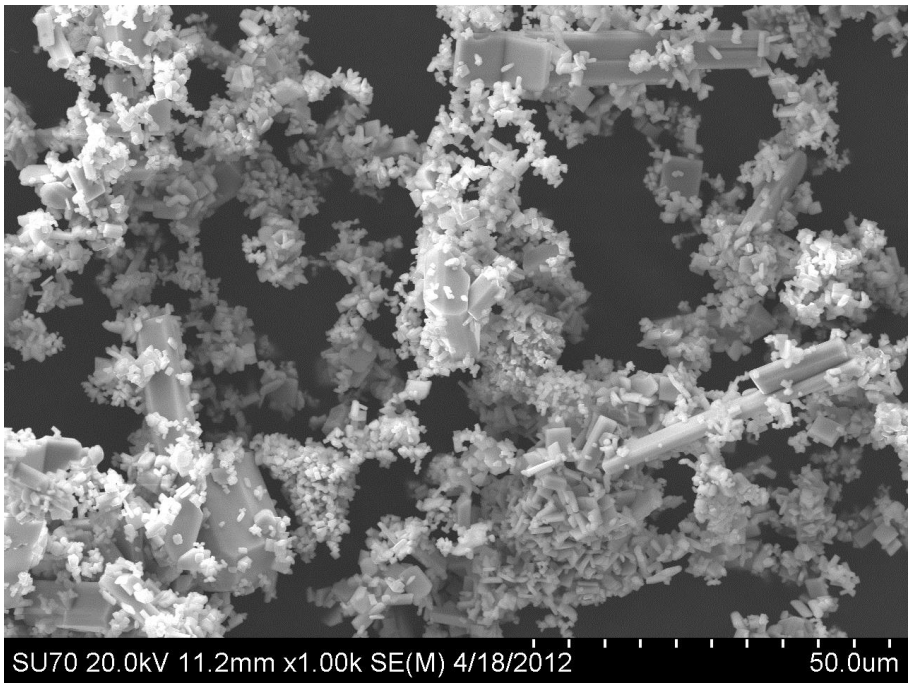


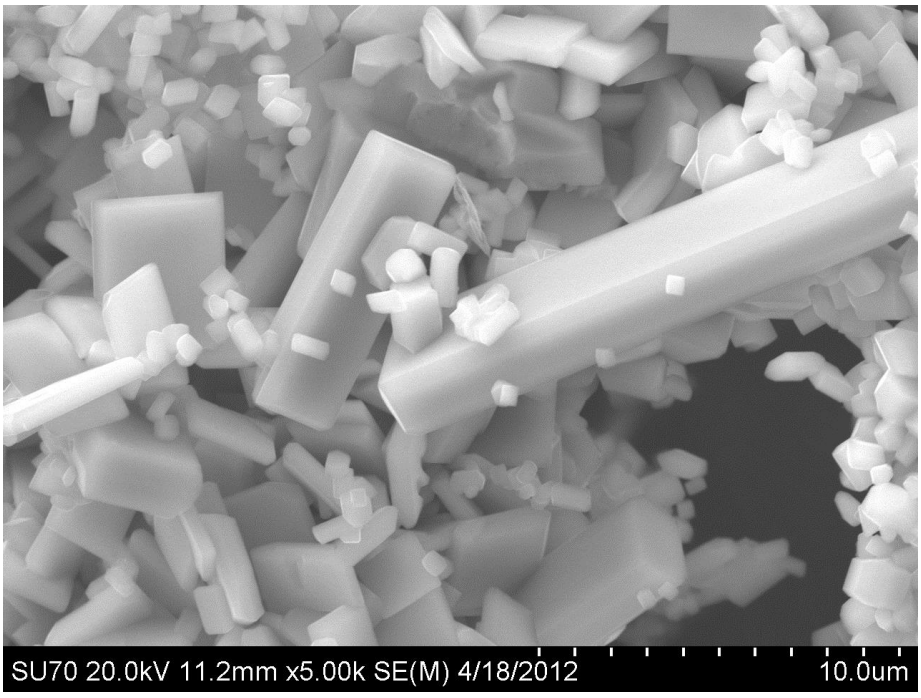


**Figure 6.** SEM images of SVPO-H at 1000x and 5000x, characterized by larger rod shaped structures and smaller granular particles.

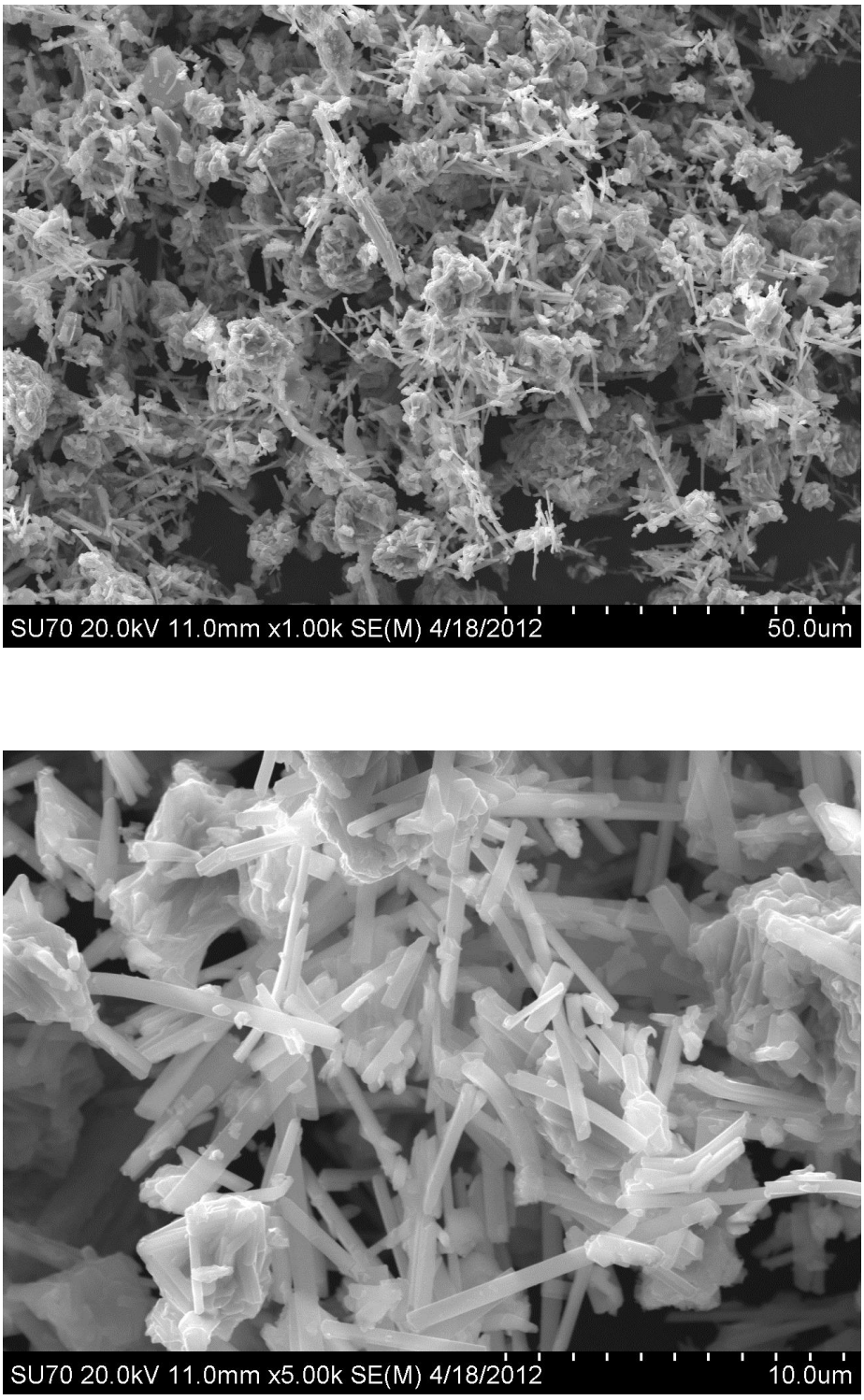


**Figure 7.** SEM images of SVO at 1000x and 5000x, characterized by needle shaped particles mixed with larger, irregularly shaped masses.

| Target Material | BET Surface Area (m2/g) | Typical Particle Size (µm) | | |
|---|---|---|---|---|
| | | D10 | D50 | D90 |
| SVO | 0.8 ± 0.2 | 0.5 | 11 | 40 |
| SVPO | 0.7 ± 0.1 | 0.5 | 0.8 | 12 |

**Table 1**. BET surface area and particle size distribution values for SVPO and SVO.

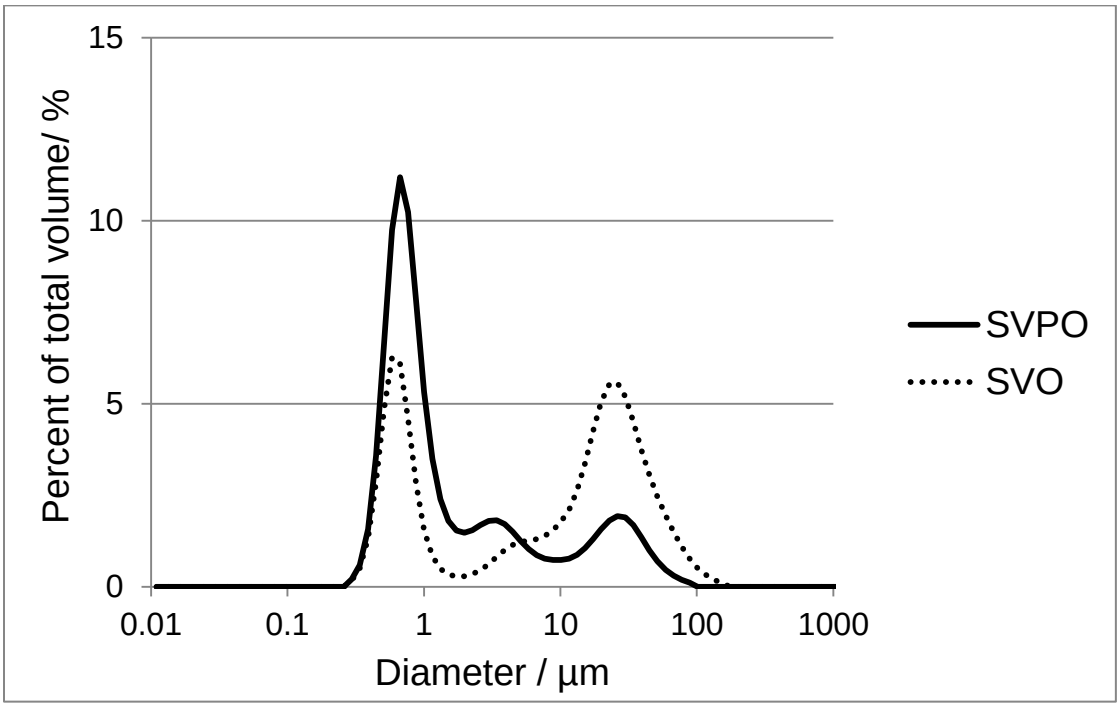


**Figure 8.** Laser scattering particle size distributions of SVPO and SVO.

2.4.2 Dissolution Study

Dissolution analyses of SVO and SVPO were performed with the purpose of comparing the solubility of the materials. Vanadium concentration data was recorded as a function of time, as opposed to static measurement, so that the kinetics of the dissolution process could be examined. Kinetic analysis of this data was determined to reasonably fit the Noyes-Whitney equation for the dissolution of solid particles.

Comparison of vanadium ion dissolution from SVO and hydrothermally prepared SVPO indicates a clear difference in the solubility between the two materials. Figure 9 shows representative plots of the levels of vanadium ions found in electrolyte solution for SVO and SVPO-H as a function of time. Of note is that after 3 weeks the amount of dissolved vanadium in solution comprised less than 1% of the mass of vanadium in the material exposed to electrolyte. In this regard, both materials are relatively stable in the $LiBF_4$ electrolyte. It is apparent that the magnitude of dissolved V ions from SVO is several times that of SVPO. With regards to the characterization measurements, the difference in vanadium solubility cannot be explained by the surface area, which was comparable among the two materials. The surface area data suggests that the observed difference in magnitude is more likely due to inherent differences in stability between the phosphate and oxide based structures.

In order to gain more insight into the vanadium solubility behavior from the two materials, the concentration-time data was fit to the Noyes-Whitney equation, used to describe the dissolution of solid particles in liquid media:[22]

$$C=C_s[1-\exp(-kt)] \qquad [3]$$

In this equation C is the concentration of the solid at time t, $C_s$ is the equilibrium solubility at the particle surface, and k is a proportionality constant. As previously discussed in

Section 1.4, equation [3] represents a diffusion layer model where the extent of dissolution is dependent upon the equilibrium solubility of the material. Non-linear regression analysis was used to fit equation [3] to experimental vanadium dissolution data from 9 individual trials. The best fits were used to evaluate the parameters $C_s$ and k. Figures 10 and 11 display the best fits for representative V concentration–time plots for SVPO and SVO, respectively. The fitting parameters and correlation coefficients for the nine individual trials are detailed in tables 2 and 3. For the SVPO material, the average value of $C_s$ was 2.2 ± 0.5 mg/L, while k was determined to be $5.8 \times 10^{-7} \pm 1.0 \times 10^{-7}$ $s^{-1}$. The average correlation coefficient for the SVPO-H fits was 0.98 ± 0.01. In contrast, the greater magnitude of V dissolution observed for SVO was quantified as having Cs and k values of 10.4 ± 1.7 mg/L and $2.1 \times 10^{-6} \pm 0.5 \times 10^{-6}$ $s^{-1}$, respectively, with the average correlation being 0.98 ± 0.01. The correlation coefficients indicate that the diffusion layer model described by equation [2] reasonably describes dissolution of V from the target compounds. SVO was found to have an average equilibrium solubility, $C_s$, which was approximately 5 times greater than SVPO-H, and a rate constant approximately 3.5 times greater than SVPO.

The surface area data suggest that the observed difference in magnitude of the equilibrium solubility is likely due to differences in stability between the phosphate and oxide based structures. Notably, the particle size distribution and surface area of the SVPO and SVO materials were similar, thus the significant difference in the vanadium solubility cannot be explained by differences in physical properties between the two materials. These data, the first direct comparison of the solubility of an oxide based material and its phosphate analog in non-aqueous electrolyte, support our initial premise that a phosphate based material will demonstrate reduced cathode solubility over and oxide based material.

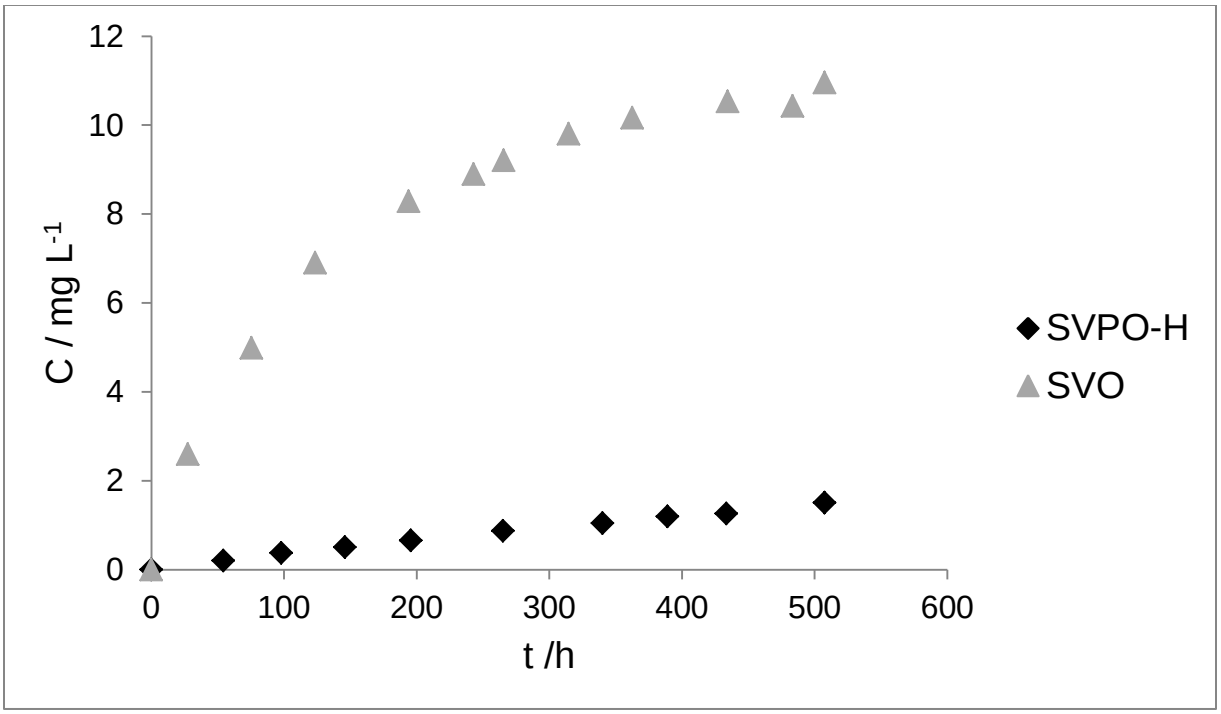


**Figure 9.** Concentration of vanadium dissolved in electrolyte as a function of time for SVPO and SVO.

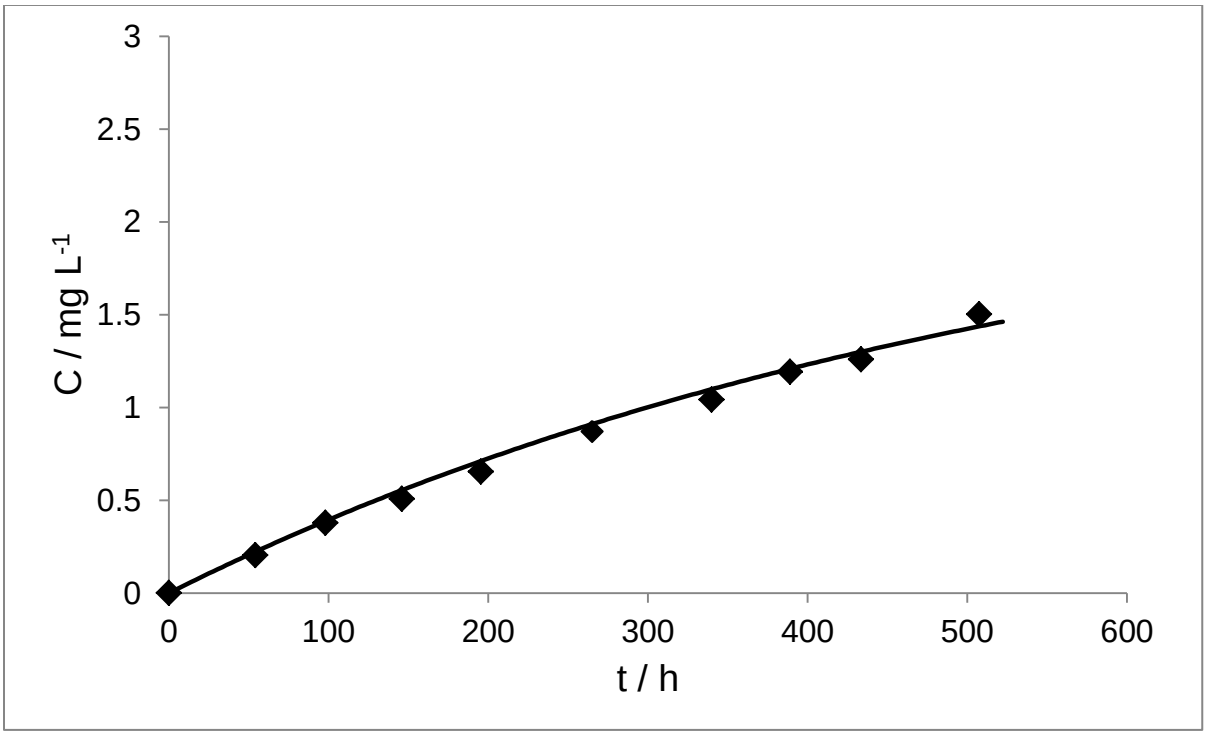


**Figure 10.** Fit of vanadium concentration data as a function of time for SVPO to diffusion layer model ($C=C_s[1-\exp(-kt)]$).

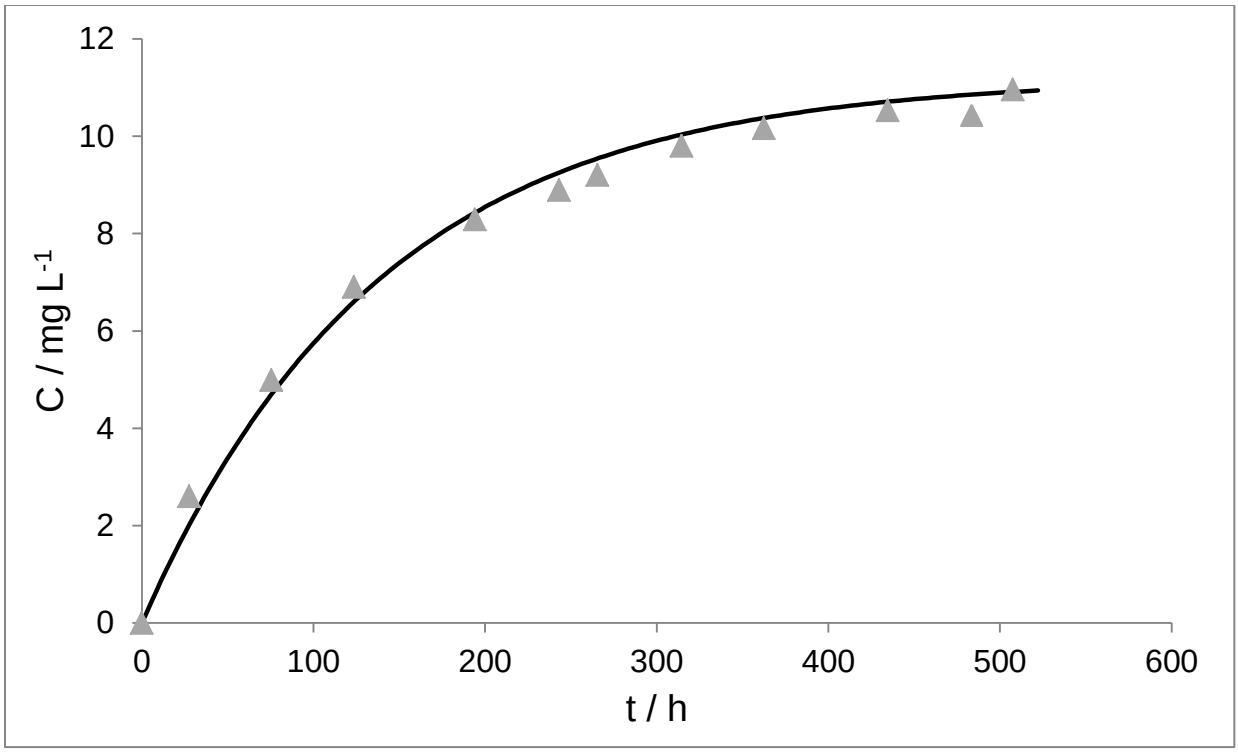


**Figure 11.** Fit of vanadium concentration data as a function of time for SVO to diffusion layer model ($C=C_s[1-exp(-kt)]$).

| Trial # | $C_s$ (mg/L) | k ($s^{-1}$) | $R^2$ |
|---|---|---|---|
| 1 | 2.4 | 0.0000005 | 0.9922 |
| 2 | 1.9 | 0.0000005 | 0.9866 |
| 3 | 2.5 | 0.0000005 | 0.9444 |
| 4 | 1.8 | 0.0000006 | 0.9815 |
| 5 | 2.65 | 0.0000006 | 0.9816 |
| 6 | 2.64 | 0.0000006 | 0.9831 |
| 7 | 2.8 | 0.0000005 | 0.9838 |
| 8 | 1.7 | 0.00000082 | 0.9812 |
| 9 | 1.65 | 0.00000057 | 0.9771 |
| Mean | 2.2 | 5.8E-07 | 0.98 |
| Standard Deviation | 0.5 | 1.0-E-07 | 0.01 |

**Table 2.** Noyes-Whitney equation fitting results: vanadium dissolution from SVPO.

| Trial # | $C_s$ (mg/L) | k ($s^{-1}$) | $R^2$ |
|---|---|---|---|
| 1 | 11.5 | 0.0000015 | 0.9891 |
| 2 | 11.4 | 0.0000015 | 0.9802 |
| 3 | 10.99 | 0.00000179 | 0.9908 |
| 4 | 11.4 | 0.0000024 | 0.9827 |
| 5 | 12 | 0.0000018 | 0.9705 |
| 6 | 9.3 | 0.0000024 | 0.9914 |
| 7 | 11.2 | 0.000002 | 0.9917 |
| 8 | 8.9 | 0.0000022 | 0.9908 |
| 9 | 6.7 | 0.0000029 | 0.973 |
| Mean | 10.4 | 2.1E-06 | 0.98 |
| Standard Deviation | 1.7 | 5.E-07 | 0.01 |

**Table 3.** Noyes-Whitney equation fitting results: vanadium dissolution from SVO.

2.4.3 AC Impedance Study

It is notable that the impedance of a battery is due to a variety of contributions, including those of the anode, the cathode and the electrolyte. In the case of silver vanadium oxide (SVO), the cathode resistance decreases with discharge, which is observed as decreased cell resistance when cells are discharged rapidly. However, over long discharge times, the cell impedance is observed to increase, which has been attributed to cathode dissolution and associated increase in resistance at the anode.[1] For silver vanadium phosphorous oxide (SVPO) based cells, there is also a significant decrease in both the cathode and cell resistance with initial discharge.[10-11] Both the cathode resistance and cell impedance as a function of depth of discharge have been reported and directly correlate over short discharge times.

One of the potential complications of cathode dissolution is raising the impedance of a battery due to the deposition of dissolution products on the anode. As the solubility experiments indicated a clear difference in the amount of transition metal ions which dissolve from SVO and SVPO cathode materials, the potential impact of vanadium dissolution with respect to the internal cell resistance with a focus on the anode was investigated. AC impedance measurements were performed on 2 electrode cells containing one V-treated Li electrode and one untreated electrode, compared with AC impedance data collected on control cells containing fresh lithium surfaces at both electrodes. For each experiment, 5 anodes treated with V were prepared. Three of the treated anodes were used to construct cells for the AC impedance study, while the remaining samples were digested and analyzed by ICP-OES to determine V content. Multiple experimental trials were performed to confirm trends in the data.

Nyquist plots overlaying a typical V-doped cell and control cell are shown in Fig. 12. Measurements were recorded at 24 hours, 72 hours, and 120 hours to observe the progression of

the internal resistance with increasing storage time. The concentration on the surface of the V-doped anodes used to construct these cells was approximately 14 µg V $cm^{-2}$. As illustrated in Fig. 13, after 24 hours at 37°C the diameter of the semicircle in the Nyquist plots was approximately 45 Ω, and 70 Ω for the control cell and V-doped cell, respectively. Passivation of the anode surface increased with time such that after 120 hours of storage these values had increased to 1400Ω and 2500Ω. The Nyquist plots clearly demonstrate that cells containing the anodes doped with V had a higher internal resistance at each time point. The implication of this result is that cathode materials which dissolve vanadium into the electrolyte will accelerate passivation of the anode surface and increase the overall cell resistance.

In order to quantify the cell resistance, the AC impedance data were fit to a simple equivalent circuit model (Figure 13). The model consisted of a resistor, $R_s$, in series with two parallel combinations of a constant phase element, CPE, and a resistor, $R_p$, where the first CPE and $R_p$ were labeled as CPE1 and $R_1$, and the second CPE and $R_p$ were labeled as CPE2 and $R_2$. For the circuit fits the weighted sum of the squares ranged from 0.004 to 0.089. $R_t$ was calculated by adding $R_s$, $R_1$, and $R_2$. The calculated $R_t$ (ohms) was then plotted versus storage time for the two groups of cells (Figure 14). Each data point denotes the mean value of three samples with error bars representative of the standard error. After 120 h of storage the cells with V-treated anodes had an average of ~1.5 times the total resistance of the control cells. Measurements taken at 24h and 72h of storage time similarly displayed a higher total resistance for the V-treated cells.

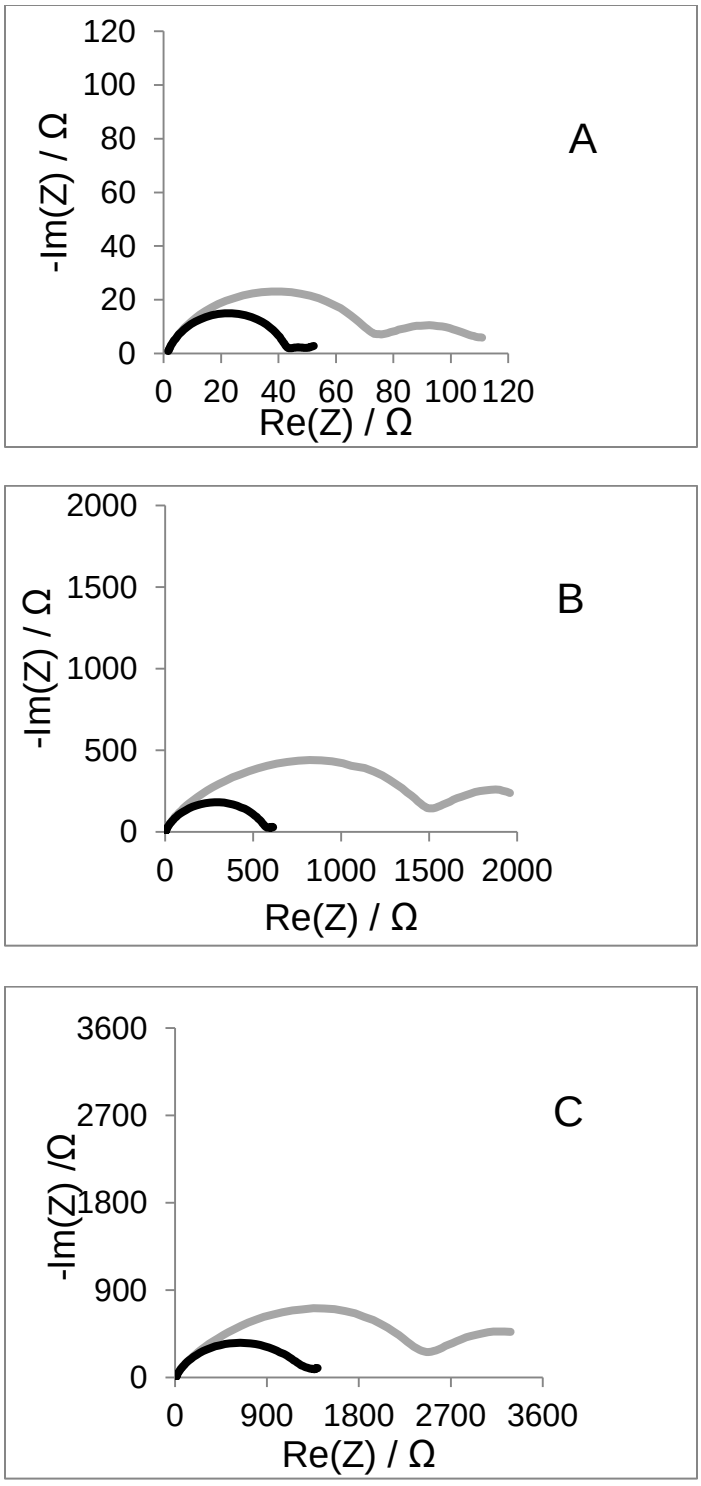


**Figure 12.** Nyquist plots of cells containing fresh lithium anodes (control, black line) and V-treated Li anodes (grey line), where AC impedance data was collected **A.** 24 h, **B.** 72 h, and **C.** 120 h after cell construction.

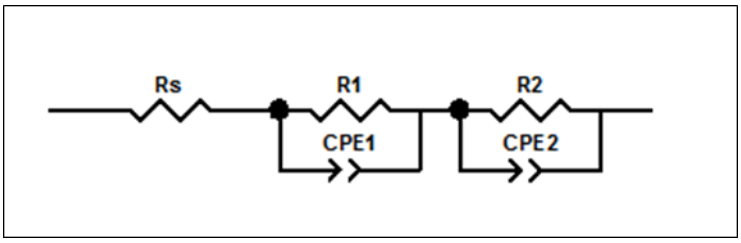


**Figure 13.** Equivalent circuit model used to fit the AC impedance data of Li /Li 2-electrode cells.

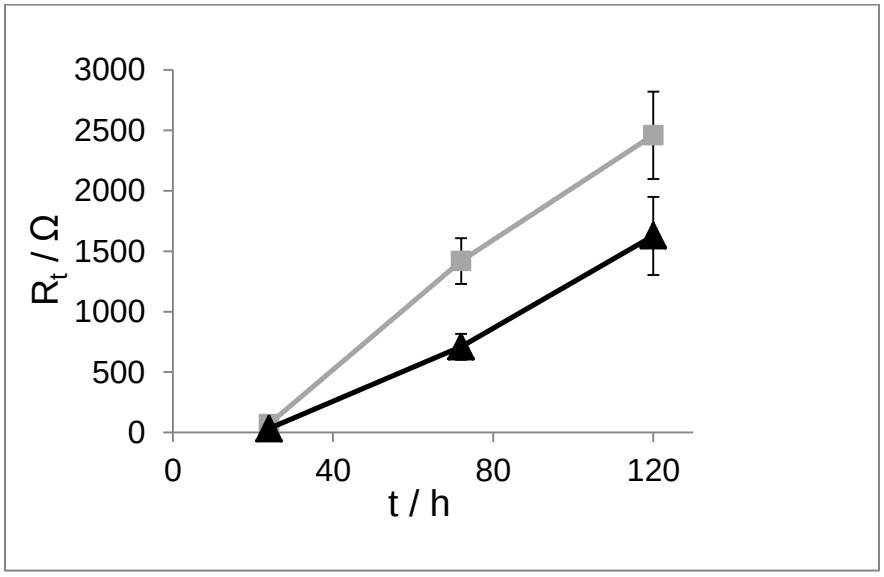


**Figure 14.** Total resistance ($R_t$) as a function of time for cells containing fresh lithium anodes (black) and V-treated Li anodes (grey).

2.4.4. Pulse test of control and V-treated Li-SVPO cells

As a means of further studying the impact of V-treatment of the lithium anode on the cell performance, pulse tests of coin cell type experimental Li/SVPO cells with fresh lithium metal anodes and V-treated anodes were conducted. The cells were tested by applying a pulse train of three 10 s pulses in a row. The pulses had a current density of 20 mA $cm^{-2}$, with a rest at open circuit voltage between pulses. Representative data of a cell from each group is shown to illustrate the impact of V-treated lithium metal anodes when compared to fresh lithium metal anodes (Figure 15). The cells with the fresh lithium metal anodes had a consistently higher operating voltage under pulse. The DC resistance of each cell was calculated from the pulse data where the calculated resistance of the cell using the fresh lithium anodes for each pulse was 39, 22, and 20 Ω. The calculated resistance of the V-treated anode cell was 45, 27, and 25 Ω. Thus, there was a 15-26% increase in the calculated cell DC resistance for the cells with V-treated anodes compared to the control cells.

The results from the AC impedance experiments may be used in conjunction with the dissolution data to support the hypothesis that silver vanadium phosphorous oxide cathode materials will minimize cell resistance resulting from anode passivation. SVO dissolved approximately 5 times more vanadium than SVPO, with the dissolution occurring at a faster rate. In consequence, the magnitude of V anode deposition would be expected to be lower in electrochemical cells having SVPO cathodes as an alternative of SVO. Because V deposition is shown to be associated with an increase cell resistance, the performance of SVPO cells is less likely to be adversely affected by cathode solubility.

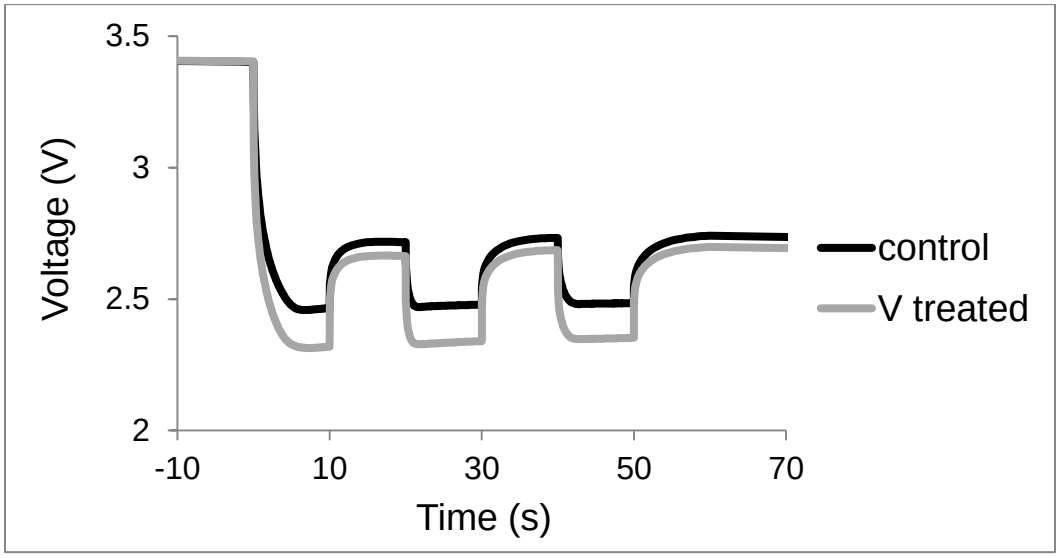


**Figure 15.** Voltage response of Li/SVPO cells during application of three 10 s pulses for fresh lithium anodes (black), and V-treated Li anodes (grey).

## 2.5 Summary

Vanadium dissolution studies of SVPO, $Ag_2VO_2PO_4$, and SVO, $Ag_2V_4O_{11}$, in electrolyte solutions were conducted. The equilibrium solubility of the vanadium component of SVO was found to be approximately 5 times greater than that of SVPO, with a rate constant of dissolution approximately 3.5 times greater than SVPO. Good correlations of the data with the Noyes-Whitney equation support describing vanadium dissolution of SVO and SVPO using a diffusion layer model.

AC impedance experimental results of anodes treated with V indicated that cells with V-treated anodes had a higher internal resistance compared to control cells at multiple time points after construction. Further, pulse tests of Li/SVPO cells with V-treated anodes compared to control anodes also affirmed higher cell resistance for the V-treated anode cells. The implication of these results is that cathode materials which dissolve vanadium into the electrolyte will accelerate passivation of the anode surface and increase the overall cell resistance. This data, when combined with the dissolution results, provide evidence that silver vanadium phosphorous oxide (SVPO) will minimize cell resistance resulting from anode passivation. Because SVO dissolved approximately 5 times more V than SVPO, the magnitude of V anode deposition should be lower in electrochemical cells having SVPO cathodes as opposed to SVO. Thus, cells utilizing SVPO cathodes are less likely to exhibit performance deterioration associated with vanadium dissolution.

## 2.6 References


(1) Root, M. J., Resistance Model for Lithium-Silver Vanadium Oxide Cells. *J. Electrochem. Soc.* **2011,** 158, A1347-A1353.

(2) Gan, H.; Takeuchi, E. In *Correlation of anode surface film composition and voltage delay,* 198th Electrochemical Society Meeting, **2000**.

(3) Ellis, B. L.; Lee, K. T.; Nazar, L. F., Positive Electrode Materials for Li-Ion and Li Batteries. *Chem. Mater.* **2010,** 22, 691-714.

(4) Iltchev, N.; Chen, Y.; Okada, S.; Yamaki, J.-i., LiFePO4 storage at room and elevated temperatures. *J. Power Sources* **2003,** 119-121, 749-754.

(5) Hautier, G.; Jain, A.; Ong, S. P.; Kang, B.; Moore, C.; Doe, R.; Ceder, G., Phosphates as Lithium-Ion Battery Cathodes: An Evaluation Based on High-Throughput ab Initio Calculations. *Chem. Mater.* **2011,** 23, 3495-3508.

(6) Padhi, A. K.; Nanjundaswamy, K. S.; Goodenough, J. B., Phospho-olivines as positive-electrode materials for rechargeable lithium batteries. *J. Electrochem. Soc.* **1997,** 144, 1188-1194.

(7) Kim, D.-H.; Kim, J., Synthesis of LiFePO4 Nanoparticles in Polyol Medium and Their Electrochemical Properties. *Electrochem. Solid-State Lett.* **2006,** 9, A439-A442.

(8) Marschilok, A. C.; Takeuchi, K. J.; Takeuchi, E. S., Evaluation of silver vanadium phosphorous oxide as a cathode material in lithium primary cells. *AIChE Annu. Meet., Conf. Proc.* **2008**, 122/1-122/10.

(9) Marschilok, A. C.; Takeuchi, K. J.; Takeuchi, E. S., Preparation and electrochemistry of silver vanadium Phosphorous oxide, Ag2VO2PO4. *Electrochem. Solid-State Lett.* **2008,** 12, A5-A9.

(10) Takeuchi, E. S.; Marschilok, A. C.; Tanzil, K.; Kozarsky, E. S.; Zhu, S.; Takeuchi, K. J., Electrochemical Reduction of Silver Vanadium Phosphorus Oxide, Ag2VO2PO4: The Formation of Electrically Conductive Metallic Silver Nanoparticles. *Chem. Mater.* **2009,** 21, 4934-4939.

(11) Marschilok, A. C.; Kozarsky, E. S.; Tanzil, K.; Zhu, S.; Takeuchi, K. J.; Takeuchi, E. S., Electrochemical reduction of silver vanadium phosphorous oxide, Ag2VO2PO4: Silver metal deposition and associated increase in electrical conductivity. *J. Power Sources* **2010,** 195, 6839-6846.

(12) Takeuchi, E. S.; Kim, Y. J.; Lee, C.-Y.; Kozarsky, E. S.; Sharma, M. K.; Zhu, S.; Marschilok, A. C.; Takeuchi, K. J., Silver vanadium phosphorous oxide: Resistivity and morphology study. *Abstracts of Papers, 240th ACS National Meeting, Boston, MA, United States, August 22-26, 2010* **2010**, ANYL-283.

(13) Kim, Y. J.; Marschilok, A. C.; Takeuchi, K. J.; Takeuchi, E. S., Silver vanadium phosphorous oxide, Ag2VO2PO4: Chimie douce preparation and resulting lithium cell electrochemistry. *J. Power Sources* **2011,** 196, 6781-6787.

(14) Patridge, C. J.; Jaye, C.; Abtew, T. A.; Ravel, B.; Fischer, D. A.; Marschilok, A. C.; Zhang, P.; Takeuchi, K. J.; Takeuchi, E. S.; Banerjee, S., An X-ray Absorption Spectroscopy Study of the Cathodic Discharge of Ag2VO2PO4: Geometric and Electronic Structure Characterization of Intermediate phases and Mechanistic Insights. *J. Phys. Chem. C* **2011,** 115, 14437-14447.

(15) Kang, H. Y.; Wang, S. L.; Tsai, P. P.; Lii, K. H., Hydrothermal synthesis, crystal structure and ionic conductivity of silver vanadium oxide phosphate, Ag2VO2PO4: a new layered phosphate of vanadium(V). *J. Chem. Soc., Dalton Trans.* **1993**, 1525-8.

(16) Gaubicher, J.; Mercier, T. L.; Chabre, Y.; Angenault, J.; Quarton, M., Li/β-VOPO4: a new 4V system for lithium batteries. *J. Electrochem. Soc.* **1999,** 146, 4375-4379.

(17) Tarascon, J. M.; Armand, M., Issues and challenges facing rechargeable lithium batteries. *Nature (London, U. K.)* **2001,** 414, 359-367.

(18) Leising, R. A.; Takeuchi, E. S., Solid-state cathode materials for lithium batteries: effect of synthesis temperature on the physical and electrochemical properties of silver vanadium oxide. *Chem. Mater.* **1993,** 5, 738-42.

(19) Georgiou, D.; Papangelakis, V. G., Sulfuric acid pressure leaching of a limonitic laterite: chemistry and kinetics. *Hydrometallurgy* **1998,** 49, 23-46.

(20) Li, M.; Wei, C.; Qiu, S.; Zhou, X.; Li, C.; Deng, Z., Kinetics of vanadium dissolution from black shale in pressure acid leaching. *Hydrometallurgy* **2010,** 104, 193-200.

(21) Onoda, M.; Kanbe, K., Crystal structure and electronic properties of the Ag2V4O11 insertion electrode. *J. Phys. Condens. Matter* **2001,** 13, 6675-6685.

(22) Noyes, A. A.; Whitney, W. R., The rate of solution of solid substances in their own solutions. *J. Am. Chem. Soc.* **1897,** 19, 930-4.

# Chapter 3

## Dissolution of silver and vanadium from silver vanadium oxide and silver vanadium phosphorous oxide: a mechanistic study

Reproduced in part from [Bock, D. C.; Takeuchi, K. J.; Marschilok, A. C.; Takeuchi, E. S., Silver vanadium oxide and silver vanadium phosphorous oxide dissolution kinetics: a mechanistic study with possible impact on future ICD battery lifetimes. *Dalton Trans.* **2013,** 42, 13981-13989] with permission from The Royal Society of Chemistry.

### 3.1. Introduction

An understanding of the significant factors associated with battery lifetimes for the implantable cardioverter defibrillator (ICD) is critical for the development of new ICD batteries. As stated in the introduction, the solubility of the cathode material has been identified as a significant life-limiting factor for these batteries. In the previous chapter, it was shown that the chemical composition of the cathode (i.e. phosphate versus an oxide, SVPO versus SVO) can have a large impact on the dissolution of the cathode material. This approach, using a material with new structure and composition, is one of two major strategies for materials design. The second major strategy, exemplified by the implementation of nanoscale materials, is to modify the physical properties of the material via dimensional control. This chapter extends the previous work by incorporating both of these material strategies, as the impact of material composition and the impact of dimensional control are both addressed. Further, results presented in this chapter probe the solubility of silver from the cathode materials and analyze it with respect to the vanadium solubility to provide insight into the mechanism by which the dissolution process occurs.

The initial studies of SVPO-H (identified as SVPO-H due to the hydrothermal synthetic method) demonstrated that vanadium dissolution into a battery relevant electrolyte had an equilibrium concentration of vanadium that was approximately 5 times less compared to SVO, providing promise of improving lifetime of ICD batteries. A lower temperature synthesis of SVPO using a reflux based method (as such identified as SVPO-R) has been developed which enhances the performance under high rate pulse discharge.[1] The prepared SVPO-R material has a smaller particle size and higher surface area relative to SVPO-H, and these properties appear to positively impact the electrochemical performance of the material as a lithium battery cathode. However, gains in performance at the cathode could potentially be offset by performance losses at the anode, if the dissolution is significantly affected by the differing physical properties resulting from the new synthetic method. The degradation of performance due to solubility of the cathode material is likely to be manifested as a long term effect due to the slow rate of dissolution, and thus would not be observed under the short term electrochemical tests used to characterize the materials. As such, in order to properly evaluate the impact of SVPO-R solubility, the dissolution of Ag and V from the material in a non-aqueous electrolyte was examined relative to SVPO-H and SVO. By performing this type of systematic investigation, the mechanism of dissolution as function of material composition (SVO versus SVPO) and as a function of material composition (SVPO-H versus SVPO-R) effectively compared.

In summary, this chapter contains the kinetic analyses of both silver and vanadium dissolution from the benchmark silver vanadium oxide (SVO) material and silver vanadium phosphorous oxide (SVPO) prepared by two different synthetic pathways in a non-aqueous ICD battery electrolyte.

## 3.2. Experimental

### 3.2.1 Materials synthesis and characterization

Silver vanadium phosphorous oxide ($Ag_2VO_2PO_4$) was synthesized by both hydrothermal and reflux reactions according to previously reported methods.[1-2] The hydrothermally prepared material (SVPO-H) was synthesized by heating silver (I) oxide ($Ag_2O$), vanadium (V) oxide ($V_2O_5$) and phosphoric acid ($H_3PO_4$, 85%) for 96 h at 230 C. The reflux synthesized material (SVPO-R) was prepared using the same starting materials with a reaction time of 72 h. Silver vanadium oxide ($Ag_2V_4O_{11}$) was prepared through the literature method.[3] All synthesized materials were ground and put through a 200 mesh sieve prior to being utilized in dissolution studies.

Various characterization techniques were utilized to interrogate the target materials. Differential scanning calorimetry (DSC) analysis was performed using a TA instruments Q20 with a temperature range of 40-580C. Powder X-ray diffraction (XRD) measurements were recorded with a Rigaku Ultima IV X-ray diffractometer. Cu Kα radiation was used with Bragg-Brentano focusing geometry for the XRD measurements, and the collected data was analyzed using MDI Jade 8 software. Surface area was determined with a Micromeritics Tristar II 3020 through multipoint BET (Brunauer, Emmett, and Teller) method. Scanning electron microscope (SEM) images were collected on a Hitachi SU-70 field emitting scanning electron microscope.

### 3.2.2 Dissolution Analysis

Solubility behavior of the cathode materials was investigated using the methods and procedures detailed in section 2.3.2.

## 3.3 Results and Discussion

### 3.3.1 Material Characterization

The prepared silver vanadium phosphorous oxide (SVPO-H and SVPO-R) and silver vanadium oxide (SVO) target materials were characterized using X-ray powder diffraction. Experimentally recorded patterns were matched with reported literature reference patterns to confirm the crystal structure. Differential scanning calorimetry was utilized to evaluate the synthesized silver vanadium phosphorous oxide materials and results were consistent with previous characterizations for SVPO.[1, 4]

SEM imaging was used to determine the morphology and the particle dimensions of the study materials. The synthesized SVPO-H was characterized by larger rod shaped particles mixed with comparably smaller particles with a rectangular shape (Fig. 1A). The larger rods had a typical length greater than 20 microns in length with a width approximately 3-4 μm, whereas the smaller particles had dimensions ranging from 0.5 to 3 microns. The synthesized SVPO-R was characterized by smaller, more granular primary particles with sub-micron diameters, with some short rod shaped particles also present (Figure 1B). SVO particles, in contrast, were characterized as having a needle like morphology with a length ranging from 2-10 μm and a typical diameter of 0.5 μm (Figure 1C). Also apparent in the images of SVO were larger, irregular masses with an average diameter of 20 μm. Silver vanadium phosphorous oxide (SVO) had a surface area of 0.66 $m^2 g^{-1}$, while the surface area of hydrothermally prepared silver vanadium oxide (SVPO-H) was 1.03 $m^2 g^{-1}$ and reflux prepared silver vanadium oxide (SVPO-R) was 5.64 $m^2 g^{-1}$, a greater than 5x increase.

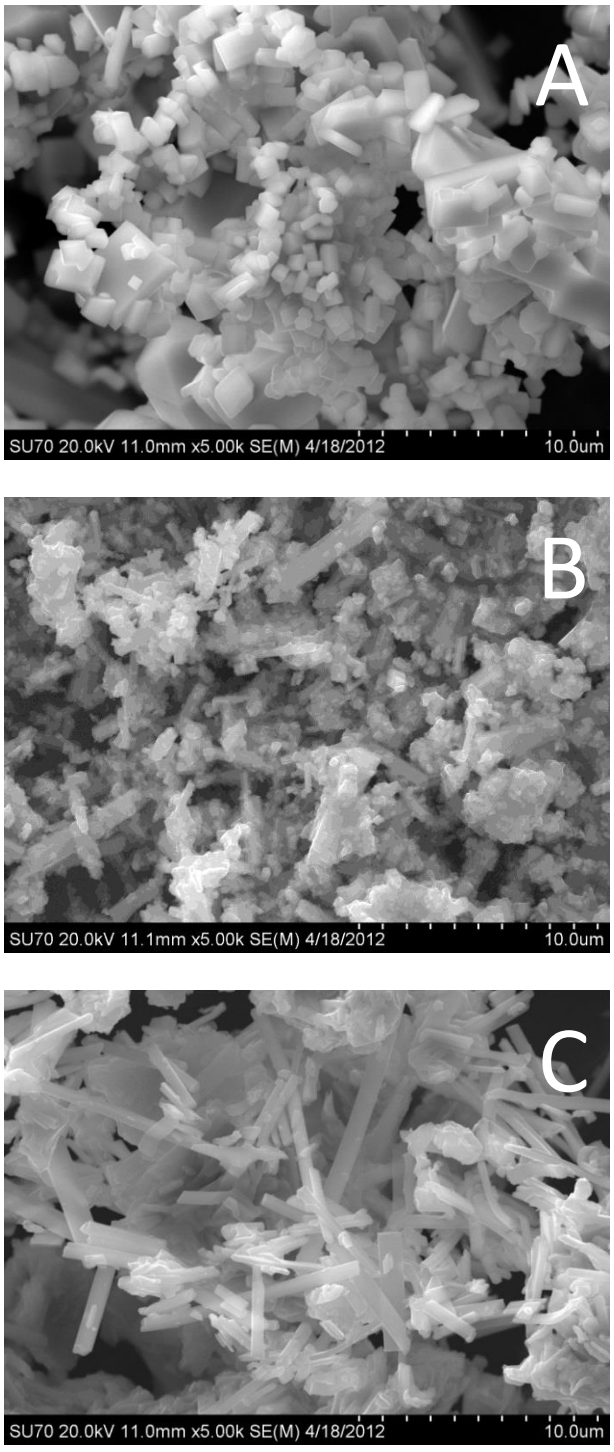


**Figure 1.** Scanning electron micrographs of **A.** hydrothermal silver vanadium phosphorous oxide (SVPO-H), **B.** reflux silver vanadium phosphorous oxide (SVPO-R), and **C.** silver vanadium oxide (SVO).

3.3.2 Vanadium dissolution analysis.

Dissolution of vanadium from the target materials was monitored in a 1M concentration of $LiBF_4$ salt in 50:50 PC-DME solvent. Representative vanadium ion concentrations found in solution for SVPO-H and SVPO-R as a function of time are plotted in Figure 2. Dissolution of SVPO-H appears in the previous section, but is shown here to emphasize the difference between SVPO-H and SVPO-R. Additional samples were analyzed to confirm the previous results. Of note is that dissolution profiles from the two SVPO materials, SVPO-H and SVPO-R, display a different profile. The vanadium concentration versus time data for the SVPO-H material is adequately modelled using the Noyes-Whitney equation with an $R^2$ value of $0.98 \pm 0.1$ (Table 1).

In contrast to SVPO-H, the dissolution of vanadium from SVPO-R is not well described by the Noyes Whitney equation. A higher level of vanadium dissolution is initially observed than would be predicted by the Noyes Whitney model. The higher vanadium concentration of SVPO-R early in the experiment may be a result of the 5 times greater surface area compared to SVPO-H. SVPO-R would have more vanadium centers at the solid liquid interface with incomplete coordination environments, possibly leading to initial increases in solubility relative to the SVPO-H. Another possible explanation is that because the reflux material is synthesized at a lower temperature compared with the hydrothermal material, there is the possibility that phases form which may less thermodynamically stable and thus more soluble, even though the composition of the bulk material is the same. If there are multiple phases dissolving with differing dissolution rates, this could explain the deviation from the model.

Because the dissolution of vanadium from SVPO-R was not well described by the Noyes-Whitney equation, an alternative model was investigated for SVPO-R. The Weibull distribution

function (detailed description in section 1.4) an empirical model used previously to fit dissolution data with steeper initial slopes, was found to produce fits with a high correlation to the experimental data from SVPO-R (Table 5). The Weibull distribution may be expressed in the general form[5]:

$$m = 1\text{-}\exp(-\alpha t^{b}) \qquad [1]$$

where *m* is the accumulated fraction of dissolved material at time t, α is a time scaling constant, and b is a constant which defines the shape of the curve. The model has been utilized previously to quantitatively compare dissolution of pharmaceutical drugs in aqueous solutions.[6-16] It has been successfully used to fit numerous dissolution profiles, including those with a steep initial slope for which diffusion based models may not provide an adequate fit. In this case, the Weibull distribution was fit to the fraction of vanadium dissolved vs. time data using non-linear regression analysis. To the best of our knowledge, the current study is the first time the Weibull approach has been utilized to characterize the solubility of cathode materials in the non-aqueous electrolyte. Representative SVPO-R vanadium dissolution data which is fit with the Weibull distribution function is shown in figure 3. Dissolution of vanadium from SVO was also investigated to compare with the dissolution from SVPO-H and SVPO-R. As with SVPO-H, vanadium dissolution from SVO was fit using the Noyes-Whitney equation (Table 3) Additional samples were run to confirm the results SVO dissolution results presented in Chapter 2. By comparison, the level of vanadium dissolved from SVPO-H and SVPO-R was determined to be several times lower than SVO. At the end of the experimental window, the average concentrations of vanadium dissolved from SVPO-H, SVPO-R, and SVO were 1.6 mg $L^{-1}$, 1.3 mg $L^{-1}$, and 8.8 mg $L^{-1}$, respectively, where n=15 for SVPO-H, n=9 for SVPO-R, and n=18 for SVO. These average concentration data after 21 days are compared in figure 4. Error bars

represent the standard deviation from the mean measured value. The chart illustrates the clear difference in the vanadium solubility from SVO compared to the two SVPO compounds. While the initial shape of the dissolution curve for SVPO-R is different than that for SVPO-H, the vanadium concentration at 21 days is the same for both materials within experimental error, indicating reduced solubility in both SVPO materials compared to SVO. As such, SVPO-R is not likely to experience long term performance losses due to vanadium dissolution..

The magnitude of vanadium dissolved from SVO was approximately 5 times greater than the magnitude of vanadium dissolved from either SVPO material. This data indicates that changes in chemical composition of the materials play a larger role in influencing the vanadium dissolution than the material physical properties. The observed difference in vanadium solubility between the SVO and SVPO, highlighted by figure 19, is possibly due to differences in the crystal structure of the phosphate and oxide based materials. The SVPO lattice contains $PO_4^{3-}$ polyanions which impart stability to the molecular framework. When $PO_4^{3-}$ polyanions are introduced into the lattice, electronegative phosphorous atoms polarize electrons in the P-O bond, reducing the covalency of the M-O bond.[17-19] This type of inductive effect can stabilize the overall structure by making oxygen atoms more difficult to extract from the lattice.[20] A material will dissolve only when the free energy of solvation is greater than the lattice energy[21], so compounds with higher lattice energy are thermodynamically less likely to dissolve. Because increasing polarization results in an increase in lattice energy[22], the introduction of polarizing $PO_4$ moieties into the SVPO structure should result in a higher lattice energy and account for the observation that the material is less likely to dissolve when compared to its oxide based analogue, SVO. The previously reported lack of change in interlayer spacing upon discharge of SVPO supports the idea that phosphorous oxide moieties in the molecular framework impart

stability and rigidity.[1] In contrast, SVO exhibits a 13% decrease in interlayer spacing in the c direction when discharged. [23]

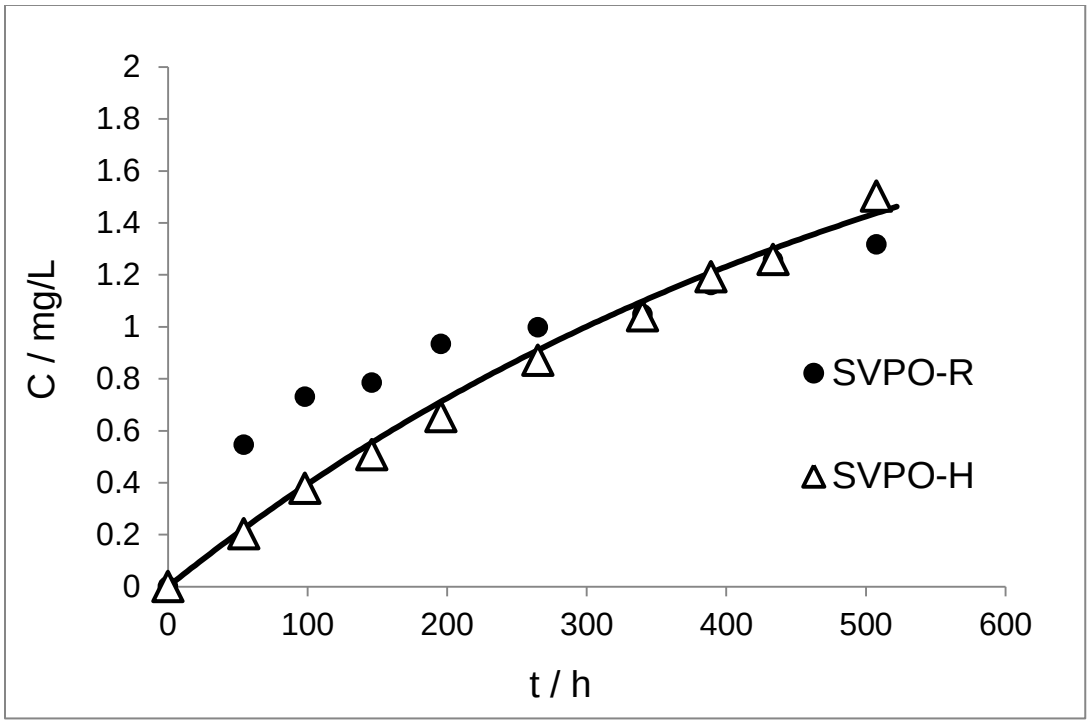


**Figure 2.** Representative vanadium concentrations found in solution for SVPO-H and SVPO-R as a function of time. The SVPO-H data is fit using the Noyes-Whitney function to emphasize the general difference in the dissolution profiles of the two materials.

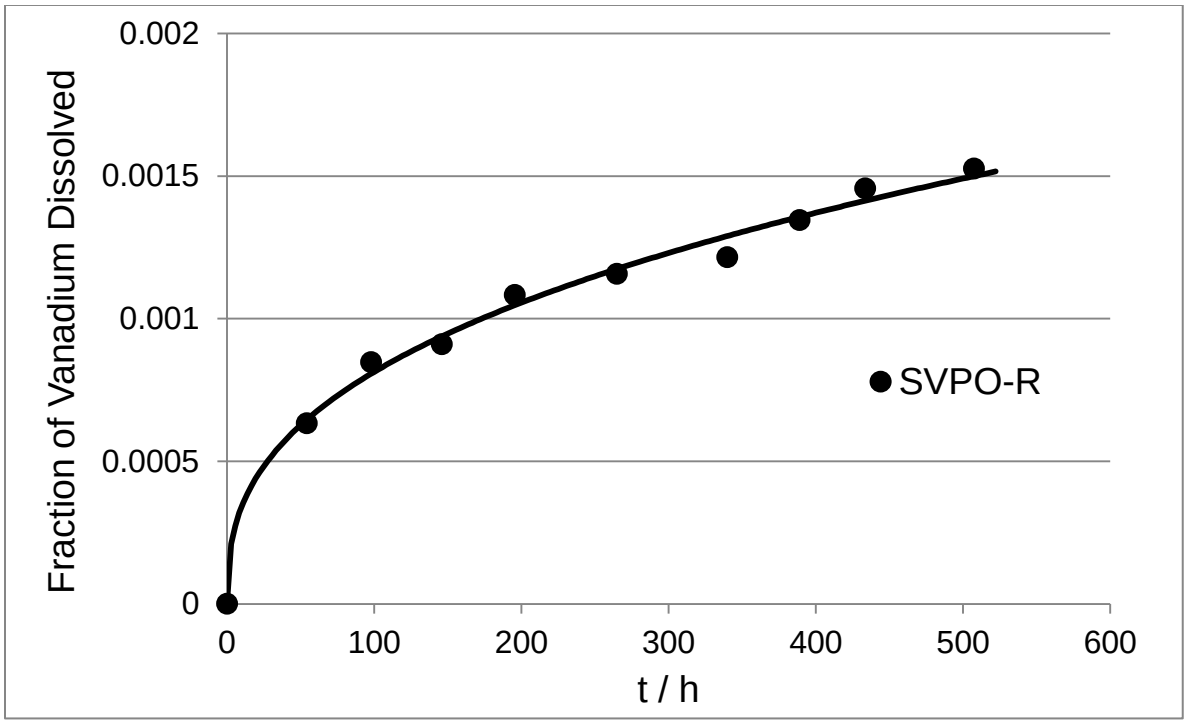


**Figure 3.** Representative V dissolution from SVPO-R fit to the Weibull distribution model.

| Trial # | $C_s$ (mg/L) | k ($s^{-1}$) | $R^2$ |
|---|---|---|---|
| 1 | 2.4 | 5.0E-07 | 0.99 |
| 2 | 1.9 | 5.0E-07 | 0.99 |
| 3 | 2.5 | 5.0E-07 | 0.94 |
| 4 | 1.8 | 6.0E-07 | 0.98 |
| 5 | 2.65 | 6.0E-07 | 0.97 |
| 6 | 2.64 | 6.0E-07 | 0.98 |
| 7 | 2.8 | 5.0E-07 | 0.98 |
| 8 | 1.7 | 8.2E-07 | 0.98 |
| 9 | 1.65 | 5.7E-07 | 0.98 |
| 10 | 2 | 1.3E-06 | 0.98 |
| 11 | 2.1 | 1.9E-06 | 0.97 |
| 12 | 1.95 | 1.9E-06 | 0.99 |
| 13 | 1.8 | 1.1E-06 | 0.96 |
| 14 | 1.9 | 1.7E-06 | 0.99 |
| 15 | 1.85 | 1.6E-06 | 0.97 |
| Mean | 2.1 | 9.8E-07 | 0.98 |
| Standard Deviation | 0.4 | 5.5E-07 | 0.01 |

**Table 1.** Noyes-Whitney fitting results for dissolution of vanadium from SVPO-H.

| **Trial #** | **α** | β | **$R^2$** |
|---|---|---|---|
| 1 | 6.6E-06 | 3.8E-01 | 0.99 |
| 2 | 1.5E-07 | 6.7E-01 | 0.97 |
| 3 | 2.2E-06 | 4.6E-01 | 0.96 |
| 4 | 1.0E-04 | 1.6E-01 | 0.98 |
| 5 | 2.1E-05 | 3.0E-01 | 0.98 |
| 6 | 1.0E-05 | 3.5E-01 | 0.99 |
| 7 | 1.6E-05 | 3.2E-01 | 0.98 |
| 8 | 1.6E-05 | 3.2E-01 | 0.94 |
| 9 | 2.5E-05 | 2.8E-01 | 0.94 |
| Mean | 2.0E-05 | 3.6E-01 | 0.97 |
| Standard Deviation | 3.0E-05 | 1.4E-01 | 0.02 |

**Table 2.** Weibull model fitting results for vanadium dissolution from SVPO-R.

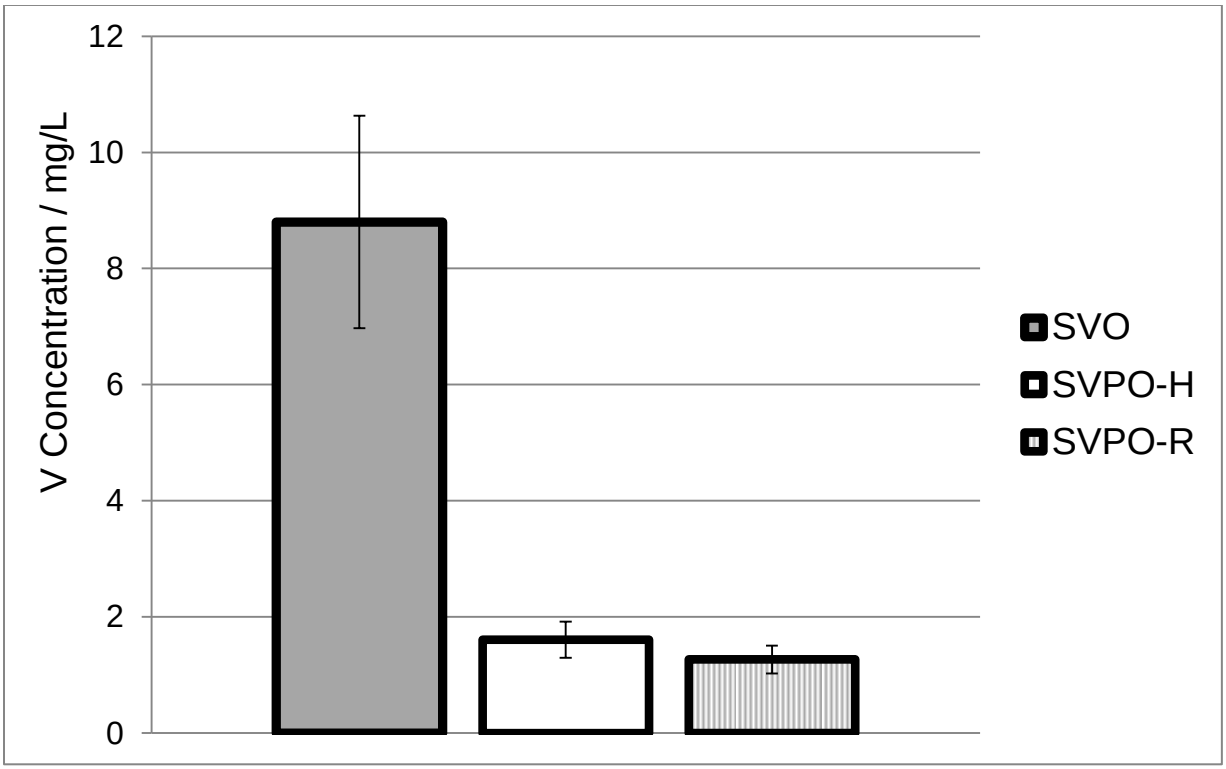


**Figure 4.** Vanadium concentrations in the electrolyte solution after 21 days for SVPO-H, SVPO-R, and SVO.

| Trial # | $C_s$ (mg/L) | k ($s^{-1}$) | $R^2$ |
|---|---|---|---|
| 1 | 8.3 | 3.1E-06 | 0.99 |
| 2 | 8.6 | 3.1E-06 | 0.99 |
| 3 | 8.6 | 3.1E-06 | 1.00 |
| 4 | 7.1 | 3.0E-06 | 0.99 |
| 5 | 7.2 | 2.2E-06 | 0.99 |
| 6 | 6.8 | 2.2E-06 | 0.99 |
| 7 | 8 | 3.0E-06 | 0.99 |
| 8 | 7.2 | 3.0E-06 | 1.00 |
| 9 | 7 | 2.5E-06 | 0.99 |
| 10 | 11.5 | 1.5E-06 | 0.99 |
| 11 | 11.4 | 1.5E-06 | 0.98 |
| 12 | 10.99 | 1.8E-06 | 0.99 |
| 13 | 11.4 | 2.4E-06 | 0.98 |
| 14 | 12 | 1.8E-06 | 0.97 |
| 15 | 9.3 | 2.4E-06 | 0.99 |
| 16 | 11.2 | 2.0E-06 | 0.99 |
| 17 | 8.9 | 2.2E-06 | 0.99 |
| 18 | 6.7 | 2.9E-06 | 0.97 |
| Mean | 9.0 | 2.4E-06 | 0.99 |
| Standard Deviation | 1.9 | 5.7E-07 | 0.01 |

**Table 3.** Noyes-Whitney fitting results for dissolution of vanadium from SVO.

### 3.3.3 Silver dissolution analysis

For the three materials studied, the silver concentration-time data was not adequately modeled by the Noyes-Whitney equation describing solid dissolution. Instead, the Weibull distribution was used to model the silver dissolution data for the SVPO-H, SVPO-R, and SVO materials. The fits of the function to the experimental data are illustrated in Figure 5. The $\alpha$, $\beta$, and $R^2$ values for the best fits to the data are compiled for SVPO-H, SVPO-R, and SVO in tables 4, 5, and 6, respectively. The high coefficient of determination values from the regression analysis indicate that the Weibull distribution is an acceptable function for modeling the dissolution of silver from the target materials.

The solubility of silver from the target materials was compared (Figure 6). The averages of the measured silver concentration values at 21 days were used (n=15 for SVPO-H, n=9 for SVPO-R, n=18 for SVO). Error bars represent the standard deviation from the mean measured values. Interestingly, the magnitude of silver dissolution was comparable for both SVPO materials as well as SVO, within experimental error.

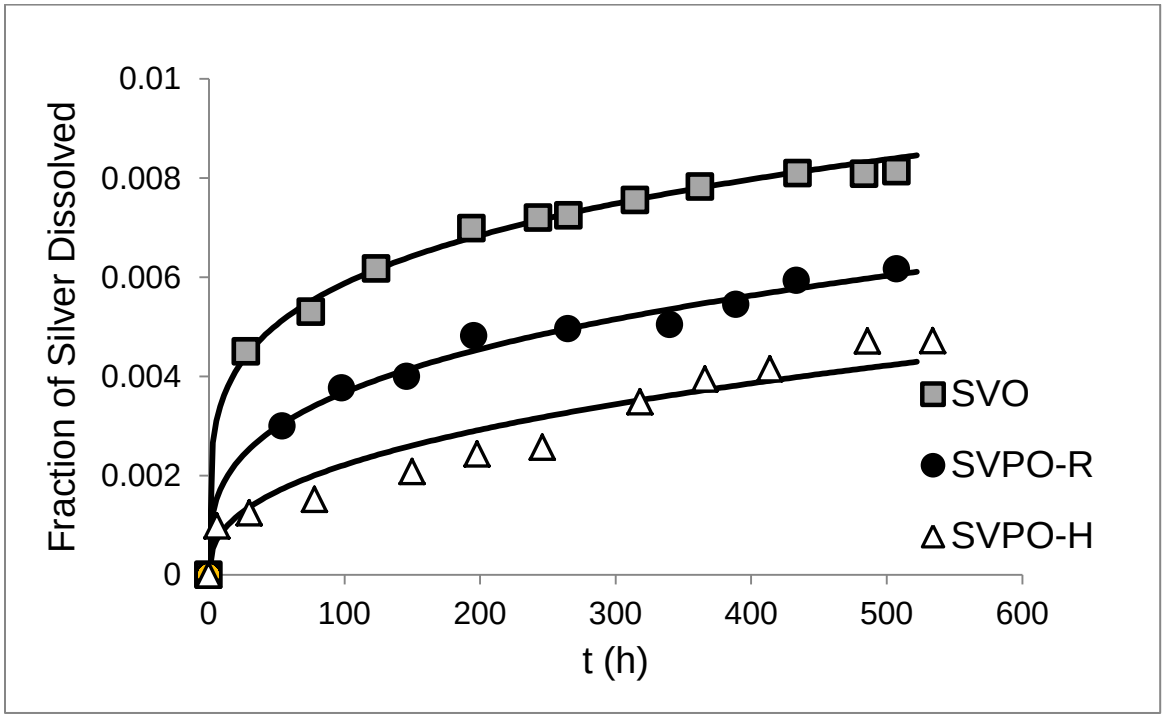


**Figure 5.** Silver fraction dissolved for SVPO-H, SVPO-R, and SVO. Lines represent fits using the Weibull equation.

| Trial # | α | β | $R^2$ |
|---|---|---|---|
| 1 | 5.3E-06 | 4.3E-01 | 0.97 |
| 2 | 2.9E-05 | 3.0E-01 | 0.89 |
| 3 | 5.7E-06 | 4.4E-01 | 0.97 |
| 4 | 3.7E-05 | 2.9E-01 | 0.96 |
| 5 | 1.3E-05 | 3.8E-01 | 0.94 |
| 6 | 7.6E-06 | 4.2E-01 | 0.90 |
| 7 | 9.1E-06 | 4.1E-01 | 0.96 |
| 8 | 2.5E-05 | 3.3E-01 | 0.99 |
| 9 | 4.8E-05 | 2.7E-01 | 0.98 |
| 10 | 8.4E-06 | 4.6E-01 | 0.98 |
| 11 | 7.1E-06 | 4.8E-01 | 0.97 |
| 12 | 7.3E-06 | 4.7E-01 | 0.97 |
| 13 | 1.3E-05 | 4.0E-01 | 0.92 |
| 14 | 4.9E-06 | 5.0E-01 | 0.99 |
| 15 | 7.4E-06 | 4.6E-01 | 0.97 |
| Mean | 1.5E-05 | 4.0E-01 | 0.96 |
| Standard Deviation | 1.3E-05 | 7.3E-02 | 0.03 |

**Table 4.** Weibull equation fitting results for dissolution of silver from SVPO-H.

| Trial # | α | β | $R^2$ |
|---|---|---|---|
| 1 | 7.2E-05 | 3.1E-01 | 0.99 |
| 2 | 1.5E-05 | 4.3E-01 | 0.99 |
| 3 | 9.3E-05 | 2.8E-01 | 0.90 |
| 4 | 2.3E-04 | 2.1E-01 | 0.96 |
| 5 | 1.6E-04 | 2.5E-01 | 0.98 |
| 6 | 1.6E-04 | 2.4E-01 | 0.95 |
| 7 | 1.1E-04 | 2.8E-01 | 0.99 |
| 8 | 2.6E-05 | 4.0E-01 | 0.99 |
| 9 | 1.3E-04 | 2.6E-01 | 0.99 |
| Mean | 1.1E-04 | 3.0E-01 | 0.97 |
| Standard Deviation | 6.8E-05 | 7.4E-02 | 0.03 |

**Table 5.** Weibull equation fitting results for dissolution of silver from SVPO-R.

| Trial # | α | β | $R^2$ |
|---|---|---|---|
| 1 | 5.6E-04 | 1.9E-01 | 0.94 |
| 2 | 3.2E-04 | 2.3E-01 | 0.98 |
| 3 | 2.5E-04 | 2.5E-01 | 0.98 |
| 4 | 2.5E-04 | 2.5E-01 | 0.97 |
| 5 | 2.5E-04 | 2.5E-01 | 0.99 |
| 6 | 2.8E-04 | 2.3E-01 | 0.98 |
| 7 | 2.0E-04 | 2.7E-01 | 0.99 |
| 8 | 2.4E-04 | 2.5E-01 | 0.99 |
| 9 | 2.3E-04 | 2.5E-01 | 0.99 |
| 10 | 1.2E-04 | 2.9E-01 | 0.99 |
| 11 | 7.0E-05 | 3.3E-01 | 0.97 |
| 12 | 2.2E-04 | 2.5E-01 | 0.96 |
| 13 | 3.9E-04 | 2.2E-01 | 0.99 |
| 14 | 3.1E-04 | 2.3E-01 | 0.97 |
| 15 | 2.7E-04 | 2.3E-01 | 0.99 |
| 16 | 3.5E-04 | 2.2E-01 | 1.00 |
| 17 | 2.5E-04 | 2.4E-01 | 1.00 |
| 18 | 4.1E-04 | 2.0E-01 | 1.00 |
| Mean | 2.8E-04 | 2.4E-01 | 0.98 |
| Standard Deviation | 1.1E-04 | 3.1E-02 | 0.02 |

**Table 6.** Weibull equation fitting results for dissolution of silver from SVO.

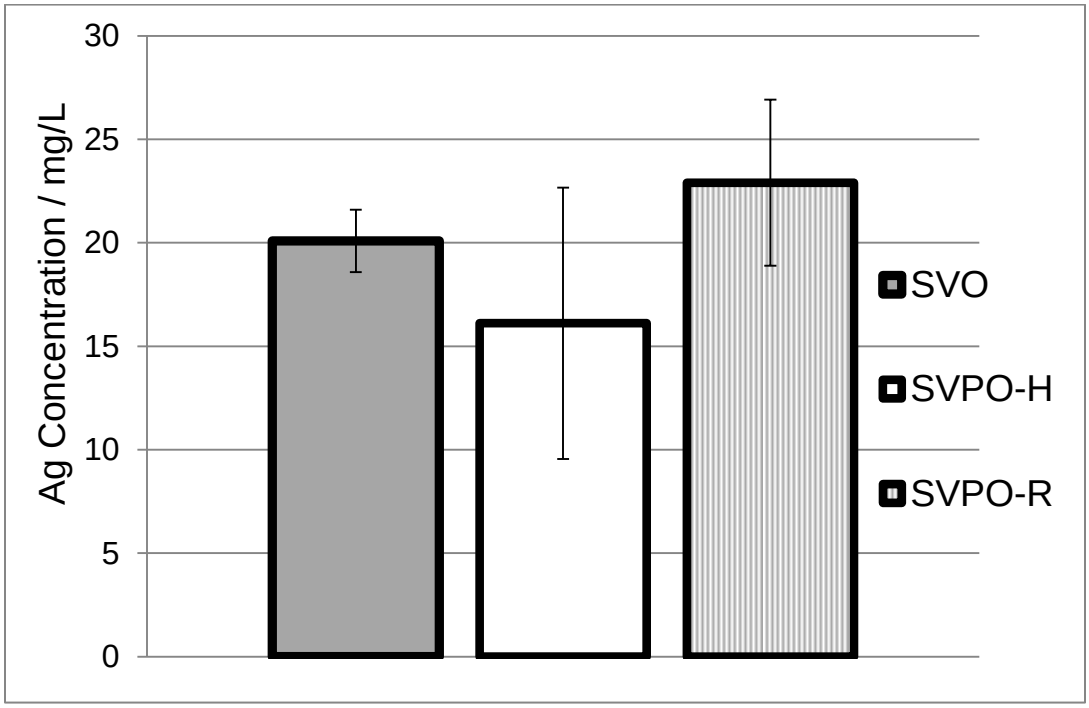


**Figure 6.** Silver concentrations in the electrolyte solution after 21 days for SVPO-H, SVPO-R, and SVO.

3.3.4. Comparison of vanadium dissolution and silver dissolution

It is significant that for all three target materials, the moles of dissolved vanadium in solution after 21 days are representative of less than 1% of the total moles of vanadium exposed to electrolyte. In this regard, both SVO and SVPO are relatively stable in the 1M $LiBF_4$ electrolyte. The amount of vanadium going into solution can be accounted for by only the vanadium on surface of the crystallites of the material. However, quantifying the dissolution properties of these ICD cathode materials is critical, since cathode solubility of SVO can have a significant impact on battery performance.

In order to determine if the dissolved vanadium and silver could be accounted for by the vanadium and the silver available on the outer surface of the crystallites (one unit cell layer thick), the Scherrer equation[24] was used in conjunction with the unit cell dimensions. It was found that, had all of the vanadium in the entire outer unit cell layer of the crystallites gone into solution under the described experimental conditions, the estimated vanadium in solution would be more than 20x greater than the amount of vanadium which was observed in solution. In the case of silver, had all of the silver in the entire outer unit cell layer of the crystallite gone into solution under the described experimental conditions, the estimated silver concentration in solution would be more than 8x greater than the amount of silver which was observed in solution. Therefore, the amounts of silver and vanadium dissolved can be accounted for by assuming that dissolution is only occurring from the surfaces of the crystallites of SVPO-R, SVPO-H, and SVO.

The vanadium dissolution was adequately fit with the Noyes-Whitney equation describing solid dissolution for the lower surface area SVPO-H and SVO materials. The consistent fit with Noyes-Whitney suggests that the mechanism by which vanadium dissolves

into the electrolyte for these materials may be diffusion controlled. For the higher surface area SVPO-R material, the concentration time data was better fit using the Weibull function. This is attributed to additional vanadium centers at the solid liquid interface with incomplete coordination environments in the higher surface area material, which could possibly lead to initial increases in solubility relative to the SVPO-H and would account for the general difference in the dissolution profiles.

In contrast to vanadium, silver dissolution proceeded via a higher initial rate and could not be described using the Noyes-Whitney model, irrespective of the surface area of the material studied. As such, a more complex dissolution mechanism than pure diffusion control needs to be considered for silver. One suggested explanation is that dissolution of silver ions into solution may proceed through an ion exchange mechanism simultaneous to solvation of the ordered crystal structure, such that both ion exchange processes and dissolution processes contribute to the observed kinetics. Kinetics of ion exchange processes are complex, depending upon multiple factors including concentration and electrical charge gradients, ionic interactions, structure of the exchanger, and chemical reactions occurring in the exchanger or the electrolyte.[25-26] Ion exchange mechanisms have previously been proposed for V dissolution from $Li_5V_3O_8$[27] and Mn dissolution from $LiMn_2O_4$.[28] In the layered silver vanadium phosphorous oxide and silver vanadium oxide structures, $Ag^+$ ions located between the layers of edge sharing $VO_6$ and $PO_4$ polyhedra are more likely to undergo ion exchange than vanadium, as they may exchange with $Li^+$ ions in the electrolyte without collapsing the material's structure.

The molar ratio of dissolved silver to dissolved vanadium was determined for SVPO-H, SVPO-R, and SVO (Figure 7). The dashed lines indicate the molar ratio of each material based upon the stoichiometry. For all three of the materials, the amount of silver dissolved was at least

double what was predicted by the chemical formula. These data show that the dissolution is non-stoichiometric. Ag and V ions entering the electrolyte solution via a traditional dissolution mechanism, in which the crystal lattice is broken down and individual ions are solvated by the electrolyte, should exhibit a molar ratio of dissolved ions which is equivalent to the stoichiometric ratio of elements in the dissolving material. Thus, the molar ratio data supports a more complex dissolution process where vanadium and silver dissolve into the electrolyte solution at distinct rates.

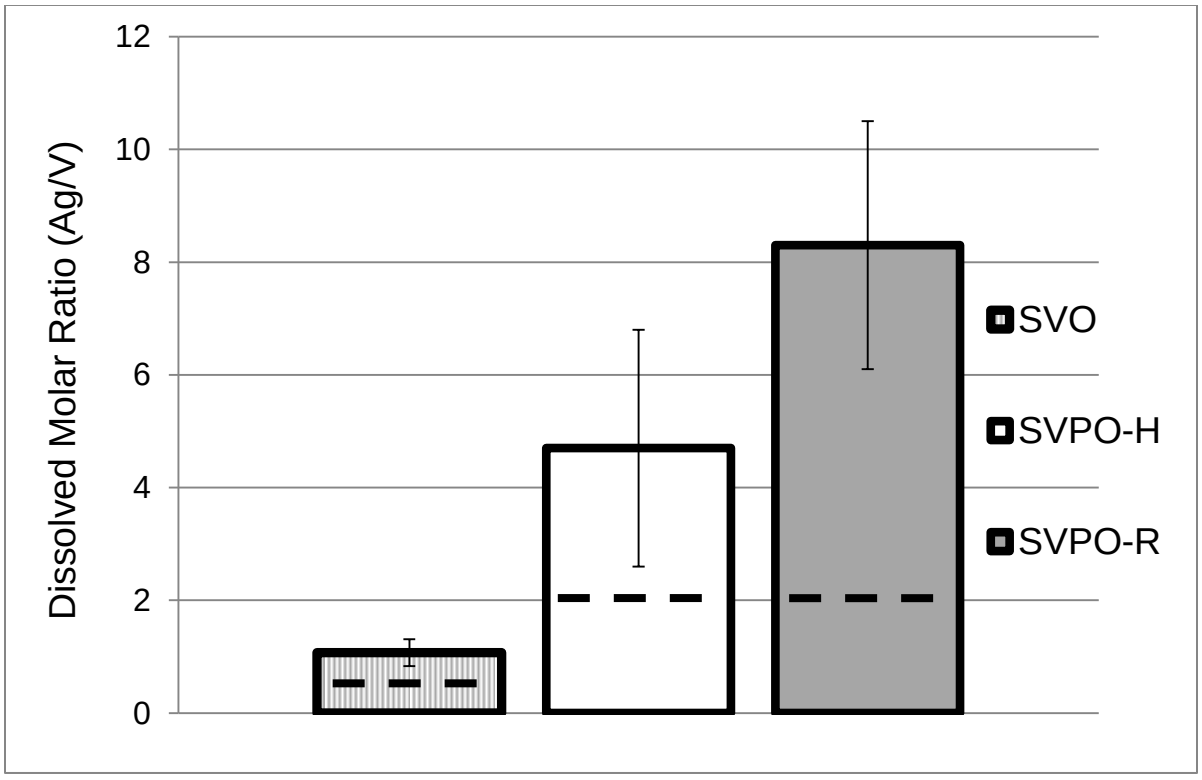


**Figure 7.** Molar Ratios (Ag/V) for SVO, SVPO-H and SVPO-R in 1M $LiBF_4$ PC/DME electrolyte after 21 days. The dashed lines indicate the molar ratio of the non-dissolved material based upon the stoichiometry.

### 3.4 Summary

This chapter describes the dissolution of Ag and V for the benchmark cathode material used in ICD's (SVO) and a phosphate based analog (SVPO) in a non-aqueous battery electrolyte. To study the impact of dimensional control of the cathode material on the dissolution kinetics, in addition to chemical composition, two synthetic methods were used to prepare the SVPO material. The higher temperature hydrothermal method resulted in a lower surface area material (SVPO-H), while the lower temperature reflux method resulted in a higher surface area material (SVPO-R). It was found that the dissolution of vanadium from the lower surface area materials (SVO and SVPO-H) could be described using the Noyes Whitney dissolution model, suggesting that the dissolution is diffusion controlled. Vanadium dissolution from the higher surface area material (SVPO-R) showed a different dissolution profile and was fit using the Weibull equation. While the initial shape of the dissolution curve for SVPO-R is different than that for SVPO-H, the vanadium concentration at 21 days was the same for both materials within experimental error, indicating ~5x less solubility from either SVPO material compared to SVO. As such, it appears as though the chemical composition of the cathode material has a larger influence on vanadium dissolution than the surface area.

The silver concentration-time data was analyzed using the Weibull function since the Noyes-Whitney model did not adequately fit the data for any of the materials studied, regardless of surface area. This suggests that a more complex mechanism governs the silver dissolution relative to vanadium. One explanation may be that the dissolution of silver proceeds via an ion exchange mechanism simultaneous to the solvation of the ordered crystal structure, such that both ion exchange and dissolution contribute to the observed kinetics. This hypothesis is supported by the observation that Ag and V concentrations in solution do not reflect the

stoichiometry of the solids, with dissolved Ag/V ratios being at least double what is predicted from the stoichiometric ratio.

## 3.5 References


(1) Kim, Y. J.; Marschilok, A. C.; Takeuchi, K. J.; Takeuchi, E. S., Silver vanadium phosphorous oxide, Ag2VO2PO4: Chimie douce preparation and resulting lithium cell electrochemistry. *J. Power Sources* **2011,** 196, 6781-6787.

(2) Kang, H. Y.; Wang, S. L.; Tsai, P. P.; Lii, K. H., Hydrothermal synthesis, crystal structure and ionic conductivity of silver vanadium oxide phosphate, Ag2VO2PO4: a new layered phosphate of vanadium(V). *J. Chem. Soc., Dalton Trans.* **1993**, 1525-8.

(3) Leising, R. A.; Takeuchi, E. S., Solid-state cathode materials for lithium batteries: effect of synthesis temperature on the physical and electrochemical properties of silver vanadium oxide. *Chem. Mater.* **1993,** 5, 738-42.

(4) Marschilok, A. C.; Takeuchi, K. J.; Takeuchi, E. S., Preparation and electrochemistry of silver vanadium Phosphorous oxide, Ag2VO2PO4. *Electrochem. Solid-State Lett.* **2008,** 12, A5-A9.

(5) Langenbucher, F., Linearization of dissolution rate curves by the Weibull distribution. *J. Pharm. Pharmacol.* **1972,** 24, 979-81.

(6) D'Souza Susan, S.; Faraj Jabar, A.; DeLuca Patrick, P., A model-dependent approach to correlate accelerated with real-time release from biodegradable microspheres. *AAPS PharmSciTech* **2005,** 6, E553-64.

(7) Van Vooren, L.; Krikilion, G.; Rosier, J.; De Spiegeleer, B., A novel bending point criterion for dissolution profile interpretation. *Drug Dev. Ind. Pharm.* **2001,** 27, 885-892.

(8) Lin, C.-W.; Cham, T.-M., Effect of particle size on the available surface area of nifedipine from nifedipine-polyethylene glycol 6000 solid dispersions. *Int. J. Pharm.* **1996,** 127, 261-72.

(9) Sathe, P. M.; Venitz, J., Comparison of neural network and multiple linear regression as dissolution predictors. *Drug Dev. Ind. Pharm.* **2003,** 29, 349-355.

(10) Chevalier, E.; Viana, M.; Artaud, A.; Chomette, L.; Haddouchi, S.; Devidts, G.; Chulia, D., Comparison of three dissolution apparatuses for testing calcium phosphate pellets used as ibuprofen delivery systems. *AAPS PharmSciTech* **2009,** 10, 597-605.

(11) Nagarwal, R. C.; Ridhurkar, D. N.; Pandit, J. K., In vitro release kinetics and bioavailability of gastroretentive cinnarizine hydrochloride tablet. *AAPS PharmSciTech* **2010,** 11, 294-303.

(12) Varma, M. V. S.; Kaushal, A. M.; Garg, S., Influence of micro-environmental pH on the gel layer behavior and release of a basic drug from various hydrophilic matrices. *J. Controlled Release* **2005,** 103, 499-510.

(13) Koester, L. S.; Ortega, G. G.; Mayorga, P.; Bassani, V. L., Mathematical evaluation of in vitro release profiles of hydroxypropylmethylcellulose matrix tablets containing carbamazepine associated to β-cyclodextrin. *Eur. J. Pharm. Biopharm.* **2004,** 58, 177-179.

(14) Adams, E.; Coomans, D.; Smeyers-Verbeke, J.; Massart, D. L., Non-linear mixed effects models for the evaluation of dissolution profiles. *Int. J. Pharm.* **2002,** 240, 37-53.

(15) Bonferoni, M. C.; Rossi, S.; Ferrari, F.; Bertoni, M.; Bolhuis, G. K.; Caramella, C., On the employment of λ carrageenan in a matrix system. III. Optimization of a λ carrageenan-HPMC hydrophilic matrix. *J. Controlled Release* **1998,** 51, 231-239.

(16) Papadopoulou, V.; Kosmidis, K.; Vlachou, M.; Macheras, P., On the use of the Weibull function for the discernment of drug release mechanisms. *Int. J. Pharm.* **2006,** 309, 44-50.

(17) Ellis, B. L.; Lee, K. T.; Nazar, L. F., Positive Electrode Materials for Li-Ion and Li Batteries. *Chem. Mater.* **2010,** 22, 691-714.

(18) Hautier, G.; Jain, A.; Ong, S. P.; Kang, B.; Moore, C.; Doe, R.; Ceder, G., Phosphates as Lithium-Ion Battery Cathodes: An Evaluation Based on High-Throughput ab Initio Calculations. *Chem. Mater.* **2011,** 23, 3495-3508.

(19) Padhi, A. K.; Nanjundaswamy, K. S.; Goodenough, J. B., Phospho-olivines as positive-electrode materials for rechargeable lithium batteries. *J. Electrochem. Soc.* **1997,** 144, 1188-1194.

(20) Kim, D.-H.; Kim, J., Synthesis of LiFePO4 Nanoparticles in Polyol Medium and Their Electrochemical Properties. *Electrochem. Solid-State Lett.* **2006,** 9, A439-A442.

(21) Reichardt, C. W., T., *Solvents and Solvent Effects in Organic Chemistry*. 4th ed.; Wiley-VCH: Weinheim, Germany, **2011**.

(22) Rohrer, G. S., *Structure and Bonding in Crystalline Materials*. Cambridge University Press: United Kingdom, **2001**; p 540.

(23) Leising, R. A.; Thiebolt, W. C., III; Takeuchi, E. S., Solid-State Characterization of Reduced Silver Vanadium Oxide from the Li/SVO Discharge Reaction. *Inorg. Chem.* **1994,** 33, 5733-40.

(24) Patterson, A. L., The Scherrer formula for x-ray particle-size determination. *Phys. Rev.* **1939,** 56, 978-82.

(25) Harland, C. E., *Ion Exchange: Theory and Practice*. 2 ed.; **1994**.

(26) Helfferich, F., *Ion Exchange*. **1962**.

(27) Jouanneau, S.; Le, G. L. S. A.; Verbaere, A.; Guyomard, D., The Origin of Capacity Fading upon Lithium Cycling in Li1.1V3O8. *J. Electrochem. Soc.* **2005,** 152, A1660-A1667.

(28) Blyr, A.; Sigala, C.; Amatucci, G.; Guyomard, D.; Chabre, G. Y.; Tarascon, J. M., Self-discharge of LiMn2O4/C Li-ion cells in their discharged state. Understanding by means of three-electrode measurements. *J. Electrochem. Soc.* **1998,** 145, 194-209.

# Chapter 4

## Analysis of silver and vanadium dissolution from $Ag_{0.49}VOPO_4 \cdot 1.9H_2O$ and $Ag_2VP_2O_8$: structural and silver/vanadium ratio effects on solution formation kinetics

Reproduced in part from [Bock, D. C.; Takeuchi, K. J.; Marschilok, A. C.; Takeuchi, E. S., Structural and silver/vanadium ratio effects on silver vanadium phosphorous oxide solution formation kinetics: Impact on battery electrochemistry. *Phys. Chem. Chem. Phys.* **2015,** 17, 2034-2042] with permission of PCCP Owner Societies.

### 4.1 Introduction

Previous chapters have explored the dissolution of silver and vanadium from the cathode material silver vanadium oxide, $Ag_2V_4O_{11}$, and a phosphate based analogue, $Ag_2VO_2PO_4$. Results indicated that the phosphate material dissolved lower levels of vanadium compared with the oxide, while levels of silver dissolved were comparable within experimental error. In order to further probe the relationship between material structure and solubility, this chapter extends the dissolution analysis to two other members of the silver vanadium phosphorous oxide family, $Ag_{0.48}VOPO_4 \cdot 1.9H_2O$, and $Ag_2VP_2O_8$.

Reports of $Ag_{0.48}VOPO_4 \cdot 1.9H_2O$ as a cathode material in primary lithium batteries have been published.[1-2] Magnetic susceptibility measurements of the discharged material indicated that, contrary to $Ag_2VO_2PO_4$, vanadium reduction is the dominant initial reduction process, from $0 \leq 0.52$ electron equivalents, while silver reduction dominates from $0.52 \leq x \leq 1.0$ electron equivalents. The discharge profile of $Ag_{0.48}VOPO_4 \cdot 1.9H_2O$ remains above 3.0 V for a large portion of the discharge, and there are multiple plateaus which are advantageous for end of charge notification. The material shows good pulse discharge capability, making it a promising cathode material for biomedical applications. In terms of composition, $Ag_{0.48}VOPO_4 \cdot 1.9H_2O$ is

unique from $Ag_2VO_2PO_4$ in that water molecules are incorporated into its structure. Also unique to $Ag_{0.48}VOPO_4 \cdot 1.9H_2O$ is that vanadium in this material exists in two oxidation states, V (IV) and V (V). These factors are considered in analyzing the dissolution of silver and vanadium from the material.

$Ag_2VP_2O_8$ is a third member of the SVPO family which has been investigated as a primary battery cathode material.[3] As with $Ag_2VO_2PO_4$, $Ag_2VP_2O_8$ displays in-situ formation of silver metal nanoparticles when it is initially reduced, improving the material's conductivity. Continued discharge results in fracture of the particles, however, which reduces the conductivity significantly. $Ag_2VP_2O_8$ is unique from the other silver vanadium phosphorous oxides in that it is a diphosphate material. The presence of the diphosphate anion may play a role in influencing dissolution from the material.

In order to better probe the relationships between material structure and solution formation, this chapter presents solution formation analysis of two other members of the silver vanadium phosphorous oxide family, $Ag_{0.48}VOPO_4 \cdot 1.9H_2O$, and $Ag_2VP_2O_8$, with $Ag_2VO_2PO_4$ and $Ag_2V_4O_{11}$ materials used as comparative benchmarks. By investigating a family of compositionally related yet structurally different materials, insight into the deterministic structure factors influencing long term stability of energy storage materials will be gained. These results will identify which members of the SVPO material family show the most promise for reducing cathode solution concentrations in battery electrolyte while also providing appropriate electrochemistry as cathode materials.

## 4.2 Experimental Section

### 4.2.1 Materials Synthesis and Characterization

Silver vanadium oxide ($Ag_2V_4O_{11}$) was prepared via a previously reported solid state reaction method.[4] $Ag_2VO_2PO_4$ was synthesized by a hydrothermal reaction method reported in the literature.[5] Adaptation of a previously reported hydrothermal method was also used to prepare $Ag_{0.49}VOPO_4 \cdot 1.9H_2O$.[6] $Ag_2VP_2O_8$ was prepared via a solid state reaction.[7]

Scanning electron microscope (SEM) images were taken using a Hitachi SU-70 field emitting scanning electron microscope. Differential scanning calorimetry (DSC) analysis was performed using a TA instruments Q20 and thermogravimetric analysis (TGA) was performed using a TA instruments SDT Q600. Powder X-ray diffraction (XRD) measurements were recorded with a Rigaku Smart Lab X-ray diffractometer with Cu Kα radiation and Bragg-Brentano focusing geometry. Elemental analysis was done using inductively coupled plasma optical emission spectroscopy (ICP-OES) with a Thermo Scientific iCAP 6000 series spectrometer. Surface area determination was done with a using the multipoint BET (Brunauer, Emmett, and Teller) method.

### 4.2.2 Dissolution Analysis

Solubility behavior of the cathode materials was investigated using the methods and procedures detailed in section 2.3.2.

## 4.3 Results and Discussion

### 4.3.1 Materials Characterization

The low silver ratio silver vanadium phosphorous oxide, $Ag_{0.49}VOPO_4 \cdot 1.9H_2O$, was characterized using a combination of techniques, including inductively coupled plasma optical emission spectroscopy (ICP-OES), thermogravimetric analysis (TGA) and XRD. The silver to vanadium ratio was determined to be 0.49 by ICP-OES, which is a slightly higher silver content than the value of 0.43 reported in the original literature[6] and consistent with the Ag/V ratio of 0.48 published in a more recent paper.[1]

Thermogravimetric analysis was used to determine the water content of the material at 1.9 water molecules per formula unit. The formula of the material was then assigned as $Ag_{0.49}VPO_4 \cdot 1.9H_2O$. Surface area was $1.0 \pm 0.1$ $m^2/g$.

The experimentally recorded pattern of the synthesized $Ag_{0.49}VOPO_4 \cdot 1.9H_2O$ material compared well with the reference pattern for Ag0.43VOPO4·2H2O (PDF#00-052-1416). Structurally, the material crystallizes in a layered structure with a V-O-P-O framework.[6] (Figure 1A) Silver ions and water molecules are located between the layers. Ag is in a distorted octahedral environment, with four of the oxygen atoms being associated with water molecules and the remaining two oxygen atoms which are part of the V-O-P-O layer.

The second silver vanadium phosphorous oxide was characterized and confirmed as $Ag_2VP_2O_8$. ICP-OES showed the Ag/V ratio of 2:1 and the V/P ratio of 1/2. BET surface area of the synthesized material was $0.7 \pm 0.1$ $m^2/g$. The XRD of the synthesized material matched the reference pattern[7] (PDF #01-088-0436). The diphosphate structure of $Ag_2VP_2O_8$ (Figure 2A) is characterized by layers stacking along the [010] direction,

with those layers consisting of interconnecting $[V_2P_2O_8]_\infty$ chains running parallel to the [100] direction.[7] Vanadium resides in a $VO_6$ octahedron having five corners shared with five $P^{5+}$ tetrahedrons and the $6^{th}$ oxygen unshared with neighboring polyhedra.[3] The vanadium in the octahedron is located nearer to the unshared oxygen, giving long and short bond lengths.[3] Monovalent $Ag^+$ cations are located in two independent sites, with Ag(1) and Ag(2) located in tunnels.

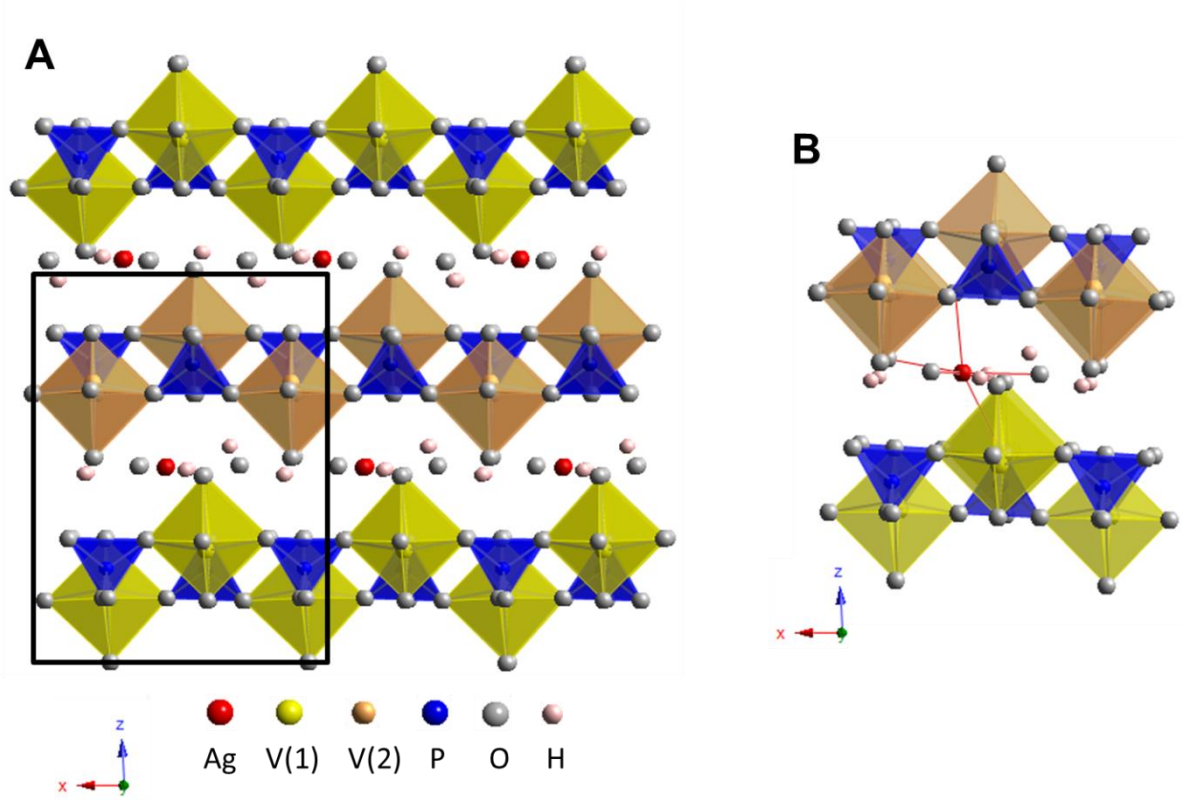


**Figure 1A.** Crystal structure of $Ag_{0.43}VOPO_4 \cdot 2H_2O$ viewed along the b axis, emphasizing the V-O-P-O layer framework. **B.** Proposed coordination environment of $Ag^+$ ions at the edge of the structure.

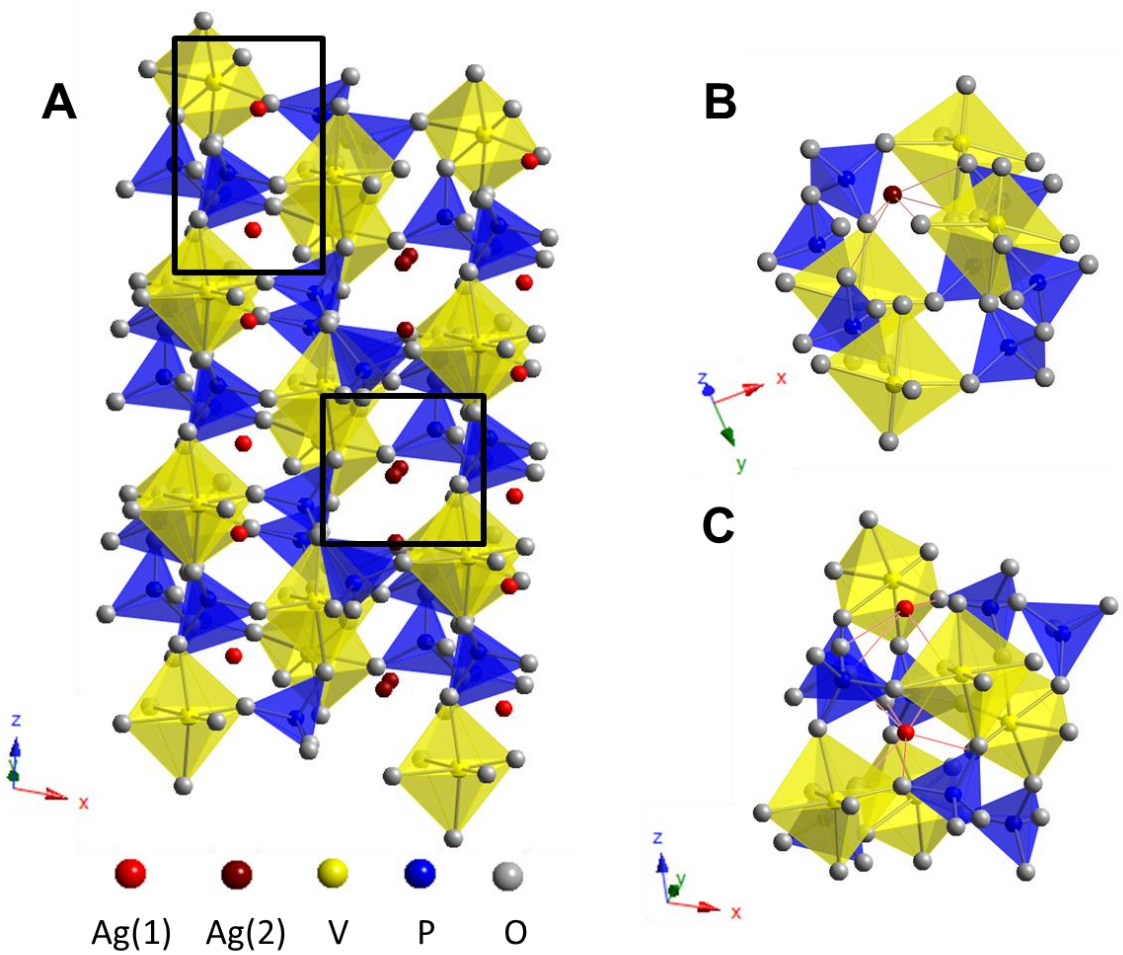


**Figure 2A.** Crystal structure of $Ag_2VP_2O_8$ viewed along the b axis. Proposed incomplete coordination environments of **B.** $Ag(2)^+$ ions and **C.** $Ag(1)^+$ ions located at the edge of tunnels above the plane of $VO_6$ and $PO_4$ polyhedra.

4.3.2 Dissolution Results

Average vanadium ion concentrations as a function of time for $Ag_{0.49}VOPO_4 \cdot 1.9H_2O$ and $Ag_2VP_2O_8$ are plotted in Figure 3. The experiment was repeated with 11 replicate samples for $Ag_{0.49}VOPO_4 \cdot 1.9H_2O$ and 12 replicate samples for $Ag_2VP_2O_8$ and the error bars shown represent one standard deviation from the mean values. Lower concentrations of vanadium were observed with the $Ag_2VP_2O_8$ sample compared to the $Ag_{0.49}VOPO_4 \cdot 1.9H_2O$ material. In order to quantify the solution formation results, the vanadium concentration-time data was fit using the Noyes-Whitney equation for the solution formation of solid particles in liquid media[8], described in chapters 1 and 2.

Non-linear regression analysis was used to fit the integrated Noyes-Whitney equation to the experimental vanadium solution formation data and evaluate the parameters $C_s$ and k. The average and standard deviation of these parameters as well as the coefficient of determination values for the fits for the individual trials are compiled in Table 1. The best fits of the equation to the averaged data are shown as solid lines in Figure 3 for the two materials. $Ag_{0.49}VOPO_4 \cdot 1.9H_2O$ was determined to have an equilibrium solubility $C_s$ of 7 ± 2 mg/L. In contrast, $Ag_2VP_2O_8$ had a lower equilibrium solubility of 3 ± 1 mg/L. The rate constant for the solution formation was also lower for $Ag_2VP_2O_8$, compared with $Ag_{0.49}VOPO_4 \cdot 1.9H_2O$. The lower rate constant for $Ag_2VP_2O_8$ is consistent with the observation that after three weeks, the data do not appear to come to an equilibrium concentration. The high coefficients of determination for the fit indicate that the solution formation data through three weeks is consistent with diffusion layer mechanism described by the Noyes Whitney model.

The solubility of silver from the materials was also investigated. Figure 4 plots the average fraction of silver dissolved from the various materials versus time for $Ag_{0.49}VOPO_4 \cdot 1.9H_2O$ and $Ag_2VP_2O_8$. Data points represent the mean value of 11 or 12 individual samples of each material, with error bars signifying one standard deviation. The general curve of the solution formation profiles of silver at higher electrolyte salt concentrations can be described as having a steeper initial slope for the initial 0-24 hours of exposure to electrolyte, with the concentration then rising at a lower rate. The silver concentration-time data cannot be adequately modeled by the Noyes-Whitney equation describing solid solution formation, thus, the Weibull distribution function[9], used previously to characterize the dissolution of pharmaceutical drugs in aqueous solutions.[10-20] and described in detail in chapters 1 and 3 , was used for fitting the experimental results. The silver concentration vs. time data for $Ag_{0.49}VOPO_4 \cdot 1.9H_2O$ and $Ag_2VP_2O_8$ was converted to accumulated fraction of dissolved material vs. time, and the Weibull distribution was then fit to the data using non-linear regression analysis. The average and standard deviation of the fitting parameters for the 11 and 12 individual trials of each material are compiled in Table 2. The best fits of the function to the experimental results are illustrated in Figure 4. The coefficients of determination indicate that the Weibull distribution was an acceptable function for modeling the solution formation of silver from the two materials.

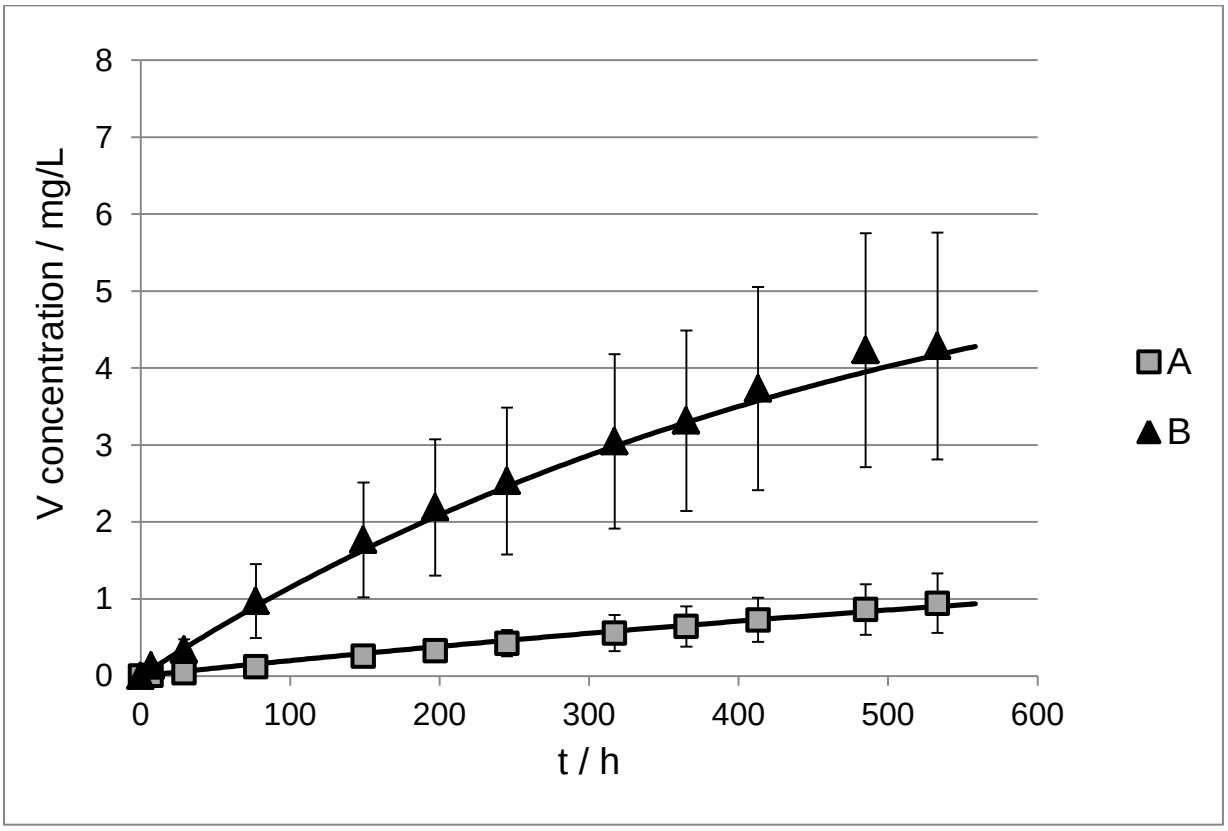


**Figure 3.** Overlays of Noyes-Whitney fits to average vanadium concentration vs. time data for A) $Ag_2VP_2O_8$ and B) $Ag_{0.49}VOPO_4 \cdot 1.9H_2O$.

| Material | $C_s$ (mg/L) | k ($s^{-1}$) | $R^2$ |
|---|---|---|---|
| $Ag_{0.49}VOPO_4 \cdot 1.9H_2O$ | 7 ± 2 | 5.7E-7 ± 1.8E-7 | 0.99 ± 0.01 |
| $Ag_2VP_2O_8$ | 3 ± 1 | 2.3E-7 ± 6.5E-8 | 0.97 ± 0.03 |

**Table 1.** Average Noyes-Whitney fitting parameters for vanadium solution formation from $Ag_2VP_2O_8$ (n=12) and $Ag_{0.49}VOPO_4 \cdot 1.9H_2O$ (n=11).

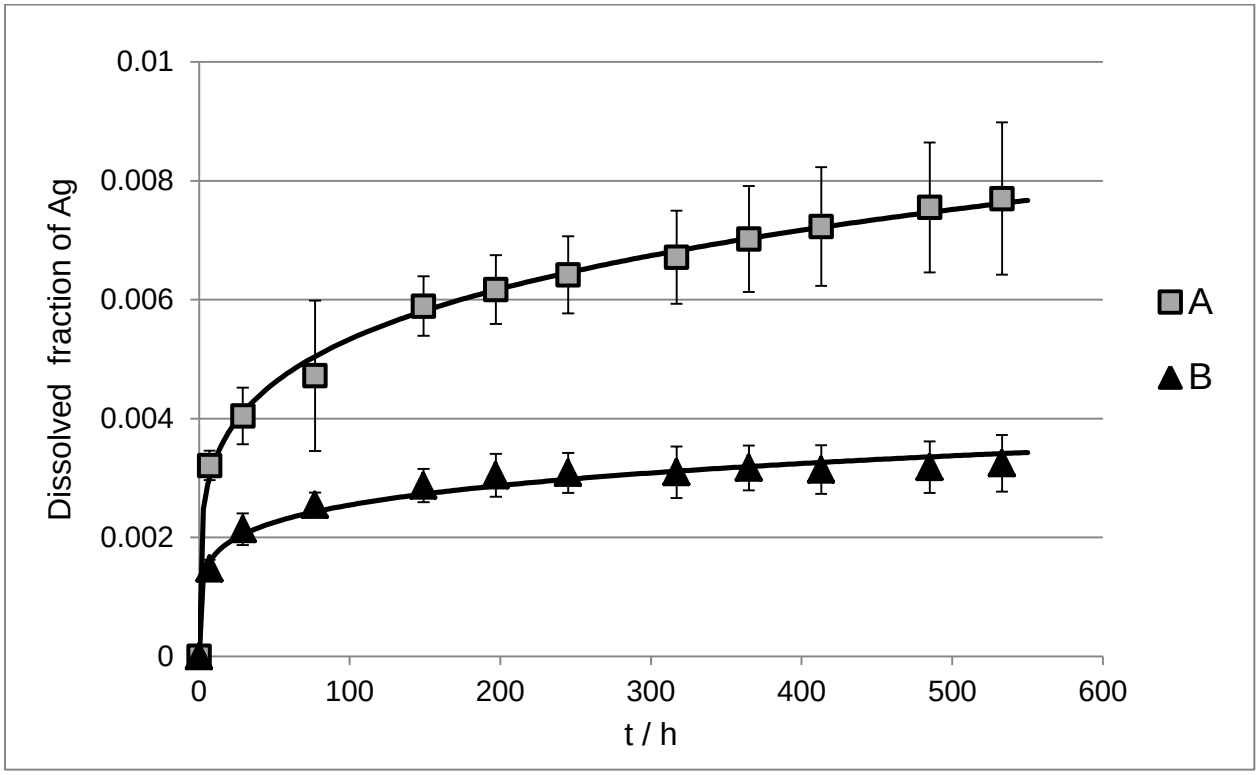


**Figure 4.** Overlays of Weibull fits to average dissolved fraction of Ag vs. time data **A.** $Ag_2VP_2O_8$ and **B.** $Ag_{0.49}VOPO_4 \cdot 1.9H_2O$.

| Material | α | β | $R^2$ |
|---|---|---|---|
| $Ag_{0.49}VOPO_4 \cdot 1.9H_2O$ | 2.8E-4 ± 1.3E-4 | 0.18 ± 0.046 | 0.97 ± 0.02 |
| $Ag_2VP_2O_8$ | 4.2E-4 ± 2.8E-4 | 0.21 ± 0.054 | 0.99 ± 0.05 |

**Table 2.** Average Weibull function fitting parameters for silver solution formation from $Ag_2VP_2O_8$ (n=12) and $Ag_{0.49}VOPO_4 \cdot 1.9H_2O$ (n=11).

### 4.3.3 Comparison of Dissolution Results with $Ag_2VO_2PO_4$ and $Ag_2V_4O_{11}$

The solubility of $Ag_2VO_2PO_4$ and $Ag_2V_4O_{11}$, was described previously in chapters 2 and 3 in 1M LiBF4 PC:DME solvent. For this study, solubility data was recollected in 1M LiBF4 PC solvent and compared with the data for $Ag_2VP_2O_8$ and $Ag_{0.49}VOPO_4 \cdot 1.9H_2O$. The mean vanadium concentration vs. time data for $Ag_2VO_2PO_4$ and $Ag_2V_4O_{11}$ is overlaid with the data for $Ag_{0.49}VPO_4 \cdot 1.9H_2O$ and $Ag_2VOP_2O_8$, Figure 5. The best fit for the Noyes-Whitney function through the mean data for each material is represented as a black line. A comparison of the mean levels of the vanadium dissolved for each material after 22 days is plotted in Figure 6I. From the two charts, it is clear that the oxide material $Ag_2V_4O_{11}$ dissolved a higher level of vanadium than any of the silver vanadium phosphorous oxide compounds, with a mean concentration of 7.6 mg/L at 21 days. Among the SVPO materials, $Ag_{0.49}VOPO_4 \cdot 1.9H_2O$ had the highest level of vanadium solution formation, at 4.3 mg/L. Vanadium solution formation was lower for $Ag_2VO_2PO_4$ and $Ag_2VP_2O_8$. However, in comparing these two materials, the Noyes Whitney fits to the data suggest that $Ag_2VP_2O_8$ may dissolve more slowly than $Ag_2VO_2PO_4$ but have a higher equilibrium concentration.

Silver solution formation from the four target materials was also compared. Figure 7I shows the mean silver concentration versus time data, while Figure 7II plots the accumulated fraction of dissolved material vs. time, with the best fit for the Weibull function through the mean data for each material represented as a black line. Figure 8I shows bar charts comparing the mean levels of silver dissolved for each material after 22 days. $Ag_2VP_2O_8$ dissolved the most Ag after 22 days, with an average concentration of approximately 23 mg/L.

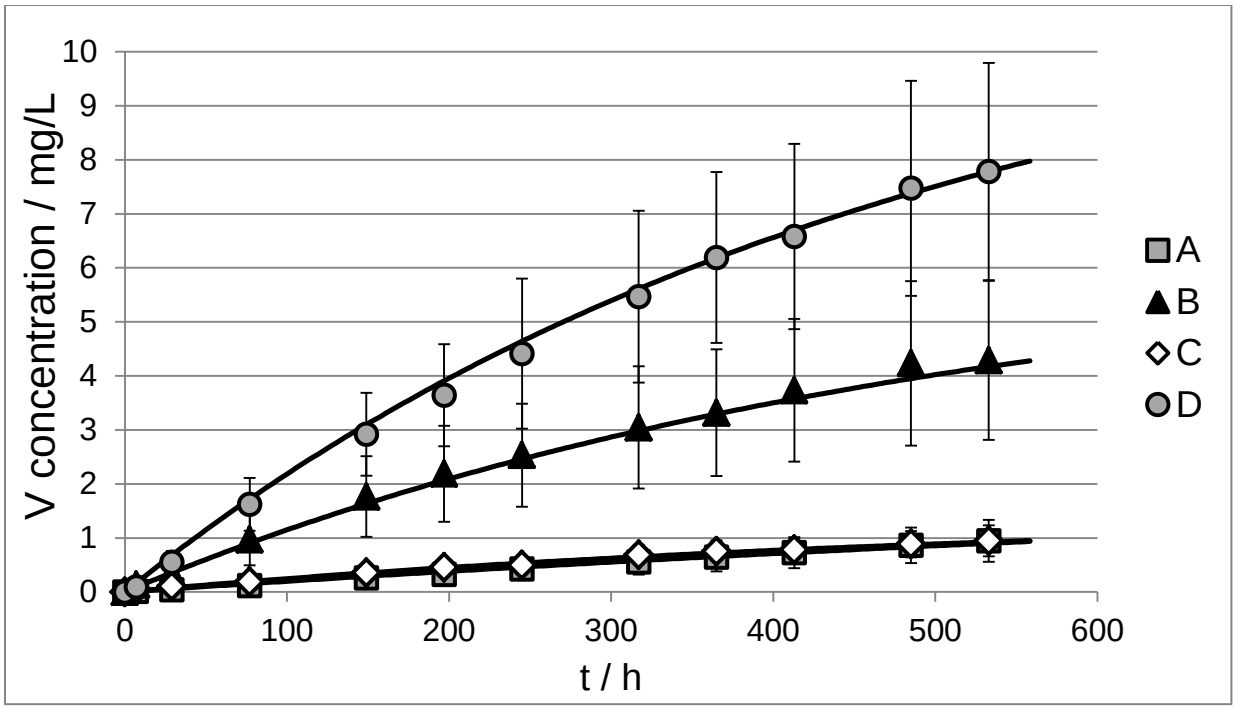


**Figure 5.** Overlays of Noyes-Whitney fits to average vanadium concentration vs. time data for **A.** $Ag_2VP_2O_8$ **B.** $Ag_{0.49}VOPO_4 \cdot 1.9H_2O$ **C.** $Ag_2VO_2PO_4$ and **D.** $Ag_2V_4O_{11}$

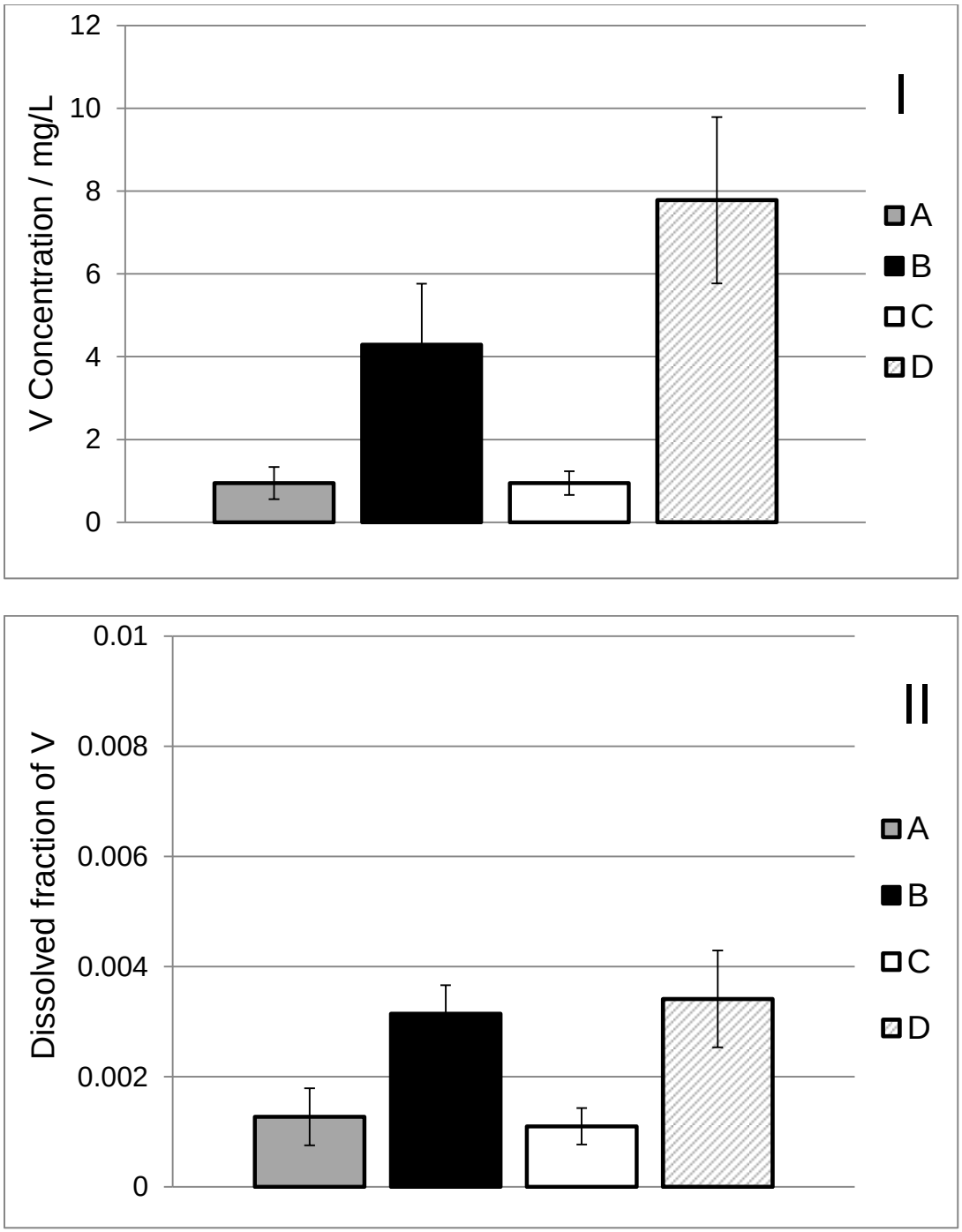


**Figure 6I.** Average concentration of dissolved vanadium and **II.** average dissolved fraction of vanadium at 22 days for **A.** $Ag_2VP_2O_8$ **B.** $Ag_{0.49}VOPO_4 \cdot 1.9H_2O$ **C.** $Ag_2VO_2PO_4$ and **D.** $Ag_2V_4O_{11}$

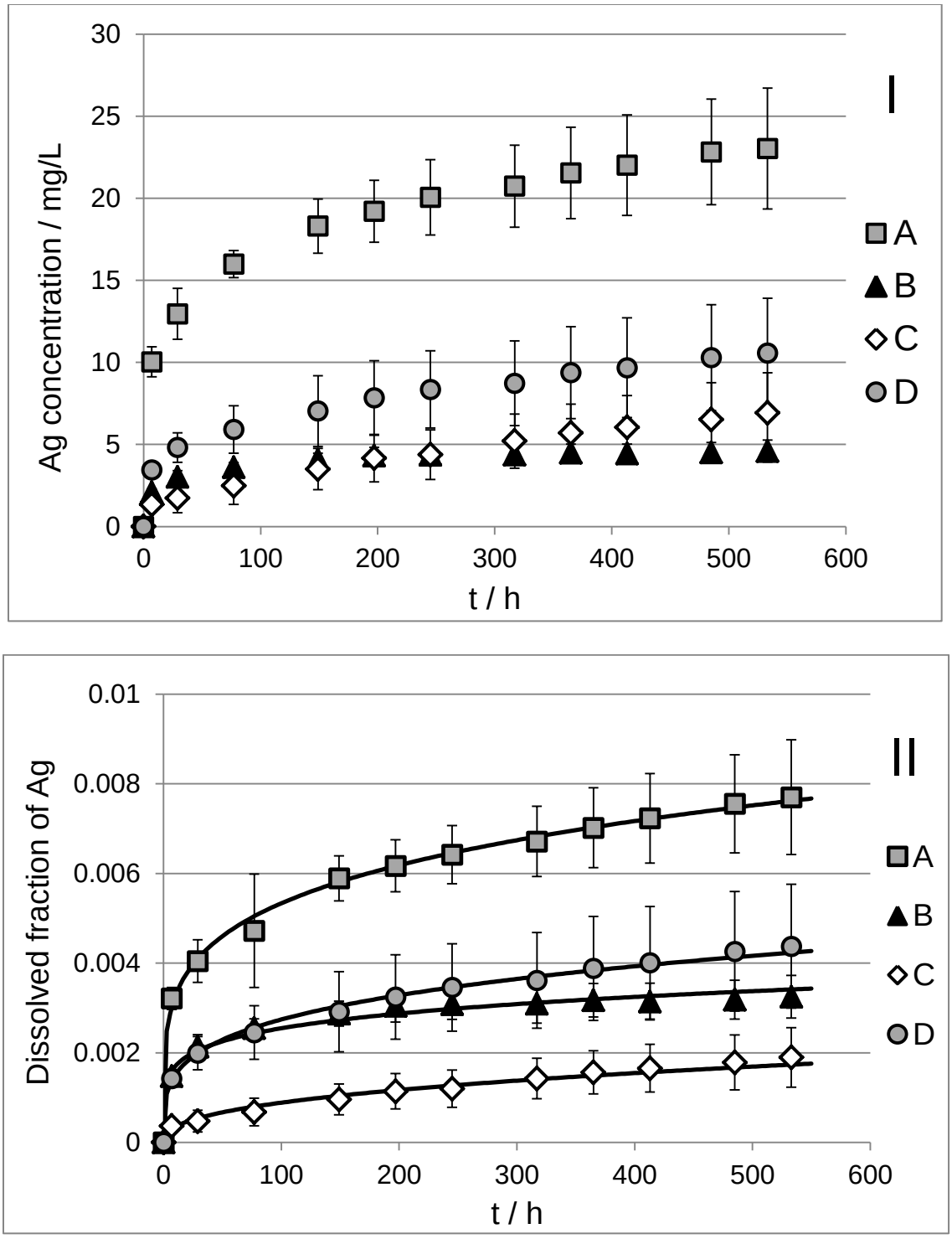


**Figure 7I.** Average silver concentration vs. time data and **II.** Weibull fits to average dissolved fraction of Ag vs. time for **A.** $Ag_2VP_2O_8$ **B.** $Ag_{0.49}VOPO_4 \cdot 1.9H_2O$ **C.** $Ag_2VO_2PO_4$ and **D.** $Ag_2V_4O_{11}$.

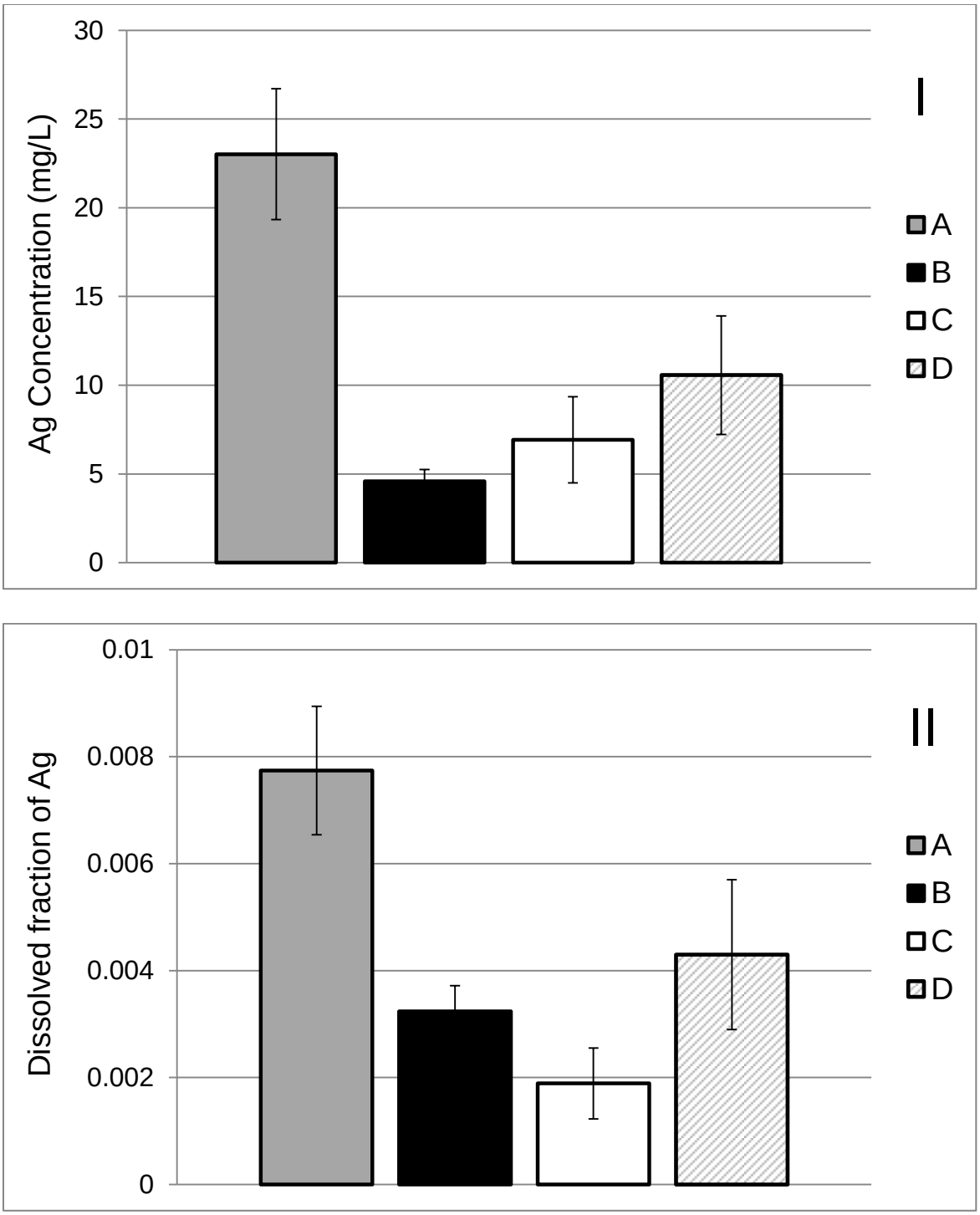


**Figure 8I.** Average concentration of dissolved silver and **II.** average dissolved fraction of silver at 22 days for **A.** $Ag_2VP_2O_8$ **B.** $Ag_{0.49}VOPO_4 \cdot 1.9H_2O$ **C.** $Ag_2VO_2PO_4$ and **D.** $Ag_2V_4O_{11}$.

4.3.4 Normalized solution formation values

The solution formation of silver and vanadium from the various target materials can also be normalized to account for the differences in stoichiometry. This was accomplished by dividing the moles of silver or vanadium dissolved by the number of moles of silver or vanadium in the target material exposed to electrolyte. Normalized vanadium and silver solution formation data are exhibited in Figures 7I and 9, respectively. From the normalized data, the rank order of moles silver dissolved per mole exposed to electrolyte, from highest to lowest, was $Ag_2VP_2O_8$, $Ag_2V_4O_{11}$, $Ag_{0.49}VOPO_4 \cdot 1.9H_2O$, and $Ag_2VO_2PO_4$. The normalized level of Ag solution formation from $Ag_2VP_2O_8$ is approximately double that of the other two phosphate based materials. The normalized vanadium solution formation data indicates that $Ag_{0.49}VOPO_4 \cdot 1.9H_2O$ and $Ag_2V_4O_{11}$ had the highest levels of moles vanadium dissolved per mole vanadium exposed to electrolyte. The average normalized vanadium solution formation values from these materials was approximately three times that of the other two phosphate based materials, $Ag_2VP_2O_8$ and $Ag_{0.49}VOPO_4 \cdot 1.9H_2O$.

To test the hypothesis that $Ag^+$ solution formation proceeds by an ion exchange mechanism with $Li^+$ ions in the electrolyte salt, initial solution formation of Ag and V were tested in both propylene carbonate only and propylene carbonate with 1M $LiBF_4$. In propylene carbonate solvent with no electrolyte salt added, only trace levels (<0.1 mg/L) of Ag dissolved into the electrolyte. In contrast, a high rate of Ag solution formation was observed after only 3 hours of exposure to the PC 1M $LiBF_4$, with concentrations after 3 hours of 1.1, 2.7, 3.4 and 5.8 mg/L for $Ag_2VO_2PO_4$, $Ag_2VP_2O_8$, $Ag_{0.49}VOPO_4 \cdot 1.9H_2O$, $Ag_2V_4O_{11}$, and $Ag_2VP_2O_8$, respectively. This data supports the hypothesis that $Li^+$ ion

exchange with $Ag^+$ plays a significant role in terms of the amount of silver detected in solution. The vanadium levels dissolved were low and similar in solutions with and without electrolyte salt, <0.3 mg/L in all cases.

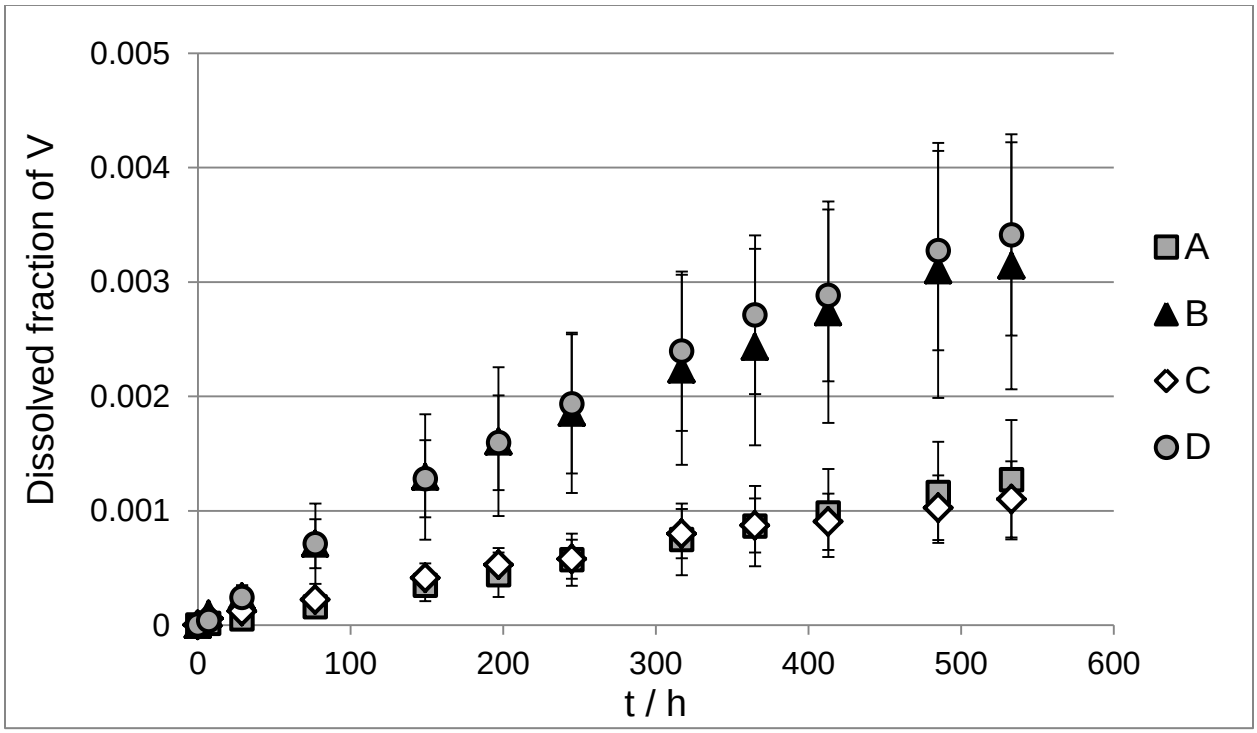


**Figure 9.** Average dissolved fraction of V vs. time for **A.** $Ag_2VP_2O_8$ **B.** $Ag_{0.49}VOPO_4 \cdot 1.9H_2O$ **C.** $Ag_2VO_2PO_4$ and **D.** $Ag_2V_4O_{11}$.

4.3.5 Effect of crystal structure on solution formation - silver

The levels of vanadium and silver dissolved from the cathode materials are less than 0.1% of the total amount of material exposed to electrolyte, as seen from the solution formation data. Therefore, all of the target materials are relatively insoluble in the electrolyte tested. It is reasonable that the majority of the exhibited solution formation is occurring from the surface of the target materials, and that limited solution formation of the bulk material takes place. Indeed, consideration of the crystallite size of the materials indicates that the levels of solution formation occurring can be accounted for by considering the silver and vanadium located in the outermost layer of unit cells for the crystallites. If the observed solution formation is mostly a surface phenomenon, then the manner in which these materials terminate at the material/electrolyte interface would play a significant role in determining how much material is dissolved. Thus, while compositionally similar, differences in crystal structure of the materials could be significant. The possible edge configurations / crystal termination structures of the silver vanadium phosphorous oxide materials were considered and are discussed below.

The material $Ag_2VP_2O_8$ exhibited the highest level of silver solution formation. The structure of $Ag_2VP_2O_8$, looking down the b axis, is shown in Figure 2A. The lower boxed region of Figure 2A focuses on $Ag(2)^+$ ions located in a 6-sided tunnel comprised of corner sharing $VO_6$ and $PO_4$ polyhedra. Figure 2B focuses on the $Ag(2)^+$ ion located at the edge of this 6-sided tunnel, where it can be located above the plane of $VO_6$ and $PO_4$ polyhedra at the edge of a crystal coordinated to five oxygen bonds ranging from 2.42 A - 3.05 Å. In this location the $Ag^+$ is not fully coordinated by vanadium oxide and phosphorous oxide polyhedra and thus may be more susceptible to solution formation into

the electrolyte. The $Ag(1)^+$ ion may also be above the surface of $Ag_2VP_2O_8$, as it is also located in tunnels made from $VO_6$ and $PO_4$ polyhedra. The $Ag^+$ at the surface is not fully coordinated when above the $VP_2O_8$ host lattice (Figure 2C) and thus may be more susceptible to solution formation or ion exchange by $Li^+$ ion from the electrolyte salt.

The two other SVPO materials, $Ag_{0.49}VOPO_4 \cdot 1.9H_2O$ and $Ag_2VO_2PO_4$, exhibited average normalized Ag solution formation levels lower than $Ag_2VP_2O_8$. Figure 1A shows the structure of $Ag_{0.49}VOPO_4 \cdot 1.9H_2O$ viewed along the b axis, emphasizing the layers of the V-O-P-O framework with $Ag^+$ ions and water molecules located between the layers. Figure 1B shows the proposed coordination environment of $Ag^+$ ions at the edge of the structure. We propose that the layered structure terminates with Ag fully coordinated with six oxygen atoms: four oxygen atoms associated with $H_2O$ molecules forming shorter bonds (2.4-2.57 A), and the two other oxygen atoms association with VPO layer framework forming longer bonds (2.65 A). As the $Ag^+$ ions are fully coordinated and not above the VPO layer framework, they would be less likely to dissolve via coordination with solvent and/or ion exchange with the lithium based electrolyte salt. Full coordination of $Ag^+$ ions in $Ag_2VO_2PO_4$ is also predicted (Figure 10B) based on the solubility data.

The fourth target material from which solution formation was studied is silver vanadium oxide, $Ag_2V_4O_{11}$. This material exhibited silver solution formation higher than that of $Ag_{0.49}VOPO_4 \cdot 1.9H_2O$ and $Ag_2VO_2PO_4$ and lower than $Ag_2VP_2O_8$. Figure 11A illustrates the crystal structure of $Ag_2V_4O_{11}$ looking down the [010] direction. Its layers are comprised of edge and corner sharing distorted $VO_6$ octahedra. Silver ions are located between these layers where they are coordinated to seven oxygen atoms. For this

material, there are two distinct possibilities for how the edge of the crystal structure terminates. The first possible structure is shown in Figure 11A, where the $Ag^+$ ion at the crystal edge is coordinated by five oxygen atoms. In this configuration, $Ag^+$ ions are more likely to be solvated by the electrolyte. In the second structure, shown in Figure 11B, the $Ag^+$ ion is fully coordinated by seven oxygen atoms, as occurs in the bulk of the crystal lattice, and will be less susceptible to solution formation. The $Ag_2V_4O_{11}$ material exhibits an intermediate level normalized Ag solution formation, attributed to the two $Ag^+$ ion termination structures described above.

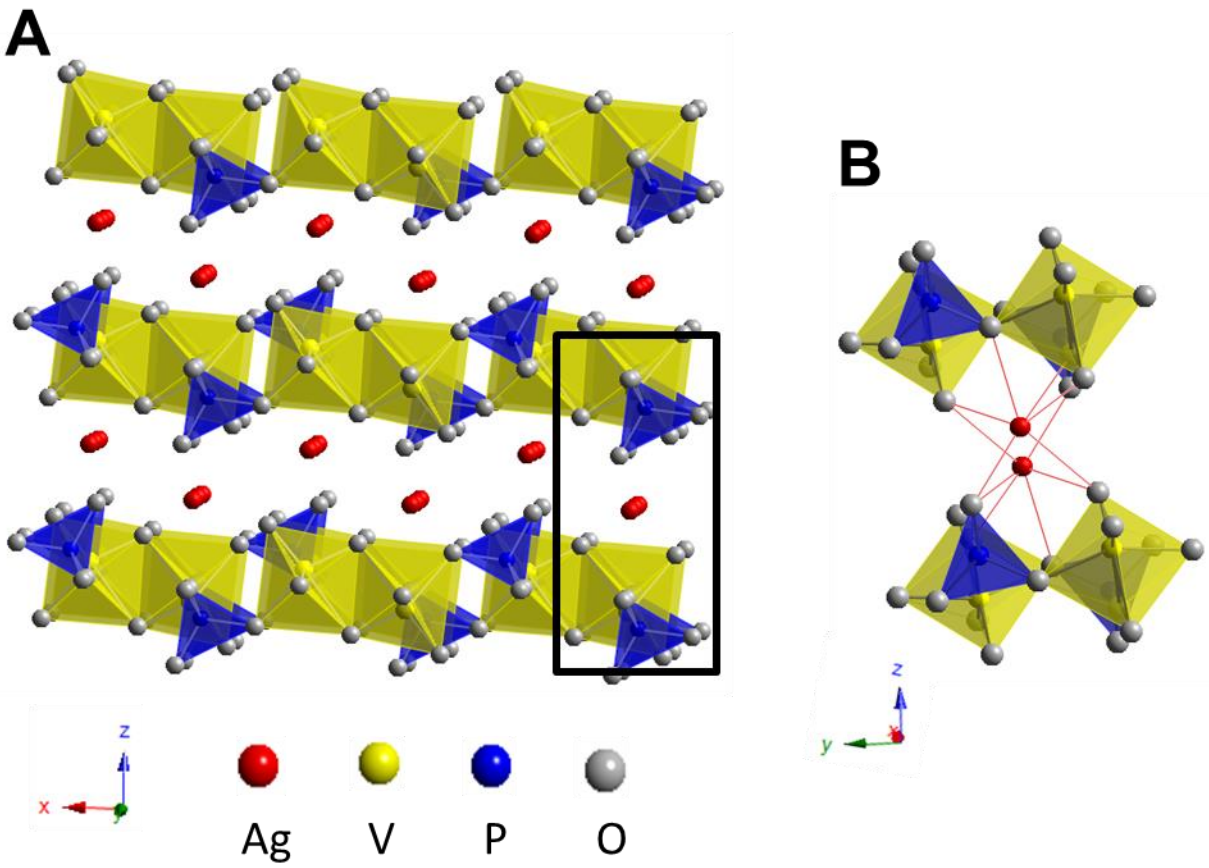


**Figure 10A.** Crystal structure of $Ag_2VO_2PO_4$ looking down the b axis. **B.** Fully coordinated $Ag^+$ ions at the structure edge.

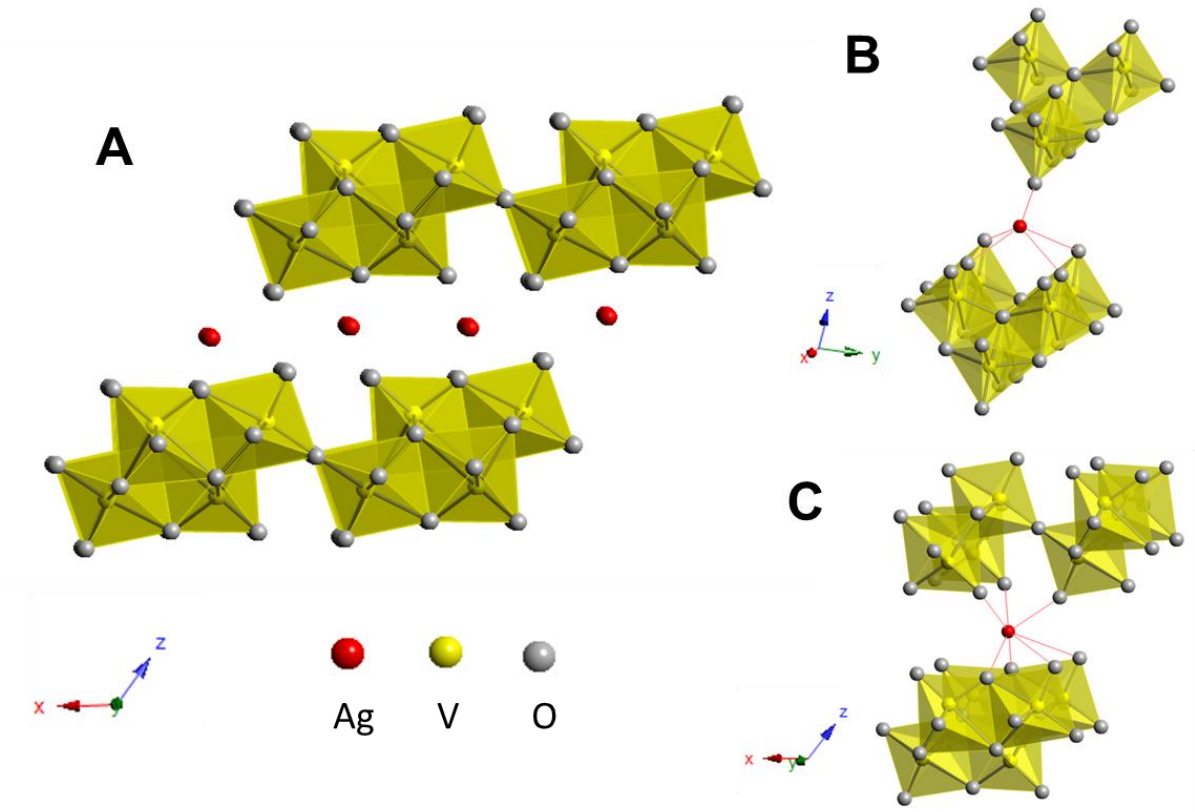


**Figure 11A.** Crystal structure of $Ag_2V_4O_{11}$. Two possible coordination environments for $Ag^+$ ions at the terminating edge of the crystal are **B.** the $Ag^+$ is partially coordinated by five oxygen atoms and **C.** the $Ag^+$ is fully coordinated by 7 oxygen atoms.

4.3.6 Effect of crystal structure on solution formation - vanadium

As indicated in Figure 5, the materials $Ag_{0.49}VOPO_4 \cdot 1.9H_2O$ and $Ag_2V_4O_{11}$ had levels of normalized vanadium solution formation which were approximately 3X that of the materials, $Ag_2VP_2O_8$ and $Ag_2VO_2PO_4$. All three phosphate based compounds have an interconnected lattice consisting of corner sharing vanadium oxide octahedra and phosphorous oxide tetrahedra. In contrast with the $Ag^+$ ions in these materials, vanadium ions are likely to be completely coordinated with oxygen atoms due to their high oxidation state. The level of distortion of vanadium oxide polyhedra in the various materials was considered in order to rationalize the solution formation data. For each material, the vanadium oxide octahedron is considerably distorted with one shorter bond (1.57-1.62 Å), one longer bond (2.15-2.41 Å) and four equatorial bonds ranging from 1.69 to 2.13 Å. In $Ag_2VP_2O_8$, five of the six oxygen atoms coordinated to vanadium oxide octahedra are also coordinated with phosphate tetrahedra including the longest bond 2.15 Å. In $Ag_2VO_2PO_4$, two of the six oxygen atoms coordinated to vanadium oxide are coordinated with phosphate tetrahedra. The longest V-O bond (2.31Å) and a bond of shorter length (1.68Å) share an edge with an adjacent vanadium oxide octahedron. In the oxide material $Ag_2V_4O_{11}$, the longest bonds share an edge with an adjacent vanadium oxide octahedron. However, the absence of phosphate tetrahedra with strong, short P-O bonds (1.53 Å on average for the three phosphate materials) may make the layer framework more susceptible to solvation by the electrolyte.

In chapters we theorized that the phosphate based material $Ag_2VO_2PO_4$ was less prone to vanadium solution formation compared with $Ag_2V_4O_{11}$ due to the presence of stabilizing $PO_4^{3-}$ polyanions in the lattice.[21] However, in this study, the phosphate based

material $Ag_{0.49}VOPO_4 \cdot 1.9H_2O$ exhibited normalized vanadium solution formation values higher than those of the other two silver vanadium phosphorous oxide materials. A detrimental effect of acidic contamination due to the presence of water in carbonate based electrolytes was previously noted for lithium iron phosphate based cathodes, resulting in increased solubility of iron species.[22-23] In order to elucidate the potential impact of the presence of water in the $Ag_{0.49}VOPO_4 \cdot 1.9H_2O$, water content of the electrolytes exposed to the target materials were measured post experiment. The electrolyte samples exposed to $Ag_{0.49}VOPO_4 \cdot 1.9H_2O$ had a water content of 160 ± 50 ppm, compared with water contents of 110 ± 30, 100 ± 30, and 100 ± 30 for $Ag_2VO_2PO_4$, $Ag_2VP_2O_8$, and $Ag_2V_4O_{11}$, respectively. Thus, it was unclear if the higher average water content of the electrolyte samples exposed to $Ag_{0.49}VOPO_4 \cdot 1.9H_2O$ was a significant contributing factor regarding the higher vanadium solution formation for $Ag_{0.49}VOPO_4$ relative to $Ag_2VO_2PO_4$ and $Ag_2VP_2O_8$. To further probe this possibility, solution formation studies were conducted in both PC 1M $LiBF_4$ and PC 1M $LiBF_4$ + 600 ppm $H_2O$ for all four materials. After 3 hours of stirring the $Ag_{0.49}VOPO_4 \cdot 1.9H_2O$ in the electrolyte solutions, the concentrations of silver dissolved were 4.1 mg/L and 2.7 mg/L for the wet and dry electrolyte solutions, respectively, indicating that the added water enhanced the solution formation of silver. In contrast, the concentration of vanadium dissolved into the wet and dry electrolytes after three hours of stirring was 0.1 mg/L. Thus, it is unlikely that the water dissolving into the electrolyte from the $Ag_{0.49}VOPO_4 \cdot 1.9H_2O$ material was the cause of the high vanadium concentration compared with the other two silver vanadium phosphorous oxide materials. Similar results were observed when water was added to the electrolyte solution formation medium for $Ag_2VO_2PO_4$, $Ag_2VP_2O_8$, and $Ag_2V_4O_{11}$. In each case, the wet electrolyte

solution enhanced the solubility of silver, but had no noticeable effect on the solution formation of vanadium.

Although the addition of water to the electrolyte did not influence the solution formation of vanadium, because the structure of $Ag_{0.49}VOPO_4 \cdot 1.9H_2O$ contains coordinated water molecules, the vanadium oxide/ phosphate layered framework may be more susceptible to solution formation. Four of the six oxygens which comprise the vanadium oxide octahedron are shared with $PO_4^{3-}$ tetrahedra, however, the long (V-O) bond belongs to a water molecule, where incomplete coordination of vanadium upon loss of water from the lattice may make the vanadium more susceptible to solution formation. $Ag_{0.49}VOPO_4 \cdot 1.9H_2O$ is also unique from the other materials in that the vanadium has a mixed oxidation state of ~4.5. It is expected that $V^{5+}$ and $V^{4+}$ are disordered within the VPO layers. This disorder may result in instability and thus susceptibility to solvation by the electrolyte.

Results from the differential scanning calorimetry experiments on the target materials support the hypothesis of weaker framework structure for $Ag_{0.49}VOPO_4 \cdot 1.9H_2O$ relative to the other phosphorous oxide materials. $Ag_2VO_2PO_4$ has an endothermic transition at 540$^{o}$C, while $Ag_2VP_2O_8$ has no transitions up to 580$^{o}$C. In contrast, $Ag_{0.49}VPO_4 \cdot 1.9H_2O$ shows numerous endothermic transitions, between 100 and 580$^{o}$C, which indicates that less energy is needed to change the lattice structure of $Ag_{0.49}VPO_4 \cdot 1.9H_2O$.

## 4.4 Summary

This study describes the appearance of silver and vanadium in solution from $Ag_{0.49}VOPO_4 \cdot 1.9H_2O$ and $Ag_2VP_2O_8$, two members of the silver vanadium phosphorous oxide ($Ag_wV_xP_yO_z$) family of materials. The vanadium concentration versus time data for both materials was consistent with the Noyes-Whitney model, which represents a diffusion controlled solution formation process. In contrast, the silver concentration versus time data for both materials proceeded at a faster initial rate and was modelled using the Weibull function, indicative of a more complex mechanism than simple solution formation. Significantly lower levels of silver were observed when testing was done without electrolyte salt, providing evidence that the presence of $Li^+$ ions in the electrolyte plays a large role in the silver dissolution mechanism.

The solution data of $Ag_{0.49}VOPO_4 \cdot 1.9H_2O$ and $Ag_2VP_2O_8$ was compared with $Ag_2VO_2PO_4$ and $Ag_2V_4O_{11}$, two additional materials for which solution formation has recently been described, in order to probe the influence of stoichiometry and crystal structure on solution formation. The trace levels of cathode in solution suggest that the solution formation processes are strongly influenced by the crystal structure at the surface of the material crystallites. As such, possible crystal termination / edge configuration structures of the target materials were considered with regards to the solution formation results. Higher levels of normalized silver solution formation occurred in those materials in which incomplete silver coordination environments at the crystal edge were possible. For vanadium, increased solution formation was observed for the oxide material $Ag_2V_4O_{11}$ as well as for the phosphate oxide $Ag_{0.49}VOPO_4 \cdot 1.9H_2O$. Increased

susceptibility to vanadium solution formation for $Ag_{0.49}VOPO_4 \cdot 1.9H_2O$ may be associated with structural water or the existence of multiple vanadium oxidation states.

This systematic investigation of multiple materials identifies the most promising members of the SVPO family for reducing vanadium solution formation as $Ag_2VO_2PO_4$ and $Ag_2VP_2O_8$. The low solution rates coupled with the ability to deliver high rate intermittent pulses make these materials promising alternatives to $Ag_2V_4O_{11}$ for the ICD application.

## 4.5 References


(1) Marschilok, A. C.; Kim, Y. J.; Takeuchi, K. J.; Takeuchi, E. S., Silver vanadium phosphorous oxide, Ag0.48VOPO4: exploration as a cathode material in primary and secondary battery applications. *J. Electrochem. Soc.* **2012,** 159, A1690-A1695.

(2) Kim, Y. J.; Lee, C.-Y.; Marschilok, A. C.; Takeuchi, K. J.; Takeuchi, E. S., AgxVOPO4: A demonstration of the dependence of battery-related electrochemical properties of silver vanadium phosphorous oxides on Ag/V ratios. *J. Power Sources* **2011,** 196, 3325-3330.

(3) Takeuchi, E. S.; Lee, C.-Y.; Cheng, P.-J.; Menard, M. C.; Marschilok, A. C.; Takeuchi, K. J., Silver vanadium diphosphate Ag2VP2O8: electrochemistry and characterization of reduced material providing mechanistic insights. *J. Solid State Chem.* **2013,** 200, 232-240.

(4) Leising, R. A.; Takeuchi, E. S., Solid-state cathode materials for lithium batteries: effect of synthesis temperature on the physical and electrochemical properties of silver vanadium oxide. *Chem. Mater.* **1993,** 5, 738-42.

(5) Kang, H. Y.; Wang, S. L.; Tsai, P. P.; Lii, K. H., Hydrothermal synthesis, crystal structure and ionic conductivity of silver vanadium oxide phosphate, Ag2VO2PO4: a new layered phosphate of vanadium(V). *J. Chem. Soc., Dalton Trans.* **1993**, 1525-8.

(6) Ayyappan, P.; Ramanan, A.; Torardi, C. C., New Metal-Intercalated Layered Vanadyl Phosphates, MxVOPO4·yH2O (M = Ag, Cu, Zn). *Inorg. Chem.* **1998,** 37, 3628-3634.

(7) Daidouh, A.; Veiga, M. L.; Pico, C., Structure characterization and ionic conductivity of Ag2VP2O8. *J. Solid State Chem.* **1997,** 130, 28-34.

(8) Noyes, A. A.; Whitney, W. R., The rate of solution of solid substances in their own solutions. *J. Am. Chem. Soc.* **1897,** 19, 930-4.

(9) Weibull, W., A statistical distribution of wide applicability. *Journal of Applied Mechanics* **1951,** 18, 293-297.

(10) D'Souza Susan, S.; Faraj Jabar, A.; DeLuca Patrick, P., A model-dependent approach to correlate accelerated with real-time release from biodegradable microspheres. *AAPS PharmSciTech* **2005,** 6, E553-64.

(11) Van Vooren, L.; Krikilion, G.; Rosier, J.; De Spiegeleer, B., A novel bending point criterion for dissolution profile interpretation. *Drug Dev. Ind. Pharm.* **2001,** 27, 885-892.

(12) Lin, C.-W.; Cham, T.-M., Effect of particle size on the available surface area of nifedipine from nifedipine-polyethylene glycol 6000 solid dispersions. *Int. J. Pharm.* **1996,** 127, 261-72.

(13) Sathe, P. M.; Venitz, J., Comparison of neural network and multiple linear regression as dissolution predictors. *Drug Dev. Ind. Pharm.* **2003,** 29, 349-355.

(14) Chevalier, E.; Viana, M.; Artaud, A.; Chomette, L.; Haddouchi, S.; Devidts, G.; Chulia, D., Comparison of three dissolution apparatuses for testing calcium phosphate pellets used as ibuprofen delivery systems. *AAPS PharmSciTech* **2009,** 10, 597-605.

(15) Nagarwal, R. C.; Ridhurkar, D. N.; Pandit, J. K., In vitro release kinetics and bioavailability of gastroretentive cinnarizine hydrochloride tablet. *AAPS PharmSciTech* **2010,** 11, 294-303.

(16) Varma, M. V. S.; Kaushal, A. M.; Garg, S., Influence of micro-environmental pH on the gel layer behavior and release of a basic drug from various hydrophilic matrices. *J. Controlled Release* **2005,** 103, 499-510.

(17) Koester, L. S.; Ortega, G. G.; Mayorga, P.; Bassani, V. L., Mathematical evaluation of in vitro release profiles of hydroxypropylmethylcellulose matrix tablets containing carbamazepine associated to β-cyclodextrin. *Eur. J. Pharm. Biopharm.* **2004,** 58, 177-179.

(18) Adams, E.; Coomans, D.; Smeyers-Verbeke, J.; Massart, D. L., Non-linear mixed effects models for the evaluation of dissolution profiles. *Int. J. Pharm.* **2002,** 240, 37-53.

(19) Bonferoni, M. C.; Rossi, S.; Ferrari, F.; Bertoni, M.; Bolhuis, G. K.; Caramella, C., On the employment of λ carrageenan in a matrix system. III. Optimization of a λ carrageenan-HPMC hydrophilic matrix. *J. Controlled Release* **1998,** 51, 231-239.

(20) Papadopoulou, V.; Kosmidis, K.; Vlachou, M.; Macheras, P., On the use of the Weibull function for the discernment of drug release mechanisms. *Int. J. Pharm.* **2006,** 309, 44-50.

(21) Ellis, B. L.; Lee, K. T.; Nazar, L. F., Positive Electrode Materials for Li-Ion and Li Batteries. *Chem. Mater.* **2010,** 22, 691-714.

(22) Koltypin, M.; Aurbach, D.; Nazar, L.; Ellis, B., On the Stability of LiFePO4 Olivine Cathodes under Various Conditions (Electrolyte Solutions, Temperatures). *Electrochem. Solid-State Lett.* **2007,** 10, A40-A44.

(23) Markevich, E.; Salitra, G.; Aurbach, D., Influence of the PVdF binder on the stability of LiCoO2 electrodes. *Electrochem. Commun.* **2005,** 7, 1298-1304.

# Chapter 5

## Mapping the anode surface-electrolyte interphase: Investigating a life limiting process in Li/SVPO and Li/SVO batteries

Adapted with permission from [Bock, D. C.; Tappero, R. V.; Takeuchi, K. J.; Marschilok, A. C.; Takeuchi, E. S., Mapping the Anode Surface-Electrolyte Interphase: Investigating a Life Limiting Process of Lithium Primary Batteries. *ACS App Mater Inter* **2015,** 7, 5429-5437]. 

### 5.1 Introduction

One of the major consequences of the dissolution of cathode material into the electrolyte in the lithium/silver vanadium oxide battery system is that dissolved species deposit onto the lithium anode, which increases the internal resistance of the cell.[1] In Chapter 2, the influence of anode vanadium deposition on electrochemical performance was explored by running electrochemical impedance spectroscopy and pulse discharge tests on cells having anodes treated with vanadium. This section further explores vanadium deposition in electrochemical cells having either $Ag_2V_4O_{11}$ (SVO) or $Ag_2VO_2PO_4$ (SVPO) cathodes by subjecting the cells to long term (~1 year rate) testing and recovering the lithium anodes. Subsequent analysis by X-ray microfluorescence and ICP-OES was performed to determine the relationships between cathode dissolution, vanadium and silver deposition on the anode surface, and electrochemical performance. While the reduction process of the cathodes in $Li/Ag_2V_4O_{11}$ and $Li/Ag_2VO_2PO_4$ batteries have been studied through characterization of the cathode material at various stages of discharge,[2-6] this is the first report which analyzes the anode surface.

There are limited reports of negative electrodes analyses from cells including those containing manganese oxide cathodes.[7] Surface films containing manganese (II) were detected on graphite electrodes using electrolytes contaminated with manganese ions and were associated with a ~15 times increase in the lithium-ion transfer resistance.[8-9] X-ray absorption near edge spectra (XANES) of lithium metal, lithium titanate, and graphite anodes from cycled cells with $LiMn_2O_4$ cathodes showed films containing manganese(II) and manganese metal were reported; however locational information (i.e. mapping) was not available.[10-11] Detailed understanding of the location, composition and role of the transition metal deposits on the negative electrode surfaces is lacking.

In this study, the negative electrodes of lithium/silver vanadium oxide and lithium/silver vanadium phosphorous oxide electrochemical cells were investigated by several techniques including mapping by synchrotron based x-ray microfluorescence (XRμF) and oxidation state determination by microbeam x-ray absorption spectroscopy (μXAS). Quantitative analysis of digested samples was done using inductively coupled plasma-optical emission spectroscopy (ICP-OES). These methods enabled visualization of the anode surface and solid electrolyte interphase (SEI) through mapping, determination of the vanadium oxidation state, and quantification of the silver and vanadium content of the recovered anodes. The findings indicate significant differences for the anode surfaces from the two cell types based on oxide versus phosphate based cathodes, clearly demonstrating lower deposition on the anode from the $Ag_2VO_2PO_4$ cells. This observation was considered in light of the improved long term electrochemical performance to propose a conceptual model of the location and role of the metal ions deposited at the negative electrode. Thus, from this study arises a paradigm to investigate use based performance degradation in battery systems through elucidation of the composition

and geography of the negative electrode surface and SEI which will aid the broader community in more fully understanding this significant battery failure mechanism.

This work was done in collaboration with Ryan V. Tappero. Ryan collected the XRμF and μXAS data. I prepared the samples, collected electrochemical measurements and analyzed the XAS data.

## 5.2 Experimental

### 5.2.1 Materials Synthesis and Characterization

Silver vanadium phosphorous oxide ($Ag_2VO_2PO_4$) was synthesized by a hydrothermal reaction according to a method previously reported in the literature using silver(I) oxide ($Ag_2O$), vanadium(V) oxide ($V_2O_5$) and phosphoric acid ($H_3PO_4$, 85%) as starting materials.[12] Silver vanadium oxide ($Ag_2V_4O_{11}$) was synthesized by a previously reported method.[13] Differential scanning calorimetry (DSC) analysis was performed using a TA instruments Q20. Powder X-ray diffraction (XRD) measurements were recorded with a Rigaku Smart Lab X-ray diffractometer, using Cu Kα radiation and Bragg-Brentano focusing geometry.

### 5.2.2 Electrochemical Testing

Electrochemical tests were performed using coin-cell type experimental cells. Composite cathodes were prepared by mixing conductive carbon with silver vanadium phosphorous oxide or silver vanadium oxide. The 250 mg cathode pellets were comprised of 85% active material and 15% graphite conductive additive. The anode was lithium foil and the electrolyte was 1M $LiBF_4$ in propylene carbonate. The electrodes were separated by two layers of Celgard 2500 separators, each of 25 μm thickness. The ratio of electrolyte to cathode material in the cells was 200 mg / 250 mg. Constant current discharge and pulse discharge tests were performed at 37°C.

Treated lithium metal foil anodes were prepared by exposure to silver or vanadium containing solutions. ICP-OES of the treated anodes showed quantities of 21 and 14 μg/cm$^2$ for silver and vanadium, respectively. Electrochemical cells were constructed using one treated lithium as the working electrode and one fresh lithium foil as the counter electrode. Control cells were also constructed, utilizing fresh lithium for both electrodes. The area of the lithium test electrodes was 1.6 cm$^2$. Cells were constructed using 2 layers of Celgard 2500 separator. The AC impedance measurements were collected using a BioLogic VSP multichannel potentiostat using a 5 mV sinus amplitude and a frequency range of 10 mHz to 100 kHz. Analysis of AC impedance data was performed using ZView software, Version 3.3b. The data was fit to an equivalent circuit model to quantify the cell resistance.

### 5.2.3 Ex-Situ Analysis

Post discharge, coin cells were disassembled under inert atmosphere. Disassembled anodes and cathodes were rinsed with a dimethyl carbonate solvent and dried under vacuum. Lithium anodes from $Ag_2V_4O_{11}$ and $Ag_2VO_2PO_4$ cells were prepared for analysis by x-ray microfluorescence, by transferring a portion of the anode to a sample holder with a beryllium window and an o-ring seal.

Synchrotron-based X-ray microfluorescence (XRμF) images of lithium anodes recovered from the coin cells were acquired using Beamline X27A of the National Synchrotron Light Source (NSLS I) at Brookhaven National Laboratory (Upton, NY). This bend-magnet beamline uses Kirkpatrick-Baez (KB) mirrors to produce a focused spot (7 by 14 mm) of hard X-rays with tunable energy achieved via Si(111) or Si(311) channel-cut monochromator crystals.[14] For mSXRF imaging, the Si(111) monochromator was calibrated using a vanadium(V) metal foil and

set to fixed energy of 5.5 keV to excite the V K-edge. Samples were contained in a custom environmental cell with inert atmosphere and Be window. Samples were oriented 45° to the incident beam and rastered in the path of the beam by an XY stage while X-ray fluorescence was detected with a 4-element Vortex Silicon Drift Detector (SDD) positioned at 90° to the incident beam. Typical elemental maps were collected from a 1 x 2 mm sample area using a step size of 8 μm and a transit time of 80 milliseconds. In the pre-edge region from 5395.0 eV to 5455.0 eV, and the post edge region from 5496.0 eV to 5615.0 eV, the incident beam energy was scanned using 2.0 eV energy steps. Across the vanadium K-edge from 5455.5 eV to 5495.0 eV, the step size was decreased to 0.5 eV for enhanced resolution. Vanadium compounds of varying oxidation states were used as reference materials, specifically vanadium metal foil, $V_2O_3$, $V_2O_4$, and $Ag_2VO_2PO_4$. For microbeam vanadium K-edge X-ray absorption spectroscopy (μXAS) measurements, the incident beam energy was scanned across the vanadium K-edge using 0.5 eV energy steps. All fluorescence signals were normalized to changes in intensity of the X-ray beam ($I_0$). Data acquisition and visualization were performed using IDL-based beamline software developed for NSLS Beamline X26A. XAS data analysis was performed using Athena.[15] Inductively coupled plasma-optical emission spectroscopy (ICP-OES) was used to quantify the amount of silver and vanadium on the lithium anodes by digestion in a nitric acid solution and subsequent analysis using a Thermofisher iCAP 6300 series ICP-OES.

## 5.3 Results and Discussion

### 5.3.1 Materials and Characterization

Silver vanadium oxide ($Ag_2V_4O_{11}$, SVO) and silver vanadium phosphorous oxide ($Ag_2VO_2PO_4$, SVPO) materials were characterized using powder X-ray diffraction. Differential

scanning calorimetry was used to confirm the phase purity of both materials. Surface areas measured using the BET technique were 1.1 ± 0.1 and 0.9 ± 0.1 for $Ag_2VO_2PO_4$ and $Ag_2V_4O_{11}$, respectively.

### 5.3.2 Electrochemical Testing

After synthesis and confirmation of the structure of silver vanadium oxide ($Ag_2V_4O_{11}$, SVO), and silver vanadium phosphorous oxide ($Ag_2VO_2PO_4$, SVPO), the materials were used as cathodes in lithium metal anode coin cells. Cells were discharged at 37°C under constant current over 100 and 150 days to 2 and 3 electron equivalents, respectfully (Figure 1A.) This discharge rate corresponded to a current of 7.9 x $10^{-6}$ A for the SVO cells and a current of 1.18 x $10^{-5}$ A for the SVPO cells. Silver vanadium phosphorous oxide can be reduced by up to 4 electrons, and as such, the 2 and 3 electron equivalent discharge levels are representative of depth 50% and 75% depth of discharge. For silver vanadium oxide, 7 moles of lithium can be incorporated into the structure, so 2 and 3 electrons equate to 28.5% and 42.8% depth of discharge, respectfully. Discharge was done slowly to mimic long term use in patients where the ICD devices would be powering background functions. This allows probing of low levels of cathode dissolution and subsequent deposition of silver and vanadium from the cathode materials onto the lithium anode surfaces.

After the cells attained the targeted level of discharge, constant current pulses were applied to the cells to simulate intermittent therapy delivery of an ICD. One cell at each condition was pulse tested where two 10s, 20 mA/$cm^2$ pulses were applied with a 20s rest period between pulses. The voltage versus time response is shown in Figures 1B and 1C. After reduction by 2 electron equivalents, comparable performance was seen for the $Ag_2V_4O_{11}$ and $Ag_2VO_2PO_4$ cells where both cells could sustain pulse voltages above 1.5 V, Figure 1B. Pulse testing after 3 electron equivalents of reduction showed that the $Ag_2VO_2PO_4$ cells displayed a small amount of voltage delay where the leading edge of the voltage under pulse was lower (~1.0 V) than the 10 second point of the pulse (~1.1 V), Figure 1C. The minimum

voltage under the second pulse was higher at 1.2 V. In contrast, the $Ag_2V_4O_{11}$ cell discharged to 3 electron equivalents exhibited significant polarization upon pulsing. While there was some amount of voltage delay as the leading edge of the pulse dropped to 0.9 V and recovered slightly, the pulse voltage then dropped sharply as the pulse continued to a minimum voltage of ~0.1 V. The second pulse could not deliver useful power as the voltage under the second pulse dropped to ~0.1 V as well.

The DC resistance ($R_{DC}$) for the four pulse discharged cells was calculated and is tabulated in Table 1. The $R_{DC}$ of the $Ag_2V_4O_{11}$ and $Ag_2VO_2PO_4$ cells were comparable after discharge to 2 electron equivalents, but after discharge to 3 electron equivalents the $R_{DC}$ of the $Ag_2V_4O_{11}$ cell was approximately 2X that of the $Ag_2VO_2PO_4$ cell. In practical device terms, appropriately designed cells based on $Ag_2VO_2PO_4$ or $Ag_2V_4O_{11}$ could successfully deliver sufficient energy, ~30 J, to deliver therapy in an ICD after discharge equivalent to 2 electrons. However, after 3 electrons of discharge, the $Ag_2V_4O_{11}$ would no longer be able to support delivery of a therapy pulse. The electrochemical results affirm that after slow discharge to 3 electron equivalents, cells with $Ag_2VO_2PO_4$ cathodes can sustain significantly higher pulse voltage than $Ag_2V_4O_{11}$ cells. These results motivated studies of the cell components, in particular the cell anodes, to determine if a correlation between the anode surface composition and electrochemical performance could be established.

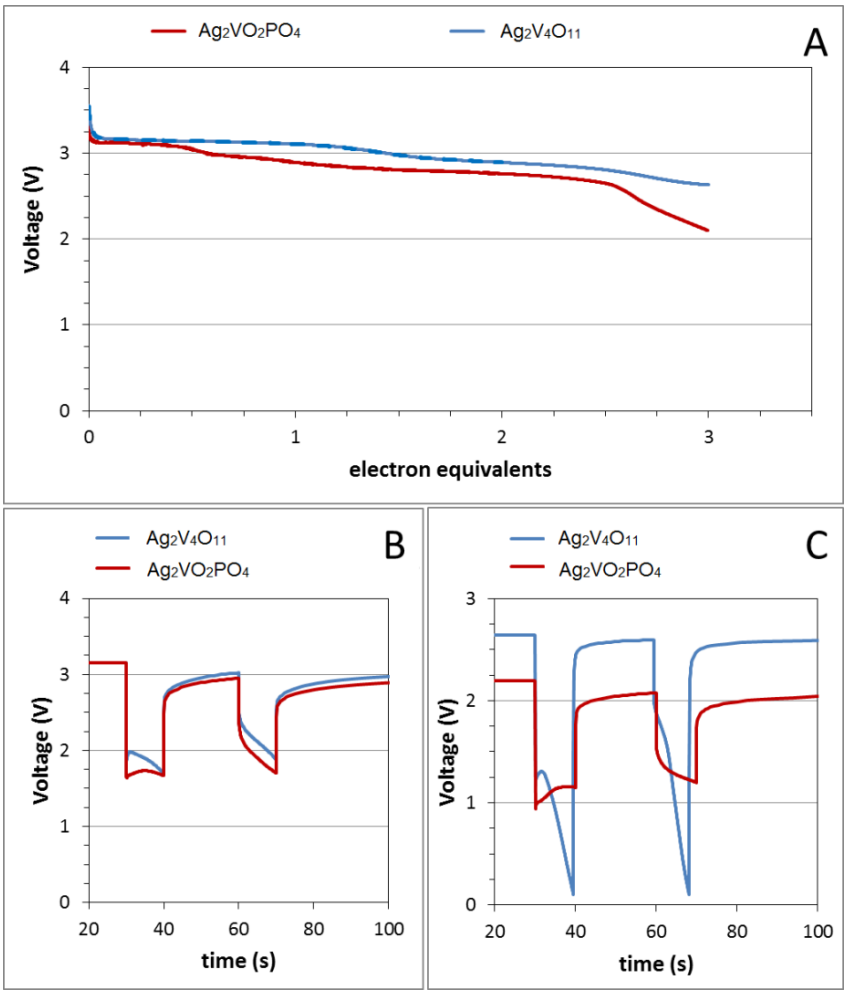


**Figure 1A.** Long term (~1 year rate) discharge for lithium anode cells containing silver vanadium oxide ($Ag_2V_4O_{11}$) and silver vanadium phosphorous oxide ($Ag_2VO_2PO_4$) cathodes. **B.** Voltage versus time for pulse discharge at 2 electron equivalents of discharge. **C.** Voltage versus time for pulse discharge at 3 electron equivalents of discharge.

| cell type | electron equivalents | $R_{DC}$ (Ω) | |
|---|---|---|---|
| | | Pulse 1 | Pulse 2 |
| $Li/Ag_2VO_2PO_4$ | 2 | 56 | 46 |
| | 3 | 39 | 32 |
| $Li/Ag_2V_4O_{11}$ | 2 | 55 | 43 |
| | 3 | 95 | 93 |

**Table 1.** Calculated Direct Current Resistance ($R_{DC}$) for $Li/Ag_2VO_2PO_4$ and $Li/Ag_2V_4O_{11}$ cells under pulse discharge at 2 and 3 electron equivalents.

5.3.3 Ex-situ cathode characterization

Post discharge, cell cathodes were recovered and analyzed by X-ray powder diffraction. XRD patterns indicated the presence of silver metal for both cathode materials discharged to two and three electron equivalents. The integrated area of the silver peak at 44.2° 2-theta is higher for the $Ag_2VO_2PO_4$ (6000 and 6500 at 2 and 3 electron reduction, respectively) material compared to $Ag_2V_4O_{11}$ (3800 and 4100 at 2 and 3 electron reduction, respectively) indicating slightly higher levels of reduced silver in the $Ag_2VO_2PO_4$ cathode. As has been previously reported for silver–vanadium bimetallic materials, some vanadium reduction takes place in parallel with the reduction of silver.[2, 5-6, 16-17] Previous studies of discharged $Ag_2V_4O_{11}$[2, 4] indicate that vanadium oxidation states of V, IV, and III can co-exist once the material is discharged past 2 electron equivalents. For $Ag_2VO_2PO_4$, a recent X-ray absorption spectroscopy study[6] has shown that the vanadium is present as a mixture of oxidation states IV and III when the material is discharged to 3 electron equivalents. Thus, both oxidation states of IV and III are expected to be present in $Ag_2V_4O_{11}$ and $Ag_2VO_2PO_4$ cathode materials when discharged to 3 electron equivalents.

5.3.4 Ex-situ lithium anode characterization – X-ray microfluorescence

Vanadium K-edge elemental maps of anodes from cells discharged to 2 electron equivalents are shown in Figures 2A and 2B for the anodes from the $Ag_2V_4O_{11}$ and $Ag_2VO_2PO_4$ cells, respectively. Within the 1 x 1 mm area analyzed, the anodes from the $Ag_2V_4O_{11}$ cell and the $Ag_2VO_2PO_4$ cell appear relatively similar. There are some areas of higher and lower vanadium intensity visible, likely a result of some surface roughness of the partially discharged

lithium surface. Experiments on lithium stripping in carbonate based electrolytes have indicated that the lithium surface is locally dissolved to form a randomized, pitted surface due to areas of passivation film breakdown.[18] Thus, some regions of the electrode may have thicker regions of SEI where higher concentrations of V are expected. Vanadium K-edge elemental maps of anodes from cells discharged to 3 electron equivalents were recorded and are shown in Figures 2C and 2D for the anodes from the $Ag_2V_4O_{11}$ and $Ag_2VO_2PO_4$ cells, respectively. Contrary to the anodes from the cells depleted by 2 electrons, the anodes from the $Ag_2V_4O_{11}$ and $Ag_2VO_2PO_4$ cells are different in appearance. Within the 1 x 2 mm area analyzed, the anode from the $Ag_2V_4O_{11}$ cell exhibits large and distinct areas of much higher intensity of the vanadium signal. In contrast, the anode from the $Ag_2VO_2PO_4$ cell exhibited low vanadium signal intensity for the majority of the analyzed area, with a few small localized regions of high intensity, illustrating differences in the vanadium content over the lithium surface.

The result of the x-ray microfluorescence (XRμF) can be considered in conjunction with the pulse discharge data. In chapter 2 it was demonstrated that lithium metal surfaces treated with electrolyte containing dissolved vanadium significantly increased the impedance of a cell.[19] From those results, it would be reasonable to expect that the cells displaying low pulse voltage and high resistance would have higher levels of vanadium deposited on the lithium anode surfaces. For the lithium anodes from the $Ag_2V_4O_{11}$ and $Ag_2VO_2PO_4$ cells analyzed as part of this study, the vanadium detected after 2 electrons of reduction are generally low. Additionally, the vanadium detected on the lithium anode from the $Ag_2VO_2PO_4$ cell after 3 electrons of reduction is also generally low. In sharp contrast, the lithium anode from the $Ag_2V_4O_{11}$ cell discharged to 3 electrons shows much higher levels of vanadium present, consistent with the large voltage drop observed during the pulse discharge test.

Microbeam X-ray absorption spectroscopy (μXAS) measurements made in the vanadium K-edge XANES region were collected at various positions for the elemental maps of the anodes to interrogate the nature of the vanadium species deposited on the anode surface. For the $Ag_2VO_2PO_4$ 3e discharged cell, XANES spectra collected at positions on the elemental map exhibiting low vanadium K-edge signal intensity exhibited low signal to noise due to the small amount of vanadium present on the surface. In areas with very low levels of vanadium, the signal intensity was low, but the vanadium species indicate an average oxidation state between I and III. Spectra collected at the highest intensity region on the map, at x = 1.2, y = 0.8, are plotted and overlaid with the vanadium foil spectrum, Figure 3A. The similarity in edge position and profile of the sample and the reference foil suggests that the vanadium deposited on the lithium anode surface in this localized region was reduced to vanadium metal. Comparable spectra were also collected at the higher intensity region x = 1.5, y = 0.9. These data provide evidence that the vanadium species on the anode from the $Ag_2VO_2PO_4$ cell showing highest intensity are vanadium metal.

XANES data collected at various positions for the anodes from the $Ag_2V_4O_{11}$ cells discharged to 3 electron equivalents show similar spectra. A representative XANES spectrum for the 3e $Ag_2V_4O_{11}$ anode sample collected at location x = 1.0, y = 0.5 is overlaid with the vanadium standards, Figure 3B. The vanadium K-edge of the sample spectrum is positioned at an energy between the K-edge for the vanadium(0) and vanadium(III) standards, suggesting that the vanadium species deposited on the anode are not fully reduced to vanadium metal and that more than a single vanadium oxidation state may be present. Further, the general profile of the sample spectra differ from those of the reference materials suggesting that the chemistry of deposited vanadium species is different from the vanadium foil and oxide reference materials.

The XANES data indicate that there are some differences in the overall vanadium species deposited on the lithium anode in the $Ag_2V_4O_{11}$ cell compared to the anode in the $Ag_2VO_2PO_4$ cell. For the anode recovered from the $Ag_2V_4O_{11}$ cell after 3 electrons, the data suggests that the average oxidation state of the vanadium species on the surface is between III and 0, not fully reduced to vanadium metal. The anode from the $Ag_2VO_2PO_4$ cell shows that there are localized areas of high concentration vanadium that are fully reduced to vanadium metal. Measurement of the lithium surfaces remote from the areas of high concentration showed little vanadium present, with average oxidation states between I and III.

The results of these findings can be rationalized as follows. Multiple oxidation states of vanadium may be present in solution including vanadium(V), vanadium(IV), and vanadium(III). As the vanadium centers approach the lithium surface, the vanadium species will encounter the solid electrolyte interphase (SEI) at the lithium surface. Based on the difference in standard reduction potentials of vanadium and lithium, at lithium potential, the vanadium ions may be reduced with some reduced to vanadium metal. The data indicate that some of the vanadium detectable on the anode surface is not fully reduced to vanadium metal. Thus, consideration of the nature of the SEI is warranted. The SEI can be viewed as having two layers where the outer layer is porous and has significant organic content and the inner denser layer is considered to have significant inorganic content. Notably, two differing mechanisms have been proposed for ion migration through the layers where lithium ions diffuse via pore diffusion through the outer layer and a knock-off mechanism through the inner dense layer.[20-21] Thus, migration of the charged vanadium species through the SEI may take place under two regimes. The vanadium ions more readily diffuse through the more porous outer SEI layer, yet diffuse slowly through the inner layer. In the case of the anodes from the $Ag_2VO_2PO_4$ cells, low levels of charged

vanadium are detectable across the surface of the anode consistent with the migration of the species through the electrolyte and into the porous layer of the SEI. There are some localized areas where the vanadium is fully reduced to vanadium metal indicating that the vanadium species migrated successfully through the inner SEI on a limited basis to reach the lithium surface and are reduced to vanadium metal. This is schematically depicted in Figure 4.

The anodes from the $Ag_2V_4O_{11}$ cells show an average oxidation state from the XANES data between vanadium(0) and vanadium(III) for the entire surface. In the case of the anode from the $Ag_2V_4O_{11}$ cell where significant amounts of vanadium are in solution, much of the vanadium found on the anode surface has not fully migrated through the SEI and reduced to vanadium metal, but has heavily loaded the porous outer layer of the SEI. The inner layer would also be expected to contain some vanadium in more limited amounts. It is reasonable to project that the presence of these positively charged vanadium species in the SEI may inhibit facile movement of the positively charged lithium ions. This supports the strong correlation of the poor pulse discharge results with the level of vanadium on the surface as observed with the $Ag_2V_4O_{11}$ cell discharged to 3 electron equivalents. The results also provide insight into the kinetic behavior of the various steps in the process. The data imply that vanadium dissolution and migration to the anode is a relatively fast process as is the migration of the vanadium cations into the outer layer of the SEI when compared to the slower migration of the charged vanadium ions through the dense inner layer of the SEI.

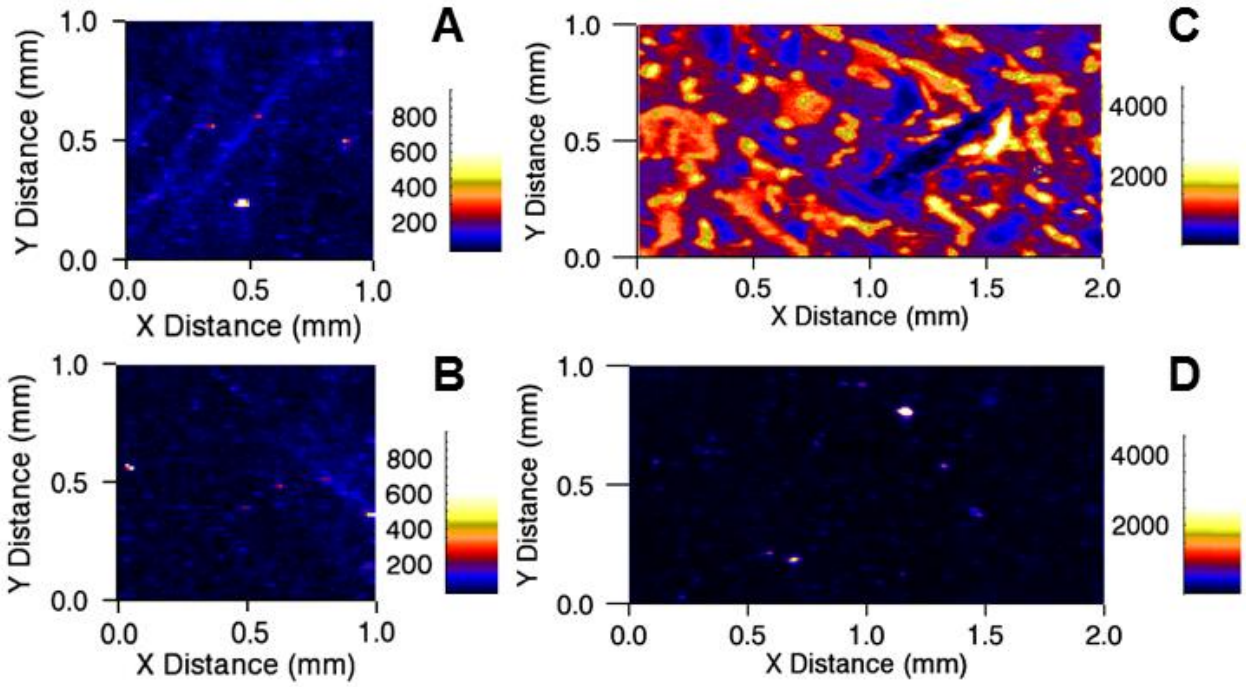


**Figure 2.** Vanadium elemental maps of anodes from **A.** $Li/Ag_2V_4O_{11}$ cell discharged to 2 electron equivalents. **B.** $Li/Ag_2VO_2PO_4$ cell discharged to 2 electron equivalents. **C.** $Li/Ag_2V_4O_{11}$ cell discharged to 3 electron equivalents. **D.** $Li/Ag_2VO_2PO_4$ cell discharged to 3 electron equivalents.

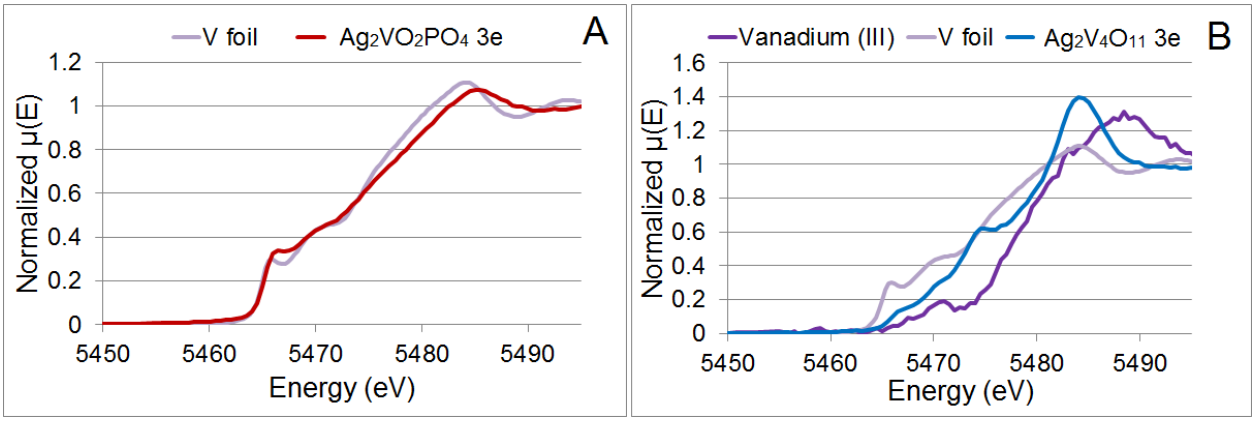


**Figure 3A.** XANES spectra from lithium surface of $Ag_2VO_2PO_4$ 3 electron equivalent cell at a region of high intensity, overlaid with the vanadium foil ($V^0$) standard. **B.** XANES spectra from lithium surface of $Ag_2V_4O_{11}$ 3 electron equivalent cell overlaid with vanadium (III) ion ($V^{3+}$) and vanadium foil ($V^0$) standards.

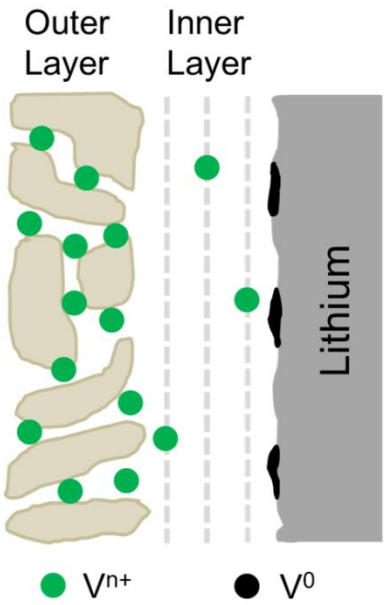


**Figure 4.** Schematic of lithium anode surface including solid electrolyte interphase (SEI) indicating location of positively charged vanadium ions, $V^{n+}$, and vanadium metal, $V^0$.

5.3.5 Quantitative analysis of anodes

Subsequent to the X-ray microfluorescence (XRμF) experiment, lithium anodes recovered from the cells were digested and quantitatively analyzed by ICP-OES to determine the levels of silver and vanadium present. Figures 5A and 5B show the results of the ICP-OES analysis for silver and vanadium, respectively. Silver and vanadium dissolution from $Ag_2V_4O_{11}$ and $Ag_2VO_2PO_4$ materials in electrolyte solutions have been previously quantified for the unreduced materials.[19, 22]

The concentration of silver deposited onto the anode surfaces ranged from 2.7 to 6.5 μg/cm$^2$. The anodes recovered from the $Ag_2VO_2PO_4$ cells showed slightly higher amounts of silver than those from the $Ag_2V_4O_{11}$ cells after 2 electrons of reduction. After 3 electrons, the trend reversed where the anodes from the $Ag_2V_4O_{11}$ cells showed slightly higher levels of silver, however, in both cases the differences are relatively small. Analysis of the vanadium deposited onto the lithium anodes by ICP-OES indicated similar levels of deposition for the 2 and 3 electron equivalent reduced $Ag_2VO_2PO_4$ cells and the 2 electron equivalent reduced $Ag_2V_4O_{11}$ cells where the values ranged from 0.3 to 1.2 μg/cm$^2$. In contrast, anodes from the $Ag_2V_4O_{11}$ cells discharged to 3 electron equivalents exhibited a higher level of vanadium deposition, where individual anodes had vanadium surface concentrations of 3.3 and 3.4 μg/cm$^2$, higher by a factor of ≥3X. It is notable that the levels of silver deposition onto the anode surface are higher than that of vanadium consistent with previous reports of dissolution from the non-discharged materials where silver dissolution levels through 3-weeks was approximately 2X and 7X that of vanadium for $Ag_2V_4O_{11}$ and $Ag_2VO_2PO_4$, respectively.

Higher levels of vanadium dissolution are observed for the Li/$Ag_2V_4O_{11}$ cells discharged to 3 electron equivalents. At this depth of discharge, multiple vanadium oxidation states of V,

IV, and III may be present.[2, 4] Limited literature exists regarding the influence of vanadium oxidation state on solubility.[23] In aqueous solution, V(V) forms oxyanions such as $H_nVO_4^{n-3}$, V(IV) is primarily present as vanadyl, $VO^{2+}$, while V(III) forms vanadium hydroxide, $V(OH)_3$.[24] The highly ionic V(IV) and V(V) species are reported to be more soluble than V(III) in aqueous media.[24] Since solubility is a function of both lattice energy and solvation energy, it can be proposed that in aqueous solution, the hydration energies associated with higher oxidation states of vanadium can overcome the associated lattice energies, resulting in enhanced dissolution of higher oxidations states of vanadium. Conversely, in non-aqueous solutions where the polarity of the solvent is reduced, the solvation energies are expected to be much lower than the corresponding lattice energies for high oxidation states of vanadium. However, for V(III), the solvation energy may be able to compete with the reduced lattice energy, resulting in increased dissolution for V(III) relative to V(V) in nonaqueous solution. Thus, in nonaqueous electrolyte, dissolution may become more favorable for discharged $Ag_2V_4O_{11}$ oxide material reduced by 3 electron equivalents which contains V(III) metal centers. Notably, the low vanadium oxidation state of the discharged $Ag_2VO_2PO_4$ material reduced by 3 electron equivalents does not result in significantly higher solubility, consistent with our hypothesis that the strong covalent P-O bonds from the inclusion of $PO_4^{3-}$ polyanions would stabilize the vanadium oxide framework regardless of vanadium oxidation state.

To further elucidate the role of vanadium and silver on the surface of a lithium anode, lithium anodes were surface treated by immersion in silver ion and vanadium ion containing solutions. Post treatment, the anodes were used for impedance studies which revealed that silver treatment of the anode does not increase the impedance of the system while the vanadium treated samples displayed higher impedance, Figure 6. The equivalent circuit analysis yielded $R_{total}$

values of 570, 487, and 1538 Ω for the untreated, silver-treated, and vanadium-treated anodes, respectively. Increased cell resistance with accompanying voltage drop under pulse for the vanadium treated anodes has been previously discussed in Chapter 2. Here we focus on vanadium deposition on the anode where the impedance was demonstrated to change, in contrast to the silver deposition which does not contribute to increased cell resistance.[19] These results highlight the complex nature of the SEI where composition is critical to the resultant impedance of the electrode.

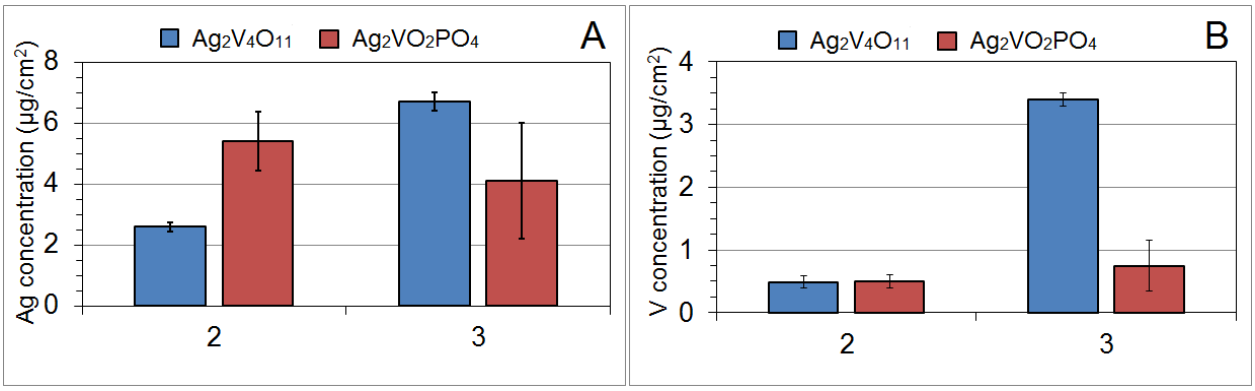


**Figure 5.** Quantitative analysis of lithium anodes recovered from $Ag_2V_4O_{11}$ and $Ag_2VO_2PO_4$ cathode cells discharged to 2 and 3 electron equivalents for **A.** silver (Ag), and **B.** vanadium (V).

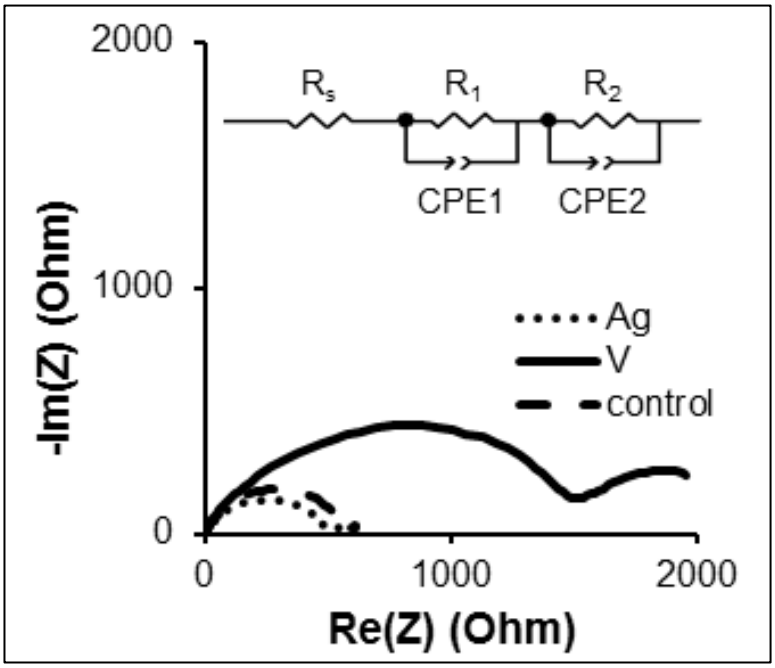


**Figure 6.** AC impedance results plotted in Nyquist format for lithium/lithium cells showing untreated, silver (Ag) treated and vanadium (V) treated samples. Inset shows equivalent circuit used for analysis.

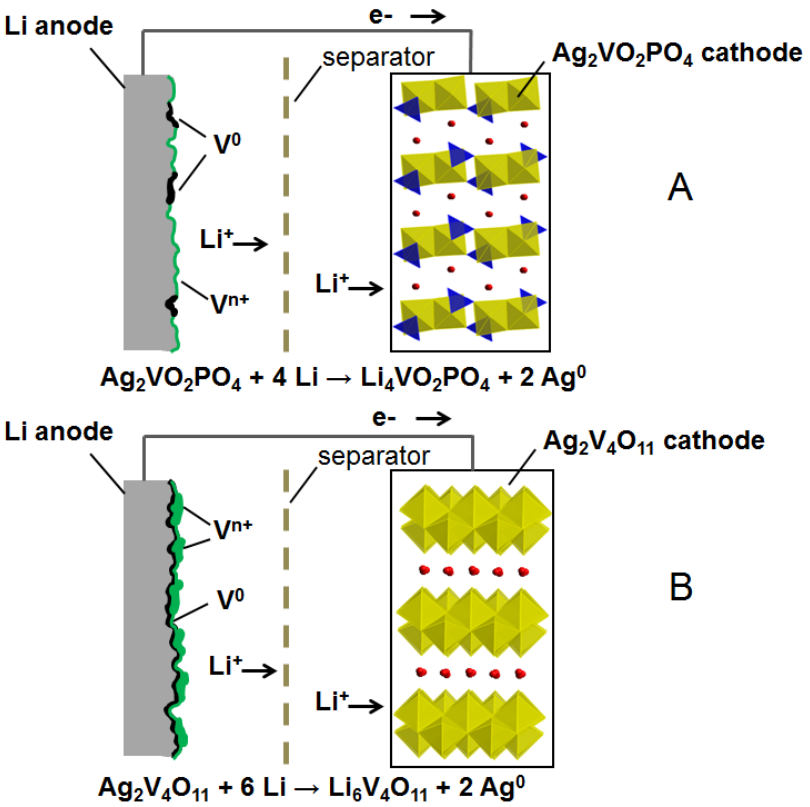


**Figure 7.** Schematic cell representations of indicating deposition of vanadium species on the anode surfaces for **A.** lithium/silver vanadium phosphorous oxide ($Li/Ag_2VO_2PO_4$) cell, and **B.** lithium/silver vanadium oxide ($Li/Ag_2V_4O_{11}$) cell.

## 5.4 Summary

Based on the data, a conceptual model for the interaction of the charged vanadium species and the SEI at the anode of lithium/silver vanadium oxide and lithium/silver vanadium phosphorous oxide batteries is proposed. The soluble vanadium ions migrate through the electrolyte and penetrate the pores of the outer layer of the SEI where the vanadium ions maintain a positive charge. More slowly, some vanadium ions reach the lithium surface with some reduced to vanadium metal. There is a strong correlation with the observed increase in battery resistance and the presence of vanadium on the surfaces of the anodes and vanadium cations in the SEI layer. It is reasonable to project that: (1) the presence of metallic vanadium on the lithium anode surface would significantly reduce usable current, and (2) vanadium cations within the SEI may inhibit facile movement of the positively charged lithium ions. These findings shed light on the nature and composition of the anode solid electrolyte interphase (SEI) and further highlight its importance in understanding and predicting decreases in battery performance. Further, the findings indicate significant differences for the anode surfaces recovered from the $Ag_2V_4O_{11}$ and $Ag_2VO_2PO_4$ cell types, and are conceptually summarized in Figure 7. The results clearly support that $Ag_2VO_2PO_4$ cathode material provides the opportunity for future development of ICD batteries with improved charge time stability under long term use. Finally, the strategy presented for analysis of anodes from the $Ag_2V_4O_{11}$ and $Ag_2VO_2PO_4$ cell systems could be extended to systems with cathodes of other metallic compositions; thus by analogy we propose a new paradigm for probing a critical long term failure mode for a number of battery systems.

## 5.5 References


(1) Root, M. J., Resistance Model for Lithium-Silver Vanadium Oxide Cells. *J. Electrochem. Soc.* **2011,** 158, A1347-A1353.

(2) Leising, R. A.; Thiebolt, W. C., III; Takeuchi, E. S., Solid-State Characterization of Reduced Silver Vanadium Oxide from the Li/SVO Discharge Reaction. *Inorg. Chem.* **1994,** 33, 5733-40.

(3) Takeuchi, E. S.; Thiebolt, W. C., III, The reduction of silver vanadium oxide in lithium/silver vanadium oxide cells. *J. Electrochem. Soc.* **1988,** 135, 2691-4.

(4) Leifer, N. D.; Colon, A.; Martocci, K.; Greenbaum, S. G.; Alamgir, F. M.; Reddy, T. B.; Gleason, N. R.; Leising, R. A.; Takeuchi, E. S., Nuclear Magnetic Resonance and X-Ray Absorption Spectroscopic Studies of Lithium Insertion in Silver Vanadium Oxide Cathodes. *J. Electrochem. Soc.* **2007,** 154, A500-A506.

(5) Marschilok, A. C.; Kozarsky, E. S.; Tanzil, K.; Zhu, S.; Takeuchi, K. J.; Takeuchi, E. S., Electrochemical reduction of silver vanadium phosphorous oxide, Ag2VO2PO4: Silver metal deposition and associated increase in electrical conductivity. *J. Power Sources* **2010,** 195, 6839-6846.

(6) Patridge, C. J.; Jaye, C.; Abtew, T. A.; Ravel, B.; Fischer, D. A.; Marschilok, A. C.; Zhang, P.; Takeuchi, K. J.; Takeuchi, E. S.; Banerjee, S., An X-ray Absorption Spectroscopy Study of the Cathodic Discharge of Ag2VO2PO4: Geometric and Electronic Structure Characterization of Intermediate phases and Mechanistic Insights. *J. Phys. Chem. C* **2011,** 115, 14437-14447.

(7) Yang, L.; Takahashi, M.; Wang, B., A study on capacity fading of lithium-ion battery with manganese spinel positive electrode during cycling. *Electrochim. Acta* **2006,** 51, 3228-3234.

(8) Ochida, M.; Domi, Y.; Doi, T.; Tsubouchi, S.; Nakagawa, H.; Yamanaka, T.; Abe, T.; Ogumi, Z., Influence of manganese dissolution on the degradation of surface films on edge plane graphite negative-electrodes in lithium-ion batteries. *J. Electrochem. Soc.* **2012,** 159, A961-A966.

(9) Delacourt, C.; Kwong, A.; Liu, X.; Qiao, R.; Yang, W. L.; Lu, P.; Harris, S. J.; Srinivasan, V., Effect of manganese contamination on the solid-electrolyte-interphase properties in Li-ion batteries. *J. Electrochem. Soc.* **2013,** 160, A1099-A1107.

(10) Zhan, C.; Lu, J.; Kropf, A. J.; Wu, T.; Jansen, A. N.; Sun, Y.-K.; Qiu, X.; Amine, K., Mn(II) deposition on anodes and its effects on capacity fade in spinel lithium manganate-carbon systems. *Nat. Commun.* **2013,** 4, 3437, 8 pp.

(11) Gowda, S. R.; Gallagher, K. G.; Croy, J. R.; Bettge, M.; Thackeray, M. M.; Balasubramanian, M., Oxidation state of cross-over manganese species on the graphite electrode of lithium-ion cells. *Phys. Chem. Chem. Phys.* **2014,** 16, 6898-6902.

(12) Kang, H. Y.; Wang, S. L.; Tsai, P. P.; Lii, K. H., Hydrothermal synthesis, crystal structure and ionic conductivity of silver vanadium oxide phosphate, Ag2VO2PO4: a new layered phosphate of vanadium(V). *J. Chem. Soc., Dalton Trans.* **1993**, 1525-8.

(13) Leising, R. A.; Takeuchi, E. S., Solid-state cathode materials for lithium batteries: effect of synthesis temperature on the physical and electrochemical properties of silver vanadium oxide. *Chem. Mater.* **1993,** 5, 738-42.

(14) Ablett, J. M.; Kao, C. C.; Reeder, R. J.; Tang, Y.; Lanzirotti, A., X27A-A new hard X-ray micro-spectroscopy facility at the National Synchrotron Light Source. *Nucl. Instrum. Methods Phys. Res., Sect. A* **2006,** 562, 487-494.

(15) Ravel, B.; Newville, M., ATHENA, ARTEMIS, HEPHAESTUS: data analysis for x-ray absorption spectroscopy using IFEFFIT. *J. Synchrotron Radiat.* **2005,** 12, 537-541.

(16) Takeuchi, E. S.; Marschilok, A. C.; Tanzil, K.; Kozarsky, E. S.; Zhu, S.; Takeuchi, K. J., Electrochemical Reduction of Silver Vanadium Phosphorus Oxide, Ag2VO2PO4: The Formation of Electrically Conductive Metallic Silver Nanoparticles. *Chem. Mater.* **2009,** 21, 4934-4939.

(17) Kirshenbaum, K. C.; Bock, D. C.; Zhong, Z.; Marschilok, A. C.; Takeuchi, K. J.; Takeuchi, E. S., In situ profiling of lithium/Ag2VP2O8 primary batteries using energy dispersive X-ray diffraction. *Phys. Chem. Chem. Phys.* **2014,** 16, 9138-9147.

(18) Gireaud, L.; Grugeon, S.; Laruelle, S.; Yrieix, B.; Tarascon, J. M., Lithium metal stripping/plating mechanisms studies: A metallurgical approach. *Electrochem. Commun.* **2006,** 8, 1639-1649.

(19) Bock, D. C.; Marschilok, A. C.; Takeuchi, K. J.; Takeuchi, E. S., A kinetics and equilibrium study of vanadium dissolution from vanadium oxides and phosphates in battery electrolytes: Possible impacts on ICD battery performance. *J. Power Sources* **2013,** 231, 219-235.

(20) Shi, S.; Lu, P.; Liu, Z.; Qi, Y.; Hector, L. G.; Li, H.; Harris, S. J., Direct Calculation of Li-Ion Transport in the Solid Electrolyte Interphase. *J. Am. Chem. Soc.* **2012,** 134, 15476-15487.

(21) Lu, P.; Li, C.; Schneider, E. W.; Harris, S. J., Chemistry, Impedance, and Morphology Evolution in Solid Electrolyte Interphase Films during Formation in Lithium Ion Batteries. *J. Phys. Chem. C* **2014,** 118, 896-903.

(22) Bock, D. C.; Takeuchi, K. J.; Marschilok, A. C.; Takeuchi, E. S., Silver vanadium oxide and silver vanadium phosphorous oxide dissolution kinetics: a mechanistic study with possible impact on future ICD battery lifetimes. *Dalton Trans.* **2013,** 42, 13981-13989.

(23) Crans, D. C., Fifteen years of dancing with vanadium. *Pure Appl. Chem.* **2005,** 77, 1497-1527.

(24) Wanty, R. B.; Goldhaber, M. B., Thermodynamics and kinetics of reactions involving vanadium in natural systems: accumulation of vanadium in sedimentary rocks. *Geochim. Cosmochim. Acta* **1992,** 56, 1471-83.

# Chapter 6

## Advanced measurement techniques for investigation of $Ag_wV_xP_yO_z$ cathode materials – *In-situ* profiling of lithium/$Ag_2VP_2O_8$ batteries using energy dispersive X-ray diffraction (EDXRD) and nanoprobe conductivity measurements of discharged $Ag_2VO_2PO_4$ single particles

Reproduced in part from [Kirshenbaum, K. C.; Bock, D. C.; Zhong, Z.; Marschilok, A. C.; Takeuchi, K. J.; Takeuchi, E. S., In situ profiling of lithium/Ag2VP2O8 primary batteries using energy dispersive X-ray diffraction. *Phys. Chem. Chem. Phys.* **2014**, 16, 9138-9147] and [Kirshenbaum, K. C.; Bock, D. C.; Brady, A. B.; Marschilok, A. C.; Takeuchi, K. J.; Takeuchi, E. S., Electrochemical reduction of an Ag2VO2PO4 particle: dramatic increase of local electronic conductivity. *Phys. Chem. Chem. Phys.* **2015**, 17, 11204-11210] with permission from PCCP Owner Societies.

Further work published in [Kirshenbaum, K.; Bock, D. C.; Lee, C.-Y.; Zhong, Z.; Takeuchi, K. J.; Marschilok, A. C.; Takeuchi, E. S., In situ visualization of Li/Ag2VP2O8 batteries revealing rate-dependent discharge mechanism. *Science* **2015,** 347, 149-154].

### 6.1 Introduction

The stability of the cathode material in the electrolyte, detailed in previous chapters, is an important property which needs to be considered when selecting the appropriate cathode material for a primary battery application. Nevertheless, other properties of the cathode, including capacity and rate capability, are significant in defining performance. For the next generation of battery materials, the ability to access all of the capacity in an electrode is particularly important.[1] Currently, commercial battery systems utilize composite electrodes containing conductive additives to improve electrical contact between different regions of the electrode. These composites are typically prepared by mixing the active material, a conductive additive, and a polymer binder in a suitable solvent to create a slurry, which is then cast onto a metal foil

and dried. While this physical mixing technique is generally effective in improving rate capability and increasing realized capacity, it is an imperfect approach for several reasons. Aggregation of active material can cause incomplete dispersion[2-3], and when combined with poor electrical contact between particles, incomplete electron access to all regions of the electrode prevents full energy utilization. Furthermore, the conductive additives do not add to the capacity of the battery, reducing energy density.

Because traditional composite electrodes are not optimized for complete energy extraction, other approaches need to be developed which approximate an ideal electrode in which each individual active material particle is electrically connected to the current collector. One such method for creating sufficient electrical contacts between all active material particles is to generate an in-situ conductive network in the electrode. In previous studies, [4-8] it was demonstrated that upon discharging silver vanadium phosphorous oxide cathodes, Ag metal is reduced and migrates to the surfaces of the active material particles, forming a 3-dimensional conductive matrix. The formation of metallic nanoparticles which coat the active material particle surfaces allows for individual particles to be electrically connected. As a result of in-situ Ag network formation, the conductivity of the material increases by 15000 fold.[4]

This chapter details advanced measurement techniques that were used to gain insight into the details of Ag metal network formation and associated increase in conductivity in electrochemically reduced $Ag_wV_xP_yO_z$ cathode materials. The first of these techniques was *in situ* energy dispersive X-ray spectroscopy (EDXRD). EDXRD measurements were conducted on lithium primary cells having the cathode material $Ag_2VP_2O_8$. $Ag_2VP_2O_8$ can incorporate 3 electron equivalents into its structure upon reduction, with $Ag^+$ reducing to silver metal and $V^{4+}$ reducing to $V^{3+}$. Because $Ag^0$ strongly scatters electrons, the $Li/Ag_2VP_2O_8$ system is appropriate

for analysis by this technique.[9] The spatial resolution of electrochemical cells with partially discharged $Ag_2VP_2O_8$ cathodes was measured in situ to give an accurate picture of how the reduction process occurs in this silver vanadium phosphorous oxide cathode material. This work was done in collaboration with Kevin C. Kirshenbaum. My contributions included preparation of the cathode material, preparation of the electrochemical cells, assistance in collecting the impedance and EDXRD measurements, and analysis of the recovered Li anodes.

Although EDXRD is an excellent technique for probing the formation of silver metal in a discharged bulk SVPO electrode, additional techniques were needed to provide information at the particle level. Thus, to further interrogate the increase in conductivity which occurs in silver vanadium phosphorous oxide materials upon discharge, individual particles of $Ag_2VO_2PO_4$ were electrochemically reduced and measured for changes in conductivity using a nanoprobe system. $Ag_2VO_2PO_4$ was selected for this type of analysis because hydrothermal synthesis of the material produces blade like particles which are large enough to be discharged individually. Post discharge, the resistance at different locations within the particles was measured. The nanoprobe technique allowed for local resistance changes as a function of particle reduction to be evaluated, furthering understanding of the discharge mechanism and its relationship with material conductivity. This work was done in collaboration with Kevin C. Kirshenbaum and Alexander S. Brady. Alexander and I both prepared samples, Kevin developed the discharge methodology and I assisted in the measurement of the material after discharge.

## 6.2 Experimental

6.2.1 – *In-situ* Energy Dispersive X-ray Diffraction (EDXRD) measurements of Li/$Ag_2VP_2O_8$ coin cells

$Ag_2VP_2O_8$ was prepared via a solid-state reaction previously reported in the literature.[10] X-ray diffraction of the synthesized material matched the reference pattern (PDF #01-088-0436) with no impurity phases present. Coin cell type electrochemical cells with stainless steel housings were constructed with lithium anodes and $Ag_2VP_2O_8$ cathodes. 1M $LiPF_6$ in 30:70 ethylene carbonate: dimethyl carbonate was used as the electrolyte. The cells were discharged to 0, 0.1, and 0.5 electron equivalents to determine how the formation of the conductive network proceeded within the initial stages of discharge. Electrochemical impedance spectroscopy was measured before and after discharge of the cells using a frequency range of 0.5 mHz to 100 kHz with a 5 mA amplitude. EIS measurements were also collected after EDXRD measurements to verify that the X-ray beam did not affect the status of the cells; there was not a discernable difference in EIS response of the cells after the EDXRD measurements.

Energy dispersive X-ray diffraction (EDXRD) measurements were performed at beamline X17B1 at the National Synchrotron Light Source at Brookhaven National Laboratory. At this beamline, radiation with a spectrum up to 200 keV in energy is produced by a wiggler, and lower energies of the radiation are subsequently filtered out by a Cu foil. Standards of $CeO_2$ and $LaB_6$ were used to calibrate the detector. Before measuring the coin cells using the experimental setup, measurements were taken on both non-discharged $Ag_2VP_2O_8$ powder and coin cell parts in order determine their diffraction patterns. Good agreement in the peak positions of the measured materials with reference patterns was observed. However, intensities

in the diffraction patterns measured by EDXRD are different than the intensities in the diffraction patterns collected by angle resolved XRD. This is because unlike angle-resolved masurements which use X-rays of a constant energy, the intensity profile of the X-rays coming from the wiggler beam changes with energy. The signal is also attenuated by potions of the cell outside of the measured gauge volume and the Cu filter foil.

The experimental setup used to collect in situ EDXRD measurements on Li/$Ag_2VP_2O_8$ coin cells is illustrated in Figure 1. The parallel incident beam impinged upon the sample was 20 μm in height, and the germanium detector used to measure the diffracted radiation was set at $2\theta = 3.05°$. The slit size for the detector was set such that the length of the y-direction from which diffracted X-rays were collected was ~2.0 mm. In the x-direction, the width of the incident beam was 2.0 mm, making the dimensions of the gauge volume approximately 2.0 x 2.0 x 0.02 mm. The coin cell to be measured was placed on an automated stage that could be moved in the z-direction. Thus, diffraction patterns were collected as a function of z, and a spatial profile for each cell was collected.

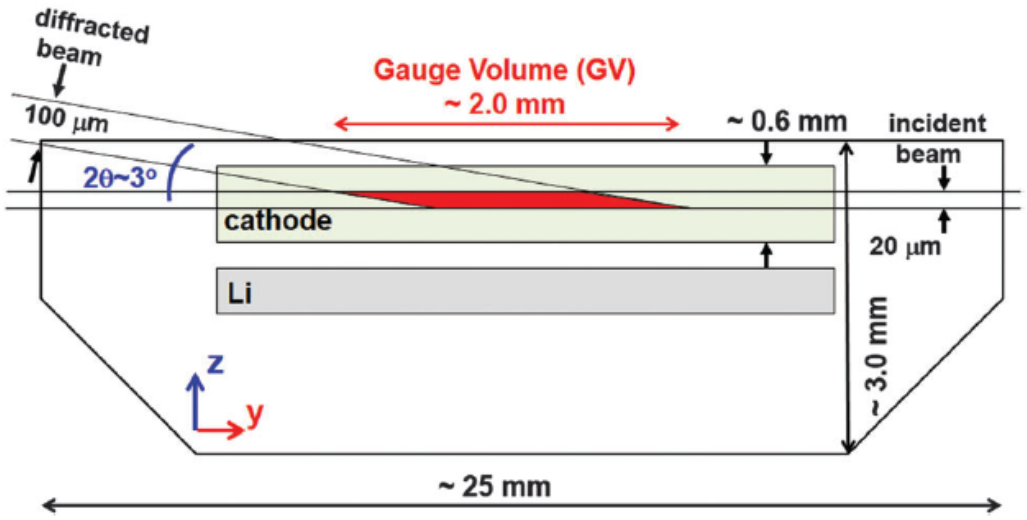


**Figure 1.** Experimental setup used to collect in situ EDXRD measurements on Li/ $Ag_2VP_2O_8$ coin cells.

6.2.2 Electrochemical Reduction of $Ag_2VO_2PO_4$ single particles and nanoprobe conductivity measurement

$AgVO_2PO_4$ was synthesized using a previously reported hydrothermal method.[11] Along with some smaller particles, the synthesis yields millimeter sized individual particles which can be isolated by hand. These particles form blade like shapes approximately 1 to 2 mm in length, 0.1 to 0.2 mm wide, and with a thickness between 0.05 and 0.15 mm. X-ray diffraction of the synthesized material matched the reference pattern (PDF #97-007-380) with no impurity phases present.

The individual particles were used to construct working electrodes using two techniques. For both methods, reproducible working electrode particles were individually selected for size and uniformity using an optical microscope in conjunction with a stage micrometer. The crystals were attached to Pt wire using conductive Au paste which was then covered in Torr Seal epoxy. Alternatively, the crystals were attached to steel wire using conductive carbon paste.

The fabricated working electrodes were used in a three-electrode configuration, with lithium metal attached to wire used as both counter and reference electrodes. The electrodes were placed in a shallow dish under an optical microscope and then submerged in a carbonate electrolyte (1M $LiPF_6$ in propylene carbonate). A CH1140A single channel potentiostat was used for electrochemical testing. The capacity of the particles was estimated from the particle dimensions and ranged from 10 to 100 μA h. The current used to discharge the particles was 0.1 and 10 μA depending on the particle size and desired rate. All discharge experiments were performed in a controlled humidity dry room to prevent passivation of the lithium electrodes.

Conductivity measurements of the individual particles were obtained using an Omnicron Nanotechnologies nanoprobe system at the Center for Functional Nanomaterials at Brookhaven

National Laboratory. To perform the measurement, particles were affixed to a graphite substrate by applying epoxy at each end of the particle. SEM imaging was used to adjust the placement of the Pt-W STM tips such that the tips were pressed into the surface of the particle. Conductance was then measured using a Keithley model 4200 semiconductor characterization system.

### 6.3 Results and Discussion

6.3.1 *In-situ* Energy Dispersive X-ray Diffraction (EDXRD) measurements of $Li/Ag_2VP_2O_8$ coin cells

$Li/Ag_2VP_2O_8$ coin cells were discharged to 0, 0.1, and 0.5 electron equivalents and were characterized by electrochemical impedance spectroscopy prior to the EDXRD measurements (Figure 2). The collected EIS data was fit to an equivalent circuit model, allowing for a quantitative comparison of the resistor-capacitor elements to be made. The model is a modified version of the Randles circuit with Voight-type RC elements in series[12-13] and was used for both unreduced and partially discharged cells. In this model, the two Voight-type RC elements accurately fit the two semicircles seen in the impedance measurement and are tabulated in Table 1. The first resistor ($R_s$) is attributed to series resistance, the first parallel resistor-capacitor circuit component ($R_m$, $C_{dl,1}$) is attributed to the anode, and the second resistor ($R_{ct}$) and Warburg element ($Z_w$) in parallel with capacitor ($C_{dl,2}$) circuit component is attributed to the cathode. While the values of most circuit elements do not change with electrochemical reduction, the resistance associated with the cathode ($R_{ct}$) decreased dramatically, from 1 MΩ for the non-discharged cell to 1500 Ω and 500 Ω for the 0.1 and 0.5 electron equivalent cells, respectively. The ~700 times reduction in the resistance in the cathode was believed to be due to formation of $Ag^0$ during the discharge process. This assignment for $R_{ct}$ resistance is consistent with prior

studies in which the $R_{ct}$ resistance was assigned to the charge transfer layer in both porous[14-15] and non-porous[16-17] electrodes. This data was considered in conjunction with the EDXRD measurements to determine if the dramatic decrease in resistance was associated with Ag formation in the cathode.

EDXRD data was collected for the three cells with discharged levels of 0, 0.1, and 0.5 electron equivalents. Because measurements were taken at varying z-positions, the collected diffraction patterns could be viewed as a function of height. Patterns were collected every 20 μm, corresponding to the height of the gauge volume. A plot showing the intensity of the various diffraction peaks, with peak position on the x-axis, and the varying z position on the y-axis, is shown in Figure 3 for the Li/$Ag_2VP_2O_8$ cell discharged to 0.5 electron equivalents. Intensity is plotted on a logarithmic scale, with white points corresponding to high intensity and black corresponding to low intensity. The lower portion of the figure corresponds to the data collected from the Li anode, the middle section corresponds to the $Ag_2VP_2O_8$ cathode, and the top portion corresponds to the stainless steel can. Positions of peaks for Li, stainless steel, and Ag are labeled in the figure. Of particular significance is that existence of $Ag^0$ metal in the cell was monitored by tracking the intensity of the Ag(111) peak, positioned at 1/d = 0.4239 Å.

The intensity of the Ag(111) peak, the intensity of the Li(110) peak, and the average intensity of three $Ag_2VP_2O_8$ peaks (1/d = 0.5130, 0.5303, and 0.5506) as a function of the z-position is plotted in figure 4 for the (a) 0, (b) 0.1, and (c) 0.5 discharged cells. In all three cells, the presence of Ag is detected in the region of cathode side facing the lithium anode, with the lowest intensity in the non-discharged cell and the highest intensity in the 0.5 electron equivalent cell. Because it was unexpected that $Ag^0$ would be present in the non-discharged cell, two additional coin cells were constructed and allowed to rest at open circuit potential for 10 days

before disassembly. Ex situ XRD analysis of the cathodes did not indicate the presence of $Ag^0$. However, the Li anodes showed a dark surface film, and ICP-OES of the anodes confirmed that silver was present on the anode surface. This result is consistent with the experiments presented in chapter 5, which indicated that high levels of Ag dissolved from non-discharged $Ag_2VP_2O_8$ material. The amount of silver found to be present on the anodes recovered from the non-discharged cells would form a layer of $Ag^0$ that was 0.1 μm thick if uniformly distributed over the surface. Thus, it is possible that the $Ag^0$ detected by EDXRD at the anode facing side of the cathode in the non-discharged cell is due to dissolution from the cathode material and subsequent reduction on the Li metal surface to from $Ag^0$. The breadth of the $Ag^0$ peak into the cathode region is likely due to cell tilt when the measurement was taken. Although the cells were manually leveled prior to measurement, even a small tilt of 2° would create a 70 micron difference between two sides of the gauge volume, in effect causing broadened signals that would blur the boundary between the different regions of the cell. For the two cells that were partially discharged, higher intensities of silver are observed at the cathode/anode interface compared to the non-discharged cell. The higher intensity is likely due to a combination of dissolved $Ag^0$ deposited on the lithium surface, as well as $Ag^0$ formed through reduction of the $Ag_2VP_2O_8$ cathode material.

In the 0.1 electron equivalent partially discharged cell, $Ag^0$ metal is also visible on the side of the cathode facing the steel current collector. At the same time, in the region where $Ag^0$ is present, there is a decrease in the intensity of the $Ag_2VP_2O_8$ peaks, which is consistent with the reduction of $Ag_2VP_2O_8$ and formation of $Ag^0$ metal. It is noteworthy that in the 0.1 electron equivalent discharged cell, $Ag^0$ is only observed in the cathode regions closest to the stainless steel current collector and to the lithium anode. In contrast, in the 0.5 electron equivalent

discharged cell, $Ag^0$ begins to be detectable throughout the cathode. This observation is significant because it indicates that reduction occurs at the cathode material nearest the current collector before the occurring throughout the bulk of cathode. The observed non-uniform discharge is likely due to the poor electrical conductivity of the material which makes the availability of electrons a limiting factor in the discharge. Thus, initial reduction of $Ag_2VP_2O_8$ occurs mostly in the region closest to the electron source at the current collector. As conductive $Ag^0$ begins to form upon reduction, more regions of the electrode have access to electrons, and by 0.5 electron equivalents, the formation of a $Ag^0$ network allows for the bulk of the cathode to be reduced.

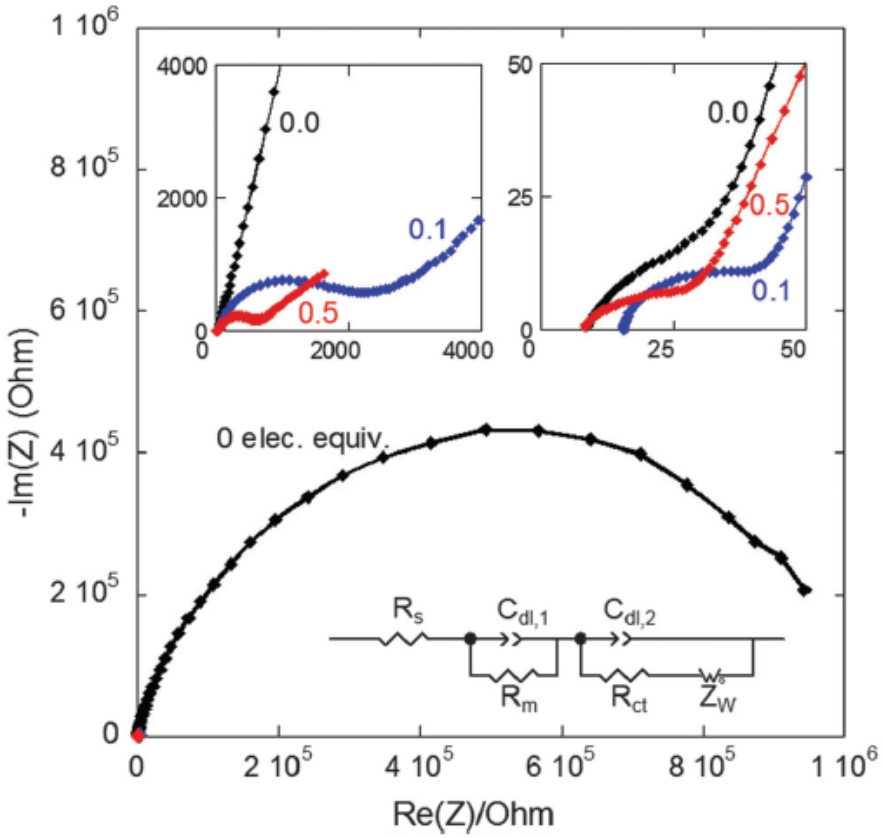


**Figure 2.** Electrochemical impedance spectroscopy measurements of Li/$Ag_2VP_2O_8$ cells reduced by 0, 0.1 and 0.5 electron equivalents. The upper inserts indicate magnified low resistance portions of the main spectra. The lower inserts show the equivalent circuit model used to fit the data.

| DOD (elec. equiv.) | 0 | 0.1 | 0.5 |
|---|---|---|---|
| $X^2$ (Z-View Fit) | 0.0005007 | 0.0001179 | 0.0000434 |
| $R_s$ (Ω) | 8.30 ± 0.10 | 14.63 ± 0.06 | 6.90 ± 0.04 |
| $C_{dl,1}$ (F) | (3.07 ± 0.28) x$10^{-5}$ | (3.19 ± 0.13) x$10^{-5}$ | (3.07 ± 0.10) x$10^{-4}$ |
| $C_{dl,1\ power}$ | 0.706 ± 0.009 | 0.713 ± 0.004 | 0.493 ± 0.003 |
| $R_m$ (Ω) | 27.22 ± 0.42 | 30.05 ± 0.19 | 28.20 ± 0.18 |
| $C_{dl,2}$ (F) | (3.587 ± 0.007) x$10^{-5}$ | (1.625 ± 0.010) x$10^{-4}$ | (4.237 ± 0.016) x$10^{-4}$ |
| $C_{dl,2\ power}$ | 0.851 ± 0.001 | 0.869 ± 0.002 | 0.855 ± 0.001 |
| $R_{ct}$ (Ω) | 1058300 ± 5420 | 1448 ± 29 | 508 ± 2 |
| $Z_{w,R}$ (Ω) | 4100 | 4266 ± 152 | 4140 ± 154 |
| $Z_{w,T}$ (Ω) | 2000 | 1174 ± 94 | 3663 ± 341 |
| $Z_{w,P}$ | 0.35 | 0.281 ± 0.008 | 0.439 ± 0.002 |

**Table 1.** Fit parameters for ACI circuit elements of Li/$Ag_2VP_2O_8$ cells at various states of electrochemical reduction.

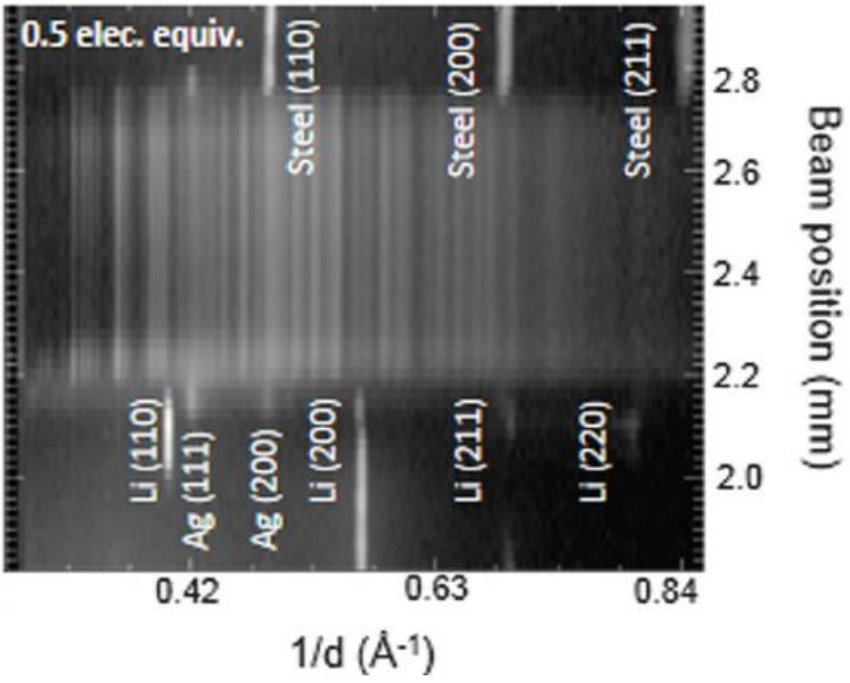


**Figure 3**. An intensity contour plot of EDXRD spectra collected on the Li/$Ag_2VP_2O_8$ cell discharged to 0.5 electron equivalents. The x-axis is the diffraction peak position and the y-axis is the z position of the incident X-ray beam. Whiter points indicate higher diffraction intensity while darker areas represent lower intensity.

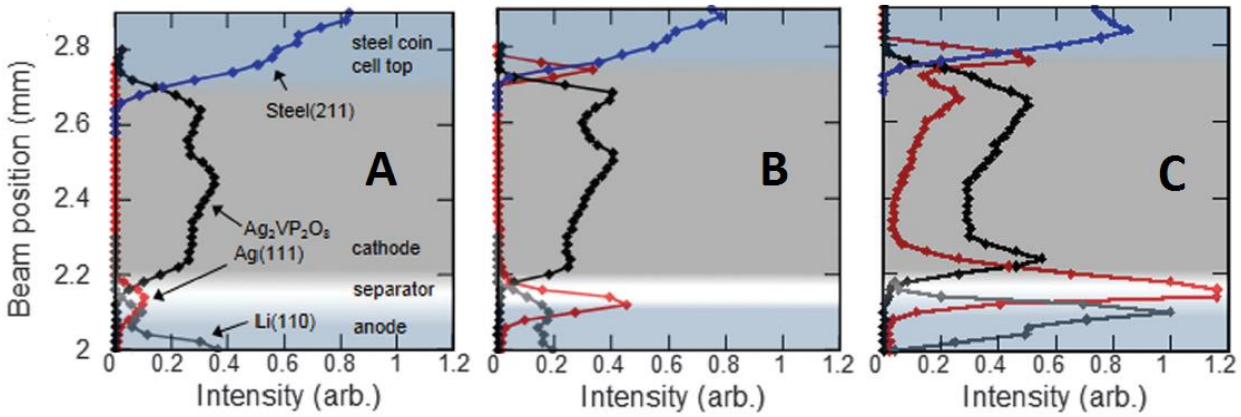


**Figure 4.** The intensity of the $Ag^0$ (111) peak (red), the intensity of the Li (110) peak (grey), the intensity of the steel (211) peak (blue) and the average intensity of three $Ag_2VP_2O_8$ peaks (black) as a function of the z-position is plotted in figure 33 for the **A.** 0, **B.** 0.1, and **C.** 0.5 discharged cells.

6.3.2 Electrochemical Reduction of $Ag_2VO_2PO_4$ single particles and nanoprobe conductivity measurement

The energy dispersive X-ray diffraction technique provided insight into how $Ag^0$ formation upon electrochemical reduction affected the conductivity of a bulk silver vanadium phosphorous oxide electrode. AC impedance measurements showed a dramatic decrease in the resistance associated with the cathode upon reduction, which EDXRD indicated coincided with the formation of $Ag^0$ metal. Because the measurements were made on a bulk electrode, however, it was unclear if the increase in conductivity of the cathode was related only to interparticle conductivity, or if the conductivity of the individual particles themselves also changed significantly. To answer this question, individual particles of $Ag_2VO_2PO_4$, another member of the $Ag_wV_xP_yO_z$ material family, were electrochemically reduced and subsequently measured for changes in conductivity using a nanoprobe system. As with $Ag_2VP_2O_8$, $Ag_2VO_2PO_4$ also forms $Ag^0$ when discharged which decreases interparticle resistance and improves conductivity.[8, 18-19] Thus, although the stoichiometry varies, the causes of increased conductivity upon reduction are expected to be the same for both materials.

Several $Ag_2VO_2PO_4$ particles were discharged using a three electrode configuration described in detail in the experimental section of this chapter. The voltage profile and corresponding optical images at various states of reduction for a typical particle discharge are shown in Figure 5. This individual particle had initial dimensions of 1.15 x 0.15 x 0.09 $mm^3$ and was discharged using a constant current of 4.5 x $10^{-7}$ A. The optical images show how the physical characteristics of the particle change with reduction. Prior to discharge, the particle can be described as being orange colored and semi-transparent. During the initial discharge ('A' through 'C'), the voltage drops below 2 V, and the color of the particle is still transparent orange.

At point ‘D’ the region of the particle closest to the current collector begins to turn black. The color change and voltage recovery continues from ‘E’ to ‘H’, at which point the particle has turned completely black. From ‘H’ to ‘K’ the voltage profile decreases slowly and is reminiscent of what is observed in bulk $Ag_2VO_2PO_4$ electrodes.[18] The voltage continues to decrease and a fracture develops and grows in ‘K’ through ‘N’. Past ‘N’, the discharge was discontinued as the particle completely fractured into several smaller pieces. At this point the sample had discharged approximately 90% of the calculated theorectical capacity, and the end voltage was 1.2 V.

The particle fracture at lower discharge voltage is believed to be due to stresses arising from lithium insertion as well as $Ag^+$ ion removal from the structure. In previous work,[4] SEM images of $Ag^0$ nanoparticles in the reduced material are consistent with a discharge mechanism whereby $Ag^+$ ions are reduced, displaced from the crystal structure, and crystallize on the surface of the particles. The XRD pattern of discharged bulk material shows only silver metal indicating electrochemical milling and amorphization of the parent $Ag_2VO_2PO_4$ material.[4] This may relate to differences in the effective ionic radii of $Li^+$ and $Ag^+$ ions (76 pm for $Li^+$, and 115 pm for $Ag^+$ for coordination number = 6).[20]

The drop in voltage on initial discharge followed by a partial recovery associated with the color change that is presented in this figure is seen in all particles discharged at comparable rates. The color change observed in the single particle is consistent with observations of color change from yellow to black in discharged $Ag_2VO_2PO_4$ bulk electrodes. Thus, the observed color change is not unique to the large single particles and is consistent with the bulk material. It is notable that the color change occurs on the side of the particle closest to the connecting wire, as this is the region closest to the electron source. $Ag_2VO_2PO_4$ is insulating and as such it is reasonable that electron access would be the limiting factor in the discharge. This observation is

supported by the EDXRD experiment which indicated that electron access was a significant limiting factor in the discharge. A similar effect is observed in this experiment where the color change is related to the enhancement of conductivity and the associated voltage increase.

In order to determine how the conductivity of the particles changed after discharging, they were measured using a nanoprobe system. For this experiment, the particles were partially discharged to a point equivalent to 'F' in Figure 5. This was done to isolate a sample with both orange and black segments such that a direct comparison of the conductivity between orange and black regions could be made. SEM and optical images of a typical partially discharged particle indicate the two regions in Figure 6. The color change in the optical image corresponds to the color change seen in the SEM micrograph (Figures 6(a) and (b), respectively). The SEM images indicate a significant difference in conductivity between the two halves of the particle as the lighter color in the SEM image shows charging effects indicating that the region is more insulating.

To measure the resistance of the particle, two nanoprobe Pt-W STM tips were pressed into the surface of the particle approximately 200 μm apart. The resistance was measured within both the black and orange sections with the tip distance held constant between the two measurements. We found that the resistance of the black region (Fig. 6(d)) was 100,000 times lower than the resistance of the orange region (Fig. 6(c)), consistent with the charging observed in the SEM images.

The resistance measurement was performed on several individual particles discharged to different levels (Table 2). Three categories of particles were tested: a) partially discharged (as in Figure 6a), b) not discharged, and c) discharged to approximately 250 mAh/g (close to the theoretical capacity of 272 mAh/g). In each case,

when resistance was measured within the orange region of a particle the resistance was high, approximately $10^{10}$ to $10^{12}$ Ω, while the resistance measured in the black region was considerably lower, around $10^5$ or $10^6$ Ω. The resistance measurements were independent of probe distance which suggests that the current path most likely includes conduction through the substrate. For this reason, the resistance values, and not resistivity, are reported in the table as the resistivity cannot be unambiguously calculated using simple measurements of the particle geometry.

These resistance measurements indicate a drastic change in the electronic conduction of individual particles early in the discharge which most likely forms a large contribution to the decrease in resistance of $Ag_2VO_2PO_4$ electrodes. Moreover, the bimodal distribution observed in the corresponding optical images associated with either the reduction of $Ag^+$ or $V^{5+}$ ions may point to a fundamental change in the material. In several vanadium oxides it has been shown that chemical substitution and doping is sufficient to lower the transition temperature of a metal-insulator transition, causing the material to transition from an insulator to a metal at room temperature[21-22]. The insertion of lithium ion into the $Ag_2VO_2PO_4$ appears to cause a similar effect.

This enhancement of conductivity explains the partial recovery of voltage as seen in 'D' though 'H' of Fig. 2. When the material is initially insulating, electron access is the limiting factor in the discharge and only the region of the particle closes to the wire contact is able to discharge. As the particle discharges and changes color the material conductivity increases dramatically. At this point there is access to additional undischarged regions of the particle and the voltage recovers.

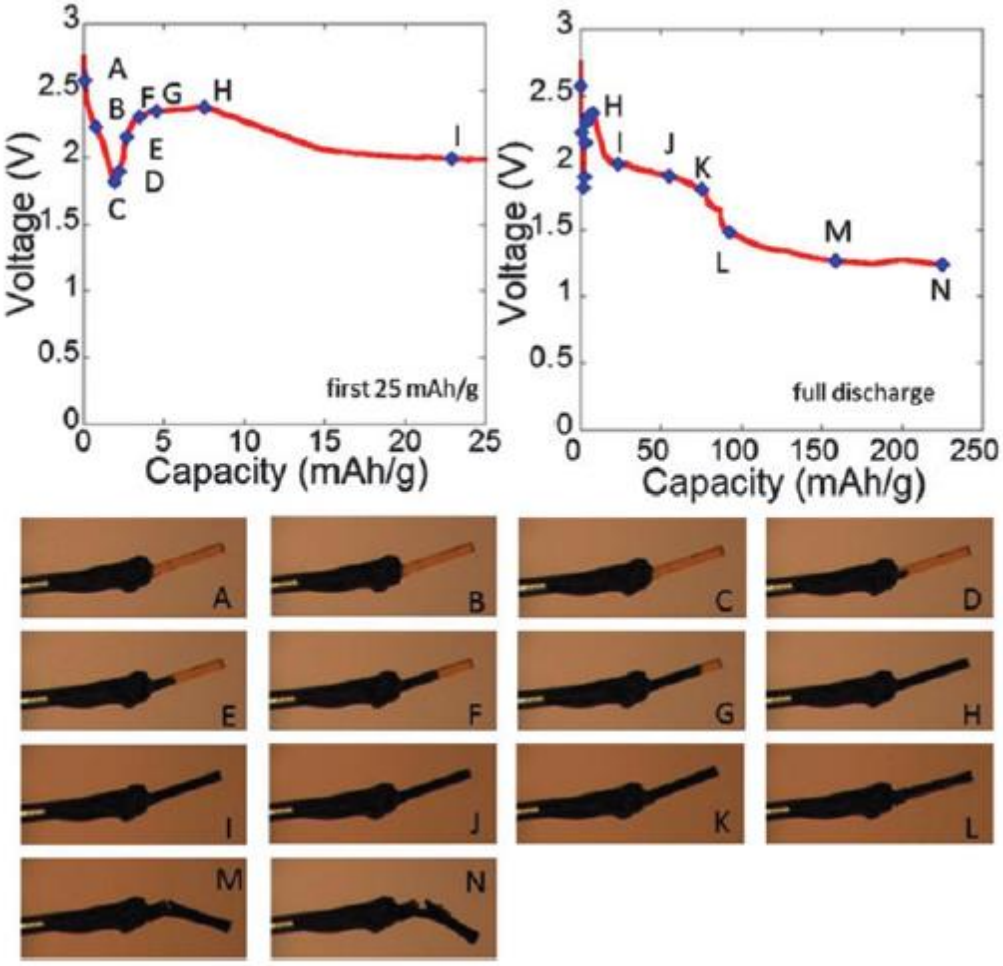


**Figure 5.** Constant current discharge of an individual particle of $Ag_2VO_2PO_4$. The voltage profile in the upper left shows the first 25 mA h $g^{-1}$ of the discharge while the voltage profile in the upper right shows the entire discharge range. The blue markers in the voltage profile correspond to the optical images taken at that discharge level.

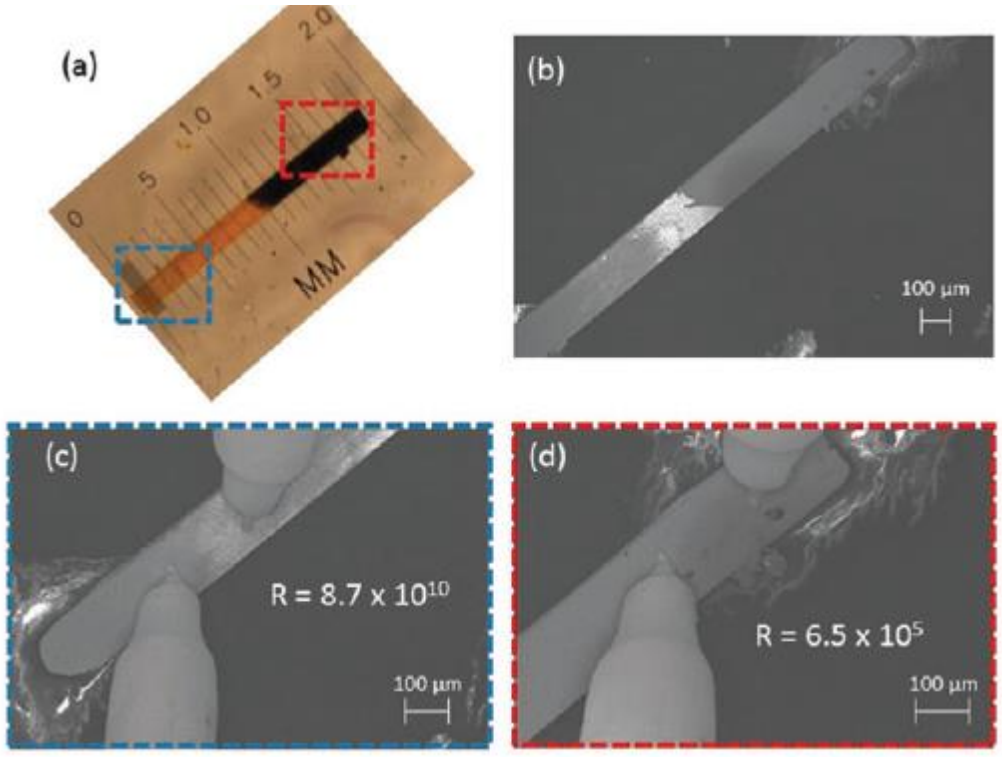


**Figure 6**. (a) Optical and (b-d) SEM images of a partially discharged individual particle of $Ag_2VO_2PO_4$. The two lower images show the placement of STM tips for resistance measurements of the (c) orange and (d) black regions of the particle.

| Particle details | Color of measured region | Resistance (Ω) | Distance between probes (μm) |
|---|---|---|---|
| **Partially discharged particle** | Black | $6.5 \times 10^{5}$ | 196 |
| | Orange | $8.7 \times 10^{10}$ | 204 |
| **Partially discharged particle** | Black | $2.0 \times 10^{6}$ | 72 |
| | Orange | $2.9 \times 10^{11}$ | 68 |
| **Non-discharged particle** | Orange | $1.4 \times 10^{12}$ | 161 |
| **Non-discharged particle** | Orange | $5.2 \times 10^{11}$ | 173 |
| **Fully discharged (to approx. 250 mAh/g)** | Black | $8.2 \times 10^{6}$ | 187 |
| | Black | $7.5 \times 10^{6}$ | 318 |
| | Black | $7.8 \times 10^{6}$ | 546 |

**Table 2.** Resistance of individual particles of $Ag_2VO_2PO_4$ prepared in three ways: partially discharged so that the particle is approximately half black and half orange, not discharged, and fully discharged to close to the theoretical maximum.

## 6.4 Summary

The measurement techniques described in this chapter were used to effectively investigate the causes of increased conductivity observed in electrochemically reduced silver vanadium phosphorous oxide cathode materials. *In-situ* EDXRD of Li/$Ag_2VP_2O_8$ coin cells revealed that the decrease in resistance is associated with the formation of $Ag^0$ throughout the cathode. Spatial resolution of $Ag^0$ formation in partially reduced cells showed that reduction initially occurs in the cathode region closest to current collector, signifying that availability of electrons is a critical factor in the discharge of the poorly conducting phosphate material. As additional $Ag^0$ forms at higher levels of reduction a conductive network forms between the particles, allow additional regions of the electrode to be reduced. Thus, an increase in interparticle conductivity upon silver metal formation is critical for discharge of the bulk electrode.

In order to further probe the observed decrease in resistance in electrochemically reduced SVPO materials, nanoprobe conductivity measurements of electrochemically discharged small individual particles of $Ag_2VO_2PO_4$ were conducted. The individual particles showed a drastic reduction in local resistance when discharged. Consequently, the increase in conductivity of SVPO cathodes is related not only to interparticle conductivity, but also to an increase in the conductivity of the particles themselves.

## 6.5 References


(1) Dudney, N. J.; Li, J., Using all energy in a battery. *Science* **2015,** 347, 131-132.

(2) Cornut, R.; Lepage, D.; Schougaard, S. B., Ohmic Drop in LiFePO4 Based Lithium Battery Cathodes Containing Agglomerates. *J. Electrochem. Soc.* **2012,** 159, A822-A827.

(3) Li, J. L.; Armstrong, B. L.; Daniel, C.; Kiggans, J.; Wood, D. L., Optimization of multicomponent aqueous suspensions of lithium iron phosphate (LiFePO4) nanoparticles and carbon black for lithium-ion battery cathodes. *J. Colloid Interface Sci.* **2013,** 405, 118-124.

(4) Takeuchi, E. S.; Marschilok, A. C.; Tanzil, K.; Kozarsky, E. S.; Zhu, S.; Takeuchi, K. J., Electrochemical Reduction of Silver Vanadium Phosphorus Oxide, Ag2VO2PO4: The Formation of Electrically Conductive Metallic Silver Nanoparticles. *Chem. Mater.* **2009,** 21, 4934-4939.

(5) Takeuchi, E. S.; Lee, C.-Y.; Cheng, P.-J.; Menard, M. C.; Marschilok, A. C.; Takeuchi, K. J., Silver vanadium diphosphate Ag2VP2O8: electrochemistry and characterization of reduced material providing mechanistic insights. *J. Solid State Chem.* **2013,** 200, 232-240.

(6) Marschilok, A. C.; Kim, Y. J.; Takeuchi, K. J.; Takeuchi, E. S., In situ-generation of electrically conductive nanoparticles in bimetallic phosphate materials for high power lithium batteries. *ECS Trans.* **2012,** 41, 1-7.

(7) Marschilok, A. C.; Kim, Y. J.; Takeuchi, K. J.; Takeuchi, E. S., Silver vanadium phosphorous oxide, Ag0.48VOPO4: exploration as a cathode material in primary and secondary battery applications. *J. Electrochem. Soc.* **2012,** 159, A1690-A1695.

(8) Marschilok, A. C.; Kozarsky, E. S.; Tanzil, K.; Zhu, S.; Takeuchi, K. J.; Takeuchi, E. S., Electrochemical reduction of silver vanadium phosphorous oxide, Ag2VO2PO4: Silver metal deposition and associated increase in electrical conductivity. *J. Power Sources* **2010,** 195, 6839-6846.

(9) Takeuchi, E. S.; Marschilok, A. C.; Takeuchi, K. J.; Ignatov, A.; Zhong, Z.; Croft, M., Energy dispersive X-ray diffraction of lithium-silver vanadium phosphorous oxide cells: in situ cathode depth profiling of an electrochemical reduction-displacement reaction. *Energy & Environmental Science* **2013,** 6, 1465-1470.

(10) Daidouh, A.; Veiga, M. L.; Pico, C., Structure characterization and ionic conductivity of Ag2VP2O8. *J. Solid State Chem.* **1997,** 130, 28-34.

(11) Kang, H. Y.; Wang, S. L.; Tsai, P. P.; Lii, K. H., Hydrothermal synthesis, crystal structure and ionic conductivity of silver vanadium oxide phosphate, Ag2VO2PO4: a new layered phosphate of vanadium(V). *J. Chem. Soc., Dalton Trans.* **1993**, 1525-8.

(12) Randles, J. E. B., KINETICS OF RAPID ELECTRODE REACTIONS. *Discussions of the Faraday Society* **1947,** 1, 11-19.

(13) Macdonald, J. R., IMPEDANCE SPECTROSCOPY AND ITS USE IN ANALYZING THE STEADY-STATE AC RESPONSE OF SOLID AND LIQUID ELECTROLYTES. *J. Electroanal. Chem.* **1987,** 223, 25-50.

(14) Harrington, D. A.; van den Driessche, P., Mechanism and equivalent circuits in electrochemical impedance spectroscopy. *Electrochim. Acta* **2011,** 56, 8005-8013.

(15) Macdonald, D. D., Reflections on the history of electrochemical impedance spectroscopy. *Electrochim. Acta* **2006,** 51, 1376-1388.

(16) Park, K. S.; Son, J. T.; Chung, H. T.; Kim, S. J.; Lee, C. H.; Kang, K. T.; Kim, H. G., Surface modification by silver coating for improving electrochemical properties of LiFePO4. *Solid State Commun.* **2004,** 129, 311-314.

(17) Bai, Y.-m.; Qiu, P.; Wen, Z.-l.; Han, S.-c., Improvement of electrochemical performances of LiFePO4 cathode materials by coating of polythiophene. *J. Alloys Compd.* **2010,** 508, 1-4.

(18) Marschilok, A. C.; Takeuchi, K. J.; Takeuchi, E. S., Preparation and electrochemistry of silver vanadium Phosphorous oxide, Ag2VO2PO4. *Electrochem. Solid-State Lett.* **2008,** 12, A5-A9.

(19) Patridge, C. J.; Jaye, C.; Abtew, T. A.; Ravel, B.; Fischer, D. A.; Marschilok, A. C.; Zhang, P.; Takeuchi, K. J.; Takeuchi, E. S.; Banerjee, S., An X-ray Absorption Spectroscopy Study of the Cathodic Discharge of Ag2VO2PO4: Geometric and Electronic Structure Characterization of Intermediate phases and Mechanistic Insights. *J. Phys. Chem. C* **2011,** 115, 14437-14447.

(20) Shannon, R. D., Revised effective ionic radii and systematic studies of interatomic distances in halides and chalcogenides. *Acta Crystallographica, Section A: Crystal Physics, Diffraction, Theoretical and General Crystallography* **1976,** A32, 751-67.

(21) Futaki, H.; Aoki, M., Effects of Various Doping Elements on Transition Temperature of Vanadium Oxide Semiconductors. *Jpn J Appl Phys* **1969,** 8, 1008-&.

(22) Imada, M.; Fujimori, A.; Tokura, Y., Metal-insulator transitions. *Rev Mod Phys* **1998,** 70, 1039-1263.

# Chapter 7

# Conclusions

## 7.1 Summary and Future Studies

The purpose of this study was to investigate cathode solubility with a focus on batteries used to power internal cardioverter defibrillators. A metal oxide based battery system, lithium/silver vanadium oxide ($Ag_2V_4O_{11}$, SVO), is primarily used in these devices due several factors including high current capability and adequate capacity. However, unpredictable long term stability limitation can arise in this system which is attributed to cathode material solubility which results in deposits on the anode, manifesting as increased battery resistance. In order to understand the solution formation of the $Ag_2V_4O_{11}$ cathode in non-aqueous solvents, this research investigated the silver vanadium phosphorous oxide ($Ag_wV_xP_yO_z$) family of materials, which exhibit electrochemical performance characteristics which are suitable for ICDs and other high rate applications, yet are structurally reminiscent of $Ag_2V_4O_{11}$. This strategy is based on the hypothesis that phosphate based cathode materials would reduce cathode component concentrations in the electrolyte, as the strong covalent P-O bonds from the inclusion of $PO_4^{3-}$ polyanions stabilize the vanadium oxide framework.

In Chapter 2, initial experiments focused on characterization of vanadium solubility from silver vanadium oxide $Ag_2V_4O_{11}$ , as well as the $Ag_wV_xP_yO_z$ material $Ag_2VO_2PO_4$. Methodology was developed to quantitatively measure the low levels of vanadium solubility from the target materials, where each compound was immersed in a battery electrolyte under inert atmosphere, and at selected time points a low volume of the parent sample was analyzed via inductively coupled plasma – optical emission spectroscopy to determine the dissolved concentration of

vanadium species in the electrolyte. By monitoring the dissolved concentration as a function of time, the technique allowed for the kinetics of the dissolution process to be examined. Furthermore, the methodology enabled detection of dissolved species in the parts per million and parts per billion ranges from an organic matrix.

In order to gain more insight into the vanadium solubility behavior from the two materials, the concentration-time data was fit to the Noyes-Whitney equation, used to describe the dissolution of solid particles in liquid media[1-2]. In this model, kinetics of dissolution process are dependent upon the rate constant for the dissolution as well as the concentration gradient between the saturated solubility at the solid/liquid interface, where the dissolution/ recrystallization is at equilibrium, and the bulk solution.[3] To our knowledge, this is the first time this model has been used to describe the dissolution of cathode materials in a non-aqueous solvent. Good correlations of the data with the Noyes-Whitney equation support describing vanadium dissolution of SVO and SVPO using this diffusion layer model. The rate of diffusion is low because of the small concentration gradient between the saturated solubility and the bulk solution for these sparingly soluble materials. Furthermore, changes in the material such increase in surface area due to fracturing of particles during dissolution do not appear to influence the observed kinetics, as the rate constant is consistent over time.

Very low levels of vanadium solubility were observed, with the amount of vanadium measured after three weeks less than 1% of the total amount of vanadium in the material exposed to the electrolyte. From this perspective, both the $Ag_2V_4O_{11}$ and $Ag_2VO_2PO_4$ materials are stable in the electrolyte, as only trace solubility is observed. However, the equilibrium solubility of the dissolved vanadium component of SVO was found to be approximately 5 times greater than that of SVPO, with a rate constant of dissolution approximately 3.5 times greater than SVPO. It is

reasonable to expect that over long periods of time, this magnitude of difference in dissolution rate and equilibrium solubility could be significant. When used as cathodes versus as lithium anode in an electrochemical cell, dissolved species will be removed from the electrolyte through deposition onto the lithium anode, and as such, continuous dissolution is expected without reaching a saturated level of solubility.

Electrochemical impedance spectroscopy results of anodes treated with V indicated that cells with V-treated anodes had a higher internal resistance compared to control cells at multiple time points after construction. Further, pulse tests of Li/SVPO cells with V-treated anodes compared to control anodes also affirmed higher cell resistance for the V-treated anode cells. The implication of these results is that cathode materials which dissolve vanadium into the electrolyte will accelerate the formation of a resistive layer on the anode surface which is detrimental to electrochemical performance. This data, when combined with the dissolution results, provide evidence that silver vanadium phosphorous oxide (SVPO) will minimize cell resistance resulting from anode passivation.

In Chapter 3, in order to study the impact of dimensional control of the cathode material on the dissolution kinetics, in addition to chemical composition, two synthetic methods were used to prepare the SVPO material. The higher temperature hydrothermal method resulted in a lower surface area material (SVPO-H), while the lower temperature reflux method resulted in a higher surface area material (SVPO-R). The dissolution of vanadium from the lower surface area materials (SVO and SVPO-H) could be described using the Noyes Whitney dissolution model, suggesting that the dissolution is diffusion controlled. In contrast, vanadium dissolution from the higher surface area material (SVPO-R) showed a different dissolution profile. A faster rate of diffusion was expected from the higher surface area material, in accordance with the

Nernst-Brenner equation.[3] However, the observed diffusion rate was too high for the concentration-time data to be fit using the Noyes Whitney model. In order to effectively model the data, the Weibull distribution function was used.[4-5] Because of the empirical nature of this function, however, mechanistic information could not be derived from the fits.

While the initial dissolution rate for the higher surface area SVPO-R was faster than the rate for SVPO-H, the vanadium concentration at 21 days was the same for both materials within experimental error. This result was expected based on the Noyes-Whitney model, which predicts that the level of dissolved material in the bulk solution will reach a saturated solubility governed by the thermodynamic stability of that material in the liquid. As such, the data shows that the chemical composition of the cathode material has a larger influence on magnitude of dissolution as compared to its physical properties. The implication of this result is that silver vanadium phosphorous oxide will provide reduced solubility relative to silver vanadium oxide regardless of the change in surface area.

The dissolution of silver from the target materials SVO, SVPO-H, and SVPO-R was also modelled using the Weibull function since the Noyes-Whitney model did not adequately fit the data for any of the materials studied, regardless of surface area. The data suggests that a more complex mechanism governs the silver dissolution relative to vanadium. We hypothesize that silver proceeds via an ion exchange mechanism simultaneous to the solvation of the ordered crystal structure, such that both ion exchange and dissolution contribute to the observed kinetics. This idea is supported by the observation that Ag and V concentrations in solution do not reflect the stoichiometry of the solids, with dissolved Ag/V ratios being at least double what is predicted from the stoichiometric ratio. Furthermore, significantly lower levels of silver were observed

when testing was done without electrolyte salt, providing evidence that the presence of $Li^+$ ions in the electrolyte plays a large role in the silver dissolution mechanism.

The dissolution analysis was extended to two additional members of the silver vanadium phosphorous oxide ($Ag_wV_xP_yO_z$) family of materials, $Ag_{0.49}VOPO_4 \cdot 1.9H_2O$ and $Ag_2VP_2O_8$, in Chapter 4. The trace levels of cathode in solution suggest that the solution formation processes are strongly influenced by the crystal structure at the surface of the material crystallites. As such, crystal termination / edge configuration structures of the target materials were considered with regards to the solution formation results. Higher levels of normalized silver solution formation occurred in those materials in which incomplete silver coordination environments at the crystal edge were possible. For vanadium, increased solution formation was observed for the oxide material $Ag_2V_4O_{11}$ as well as for the phosphate oxide $Ag_{0.49}VOPO_4 \cdot 1.9H_2O$. Increased susceptibility to vanadium solution formation for $Ag_{0.49}VOPO_4 \cdot 1.9H_2O$ may be associated with structural water or the existence of multiple vanadium oxidation states.

In Chapter 5, vanadium deposition on anodes from discharged lithium/silver vanadium oxide and lithium/silver vanadium phosphorous oxide electrochemical cells were investigated by several techniques including mapping by synchrotron based x-ray microfluorescence (XRμF) and oxidation state determination by microbeam x-ray absorption spectroscopy (μXAS). Quantitative analysis of digested samples was done using inductively coupled plasma-optical emission spectroscopy (ICP-OES). These methods enabled visualization of the anode surface and solid electrolyte interphase (SEI) through mapping, determination of the vanadium oxidation state, and quantification of the silver and vanadium content of the recovered anodes. Significant differences were

observed for the anode surfaces from the two cell types based on oxide versus phosphate based cathodes, clearly demonstrating lower deposition on the anode from the $Ag_2VO_2PO_4$ cells. A strong correlation was observed between battery resistance and the presence of vanadium on the surfaces of the anodes and vanadium cations in the SEI layer. These findings shed light on the nature and composition of the anode solid electrolyte interphase (SEI) and further highlight its importance in understanding and predicting decreases in battery performance.

Future work on the solubility of silver vanadium oxide and silver vanadium phosphorous oxide should be performed to better understand the role of ion exchange in the dissolution process. Because a high level of silver dissolution was observed after only several hours of exposure to electrolyte, investigation of the initial dissolution kinetics of silver at various electrolyte salt concentrations may provide more insight into ion exchange processes occurring in SVO and SVPO. By taking initial solubility measurements on the time scale of minutes after exposure to electrolyte, before the dissolution of vanadium is observed, it may be possible to decouple the kinetics of ion exchange from the kinetics resulting from the dissolution of the ordered crystal structure of the material.

While the work herein mainly investigated the role of material composition (i.e. oxide vs. phosphate) on solubility, another avenue for reducing dissolution is modification of the electrolyte. All experiments utilized $LiBF_4$ as the electrolyte salt. However, $LiAsF_6$ is often utilized in commercial Li/SVO systems. The developed methodology is expected to be applicable for a wide array of lithium based electrolytes, and comparison of observed solubility using $LiBF_4$ and $LiAsF_6$, as well as other Li

electrolyte salts such as $LiClO_4$ and $LiPF_6$, will improve understanding of the role of the anion on the dissolution process. Modification of the anion may change the solvation energy of dissolved species, resulting in higher or lower equilibrium solubility. Similar experiments may be performed on the electrolyte solvent. A systematic study of dissolution using a matrix of salt – solvent combinations may provide an optimum electrolyte for reducing solubility form SVO and SVPO cathode materials.

Future work should also focus on improvement of the interpretation of the collected kinetic data. The observed discrepancy between the collected dissolution data and the basic diffusion based model provides the opportunity for future work to assign physical basis to the Weibull function and improve understanding of the kinetics which it represents. Limited theoretical work has been done to propose that the Weibull distribution represents a time-dependent rate coefficient due nonhomogeneous conditions such as changes in surface area, diffusion layer thickness, and diffusivity D as the dissolution process proceeds.[6] In particular, the diffusion layer thickness and diffusivity may not be constant when particles are polydisperse or if there is an initial de-aggregation of particles.[6] Experimental studies are needed to confirm this indirect, physical basis assigned to the Weibull model. To determine if changes in surface area as dissolution proceeds impact the observed kinetics, experiments may be proposed to hold surface area constant for the experiment. To achieve this, the experimental setup may be modified such that the cathode material is pressed into a pellet of defined size using a hydraulic press. The pellet may then be placed in an apparatus such that only the top face of the pellet is exposed. Electrolyte or solvent can then be added to the dissolution vessel and an overhead stirring paddle can be used to agitate the solution at a constant rate. Dissolution will be achieved by moving a volume of the dissolution medium over the pellet face, keeping the surface area

exposed to electrolyte constant. Data collected using this methodology may then be analyzed to determine if the observed dissolution kinetics are more adequately represented by the diffusion based mechanism when keeping surface area constant.

Along these same lines, experiments may also be performed to determine if polydispersity of the particles contributes to the kinetics. Materials of uniform particle size should be synthesized for analysis of dissolution kinetics using the developed methodology. If dissolution rate is affected particle sizes/morphologies, then the solubility kinetics from monodisperse particles may be more closely represented by the diffusion based mechanism. Furthermore, it is expected testing materials of uniform size will result in highly consistent concentration versus time data.

While the work presented in this thesis focused on the dissolution from the silver vanadium oxide and silver vanadium phosphorous oxide cathodes, the methodology which was developed is highly applicable to other battery systems. As detailed in the introduction chapter, several notable lithium-ion cathode materials are reported to dissolve into electrolyte, including $LiCoO_{22}$,[7-12] $LiMn_2O_4$,[13-20] and $LiV_3O_8$,[21] and $LiNi_{1/3}Co_{1/3}Mn_{1/3}O_2$.[22-26] As such, the developments of quantitative and kinetic analysis techniques herein to characterize the dissolution process are significant, and future work can shift attention to secondary battery systems using these cathode materials. Kinetic analysis of dissolution will allow for interrogation of the mechanisms by which dissolution occurs. Furthermore, X-ray absorption based techniques can be used to elucidate the composition and geography of deposited dissolved species on the anodes used in these systems. Thus, from this work arises a paradigm to investigate performance degradation resulting from cathode solubility which will aid the broader community in more fully understanding this significant battery failure mechanism.

## 7.2 References


(1) Noyes, A. A.; Whitney, W. R., The rate of solution of solid substances in their own solutions. *J. Am. Chem. Soc.* **1897,** 19, 930-4.

(2) Costa, P.; Sousa Lobo, J. M., Modeling and comparison of dissolution profiles. *Eur. J. Pharm. Sci.* **2001,** 13, 123-133.

(3) Dokoumetzidis, A.; Macheras, P., A century of dissolution research: From Noyes and Whitney to the Biopharmaceutics Classification System. *Int. J. Pharm.* **2006,** 321, 1-11.

(4) Weibull, W., A statistical distribution of wide applicability. *Journal of Applied Mechanics* **1951,** 18, 293-297.

(5) Langenbucher, F., Linearization of dissolution rate curves by the Weibull distribution. *J. Pharm. Pharmacol.* **1972,** 24, 979-81.

(6) Macheras, P.; Dokoumetzidis, A., On the heterogeneity of drug dissolution and release. *Pharm. Res.* **2000,** 17, 108-112.

(7) Amatucci, G. G.; Tarascon, J. M.; Klein, L. C., Cobalt dissolution in LiCoO2-based non-aqueous rechargeable batteries. *Solid State Ionics* **1996,** 83, 167-73.

(8) Markovsky, B.; Rodkin, A.; Cohen, Y. S.; Palchik, O.; Levi, E.; Aurbach, D.; Kim, H. J.; Schmidt, M., The study of capacity fading processes of Li-ion batteries: major factors that play a role. *J. Power Sources* **2003,** 119-121, 504-510.

(9) Wang, Z.; Huang, X.; Chen, L., Characterization of Spontaneous Reactions of LiCoO2 with Electrolyte Solvent for Lithium-Ion Batteries. *J. Electrochem. Soc.* **2004,** 151, A1641-A1652.

(10) Markevich, E.; Salitra, G.; Aurbach, D., Influence of the PVdF binder on the stability of LiCoO2 electrodes. *Electrochem. Commun.* **2005,** 7, 1298-1304.

(11) Aurbach, D.; Markovsky, B.; Salitra, G.; Markevich, E.; Talyossef, Y.; Koltypin, M.; Nazar, L.; Ellis, B.; Kovacheva, D., Review on electrode-electrolyte solution interactions, related to cathode materials for Li-ion batteries. *J. Power Sources* **2007,** 165, 491-499.

(12) Aurbach, D.; Markovsky, B.; Rodkin, A.; Levi, E.; Cohen, Y. S.; Kim, H. J.; Schmidt, M., On the capacity fading of LiCoO2 intercalation electrodes: the effect of cycling, storage, temperature, and surface film forming additives. *Electrochim. Acta* **2002,** 47, 4291-4306.

(13) Blyr, A.; Sigala, C.; Amatucci, G.; Guyomard, D.; Chabre, G. Y.; Tarascon, J. M., Self-discharge of LiMn2O4/C Li-ion cells in their discharged state. Understanding by means of three-electrode measurements. *J. Electrochem. Soc.* **1998,** 145, 194-209.

(14) du Pasquier, A.; Blyr, A.; Courjal, P.; Larcher, D.; Amatucci, G.; Gerand, B.; Tarascon, J. M., Mechanism for limited 55°C storage performance of Li1.05Mn1.95O4 electrodes. *J. Electrochem. Soc.* **1999,** 146, 428-436.

(15) Jang, D. H.; Shin, Y. J.; Oh, S. M., Dissolution of spinel oxides and capacity losses in 4 V Li/LixMn2O4 cells. *J. Electrochem. Soc.* **1996,** 143, 2204-2211.

(16) Jang, D. H.; Oh, S. M., Electrolyte effects on spinel dissolution and cathodic capacity losses in 4 V Li/LixMn2O4 rechargeable cells. *J. Electrochem. Soc.* **1997,** 144, 3342-3348.

(17) Aoshima, T.; Okahara, K.; Kiyohara, C.; Shizuka, K., Mechanisms of manganese spinels dissolution and capacity fade at high temperature. *J. Power Sources* **2001,** 97-98, 377-380.

(18) Lu, C.-H.; Lin, S.-W., Dissolution kinetics of spinel lithium manganate and its relation to capacity fading in lithium ion batteries. *J. Mater. Res.* **2002,** 17, 1476-1481.

(19) Wang, H.-C.; Lu, C.-H., Dissolution behavior of chromium-ion doped spinel lithium manganate at elevated temperatures. *J. Power Sources* **2003,** 119-121, 738-742.

(20) Amine, K.; Liu, J.; Kang, S.; Belharouak, I.; Hyung, Y.; Vissers, D.; Henriksen, G., Improved lithium manganese oxide spinel/graphite Li-ion cells for high-power applications. *J. Power Sources* **2004,** 129, 14-19.

(21) Jouanneau, S.; Le, G. L. S. A.; Verbaere, A.; Guyomard, D., The Origin of Capacity Fading upon Lithium Cycling in Li1.1V3O8. *J. Electrochem. Soc.* **2005,** 152, A1660-A1667.

(22) Gallus, D. R.; Schmitz, R.; Wagner, R.; Hoffmann, B.; Nowak, S.; Cekic-Laskovic, I.; Schmitz, R. W.; Winter, M., The influence of different conducting salts on the metal dissolution and capacity fading of NCM cathode material. *Electrochim. Acta* **2014,** 134, 393-398.

(23) Ju, S. H.; Kang, I.-S.; Lee, Y.-S.; Shin, W.-K.; Kim, S.; Shin, K.; Kim, D.-W., Improvement of the Cycling Performance of LiNi0.6Co0.2Mn0.2O2 Cathode Active Materials by a Dual-Conductive Polymer Coating. *ACS App Mater Inter* **2014,** 6, 2546-2552.

(24) Mai, S.; Xu, M.; Liao, X.; Hu, J.; Lin, H.; Xing, L.; Liao, Y.; Li, X.; Li, W., Tris(trimethylsilyl) phosphite as electrolyte additive for high voltage layered lithium nickel cobalt manganese oxide cathode of lithium ion battery. *Electrochim. Acta* **2014,** 147, 565-571.

(25) Shi, S. J.; Tu, J. P.; Tang, Y. Y.; Zhang, Y. Q.; Liu, X. Y.; Wang, X. L.; Gu, C. D., Enhanced electrochemical performance of LiF-modified LiNi1/3Co1/3Mn1/3O2 cathode materials for Li-ion batteries. *J. Power Sources* **2013,** 225, 338-346.

(26) Zheng, H.; Sun, Q.; Liu, G.; Song, X.; Battaglia, V. S., Correlation between dissolution behavior and electrochemical cycling performance for LiNi1/3Co1/3Mn1/3O2-based cells. *J. Power Sources* **2012,** 207, 134-140.

## References


Ablett, J. M.; Kao, C. C.; Reeder, R. J.; Tang, Y.; Lanzirotti, A., X27A-A new hard X-ray micro-spectroscopy facility at the National Synchrotron Light Source. *Nucl. Instrum. Methods Phys. Res., Sect. A* **2006,** 562, 487-494.

Adams, E.; Coomans, D.; Smeyers-Verbeke, J.; Massart, D. L., Non-linear mixed effects models for the evaluation of dissolution profiles. *Int. J. Pharm.* **2002,** 240, 37-53.

Amatucci, G. G.; Pereira, N., Fluoride based electrode materials for advanced energy storage devices. *J. Fluorine Chem.* **2007,** 128, 243-262.

Amatucci, G. G.; Tarascon, J. M.; Klein, L. C., Cobalt dissolution in LiCoO2-based non-aqueous rechargeable batteries. *Solid State Ionics* **1996,** 83, 167-73.

Amine, K.; Liu, J.; Belharouak, I., High-temperature storage and cycling of C-LiFePO4/graphite Li-ion cells. *Electrochem. Commun.* **2005,** 7, 669-673.

Amine, K.; Liu, J.; Kang, S.; Belharouak, I.; Hyung, Y.; Vissers, D.; Henriksen, G., Improved lithium manganese oxide spinel/graphite Li-ion cells for high-power applications. *J. Power Sources* **2004,** 129, 14-19.

Antonijevic, M. M.; Jankovic, Z. D.; Dimitrijevic, M. D., Kinetics of chalcopyrite dissolution by hydrogen peroxide in sulphuric acid. *Hydrometallurgy* **2004,** 71, 329-334.

Aoshima, T.; Okahara, K.; Kiyohara, C.; Shizuka, K., Mechanisms of manganese spinels dissolution and capacity fade at high temperature. *J. Power Sources* **2001,** 97-98, 377-380.

Aurbach, D.; Markovsky, B.; Rodkin, A.; Levi, E.; Cohen, Y. S.; Kim, H. J.; Schmidt, M., On the capacity fading of LiCoO2 intercalation electrodes: the effect of cycling, storage, temperature, and surface film forming additives. *Electrochim. Acta* **2002,** 47, 4291-4306.

Aurbach, D.; Markovsky, B.; Salitra, G.; Markevich, E.; Talyossef, Y.; Koltypin, M.; Nazar, L.; Ellis, B.; Kovacheva, D., Review on electrode-electrolyte solution interactions, related to cathode materials for Li-ion batteries. *J. Power Sources* **2007,** 165, 491-499.

Ayyappan, P.; Ramanan, A.; Torardi, C. C., New Metal-Intercalated Layered Vanadyl Phosphates, MxVOPO4·yH2O (M = Ag, Cu, Zn). *Inorg. Chem.* **1998,** 37, 3628-3634.

Bai, Y.-m.; Qiu, P.; Wen, Z.-l.; Han, S.-c., Improvement of electrochemical performances of LiFePO4 cathode materials by coating of polythiophene. *J. Alloys Compd.* **2010,** 508, 1-4.

Blyr, A.; Sigala, C.; Amatucci, G.; Guyomard, D.; Chabre, G. Y.; Tarascon, J. M., Self-discharge of LiMn2O4/C Li-ion cells in their discharged state. Understanding by means of three-electrode measurements. *J. Electrochem. Soc.* **1998,** 145, 194-209.

Bock, D. C.; Marschilok, A. C.; Takeuchi, K. J.; Takeuchi, E. S., A kinetics and equilibrium study of vanadium dissolution from vanadium oxides and phosphates in battery electrolytes: Possible impacts on ICD battery performance. *J. Power Sources* **2013,** 231, 219-235.

Bock, D. C.; Takeuchi, K. J.; Marschilok, A. C.; Takeuchi, E. S., Silver vanadium oxide and silver vanadium phosphorous oxide dissolution kinetics: a mechanistic study with possible impact on future ICD battery lifetimes. *Dalton Trans.* **2013,** 42, 13981-13989.

Bonferoni, M. C.; Rossi, S.; Ferrari, F.; Bertoni, M.; Bolhuis, G. K.; Caramella, C., On the employment of λ carrageenan in a matrix system. III. Optimization of a λ carrageenan-HPMC hydrophilic matrix. *J. Controlled Release* **1998,** 51, 231-239.

Bowden, W.; Bofinger, T.; Zhang, F.; Iltchev, N.; Sirotina, R.; Paik, Y.; Chen, H.; Grey, C.; Hackney, S., New manganese dioxides for lithium batteries. *J. Power Sources* **2007,** 165, 609-615.

Brodd, R. J.; Bullock, K. R.; Leising, R. A.; Middaugh, R. L.; Miller, J. R.; Takeuchi, E., Batteries, 1977 to 2002. *J. Electrochem. Soc.* **2004,** 151, K1-K11.

Bruner, L.; Tolloczko, S., On the dissolution speed of firm bodies. [machine translation]. *Z. physik. Ch.* **1900,** 35, 283-90.

Cao, X.; Xie, L.; Zhan, H.; Zhou, Y., Facile preparation of Ag2V4O11 nanoparticles via low-temperature molten salt synthesis method. *Inorg. Mater.* **2008,** 44, 886-889.

Chen, K.; Merritt, D. R.; Howard, W. G.; Schmidt, C. L.; Skarstad, P. M., Hybrid cathode lithium batteries for implantable medical applications. *J. Power Sources* **2006,** 162, 837-840.

Cheng, F.; Chen, J., Transition metal vanadium oxides and vanadate materials for lithium batteries. *J. Mater. Chem.* **2011,** 21, 9841-9848.

Chevalier, E.; Viana, M.; Artaud, A.; Chomette, L.; Haddouchi, S.; Devidts, G.; Chulia, D., Comparison of three dissolution apparatuses for testing calcium phosphate pellets used as ibuprofen delivery systems. *AAPS PharmSciTech* **2009,** 10, 597-605.

Cornut, R.; Lepage, D.; Schougaard, S. B., Ohmic Drop in LiFePO4 Based Lithium Battery Cathodes Containing Agglomerates. *J. Electrochem. Soc.* **2012,** 159, A822-A827.

Costa, P.; Sousa Lobo, J. M., Modeling and comparison of dissolution profiles. *Eur. J. Pharm. Sci.* **2001,** 13, 123-133.

Crans, D. C., Fifteen years of dancing with vanadium. *Pure Appl. Chem.* **2005,** 77, 1497-1527.

Crespi, A.; Schmidt, C.; Norton, J.; Chen, K.; Skarstad, P., Modeling and characterization of the resistance of lithium/SVO batteries for implantable cardioverter defibrillators. *J. Electrochem. Soc.* **2001,** 148, A30-A37.

Crespi, A. M.; Somdahl, S. K.; Schmidt, C. L.; Skarstad, P. M., Evolution of power sources for implantable cardioverter defibrillators. *J. Power Sources* **2001,** 96, 33-38.

D'Souza Susan, S.; Faraj Jabar, A.; DeLuca Patrick, P., A model-dependent approach to correlate accelerated with real-time release from biodegradable microspheres. *AAPS PharmSciTech* **2005,** 6, E553-64.

Daidouh, A.; Veiga, M. L.; Pico, C., Structure characterization and ionic conductivity of Ag2VP2O8. *J. Solid State Chem.* **1997,** 130, 28-34.

Danckwerts, P. V., Significance of liquid-film coefficients in gas absorption. *J. Ind. Eng. Chem. (Washington, D. C.)* **1951,** 43, 1460-7.

Dash, S.; Murthy Padala, N.; Nath, L.; Chowdhury, P., Kinetic modeling on drug release from controlled drug delivery systems. *Acta Pol Pharm* **2010,** 67, 217-23.

Davis, S.; Takeuchi, E. S.; Tiedemann, W.; Newman, J., Simulation of pulse discharge of the Li-CFx system. *J. Electrochem. Soc.* **2007,** 155, A24-A28.

Davis, S.; Takeuchi, E. S.; Tiedemann, W.; Newman, J., Simulation of the Li-CFx system. *J. Electrochem. Soc.* **2007,** 154, A477-A480.

Delacourt, C.; Kwong, A.; Liu, X.; Qiao, R.; Yang, W. L.; Lu, P.; Harris, S. J.; Srinivasan, V., Effect of manganese contamination on the solid-electrolyte-interphase properties in Li-ion batteries. *J. Electrochem. Soc.* **2013,** 160, A1099-A1107.

Dicinoski, G. W.; Gahan, L. R.; Lawson, P. J.; Rideout, J. A., Application of the shrinking core model to the kinetics of extraction of gold(I), silver(I) and nickel(II) cyanide complexes by novel anion exchange resins. *Hydrometallurgy* **2000,** 56, 323-336.

Dodd, J.; Kishiyama, C.; Nagata, M.; Nakahara, H.; Yumoto, H.; Tsukamoto, H., Implantable rechargeable lithium ion batteries for medical applications: neurostimulation and cardiovascular devices. *Proc. - Electrochem. Soc.* **2004,** 2003-28, 360-367.

Dokoumetzidis, A.; Macheras, P., A century of dissolution research: From Noyes and Whitney to the Biopharmaceutics Classification System. *Int. J. Pharm.* **2006,** 321, 1-11.

Dokoumetzidis, A.; Papadopoulou, V.; Macheras, P., Analysis of Dissolution Data Using Modified Versions of Noyes-Whitney Equation and the Weibull Function. *Pharm. Res.* **2006,** 23, 256-261.

Drews, J.; Wolf, R.; Fehrmann, G.; Staub, R., Development of a hybrid battery system for an implantable biomedical device, especially a defibrillator/cardioverter (ICD). *J. Power Sources* **1999,** 80, 107-111.

Drews, J.; Wolf, R.; Fehrmann, G.; Staub, R., High-rate lithium/manganese dioxide batteries; the double cell concept. *J. Power Sources* **1997,** 65, 129-132.

du Pasquier, A.; Blyr, A.; Courjal, P.; Larcher, D.; Amatucci, G.; Gerand, B.; Tarascon, J. M., Mechanism for limited 55°C storage performance of Li1.05Mn1.95O4 electrodes. *J. Electrochem. Soc.* **1999,** 146, 428-436.

Dudney, N. J.; Li, J., Using all energy in a battery. *Science* **2015,** 347, 131-132.

Ehrlich, G. M., Lithium-ion batteries. In *Handbook of Batteries*, 3rd ed.; Linden, D.; Reddy, T. B., Eds. McGraw-Hill: **2002**.

Ellis, B. L.; Lee, K. T.; Nazar, L. F., Positive Electrode Materials for Li-Ion and Li Batteries. *Chem. Mater.* **2010,** 22, 691-714.

Fehrmann, G.; Frommel, R.; Wolf, R. Galvanic Cell having improved cathode. US Patent 5587258, 19960105., **1996**.

Futaki, H.; Aoki, M., Effects of Various Doping Elements on Transition Temperature of Vanadium Oxide Semiconductors. *Jpn J Appl Phys* **1969,** 8, 1008-&.

Gallus, D. R.; Schmitz, R.; Wagner, R.; Hoffmann, B.; Nowak, S.; Cekic-Laskovic, I.; Schmitz, R. W.; Winter, M., The influence of different conducting salts on the metal dissolution and capacity fading of NCM cathode material. *Electrochim. Acta* **2014,** 134, 393-398.

Gan, H.; Rubino, R. S.; Takeuchi, E. S., Dual-chemistry cathode system for high-rate pulse applications. *J. Power Sources* **2005,** 146, 101-106.

Gan, H.; Takeuchi, E. In *Correlation of anode surface film composition and voltage delay*, 198th Electrochemical Society Meeting, **2000**.

Gao, X.-W.; Wang, J.-Z.; Chou, S.-L.; Liu, H.-K., Synthesis and electrochemical performance of LiV3O8/polyaniline as cathode material for the lithium battery. *J. Power Sources* **2012,** 220, 47-53.

Gaubicher, J.; Mercier, T. L.; Chabre, Y.; Angenault, J.; Quarton, M., Li/β-VOPO4: a new 4V system for lithium batteries. *J. Electrochem. Soc.* **1999,** 146, 4375-4379.

Gbor, P. K.; Jia, C. Q., Critical evaluation of coupling particle size distribution with the shrinking core model. *Chem. Eng. Sci.* **2004,** 59, 1979-1987.

Georgiou, D.; Papangelakis, V. G., Sulfuric acid pressure leaching of a limonitic laterite: chemistry and kinetics. *Hydrometallurgy* **1998,** 49, 23-46.

Gerbino, P. P., *Remington: The Science and Practice of Pharmacy*. 21st Edition ed.; Lippincott Williams and Wilkins: **2005**; p 2393.

Gireaud, L.; Grugeon, S.; Laruelle, S.; Yrieix, B.; Tarascon, J. M., Lithium metal stripping/plating mechanisms studies: A metallurgical approach. *Electrochem. Commun.* **2006,** 8, 1639-1649.

Gomadam, P. M.; Merritt, D. R.; Scott, E. R.; Schmidt, C. L.; Skarstad, P. M.; Weidner, J. W., Mathematical modeling of Li/CFx-SVO batteries. *ECS Trans.* **2007,** 3, 45-54.

Gomadam, P. M.; Merritt, D. R.; Scott, E. R.; Schmidt, C. L.; Skarstad, P. M.; Weidner, J. W., Modeling Li/CFx-SVO hybrid-cathode batteries. *J. Electrochem. Soc.* **2007,** 154, A1058-A1064.

Gomadam, P. M.; Merritt, D. R.; Scott, E. R.; Schmidt, C. L.; Weidner, J. W., Modeling transients in Li/CFx-SVO hybrid-cathode batteries. *ECS Trans.* **2008,** 11, 1-6.

Gowda, S. R.; Gallagher, K. G.; Croy, J. R.; Bettge, M.; Thackeray, M. M.; Balasubramanian, M., Oxidation state of cross-over manganese species on the graphite electrode of lithium-ion cells. *Phys. Chem. Chem. Phys.* **2014,** 16, 6898-6902.

Greatbatch, W.; Holmes, C. F.; Takeuchi, E. S.; Ebel, S. J., Lithium/carbon monofluoride (Li/CFx): a new pacemaker battery. *Pacing Clin Electrophysiol* **1996,** 19, 1836-40.

Greatbatch, W.; Mead, R. T.; Rudolph, F. Lithium-Iodine Battery having Coated Anode U.S. Patent 3957533, **1976**.

Gulfen, M.; Aydin, A. O., Dissolution kinetics of calcined chalcopyrite ore in sulphuric acid solution. *Indian J. Chem. Technol.* **2008,** 15, 180-185.

Gutmann, F.; Hermann, A. M.; Rembaum, A., Solid-state electrochemical cells based on charge transfer complexes. *J. Electrochem. Soc.* **1967,** 114, 323-9.

Hagiwara, R.; Nakajima, T.; Watanabe, N., Kinetic study of discharge reaction of lithium-graphite fluoride cell. *J. Electrochem. Soc.* **1988,** 135, 2128-33.

Harland, C. E., *Ion Exchange: Theory and Practice*. 2 ed.; **1994**.

Harrington, D. A.; van den Driessche, P., Mechanism and equivalent circuits in electrochemical impedance spectroscopy. *Electrochim. Acta* **2011,** 56, 8005-8013.

Hautier, G.; Jain, A.; Ong, S. P.; Kang, B.; Moore, C.; Doe, R.; Ceder, G., Phosphates as Lithium-Ion Battery Cathodes: An Evaluation Based on High-Throughput ab Initio Calculations. *Chem. Mater.* **2011,** 23, 3495-3508.

Helfferich, F., *Ion Exchange*. **1962**.

Hixson, A. W.; Crowell, J. H., Dependence of reaction velocity upon surface and agitation. I. Theoretical considerations. *J. Ind. Eng. Chem. (Washington, D. C.)* **1931,** 23, 923-31.

Holmes, C. F., The Bourner Lecture: Electrochemical power sources - an important contributor to modern health care. *J. Power Sources* **1997,** 65, xv,xvi,xvii,xviii,xix,xx.

Holmes, C. F., Lithium/Halogen Batteries. In *Batteries for Implantable Biomedical Devices*, Owens, B. B., Ed. Plenum Press: New York, **1986**, pp 133-180.

Holmes, C. F., The lithium/iodine-polyvinylpyridine battery - 35 years of successful clinical use. *ECS Trans.* **2007,** 6, 1-7.

Hsu, W.-L.; Lin, M.-J.; Hsu, J.-P., Dissolution of solid particles in liquids: a shrinking core model. *Int. J. Chem. Biomol. Eng.* **2009,** 2, 205-210.

Ikeda, H.; Saito, T.; Tamura, H., Lithium-manganese dioxide cell. (1). *Denki Kagaku oyobi Kogyo Butsuri Kagaku* **1977,** 45, 314-18.

Iltchev, N.; Chen, Y.; Okada, S.; Yamaki, J.-i., LiFePO4 storage at room and elevated temperatures. *J. Power Sources* **2003,** 119-121, 749-754.

Imada, M.; Fujimori, A.; Tokura, Y., Metal-insulator transitions. *Rev Mod Phys* **1998,** 70, 1039-1263.

Jang, D. H.; Oh, S. M., Electrolyte effects on spinel dissolution and cathodic capacity losses in 4 V Li/LixMn2O4 rechargeable cells. *J. Electrochem. Soc.* **1997,** 144, 3342-3348.

Jang, D. H.; Shin, Y. J.; Oh, S. M., Dissolution of spinel oxides and capacity losses in 4 V Li/LixMn2O4 cells. *J. Electrochem. Soc.* **1996,** 143, 2204-2211.

Johnson, C. S., Development and utility of manganese oxides as cathodes in lithium batteries. *J. Power Sources* **2007,** 165, 559-565.

Jouanneau, S.; Le, G. L. S. A.; Verbaere, A.; Guyomard, D., The Origin of Capacity Fading upon Lithium Cycling in Li1.1V3O8. *J. Electrochem. Soc.* **2005,** 152, A1660-A1667.

Jouanneau, S.; Verbaere, A.; Lascaud, S.; Guyomard, D., Improvement of the lithium insertion properties of Li1.1V3O8. *Solid State Ionics* **2006,** 177, 311-315.

Ju, S. H.; Kang, I.-S.; Lee, Y.-S.; Shin, W.-K.; Kim, S.; Shin, K.; Kim, D.-W., Improvement of the Cycling Performance of LiNi0.6Co0.2Mn0.2O2 Cathode Active Materials by a Dual-Conductive Polymer Coating. *ACS App Mater Inter* **2014,** 6, 2546-2552.

Kang, H. Y.; Wang, S. L.; Tsai, P. P.; Lii, K. H., Hydrothermal synthesis, crystal structure and ionic conductivity of silver vanadium oxide phosphate, Ag2VO2PO4: a new layered phosphate of vanadium(V). *J. Chem. Soc., Dalton Trans.* **1993**, 1525-8.

Kim, D.-H.; Kim, J., Synthesis of LiFePO4 Nanoparticles in Polyol Medium and Their Electrochemical Properties. *Electrochem. Solid-State Lett.* **2006,** 9, A439-A442.

Kim, H.-S.; Kim, H.-J.; Cho, W.-I.; Cho, B.-W.; Ju, J.-B., Discharge characteristics of chemically prepared MnO2 and electrolytic MnO2 in non-aqueous electrolytes. *J. Power Sources* **2002,** 112, 660-664.

Kim, Y. J.; Lee, C.-Y.; Marschilok, A. C.; Takeuchi, K. J.; Takeuchi, E. S., AgxVOPO4: A demonstration of the dependence of battery-related electrochemical properties of silver vanadium phosphorous oxides on Ag/V ratios. *J. Power Sources* **2011,** 196, 3325-3330.

Kim, Y. J.; Marschilok, A. C.; Takeuchi, K. J.; Takeuchi, E. S., Silver vanadium phosphorous oxide, Ag2VO2PO4: Chimie douce preparation and resulting lithium cell electrochemistry. *J. Power Sources* **2011,** 196, 6781-6787.

Kirshenbaum, K. C.; Bock, D. C.; Zhong, Z.; Marschilok, A. C.; Takeuchi, K. J.; Takeuchi, E. S., In situ profiling of lithium/Ag2VP2O8 primary batteries using energy dispersive X-ray diffraction. *Phys. Chem. Chem. Phys.* **2014,** 16, 9138-9147.

Koester, L. S.; Ortega, G. G.; Mayorga, P.; Bassani, V. L., Mathematical evaluation of in vitro release profiles of hydroxypropylmethylcellulose matrix tablets containing carbamazepine associated to β-cyclodextrin. *Eur. J. Pharm. Biopharm.* **2004,** 58, 177-179.

Koltypin, M.; Aurbach, D.; Nazar, L.; Ellis, B., On the Stability of LiFePO4 Olivine Cathodes under Various Conditions (Electrolyte Solutions, Temperatures). *Electrochem. Solid-State Lett.* **2007,** 10, A40-A44.

Kuecuek, O.; Kocakerim, M. M.; Yartasi, A.; Copur, M., Dissolution of Kestelek's Colemanite Containing Clay Minerals in Water Saturated with Sulfur Dioxide. *Ind. Eng. Chem. Res.* **2002,** 41, 2853-2857.

Laçin, O.; Dönmez, B.; Demir, F., Dissolution kinetics of natural magnesite in acetic acid solutions. *Int. J. Miner. Process.* **2005,** 75, 91-99.

Langenbucher, F., Linearization of dissolution rate curves by the Weibull distribution. *J. Pharm. Pharmacol.* **1972,** 24, 979-81.

Lee, J.; Lee, J.-M.; Yoon, S.; Kim, S.-O.; Sohn, J.-S.; Rhee, K.-I.; Sohn, H.-J., Electrochemical characteristics of manganese oxide/carbon composite as a cathode material for Li/MnO2 secondary batteries. *J. Power Sources* **2008,** 183, 325-329.

Leifer, N. D.; Colon, A.; Martocci, K.; Greenbaum, S. G.; Alamgir, F. M.; Reddy, T. B.; Gleason, N. R.; Leising, R. A.; Takeuchi, E. S., Nuclear Magnetic Resonance and X-Ray Absorption Spectroscopic Studies of Lithium Insertion in Silver Vanadium Oxide Cathodes. *J. Electrochem. Soc.* **2007,** 154, A500-A506.

Leising, R. A.; Palazzo, M. J.; Takeuchi, E. S.; Takeuchi, K. J., Abuse testing of lithium-ion batteries characterization of the overcharge reaction of LiCoO2/graphite cells. *J. Electrochem. Soc.* **2001,** 148, A838-A844.

Leising, R. A.; Palazzo, M. J.; Takeuchi, E. S.; Takeuchi, K. J., A study of the overcharge reaction of lithium-ion batteries. *J. Power Sources* **2001,** 97-98, 681-683.

Leising, R. A.; Takeuchi, E. S., Solid-state cathode materials for lithium batteries: effect of synthesis temperature on the physical and electrochemical properties of silver vanadium oxide. *Chem. Mater.* **1993,** 5, 738-42.

Leising, R. A.; Takeuchi, E. S., Solid-State Synthesis and Characterization of Silver Vanadium Oxide for Use as a Cathode Material for Lithium Batteries. *Chem. Mater.* **1994,** 6, 489-95.

Leising, R. A.; Thiebolt, W. C., III; Takeuchi, E. S., Solid-State Characterization of Reduced Silver Vanadium Oxide from the Li/SVO Discharge Reaction. *Inorg. Chem.* **1994,** 33, 5733-40.

Levenspiel, O., *Chemical Reaction Engineering, 3rd Edition*. **1998**.

Li, J. L.; Armstrong, B. L.; Daniel, C.; Kiggans, J.; Wood, D. L., Optimization of multicomponent aqueous suspensions of lithium iron phosphate (LiFePO4) nanoparticles and carbon black for lithium-ion battery cathodes. *J. Colloid Interface Sci.* **2013,** 405, 118-124.

Li, M.; Wei, C.; Qiu, S.; Zhou, X.; Li, C.; Deng, Z., Kinetics of vanadium dissolution from black shale in pressure acid leaching. *Hydrometallurgy* **2010,** 104, 193-200.

Li, Y.; Chen, Y.; Feng, W.; Ding, F.; Liu, X., The improved discharge performance of Li/CFx batteries by using multi-walled carbon nanotubes as conductive additive. *J. Power Sources* **2011,** 196, 2246-2250.

Liang, C. C.; Bolster, M. E.; Murphy, R. M. Metal oxide composite cathode material for high energy density batteries. US patent 4310609 **1982**.

Lin, C.-W.; Cham, T.-M., Effect of particle size on the available surface area of nifedipine from nifedipine-polyethylene glycol 6000 solid dispersions. *Int. J. Pharm.* **1996,** 127, 261-72.

Linden, D.; Reddy, T. B., Lithium batteries. In *Handbook of Batteries*, Linden, D.; Reddy, T. B., Eds. McGraw-Hill: **2002**; Vol. 3rd.

Liu, F.-C.; Liu, W.-M.; Zhan, M.-H.; Fu, Z.-W.; Li, H., An all solid-state rechargeable lithium-iodine thin film battery using LiI(3-hydroxypropionitrile)2 as an I- ion electrolyte. *Energy Environ. Sci.* **2011,** 4, 1261-1264.

Lu, C.-H.; Lin, S.-W., Dissolution kinetics of spinel lithium manganate and its relation to capacity fading in lithium ion batteries. *J. Mater. Res.* **2002,** 17, 1476-1481.

Lu, P.; Li, C.; Schneider, E. W.; Harris, S. J., Chemistry, Impedance, and Morphology Evolution in Solid Electrolyte Interphase Films during Formation in Lithium Ion Batteries. *J. Phys. Chem. C* **2014,** 118, 896-903.

Macdonald, D. D., Reflections on the history of electrochemical impedance spectroscopy. *Electrochim. Acta* **2006,** 51, 1376-1388.

Macdonald, J. R., IMPEDANCE SPECTROSCOPY AND ITS USE IN ANALYZING THE STEADY-STATE AC RESPONSE OF SOLID AND LIQUID ELECTROLYTES. *J. Electroanal. Chem.* **1987,** 223, 25-50.

Macheras, P.; Dokoumetzidis, A., On the heterogeneity of drug dissolution and release. *Pharm. Res.* **2000,** 17, 108-112.

Mai, S.; Xu, M.; Liao, X.; Hu, J.; Lin, H.; Xing, L.; Liao, Y.; Li, X.; Li, W., Tris(trimethylsilyl) phosphite as electrolyte additive for high voltage layered lithium nickel cobalt manganese oxide cathode of lithium ion battery. *Electrochim. Acta* **2014,** 147, 565-571.

Markevich, E.; Salitra, G.; Aurbach, D., Influence of the PVdF binder on the stability of LiCoO2 electrodes. *Electrochem. Commun.* **2005,** 7, 1298-1304.

Markovsky, B.; Rodkin, A.; Cohen, Y. S.; Palchik, O.; Levi, E.; Aurbach, D.; Kim, H. J.; Schmidt, M., The study of capacity fading processes of Li-ion batteries: major factors that play a role. *J. Power Sources* **2003,** 119-121, 504-510.

Marschilok, A. C.; Kim, Y. J.; Takeuchi, K. J.; Takeuchi, E. S., In situ-generation of electrically conductive nanoparticles in bimetallic phosphate materials for high power lithium batteries. *ECS Trans.* **2012,** 41, 1-7.

Marschilok, A. C.; Kim, Y. J.; Takeuchi, K. J.; Takeuchi, E. S., Silver vanadium phosphorous oxide, Ag0.48VOPO4: exploration as a cathode material in primary and secondary battery applications. *J. Electrochem. Soc.* **2012,** 159, A1690-A1695.

Marschilok, A. C.; Kozarsky, E. S.; Tanzil, K.; Zhu, S.; Takeuchi, K. J.; Takeuchi, E. S., Electrochemical reduction of silver vanadium phosphorous oxide, Ag2VO2PO4: Silver metal deposition and associated increase in electrical conductivity. *J. Power Sources* **2010,** 195, 6839-6846.

Marschilok, A. C.; Takeuchi, K. J.; Takeuchi, E. S., Evaluation of silver vanadium phosphorous oxide as a cathode material in lithium primary cells. *AIChE Annu. Meet., Conf. Proc.* **2008**, 122/1-122/10.

Marschilok, A. C.; Takeuchi, K. J.; Takeuchi, E. S., Preparation and electrochemistry of silver vanadium Phosphorous oxide, Ag2VO2PO4. *Electrochem. Solid-State Lett.* **2008,** 12, A5-A9.

Merritt, D. R.; Schmidt, C. L., Impedance modeling of the lithium/manganese dioxide battery. *Proc. - Electrochem. Soc.* **1993**, 138-45.

Merritt, D. R.; Schmidt, C. L., Investigation of cathodic current collection in lithium/manganese dioxide cells by electrochemical impedance spectroscopy. *Proc. - Electrochem. Soc.* **1994,** 94-4, 169-76.

Moore, J. W.; Pearson, R. G., *Kinetics and Mechanism. 3rd Ed.* **1981**; p 455 pp.

Moser, J. R. Solid State lithium iodine primary battery. US Patent 36660163, **1972**.

Nagao, M.; Pitteloud, C.; Kamiyama, T.; Otomo, T.; Itoh, K.; Fukunaga, T.; Kanno, R., Further Understanding of Reaction Processes in Electrolytic Manganese Dioxide Electrodes for Lithium Cells. *J. Electrochem. Soc.* **2005,** 152, E230-E237.

Nagarwal, R. C.; Ridhurkar, D. N.; Pandit, J. K., In vitro release kinetics and bioavailability of gastroretentive cinnarizine hydrochloride tablet. *AAPS PharmSciTech* **2010,** 11, 294-303.

Nagata, M.; Saraswat, A.; Nakahara, H.; Yumoto, H.; Skinlo, D. M.; Takeya, K.; Tsukamoto, H., Miniature pin-type lithium batteries for medical applications. *J. Power Sources* **2005,** 146, 762-765.

Nakajima, T.; Hagiwara, R.; Moriya, K.; Watanabe, N., Discharge characteristics of poly(carbon monofluoride) prepared from the residual carbon obtained by thermal decomposition of poly(dicarbon monofluoride) and graphite oxide. *J. Electrochem. Soc.* **1986,** 133, 1761-6.

Nakajima, T.; Mabuchi, A.; Hagiwara, R.; Watanabe, N.; Nakamura, F., Discharge characteristics of graphite fluoride prepared via graphite oxide. *J. Electrochem. Soc.* **1988,** 135, 273-7.

Nardi, J. C., Characterization of the lithium/manganese dioxide multistep discharge. *J. Electrochem. Soc.* **1985,** 132, 1787-91.

Nernst, W., Theory of the Reaction Rate in Heterogeneous Systems. [machine translation]. *Z. f. physik. Ch.* **1904,** 47, 52-55.

Nishio, K., PRIMARY BATTERIES - NONAQUEOUS SYSTEMS | Lithium-Manganese Dioxide. In *Encyclopedia of Electrochemical Power Sources*, x00Fc; rgen, G., Eds. Elsevier: Amsterdam, **2009**, pp 83-92.

Nishio, K.; Yoshimura, S.; Saito, T., Discharge characteristics of manganese dioxide/lithium cells in various electrolyte solutions. *J. Power Sources* **1995,** 55, 115-17.

Noyes, A. A.; Whitney, W. R., The rate of solution of solid substances in their own solutions. *J. Am. Chem. Soc.* **1897,** 19, 930-4.

Ochida, M.; Domi, Y.; Doi, T.; Tsubouchi, S.; Nakagawa, H.; Yamanaka, T.; Abe, T.; Ogumi, Z., Influence of manganese dissolution on the degradation of surface films on edge plane graphite negative-electrodes in lithium-ion batteries. *J. Electrochem. Soc.* **2012,** 159, A961-A966.

Ohzuku, T.; Kitagawa, M.; Hirai, T., Electrochemistry of manganese dioxide in lithium nonaqueous cell. I. X-ray diffractional study on the reduction of electrolytic manganese dioxide. *J. Electrochem. Soc.* **1989,** 136, 3169-74.

Onoda, M.; Kanbe, K., Crystal structure and electronic properties of the Ag2V4O11 insertion electrode. *J. Phys. Condens. Matter* **2001,** 13, 6675-6685.

Owens, B. B.; Skarstad, P. M.; Untereker, D. F.; Passerini, S., Solid-electrolyte Batteries. In *Handbook of Batteries*, 3rd ed.; Linden, D.; Reddy, T. B., Eds. McGraw-Hill: **2002**.

Padhi, A. K.; Nanjundaswamy, K. S.; Goodenough, J. B., Phospho-olivines as positive-electrode materials for rechargeable lithium batteries. *J. Electrochem. Soc.* **1997,** 144, 1188-1194.

Papadopoulou, V.; Kosmidis, K.; Vlachou, M.; Macheras, P., On the use of the Weibull function for the discernment of drug release mechanisms. *Int. J. Pharm.* **2006,** 309, 44-50.

Park, K. S.; Son, J. T.; Chung, H. T.; Kim, S. J.; Lee, C. H.; Kang, K. T.; Kim, H. G., Surface modification by silver coating for improving electrochemical properties of LiFePO4. *Solid State Commun.* **2004,** 129, 311-314.

Paterson, R., *An Introduction to Ion Exchange*. **1970**.

Patridge, C. J.; Jaye, C.; Abtew, T. A.; Ravel, B.; Fischer, D. A.; Marschilok, A. C.; Zhang, P.; Takeuchi, K. J.; Takeuchi, E. S.; Banerjee, S., An X-ray Absorption Spectroscopy Study of the Cathodic Discharge of Ag2VO2PO4: Geometric and Electronic Structure Characterization of Intermediate phases and Mechanistic Insights. *J. Phys. Chem. C* **2011,** 115, 14437-14447.

Patterson, A. L., The Scherrer formula for x-ray particle-size determination. *Phys. Rev.* **1939,** 56, 978-82.

Phipps, J. B.; Hayes, T. G.; Skarstad, P. M.; Untereker, D. F., In-situ formation of a solid/liquid composite electrolyte in lithium-iodine batteries. *Solid State Ionics* **1986,** 18-19, 1073-7.

Pistoia, G., Some restatements on the nature and behavior of manganese(IV) oxide for lithium batteries. *J. Electrochem. Soc.* **1982,** 129, 1861-5.

Ramasamy, R. P.; Feger, C.; Strange, T.; Popov, B. N., Discharge characteristics of silver vanadium oxide cathodes. *J. Appl. Electrochem.* **2006,** 36, 487-497.

Randles, J. E. B., KINETICS OF RAPID ELECTRODE REACTIONS. *Discussions of the Faraday Society* **1947,** 1, 11-19.

Ravel, B.; Newville, M., ATHENA, ARTEMIS, HEPHAESTUS: data analysis for x-ray absorption spectroscopy using IFEFFIT. *J. Synchrotron Radiat.* **2005,** 12, 537-541.

Read, J.; Collins, E.; Piekarski, B.; Zhang, S., LiF Formation and Cathode Swelling in the Li/CFx Battery. *J. Electrochem. Soc.* **2011,** 158, A504-A510.

Reichardt, C. W., T., *Solvents and Solvent Effects in Organic Chemistry*. 4th ed.; Wiley-VCH: Weinheim, Germany, **2011**.

Rohrer, G. S., *Structure and Bonding in Crystalline Materials*. Cambridge University Press: United Kingdom, **2001**; p 540.

Root, M. J., Lithium-manganese dioxide cells for implantable defibrillator devices-Discharge voltage models. *J. Power Sources* **2010,** 195, 5089-5093.

Root, M. J., Resistance Model for Lithium-Silver Vanadium Oxide Cells. *J. Electrochem. Soc.* **2011,** 158, A1347-A1353.

Rubino, R. S.; Gan, H.; Takeuchi, E. S., A study of capacity fade in cylindrical and prismatic lithium-ion batteries. *J. Electrochem. Soc.* **2001,** 148, A1029-A1033.

Sathe, P. M.; Venitz, J., Comparison of neural network and multiple linear regression as dissolution predictors. *Drug Dev. Ind. Pharm.* **2003,** 29, 349-355.

Sauvage, F.; Bodenez, V.; Tarascon, J.-M.; Poeppelmeier, K. R., Room-Temperature Synthesis Leading to Nanocrystalline Ag2V4O11. *J. Am. Chem. Soc.* **2010,** 132, 6778-6782.

Sauvage, F.; Bodenez, V.; Vezin, H.; Morcrette, M.; Tarascon, J. M.; Poeppelmeier, K. R., Structural and transport evolution in the LixAg2V4O11 system. *J. Power Sources* **2010,** 195, 1195-1201.

Schmidt, C. L.; Skarstad, P. M., Development of an equivalent-circuit model for the lithium/iodine battery. *J. Power Sources* **1997,** 65, 121-128.

Schneider, A. A.; Bowser, G. C.; Foxwell, L. H. Lithium Iodine Primary Cells Having Novel Pelletized Depolarizer. Patent 4148975, **1979**.

Schneider, A. A.; Moser, J. R. Primary Cells and iodine-containing cathodes therefor. US Patent 3674562, **1972**.

Shannon, R. D., Revised effective ionic radii and systematic studies of interatomic distances in halides and chalcogenides. *Acta Crystallographica, Section A: Crystal Physics, Diffraction, Theoretical and General Crystallography* **1976,** A32, 751-67.

Shao-Horn, Y.; Hackney, S. A.; Cornilsen, B. C., Structural characterization of heat-treated electrolytic manganese dioxide and topotactic transformation of discharge products in the Li-MnO2 cells. *J. Electrochem. Soc.* **1997,** 144, 3147-3153.

Shi, Q.; Hu, R.; Zeng, M.; Dai, M.; Zhu, M., The cycle performance and capacity fading mechanism of a LiV3O8 thin-film electrode with a mixed amorphous-nanocrystalline microstructure. *Electrochim. Acta* **2011,** 56, 9329-9336.

Shi, S.; Lu, P.; Liu, Z.; Qi, Y.; Hector, L. G.; Li, H.; Harris, S. J., Direct Calculation of Li-Ion Transport in the Solid Electrolyte Interphase. *J. Am. Chem. Soc.* **2012,** 134, 15476-15487.

Shi, S. J.; Tu, J. P.; Tang, Y. Y.; Zhang, Y. Q.; Liu, X. Y.; Wang, X. L.; Gu, C. D., Enhanced electrochemical performance of LiF-modified LiNi1/3Co1/3Mn1/3O2 cathode materials for Li-ion batteries. *J. Power Sources* **2013,** 225, 338-346.

Takeuchi, E. S., Reliability systems for implantable cardiac defibrillator batteries. *J. Power Sources* **1995,** 54, 115-19.

Takeuchi, E. S.; Gan, H.; Palazzo, M.; Leising, R. A.; Davis, S. M., Anode passivation and electrolyte solvent disproportionation: Mechanism of ester exchange reaction in lithium-ion batteries. *J. Electrochem. Soc.* **1997,** 144, 1944-1948.

Takeuchi, E. S.; Kim, Y. J.; Lee, C.-Y.; Kozarsky, E. S.; Sharma, M. K.; Zhu, S.; Marschilok, A. C.; Takeuchi, K. J., Silver vanadium phosphorous oxide: Resistivity and morphology study. *Abstracts of Papers, 240th ACS National Meeting, Boston, MA, United States, August 22-26, 2010* **2010**, ANYL-283.

Takeuchi, E. S.; Lee, C.-Y.; Cheng, P.-J.; Menard, M. C.; Marschilok, A. C.; Takeuchi, K. J., Silver vanadium diphosphate Ag2VP2O8: electrochemistry and characterization of reduced material providing mechanistic insights. *J. Solid State Chem.* **2013,** 200, 232-240.

Takeuchi, E. S.; Leising, R. A., Lithium batteries for biomedical applications. *MRS Bull.* **2002,** 27, 624-627.

Takeuchi, E. S.; Marschilok, A. C.; Leising, R. A.; Takeuchi, K. J., Sol-gel synthesis and controlled sintering of silver vanadium oxide. *J. Power Sources* **2007,** 174, 552-553.

Takeuchi, E. S.; Marschilok, A. C.; Takeuchi, K. J.; Ignatov, A.; Zhong, Z.; Croft, M., Energy dispersive X-ray diffraction of lithium-silver vanadium phosphorous oxide cells: in situ cathode depth profiling of an electrochemical reduction-displacement reaction. *Energy & Environmental Science* **2013,** 6, 1465-1470.

Takeuchi, E. S.; Marschilok, A. C.; Tanzil, K.; Kozarsky, E. S.; Zhu, S.; Takeuchi, K. J., Electrochemical Reduction of Silver Vanadium Phosphorus Oxide, Ag2VO2PO4: The Formation of Electrically Conductive Metallic Silver Nanoparticles. *Chem. Mater.* **2009,** 21, 4934-4939.

Takeuchi, E. S.; Piliero, P., Lithium/silver vanadium oxide batteries with various silver to vanadium ratios. *J. Power Sources* **1987,** 21, 133-41.

Takeuchi, E. S.; Thiebolt, W. C., III, The reduction of silver vanadium oxide in lithium/silver vanadium oxide cells. *J. Electrochem. Soc.* **1988,** 135, 2691-4.

Takeuchi, K. J.; Leising, R. A.; Palazzo, M. J.; Marschilok, A. C.; Takeuchi, E. S., Advanced lithium batteries for implantable medical devices: mechanistic study of SVO cathode synthesis. *J. Power Sources* **2003,** 119-121, 973-978.

Takeuchi, K. J.; Marschilok, A. C.; Davis, S. M.; Leising, R. A.; Takeuchi, E. S., Silver vanadium oxides and related battery applications. *Coord. Chem. Rev.* **2001,** 219-221, 283-310.

Tarascon, J. M.; Armand, M., Issues and challenges facing rechargeable lithium batteries. *Nature (London, U. K.)* **2001,** 414, 359-367.

Touhara, H.; Fujimoto, H.; Watanabe, N.; Tressaud, A., Discharge reaction mechanism in graphite fluoride-lithium batteries. *Solid State Ionics* **1984,** 14, 163-70.

van de Waterbeemd, H.; Testa, B.; Editors, *Drug Bioavailability; Estimation of Solubility, Permeability, Absorption and Bioavailability; Second, Completely Revised Edition. [In: Methods Princ. Med. Chem., 2009; 40]*. **2009**; p 623 pp.

Van Vooren, L.; Krikilion, G.; Rosier, J.; De Spiegeleer, B., A novel bending point criterion for dissolution profile interpretation. *Drug Dev. Ind. Pharm.* **2001,** 27, 885-892.

Varma, M. V. S.; Kaushal, A. M.; Garg, S., Influence of micro-environmental pH on the gel layer behavior and release of a basic drug from various hydrophilic matrices. *J. Controlled Release* **2005,** 103, 499-510.

Wang, H.-C.; Lu, C.-H., Dissolution behavior of chromium-ion doped spinel lithium manganate at elevated temperatures. *J. Power Sources* **2003,** 119-121, 738-742.

Wang, Z.; Huang, X.; Chen, L., Characterization of Spontaneous Reactions of LiCoO2 with Electrolyte Solvent for Lithium-Ion Batteries. *J. Electrochem. Soc.* **2004,** 151, A1641-A1652.

Wanty, R. B.; Goldhaber, M. B., Thermodynamics and kinetics of reactions involving vanadium in natural systems: accumulation of vanadium in sedimentary rocks. *Geochim. Cosmochim. Acta* **1992,** 56, 1471-83.

Watanabe, K.; Fukuda, M. High energy density battery. U.S. Patent Number 3700502, **1972**.

Watanabe, K.; Fukuda, M. Primary cell for electric batteries. U.S. Patent No. 3536532, **1970**.

Watanabe, N.; Nakajima, T.; Hagiwara, R., Discharge reaction and overpotential of the graphite fluoride cathode in a nonaqueous lithium cell. *J. Power Sources* **1987,** 20, 87-92.

Weibull, W., A statistical distribution of wide applicability. *Journal of Applied Mechanics* **1951,** 18, 293-297.

Weinstein, L.; Yourey, W.; Gural, J.; Amatucci, G. G., Electrochemical Impedance Spectroscopy of Electrochemically Self-Assembled Lithium-Iodine Batteries. *J. Electrochem. Soc.* **2008,** 155, A590-A598.

Yagi, S.; Kunii, D., Combustion of carbon particles in flames and fluidized beds. *5th Symposium on Combustion, Pittsburgh* **1955**, 231-44.

Yang, L.; Takahashi, M.; Wang, B., A study on capacity fading of lithium-ion battery with manganese spinel positive electrode during cycling. *Electrochim. Acta* **2006,** 51, 3228-3234.

Zdanovskii, A. B., The role of the interphase solution in the kinetics of the solution of salts. *Zh. Fiz. Khim.* **1946,** 20, 869-80.

Zhan, C.; Lu, J.; Kropf, A. J.; Wu, T.; Jansen, A. N.; Sun, Y.-K.; Qiu, X.; Amine, K., Mn(II) deposition on anodes and its effects on capacity fade in spinel lithium manganate-carbon systems. *Nat. Commun.* **2013,** 4, 3437, 8 pp.

Zhang, S.; Li, W.; Li, C.; Chen, J., Synthesis, Characterization, and Electrochemical Properties of Ag2V4O11 and AgVO3 1-D Nano/Microstructures. *J. Phys. Chem. B* **2006,** 110, 24855-24863.

Zhang, S. S.; Foster, D.; Read, J., Carbothermal treatment for the improved discharge performance of primary Li/CFx battery. *J. Power Sources* **2009,** 191, 648-652.

Zhang, S. S.; Foster, D.; Read, J., Enhancement of discharge performance of Li/CFx cell by thermal treatment of CFx cathode material. *J. Power Sources* **2009,** 188, 601-605.

Zhang, S. S.; Foster, D.; Wolfenstine, J.; Read, J., Electrochemical characteristic and discharge mechanism of a primary Li/CFx cell. *J. Power Sources* **2009,** 187, 233-237.

Zheng, H.; Sun, Q.; Liu, G.; Song, X.; Battaglia, V. S., Correlation between dissolution behavior and electrochemical cycling performance for LiNi1/3Co1/3Mn1/3O2-based cells. *J. Power Sources* **2012,** 207, 134-140.

Zhu, H. J.; Gavril, M.; Feng, L.; Karpinet, D., Li/CFx medical battery development. *ECS Trans.* **2008,** 11, 11-17.